A Virtual Test Platform for Analyses of Rolling Tyres on Rigid and Deformable Terrains

Shahram Shokouhfar

A Thesis

in

The Department

of

Mechanical and Industrial Engineering

Presented in Partial Fulfillment of the Requirements

for the Degree of Doctor of Philosophy at

Concordia University

Montréal, Québec, Canada

January 2017

CONCORDIA UNIVERSITY

School of Graduate Studies

This is to certify that the thesis proposal prepared

By: **Shahram Shokouhfar**

Entitled: **A Virtual Test Platform for Analyses of Rolling Tyres on Rigid and Deformable Terrains**

and submitted in partial fulfilment of the requirements for the degree of

Doctor of Philosophy

complies with the regulations of this University and meets the accepted standards with respect to originality and quality.

Signed by the final examining committee:

_____ Dr. R. Jayakumar, Chair

_____ Dr. A. Khajepour, External Examiner

_____ Dr. C. Alecsandru, External to Program

_____ Dr. G. J. Gouw, Examiner

_____ Dr. A. K. W. Ahmed, Examiner

_____ Dr. S. Rakheja, Co-supervisor

_____ Dr. M. El-Gindy, Co-supervisor

Approved by _____

Chair of the Department of Mechanical and Industrial Engineering

_____

Dean of the Faculty of Engineering and Computer Science

ABSTRACT

A Virtual Test Platform for Analyses of Rolling Tyres on Rigid and Deformable Terrains

Shahram Shokouhfar,

Concordia University, 2017

Dynamic performance characteristics of wheeled vehicles highly rely on the forces/moments arising from interactions between the pneumatic tyres and the terrains. Reliable models are thus needed to estimate these forces/moments to be used in vehicle simulations for design and developments. The empirical and semi-empirical tyre models developed for vehicle dynamics simulations invariably require extensive experimental data, and may not be applicable under many practical conditions. The structural tyre models, on the other hand, are not suited for vehicle dynamics simulations due to excessive computational demands. Moreover, the tyre modeling on deformable terrains has been addressed in relatively fewer studies due to challenges associated with complex behaviors of soils under moving vehicular loads. Although the Finite Element (FE) tyre models provide accurate estimations of forces/moments on rigid surfaces, the mesh-based nature of FE models of the soils yield poor performance in modeling the soil flow beneath a rolling tyre. Alternatively, meshless methods such as the Smoothed Particle Hydrodynamics (SPH) have been proposed to account for large deformations and fragmentations of the soil.

This dissertation research aims at development of a virtual testing environment for analyses of rolling tyre interactions on rigid and soft terrains using the FE and SPH analysis methods. The virtual platform is used for parametrization and evaluation of the terramechanics-based models as an alternative to actual experiments. A 3-D finite element model of a rolling truck tyre is developed using LS-DYNA to predict its dynamic responses at speeds up to 100 km/h. The model takes into account the complex multi-layered structures of the tyre carcass and belts. A customized pre-processing algorithm is developed to facilitate model reformulations for efficient parametric analyses. The validity of the model is demonstrated by comparing the predicted responses with the experimental data.

The verified tyre model is subsequently employed to study the influences of various operating parameters on the tyre vertical and cornering properties. The modal properties

of the rolling tyre are also analyzed under varying inflation pressure and vertical load, using the large-deformation finite element theory. The eigenvalues are extracted during an explicit dynamic simulation at instants when the tyre stresses reach steady state under a given loading condition. It is shown that some of the eigen-frequencies of a free tyre diverge into two distinct frequencies in the presence of ground contact of the rolling tyre.

A computationally efficient model of the truck tyre is further formulated using the Part-Composite approach in LS-DYNA, where the layers of the rubber matrix and reinforcements are simplified by a single layer of shell elements with layered configuration. The validity of the simplified model is demonstrated through comparisons with the comprehensive tyre model as well as with the experimental data. It is shown that the proposed simplification substantially reduces the total number of elements and thereby enhances the computational efficiency.

A computational soil model is developed using the FE and SPH methods in conjunction with a contact pressure-dependent material model based on the available test data. The soil model is initially validated in terms of volumetric deformation behavior using the experimental data. The relative merits and limitations of the FE and SPH analysis methods are illustrated to justify the use of the SPH soil model for parametrization of the terramechanics formulations characterizing the normal and shear behavior of soil. The effectiveness of parameters identification method is demonstrated via comparisons with reported data obtained from classical bevameter and triaxial force measurement devices. The soil model is subsequently integrated to the simplified pneumatic tyre and rigid wheel models for analyses of tyre forces developed while traversing different deformable terrains. The simulation results obtained for the rolling and steered tyre showed good agreements with the analytically estimated contact force/moment responses.

To my dear wife, Mona,

for her love, support and patience during my pursuit of PhD degree

and to my lovely little son, Navid

ACKNOWLEDGEMENTS

I would like to appreciate my research advisor, Dr. Subhash Rakheja, for his continuous guidance and valuable criticism throughout the course of my PhD. I have learned a lot from him and I am grateful for his fatherly care and responsibility. His determination and passion for perfection always inspired me to work hard and I will be truly indebted to him throughout my life time. I would also like to thank my second advisor, Dr. Moustafa El-Gindy, for providing me with the infrastructure and requisite materials regarding my research. This research might not have been possible without his constant counsel and involvement. I extend thanks to my professors at Concordia University: Dr. Waizuddin Ahmed, Dr. Iraj Mantegh, Dr. Rajamohan Ganesan and Dr. Kinh Ha for providing me with the fundamentals of vehicle dynamics, structural analysis and finite element method. I also wish to acknowledge Concordia University, the Department of Mechanical and Industrial Engineering and the CONCAVE Research Center for their collaborations and providing financial supports.

I greatly acknowledge the guidance received from Mr. James Kennedy regarding modeling in LS-DYNA. I also thank Mr. Len Schwer for kindly providing me with his class notes on geomaterials and laboratory tests for calibrating the soil model in LS-DYNA. I extend thanks to my dear friend, Mr. Mohsen Tayefeh, for his helpful workshops on ANSYS and LS-DYNA in SimuTech Group. I am thankful to my friends: Amir Kolaei, Siavash Taheri, Azadeh Farazandeh, Hamid Khorrami, Mohammad Keshmiri, Ali Fellah Jahromi, and Alireza Hassanbeiglou for their sincere friendship which highly supported my social and educational life in Canada. I am extremely grateful to my parents and family for their endless support and abiding my ignorance during my abroad studies. Finally, I owe thanks to my dear wife, Mona Rais Esmaili, for her unconditional love and support and the patience she showed during my PhD studies. I greatly value her contribution and deeply appreciate her belief in me.

TABLE OF CONTENTS

List of Figures

List of Tables

Nomenclature

Notation	*Description*
$a_\circ, a_1, a_2$	Yield surface function coefficients
$[B]$	Strain-displacement matrix
b	Radius of circular plate, and width of tyre-soil contact region
C_{10}, C_{01}	Elastic constants in Mooney-Rivlin's material model
CSLH	Scale factor for smoothing length
c	Soil cohesion stress
c_1, c_2	Constants dependent on soil property in relation between θ_m and i
cec	Cord-end-count (number of cords per unit length)
$[D]$	Stress-strain matrix
DE	Discrete Element
d	Cord diameter
d_c	Decay coefficient in friction coefficient formulation
E, E_1, E_2, E_3	Young's modulus, Young's moduli in cord axes system
E_c, E_r	Young's modulus of twisted cords and pure rubber
EOS	Equation Of State
F_x, F_y, F_z	Contact forces in longitudinal, lateral and vertical directions
F_τ, F_σ	Thrust and resistant components of longitudinal force
FE	Finite Element
f_n	Natural frequency
f_v	Cord volume fraction
G, G_{21}, G_{31}, G_{32}	Shear modulus, shear moduli in cord axes system
$[G]$	Matrix of shape-function derivatives
HMIN, HMAX	Scale factors for max and min of smoothing length
$h_\circ$	Initial smoothing length
$h(t)$	Smoothing length
i	Longitudinal slip (or skid) ratio
J_2'	Second invariant of the deviatoric stress tensor
j, j_x, j_y	Shear displacement and that along longitudinal and lateral directions
$K, K_\circ$	Shear displacement modulus of soil and its intercept
K_u	Bulk unloading modulus of soil
$[K]$	Assembled stiffness matrix
$[K]^{(e)}$	Stiffness matrix of element (e)
$[K_{geo}]$	Geometric (or initial) stiffness matrix
$[K_{mat}]$	Material stiffness matrix
k_b	Soil material parameter defined as $k_c/b + k_\phi$
k_c, k_ϕ	Cohesive and frictional moduli in Bekker's pressure-sinkage equation

Notation	*Description*
$L_\circ, L$	Initial and current length of the specimen
M_y, M_z	Rolling resistance and aligning moments
$[M]$	Assembled mass matrix
N_c	Number of circumferential divisions
n	Exponent in Bekker's pressure-sinkage equation
p	Pressure
R_e	Tyre effective rolling radius
r, R	Radius of the unloaded and loaded tyre at the contact region
s_{ij}	Deviatoric stress tensor
SPH	Smoothed Particle Hydrodynamics
t	Composite layer thickness
V, V_{rel}	Tyre speed, relative velocity between tyre and road
$V^{(e)}$	Volume of element (e)
$V_\circ, V$	Initial and current volume of the specimen
v_x	Velocity of tyre
z	Sinkage of the circular plate or tyre into the soil
α	Side-slip angle
α_s	Mass-wighted damping coefficient for soil elements
β	Orientation of cords in element axes system
γ	Slope of shear displacement modulus
δ	Logarithmic decrement
Δ	Static tyre deflection
$\epsilon_v, \epsilon_{\log}$	Volumetric strain ($\Delta V/V_\circ$) and logarithmic volume strain ($\log V/V_\circ$)
ζ	Local sinkage at angle θ
ζ_1, ζ_2	Parameters in Halpin-Tsai equations
ζ_s	Damping ratio of soil
η	Tyre sinkage ratio
$\theta, \theta_f, \theta_r$	Angular location and that at front and rear regions of contact patch
$\theta_1, \theta_2, \theta_m$	Entrance and exit angles and that at the maximum radial stress
μ, μ_s, μ_d	Coefficient of friction, static and dynamic coefficients of friction
ν, ν_{21}, ν_{31}, ν_{32}	Poisson's ratio, Poisson's ratios in cord axes system
ρ, ρ_c, ρ_r	Density, density of twisted cords and pure rubber
$[\sigma]$	Current state of stress
$\sigma_a, \sigma_c, \sigma_\Delta$	Axial stress, confining pressure and stress difference $(\sigma_a - \sigma_c)$
σ_r	Radial stress
τ_d	Period of damped oscillations
τ_x, τ_y	Shear stresses in the longitudinal and lateral directions
$\{\Phi_i\}$	Mode shape vector (eigenvector) of mode i
ϕ	Angle of shearing resistance
ω_i	Natural circular frequency (eigenvalue) of mode i
ω_y	Angular velocity of tyre

Chapter 1

Literature Review and Scope of the Dissertation

1.1 Introduction

Automotive industries need to evaluate dynamic performance of vehicles via computer simulations under different operating conditions. Reliable models of vehicle components are thus essential for applications in such analyses. Among the various components, the pneumatic tyre and the terrain are of vital importance as the dynamic behavior of vehicles highly depends on the forces and moments produced from the tyre-terrain interactions. Extensive studies have been reported on modeling and analysis of pneumatic tyres running over rigid and soft terrains. The tyre models developed for vehicle dynamics simulations are generally based on phenomenological formulations for predicting the tyre-terrain contact force/moment responses over a range of operating parameters [1–5]. These models necessitate prior evaluations of the model parameters via comprehensive experiments [6–8], and represent only the overall tyre-terrain properties that directly affect the vehicle dynamic performance. The important effects of the structural design parameters and material properties are thus entirely ignored. Alternatively, structural tyre models have evolved for the purpose of design and developments. These models use numerical approaches such as the finite element methods, which allow for a detailed representation of the multi-layered tyre structure and material properties of individual layers [9–11]. Such structural models have been effectively applied for virtual dynamic performance tests [12], modal analyses [13],

and design sensitivity studies and optimizations [14], although the vast majority are limited to non-rolling tyres. Owing to their extensive computational demands, these model are not well-suited for vehicle system simulations [14, 15].

In vast majority of the tyre modeling studies, the terrain is assumed as a rigid surface ranging from a smooth flat road to an uneven terrain with high frequency irregularities. The interactions of rolling tyres with soft terrains, however, have been addressed in only a few studies, due to extreme challenges associated with the complex constitutive behavior of soils when subjected to rolling tyre loads. Some theoretical studies have employed the terramechanics-based models developed by Bekker [16–18] and Wong [19, 20] to predict the tyre-soil contact forces and moments via integration of the normal and tangential stresses under a rolling wheel over the contact region. These models could describe the steady-state operation of a rigid wheel on soft soils, aimed at multi-body dynamics simulations of planetary exploration rovers [21–23].

A number of studies have proposed numerical soil models using the finite element methods for integration with the structural tyre models. These have employed widely different material models to represent the constitutive behavior of soils ranging from a simple elastic-plastic model, which neglects the moisture content and cohesion between soil particles [24–26], to advanced models such as the Mohr-Coulomb and the Drucker-Prager [27–31]. The advanced material models have been developed to account for effects of both the cohesion and pressure-dependent strength of soils, while their input material data need to be determined using laboratory tests. While the finite element methods yield satisfactory modeling of complex structures of pneumatic tyres [10, 12, 24, 32], some studies have reported their poor performance when modeling large deformations associated with soil flow under dynamic vehicular loads [24, 25]. Alternatively, mesh-less approaches such as the Smoothed Particle Hydrodynamics technique [33] have been proposed to account for large deformations and fragmentations of the soil particles [34–39]. The performance potentials of the SPH technique, however, have been explored in only a few studies [25, 40]. Moreover, this technique is extremely demanding on computing resources [25, 41–45]. Consequently, most studies involving SPH soil modeling use a rigid wheel model and neglect the tyre compliance to improve computational efficiency [25]. A few recent studies have

attempted to identify the model parameters associated with analytical on-road and off-road rigid ring tyre models using virtual testing environments as an alternative to the costly hardware experiments [24, 46]. Considerable efforts in modeling of tyre-soil interactions are continuing in order to seek efficient and effective modeling techniques especially for study of off-road vehicles dynamics. Only few studies, however, have attempted tyre-soil models with only limited applications for off-road vehicles.

This dissertation research aims to develop a computational tyre-soil model using numerical techniques to be employed as a virtual test environment for evaluating dynamic response characteristics and parametrization of theoretical terramechanics-based tyre-soil interaction models. A 3-D finite element model of a truck tyre is initially developed and validated for predicting its dynamics responses on a rigid flat road. The modal properties of the tyre model are evaluated under the influences of inflation pressure, ground contact and rolling speed. A computationally efficient methodology is further proposed via simplifying the multiple layered tyre structure by a single composite part with layered configuration. Subsequently, a soil model is developed using the FE and SPH methods with a pressure-dependent material model. The soil model is utilized for parametrization of the terramechanics-based formulations characterizing normal and shear properties of the soil. Finally, the parameterized terramechanics-based models are evaluated and verified via comparisons of the theoretically estimated contact forces/moments with those predicted by the virtual tyre-soil testing platform for the stationary, rolling and steered tyre/wheel models.

1.2 Literature review

The reported studies on tyre-terrain interactions have been critically reviewed so as to achieve essential knowledge on modeling techniques and build the scope of the dissertation research. The state-of-the-art on tyre-soil modeling is summarized in the following subsections with particular focus on: (1) pneumatic tyre modeling methodologies for vehicle system analyses and developments; (2) structural tyre models developed using the finite element methods; (3) modal analysis of rolling tyres considering the effects of inflation

pressure, ground contact and rolling speed; (4) efficient representation of the multi-layered tyre structure; (5) soil modeling theories, formulations and analysis methods, and material constitutive models; and (6) computational tyre-soil interaction models using different analysis methods.

1.2.1 Tyre modeling

Computer simulations of vehicle multi-body systems have been widely adopted by automotive designers as a functional tool for evaluating dynamic performance of vehicles. Dynamic performance of ground-vehicles are strongly dependent on the forces and moments developed at the tyre-ground interface. The tyre forces/moments are complex functions of various design and operating parameters, namely, the tyre structure, material properties, inflation pressure, vertical load, rolling speed, terrain profile, tyre-ground friction and more. A number of tyre models of varying complexities have evolved over the past many decades for estimating tyre forces and moments. Considerable efforts in modeling of tyres, however, are continuing in order to seek effective and computationally efficient predictions of forces and moments for applications in vehicle dynamic analyses. The reported tyre models can be classified into three broad categories on the basis of the modeling approach, namely, physics-based, phenomenological and structural models.

Physics-based tyre models

A number of two- and three-dimensional physics-based models have been reported for predictions of in-plane and out-of-plane tyre-ground forces. These models, invariably, employ fundamental mechanical elements such as mass, spring and damping elements to describe dynamic tyre properties for estimating the forces and moments as functions of tyre deformations, longitudinal slip/skid, side-slip angle, normal load and rolling speed. Early physics-based tyre models primarily focused on vertical dynamics of non-rolling tyres for vehicle ride simulations [1, 47–50]. Captain et al. [1] proposed four different models describing different tyre-road contact geometries such as a single point-contact, a rigid roller-contact, a distributed-contact and a radial-adaptive contact, as shown in Figure 1.1.

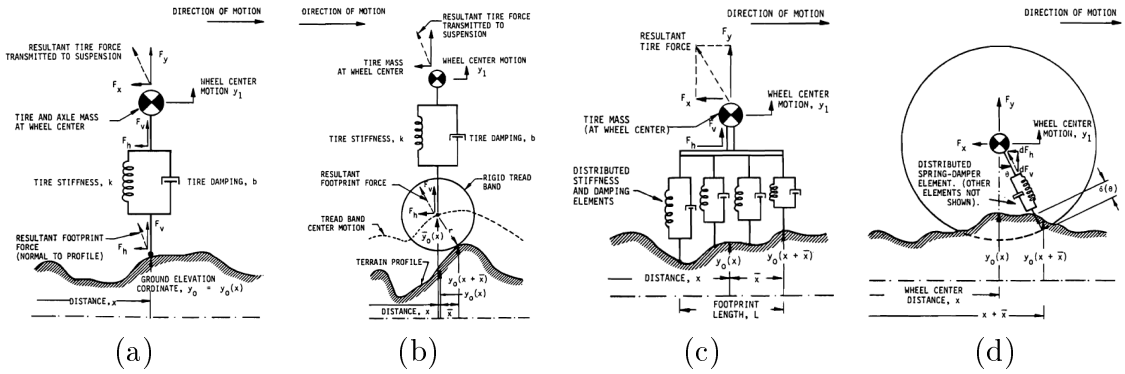

Figure 1.1: Four analytical tyre models evaluated by Captain et al. [1]: (a) point contact, (b) rigid tread band, (c) fixed footprint, (d) adaptive footprint

The vehicle ride and braking analyses mostly employ in-plane physics-based tyre models, where the belts and tyre tread are considered as a rigid or flexible ring supported on an elastic foundation representing the tyre sidewalls [3, 51–54]. Figures 1.2(a) and 1.2(b) illustrate the rigid ring tyre model by Pacejka and Zegelaar [51, 55] as well as the flexible ring tyre model by Kim and Savkoor [52], respectively. Such models have shown their effectiveness for analysis of vehicle ride vibrations under road excitations in the low- to mid-frequency ranges [47, 54, 56, 57]. Bernard [58] introduced a brush type model for ride-response analyses under higher frequency terrain excitations by incorporating tyre slip and enveloping properties. Schmeitz et al. [5] proposed an effective road profile technique to

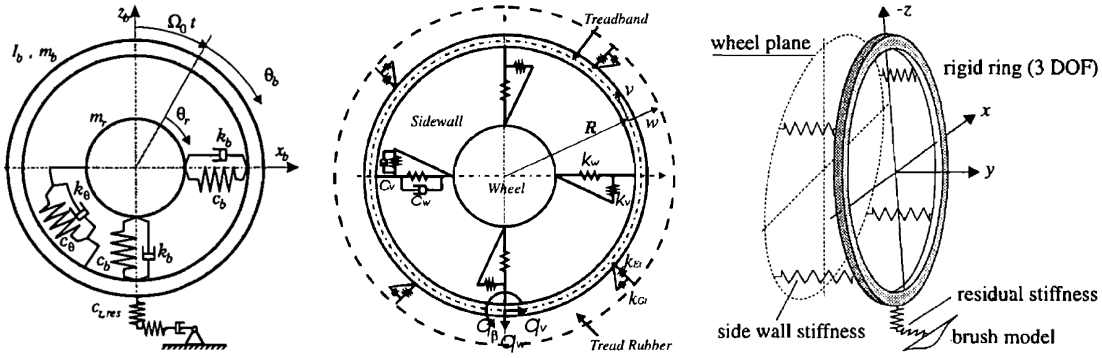

Figure 1.2: (a) Rigid ring tyre model by Zegelaar and Pacejka [51], (b) Flexible ring tyre model by Kim and Savkoor [52], and (c) 3-D rigid-ring tyre model by Maurice [4]

enhance ring tyre models applications under higher frequency excitations.

The out-of-plane behavior of a pneumatic tyre has been considered in a number of studies. Fiala [59] formulated the lateral force as well as the self-aligning moment produced due to a constant side-slip angle, considering the normal load, road friction and the tyre elastic properties. Dugoff et al. [60], Bernard [58] and Deur [61] formulated tyre models for predicting both the traction and cornering tyre responses under combined longitudinal/lateral slips. Maurice [4, 62] developed a 3-D rigid-ring tyre models by introducing the out-of-plane tyre properties to the in-plane rigid-ring tyre model, as schematically illustrated in Figure 1.2(c).

Phenomenological tyre models

Phenomenon-based models of pneumatic tyres have also been proposed on the basis of mathematical representations of measured tyre data. Bakker and Pacejka [2, 63] developed formulations known as the *Magic Formula* tyre model for estimating the steady-state contact forces/moments produced by a rolling tyre based on a number of scaled trigonometric curves. This model has been widely accepted for vehicle dynamics simulations and can provide good estimates of the cornering and braking forces as well as the aligning moment for a wide range of side-slip angles and longitudinal slips. Figure 1.3 illustrates the sample measured points as well as the fitted curves representing these force/moment characteristics. Besselink [64] extended the basic Magic Formula tyre model to include

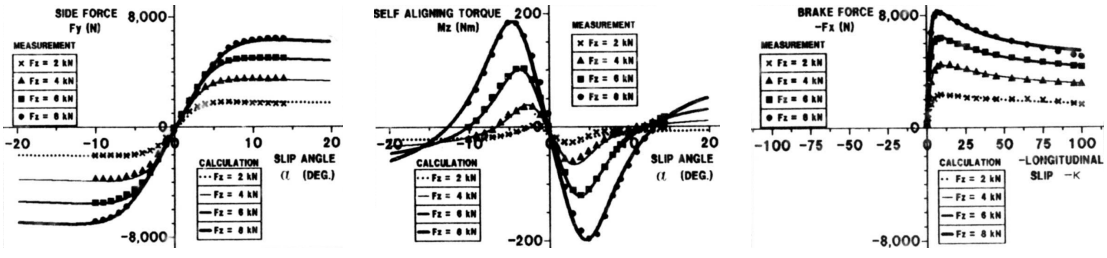

(a) (b) (c)

Figure 1.3: The Magic Formula tyre model by Bakker and Pacejka [2] for estimating (a) the lateral contact force, and (b) the aligning moment as functions of side-slip angle, and (c) the braking force as a function of longitudinal slip

the non-steady-state tyre behavior in rapid transient maneuvers undertaking oscillatory braking and steering inputs.

Semi-empirical tyre models have also been reported, which combine the physics-based and phenomenological tyre models [65–67]. The MF-SWIFT tyre model [65], shown schematically in Figure 1.4, is one of the most advanced semi-empirical tyre models that integrates the in-plane and out-of-plane rigid-ring models by Zegelaar [3, 55] and Maurice [5], the effective road surface model of Schmeitz [68], the Brush Model of Bernard [58], and the Magic Formula model by Pacejka [63]. The effectiveness of this model for handling and ride simulations has been examined by a standard benchmarking system, known as the *Tyre Model Performance Test (TMPT)* [69, 70]. The TMPT [69, 70] is a comprehensive test program to determine the relative reliability and application ranges for two groups of advanced tyre models including the handling tyre models, experiencing low frequency excitations, and the ride tyre models, subject to high frequency excitations. The TMPT has assessed several handling models such as TMeasy [21], MF-Tyre [29, 30], Hankook [22], and Uni Tire [23] as well as various ride models such as the SWIFT [16, 18], FTire [24, 25, 26] and RMOD-K [27, 28] via both measurements and vehicle dynamics analyses in

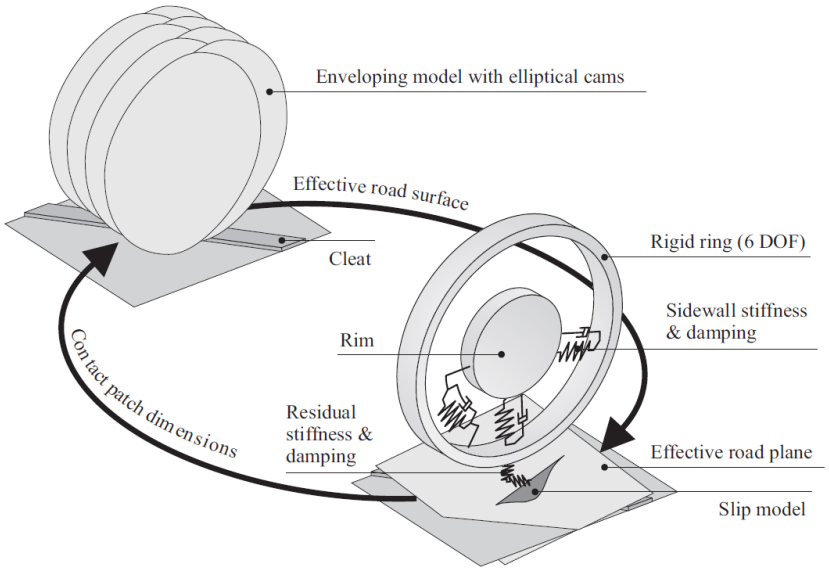

Figure 1.4: A schematic representation of the MF-SWIFT tyre model [65]

multi-body system simulation platforms such as ADAMS, DADS and SIMPACK.

The physics-based and phenomenological tyre models have been extensively used in vehicle system simulations and could yield effective predictions of tyre dynamic responses. Applications of these models, however, require prior identifications of their model parameters via costly and generally limited experiments [6–8, 71]. Moreover, the range of applicability of such models is limited in the vicinity of the operating conditions considered in the tests. Further, these models can only provide global estimations of the tyre-terrain characteristics that directly influence the vehicle performance, while the structural details and material properties of the tyre constituent are entirely disregarded. Therefore, such models do not contribute towards improvements and optimal designs of pneumatic tyres.

Structural tyre models

Structural tyre models employ numerical approaches such as the *Finite Element (FE)* methods, which allow for comprehensive representations of the multi-layered tyre structure and the material properties of individual layers. A vast number of structural models have been developed for design and development of pneumatic tyres, while their applications to vehicle dynamics simulations have been limited due to excessive computational demands. A number of early two-dimensional finite element models had taken advantage of the tyre axisymmetry to achieve computational efficiency and could predict the tyre responses under inflation pressure and centrifugal loading [72, 73]. These models, however, could not account for non-axisymmetric loading and boundary conditions such as the vertical load and ground contact. Three-dimensional finite element tyre models have also been proposed with enhancements in computer technology and numerical procedures [74–78]. These models permitted to consider the three-dimensional tyre structure under more practical loading/boundary conditions. The complex tyre structure has been represented using broadly different methodologies. Shiraishi et al. [79] developed a library of efficient tyre models for vehicle crash simulations using LS-DYNA. Figure 1.5 illustrates the 3-D view and cross-section of the tyre model, which is made of a single layer of membrane elements with orthotropic material properties and inflated as a simple airbag. Although the simplicity of these tyre models considerably enhanced their computational efficiency, their

applications were limited to predicting only the general responses of the tyre in vehicle system simulations [80–82].

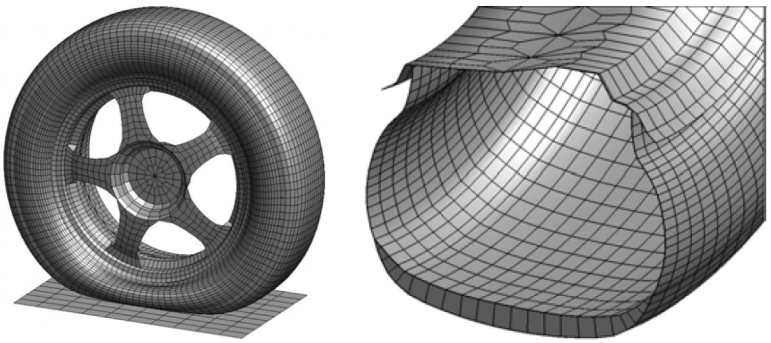

(a) (b)

Figure 1.5: (a) 3-D, and (b) section view of the simplified tyre model developed by Shiraishi and Fukushima [79, 81] for vehicle simulation applications

Zhang et al. [83] used ANSYS to develop a 3-D finite element model for a non-rolling inflated truck tyre in ground contact. Figure 1.6 illustrates the model structure as well as the multi-layered solid elements representing the carcass and belt plies using individual layers of rubber matrix and reinforcements with isotropic and orthotropic materials, respectively. The approach allowed for predicting the stresses between the individual layers and facilitated the selection of a set of tyre design parameters to minimize inter-ply shear

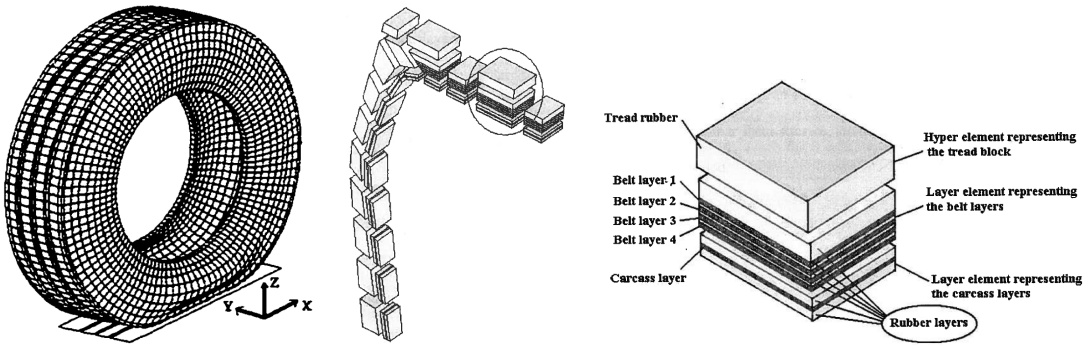

(a) (b) (c)

Figure 1.6: (a) 3-D, (b) half section, and (c) zoom view of the detailed multi-layered composite tyre structure proposed by Zhang et al. [32]

stresses and thereby enhance tyre durability. Ridha [84], Alkan [85] and Wang [86] also proposed similar tyre structure models. These models could effectively predict the contact pressure distribution, footprint size and static tyre stiffness [84–87]. However, due to the computational costs associated with the high number of elements, their applications were limited to static analyses of non-rolling tyres under inflation pressure and footprint loads.

A number of studies represented a rolling tyre model using a non-rolling mesh such that the rigid body rotation of the tyre and its deformations were separately considered in the *Eulerian* and *Lagrangian* frameworks, respectively [88–90]. This technique permitted to enhance the computational efficiency through locally refining the non-rolling mesh only near the tyre-ground contact region, as seen in Figure 1.7. This type of rolling tyre models, however, could only predict the steady-state responses of rolling tyres.

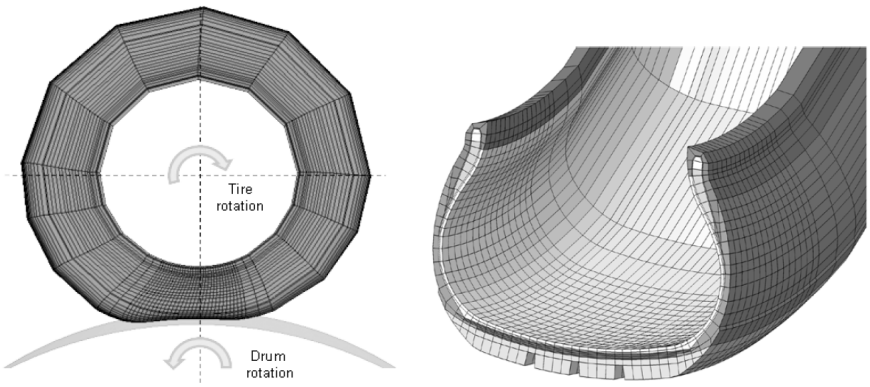

Figure 1.7: (a) 3-D, and (b) section view of the steady-state rolling tyre model proposed by Korunović [90]

The transient responses of a pneumatic tyre have also been investigated in a number of studies using explicit dynamic finite element simulations [10, 12, 91–93]. Chae et al. [92] used PAM-CRASH to develop a 3-D finite element model for a rolling radial-ply truck tyre. Figures 1.8(a) and 1.8(b) illustrate the tyre model together with its half cross-section mesh. The carcass and belt plies were represented using a three-layered membrane element to account for the rubber matrix as well as the reinforcements in the carcass and belt, as shown in Figure 1.8(c). Allen [94], Slade [24, 95], Lescoe [25, 37], Dhillon [26] and Ali [96] have effectively used this approach in PAM-CRASH to predict the transient responses of

a pneumatic truck tyre in traction and cornering test simulations.

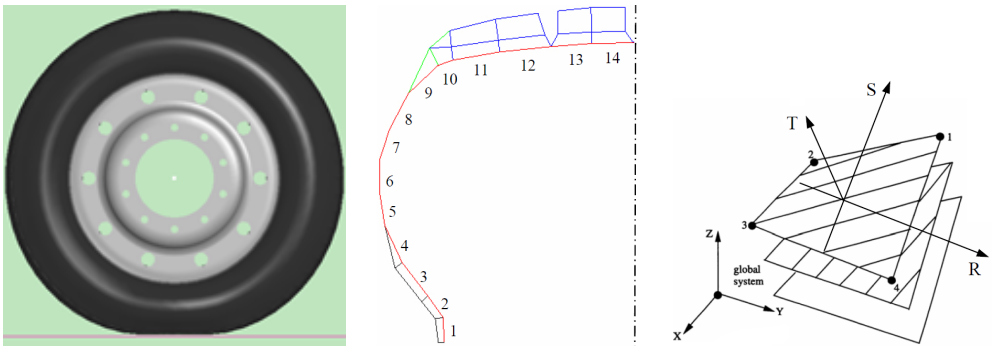

(a) (b) (c)

Figure 1.8: (a) 3-D, and (b) half cross-section of the tyre model by Chae [11], and (c) the three-layered membrane element used in the tyre structure model

Hall et al. [10] used LS-DYNA to develop a 3-D structural tyre model for predicting the tyre transient dynamic responses. Two different grids were generated, one for a stationary loaded tyre with variable mesh density refined locally at the contact region, and the other for a loaded tyre rolling on a flat rigid road with uniform density around the circumference, as shown in Figures 1.9(a) and 1.9(b), respectively. Figure 1.9(c) illustrates the cross-section mesh of the tyre and the wheel rim. The carcass and belt plies were modeled using the *discrete reinforcement* technique, where the rubber matrix was described by isotropic solid elements including discrete reinforcements represented by orthotropic shell elements.

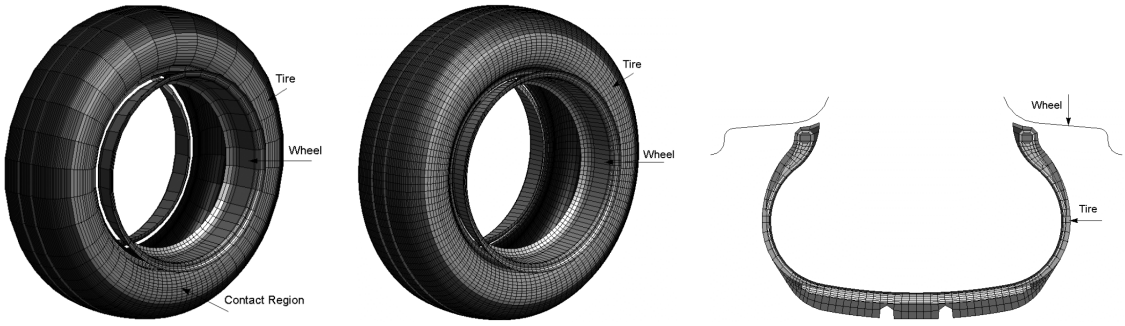

(a) (b) (c)

Figure 1.9: 3-D view of (a) the stationary, and (b) rolling tyre models developed by Hall [97], and (c) the cross-section of the tyre and wheel rim

Such structural models, however, pose unreasonable computational demands. It has been reported that the processing times for the stationary and rolling tyre models for 0.4 and 10 seconds real-time simulations were in the order of 8 and 70 days with the 360 and 750 MHz processors, respectively [97].

Providing input material properties for the tyre constituents is a complex task, particularly for the composite layers of the carcass and belts. Moreover, the tyre manufacturers tend to keep their material data confidential for competition purposes. Therefore, several reported structural tyre models have represented the reinforcing composite layers of the carcass and belts using equivalent orthotropic material properties [12, 24, 25]. Very few studies have directly derived the required input data from the material properties of pure rubber and geometric details of twisted cords [32]. Reid et al. [98] modeled the reinforcing fibers in the carcass and belt plies using beam elements running along the radial and circumferential directions, as illustrated in Figure 1.10(a). The model allowed to directly incorporate the constitutive models and material properties of the reinforcing fibers, which affect the vertical compressive strength of the tyre. Orengo [99] and Wright [100] also utilized the same approach to represent the tyre reinforcements, as illustrated in Figures 1.10(b) and 1.10(c). Such a high level of complexity, however, would result in further computational costs.

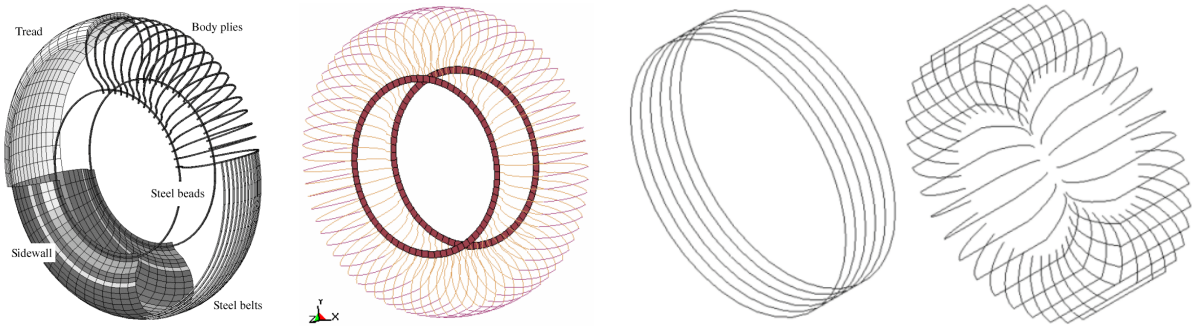

Figure 1.10: (a) Modeling the reinforcing fibers through beam elements as used by (a) Reid [98], (b) Orengo [99], and (c) Wright [100]

A number of studies have taken into account the tyre tread designs, being composed

of grooves and blocks in complex patterns [24, 101, 102]. Cho et al. [101] proposed an effective mesh generation algorithm for a car tyre considering detailed tread blocks, as shown in Figure 1.11(a). The study illustrated that the detailed mesh could predict the footprint and contact pressure more consistent with the experimental data than a simplified mesh, even though much more processing time was required. Majority of the studies, however, have modeled only the circumferential grooves so as to easily create the tyre mesh via copying and rotating the 2-D cross-section mesh of the tyre [10, 12, 32, 75, 103]. A number of studies have entirely ignored the tread patterns in order to expedite the contact calculations by excluding the local effects of the tread designs and thereby enhance the computational efficiency [25, 98–100], as exemplified in Figure 1.11(b).

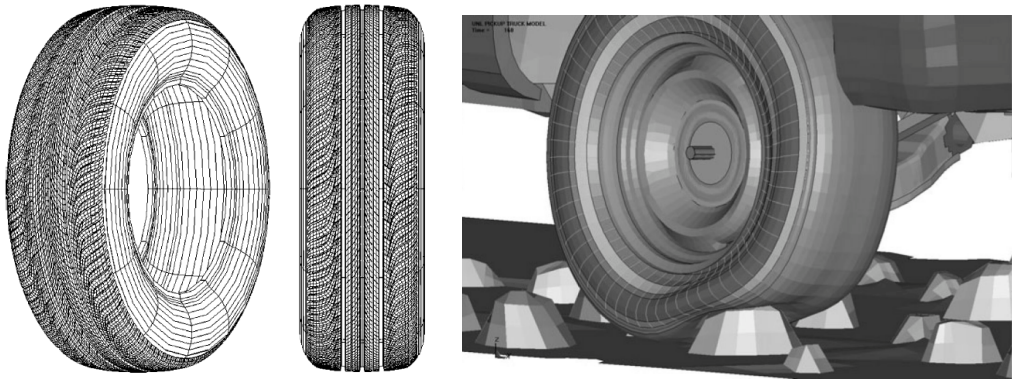

(a) (b)

Figure 1.11: (a) Detailed tyre mesh considering tread blocks proposed by Cho et al. [101], and (b) neglecting of the tyre tread designs to facilitate contact calculations [98]

The Mooney-Rivlin material model is widely adopted for representing the rubber materials in the tread and bead fillers [10, 12, 24, 32, 75]. This constitutive model is formulated based on a strain energy function in a polynomial form with two elastic constants, being identified through a scaled tensile stress-strain relationship and least squares curve fitting [104, 105]. Zhang et al. [32, 83] used the Mooney-Rivlin rubber material model, while the nonlinear equations governing the nearly-incompressible behavior of the rubber elements were derived using the mixed interpolation of the displacement and pressure formulation to enforce the incompressibility constraint. The Mooney-Rivlin elastic constants in the strain energy density function were identified based on a previous study by Papoulia [106] using

the stress-strain relation for a block of the tread rubber [9].

In the reported rolling tyre models with large element numbers, the rubber elements have been modeled using linear one-point-integration solid elements rather than fully (eight-point) integrated elements so as to diminish the process time as well as to prevent some numerical instabilities [10]. However, applying one-point-integration elements would cause the elements to give the deformed mesh an unrealistic and abnormal (zigzag) form resulting from zero energy modes, referred to as *hourglass energy*, as illustrated in Figure 1.12, that ought to be minimized through hourglass control options [97, 107].

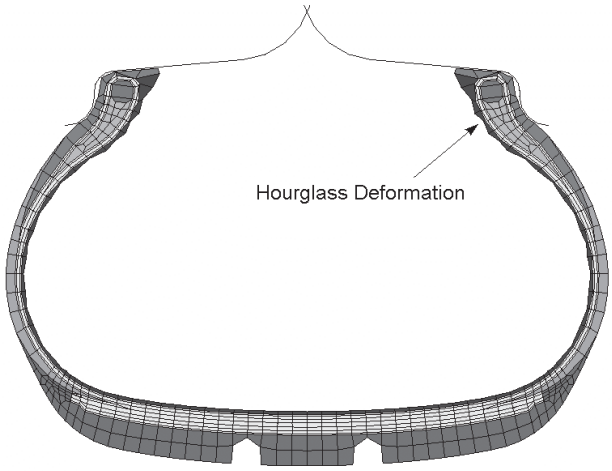

Figure 1.12: Hourglass deformation in the tyre cross-section under inflation pressure resulted from one-point integration solid elements as demonstrated by Hall et al. [10]

The tyre inflation pressure in the reported model is generally applied by a constant uniform pressure load to the inside surface of the tyre model [10, 12, 24, 83]. Studies investigating tyre responses to impact loading conditions have defined a pressurized control volume known as the *airbag* [98, 99]. The changes in tyre pressure due to volume changes resulting from tyre deformations are determined using the thermodynamics rules [105, 107]. In studies involving tyre-rim slippage [97] and tyre blow-out [99], the sidewall elements encasing the steel beads are pressed against the rim flange by the inflation pressure, and the traction/braking forces are transmitted between the rim flange and the tyre sidewalls by friction. In such studies, contact must be accurately defined between the tyre clinch and rim flange elements. In vast majority of the studies, the tyre is connected to the rim

through shared nodes assuming negligible slippage between the tyre and the rim [11, 95].

An undeformable ground made of rigid shell elements has been widely adopted in studies involving tyre interactions with roadway surface [12, 15]. The contact between the solid elements of a pneumatic tyre tread with shell elements of a rigid road can be modeled by various contact algorithms available in the finite element codes. In studies employing LS-DYNA [10, 75, 79, 81, 98, 99], the tyre-ground contact is generally modeled using the versatile surface-to-surface contact type using the penalty stiffness algorithm and Coulomb friction with smooth exponential transition between the static and dynamic coefficients of friction [105]. In some studies using ANSYS software [9], the rigid road is discretized by a set of target elements, which are coupled to the corresponding contact elements on the surface of the tread solid elements. The Augmented Lagrangian Method is employed for the nonlinear contact problem, while the contact stiffness is derived from the elastic properties of the contacted elements.

Computationally efficient structural tyre models

The finite element tyre models could effectively take into account the geometric and structural details as well as the material nonlinearities and anisotropies of pneumatic tyres and provided accurate predictions of the their static and dynamic responses under different maneuvers and loading conditions [10, 32, 78, 92, 98, 108, 109]. The high level of complexity considered in such comprehensive models, however, results in large number of finite elements and hence extensive element processing time. Such models are thus not suited for parametric and design sensitivity analyses, which involve repetitive model reformulations and simulations, especially for the case of rolling tyres on deformable terrains [24, 25, 40, 97]. Majority of the structural tyre models have thus been limited to static analyses of stationary tyres subjected to inflation and footprint loads [85–87]. Such computationally demanding tyre models have limited applications in vehicle system simulations, and design and development of pneumatic tyres. As a result, considerable attempts are still continuing for developments in tyre modeling methodologies to achieve an acceptable compromise between the model accuracy and its computational efficiency.

Chae et al. [11, 92] reported an efficient method of representing the composite plies

of the carcass and belts in a truck tyre using a three-layered membrane element from the element library of the PAM-CRASH simulation platform. Two layers of orthotropic materials with radial and circumferential cords were attributed to the carcass and belt plies, respectively, while the third layer with isotropic material properties was used for the rubber matrix, as illustrated in Figure 1.8(c). Although considering only one layer with circumferential cords could effectively represent the contribution of the belt to the overall tyre stiffness, it cannot adequately illustrate the individual effect of the belt cord angle on the dynamic responses of a rolling tyre. As a minimum, two layers with positive and negative cord angles would be required to describe the cords in the belts. for this purpose. Several other studies have also used this approach in PAM-CRASH to evaluate the static and dynamic responses of rolling truck tyres on rigid and deformable terrains [12, 24–26, 94, 96]. The majority of the reported studies on rolling tyre interactions with deformable terrains, however, have oversimplified the tyre to a rigid wheel to reduce the element processing time in the interest of focusing on terrain properties [25, 28, 29, 110, 111]. This suggests the need for an efficient yet reliable tyre model to be employed in analyses of tyre-soft terrain interactions with reasonable computational cost.

1.2.2 Modal analysis of rolling tyres

Estimating vibration modes and natural frequencies of a pneumatic tyre is of vital importance in design and development of tyre-vehicle systems for ride quality, minimal noise, and to identify critical speeds. Tyre material non-uniformities, tread block designs, and irregularities of the terrain surface are among factors that strongly affect the tyre vibration modes. Information about the tyre natural modes and frequencies can further help to provide general solutions for the tyre dynamic responses under varying loading conditions to be applied in vehicle system simulations. The modal properties of tyres have thus been reported in a number of studies using widely different empirical [112–115], theoretical [116–122], and numerical [13, 75, 123–125] methodologies. The natural frequencies and mode shapes of a structural system are generally determined through solving a linear eigenvalue problem without considering the resulting stresses from external loads. This is acceptable only for the structural systems subjected to relatively small deformations.

Under large deformations, however, where the tyre structure responds nonlinearly to the applied loads, the stiffness and thereby the vibration properties of the system vary considerably compared to the unloaded condition. This is evident from adjusting tension of a string to tune a musical instrument. The vibration modes and natural frequencies of a pneumatic tyre, as a nonlinear structure, strongly depend on the stresses caused by the inflation pressure, normal load, ground contact and rotational speed.

A number of studies have attempted to evaluate vibration characteristics of a free pneumatic tyre using experimental [112–114] and analytical [117–119] approaches without considering the tyre contact with ground. Zegelaar [122] and Yam [114] identified the resonant frequencies of stationary tyres via measurements of vibrational responses at different locations along the tyre circumference. Potts et al. [112, 113] used an optical measurement method, known as *holography*, to obtain resonant frequencies and mode shapes of rotating tyres, as illustrated in Figure 1.13. Such experimental approaches could effectively determine a number of lower natural frequencies corresponding to simpler patterns of vibrations such as radial, tangential and lateral modes. The more complex vibration modes associated with higher natural frequencies, however, could not be excited [112, 114]. Moreover, the amplitudes of the higher modes could not be accurately characterized in the frequency

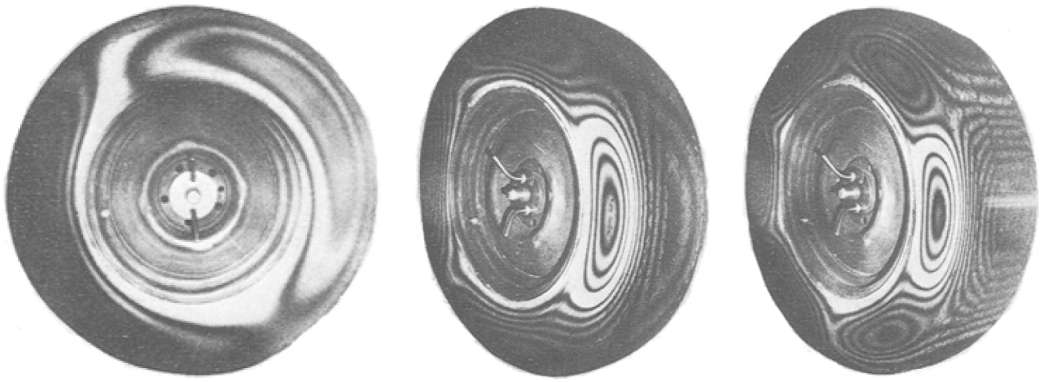

(a) (b) (c)

Figure 1.13: (a) First, (b) second, and (c) third radial mode resonances obtained for a radial-ply tyre using holography [112]

response plots since these are likely weakened by the tyre damping tendencies [118]. Further, the experimental methods do not permit to obtain the complex deformed shapes of higher modes with sufficient resolution, due to relatively limited number of measurement locations, as demonstrated in Figure 1.14 [114].

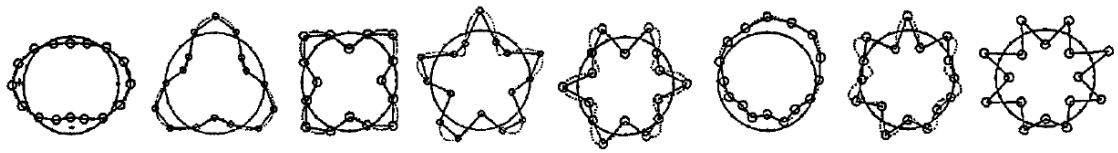

Figure 1.14: The first eight mode shapes of radial resonance obtained using experimental modal analysis by Yam et al. [114]

Early theoretical studies took advantage of tyre axisymmetric geometry and simplified it to a toroidal-shaped membrane [119] or a thin shell of revolution [117, 126–128]. This modeling approach could yield free vibration characteristics of an inflated but non-contacting tyre. The axisymmetric shell element formulation [117] permitted incorporating the pre-stress effects caused by the inflation pressure in free vibration analyses of a steel belted radial-ply tyre with orthotropic material properties. Figure 1.15(a), depicts the half cross-section section mesh considered for such an axisymmetric finite element model,

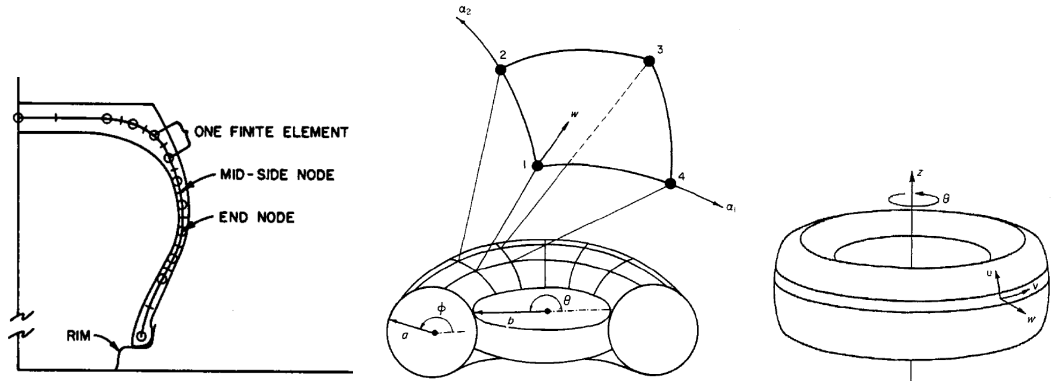

Figure 1.15: (a) The finite element shell of revolution model developed by Hunckler [117] for tyre vibration analysis, (b) the toroidal membrane finite element model by Saigal [119], and (c) the thin shell finite element of revolution by Kung [118]

and the toroidal-shaped membrane model, reported by Saigal et al. [119], is illustrated in Figure 1.15(b). The proposed membrane element formulation incorporated the geometric nonlinearities associated with large deformations of a low-pressure tyre and could detect the symmetric and twisting modes of free vibrations. The axisymmetric models developed based on thin shell of revolution could further provide the influences of the centrifugal forces on natural frequencies of a free rotating tyre, as illustrates in Figure 1.15(c) [118].

The contributions of ground contact and normal load on natural frequencies of a rolling tyre, however, have been reported in fewer studies. This is likely due to additional computing time demand of a 3-D representation of tyre geometry as well as complexities associated with varying tyre-ground contact boundary condition. The *modal expansion* approach has been widely used to provide general solutions for dynamic responses of a rolling tyre under different loading and boundary conditions in terms of the natural modes and frequencies of a free tyre [122, 127, 129–132]. Soedel [129] used this approach together with the linear thin shell theory to obtain Green function-based solutions for tyre vibrational responses under pure rolling, traction/braking and cornering maneuvers. The model was used to identify critical speeds forming *standing waves*. Soedel and Prasad [126] also proposed an analytical approach to identify the natural modes and frequencies of a tyre in ground contact from those of the free tyre [126]. Figure 1.16 illustrates the differences

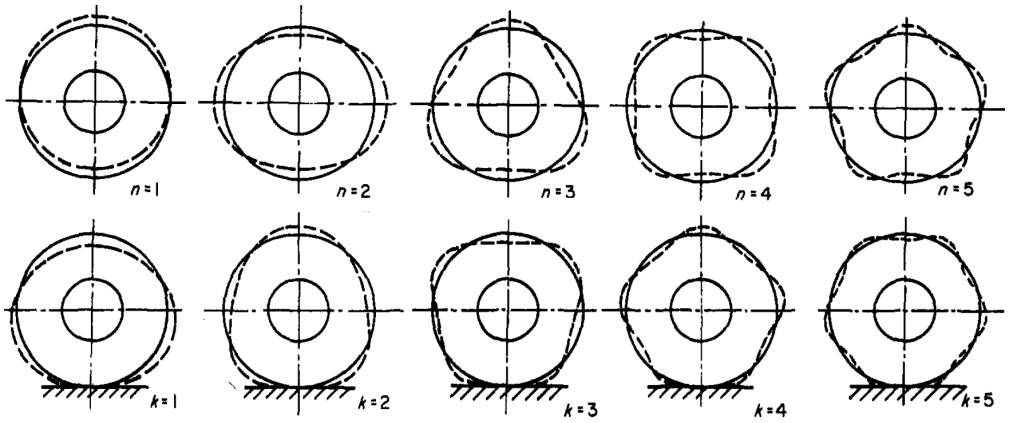

Figure 1.16: Comparisons of the mode shapes of an inflated tyre with those of a deflected tyre in ground contact, as investigated by Soedel and Prasad [126]

between the new mode shapes of the contacting tyre and those of the free tyre. The linear thin shell theory, however, could not perform well under high frequency excitations caused by road irregularities, where a thick shell element formulation would be essential to take into account the tread rubber influences.

Estimating modal properties of a contacting tyre has been also reported in several theoretical studies using the well-known *ring on elastic foundation* formulation [116, 120–122, 128, 133]. Zegelaar [122] compared the natural frequencies and mode shapes of a loaded contacting car tyre with those of a free tyre using both experimental and ring model approaches. Two identical mode shapes (with an offset in the angle of the anti-nodes) were observed corresponding to each eigen-frequency due to symmetry of the free tyre. For the contacting tyre, however, those identical modes diverged into symmetric and anti-symmetric modes at two distinct frequencies. As an example, Figure 1.17(a) illustrates the quadric mode of a free tyre, which is split in two distinct modes for the contacting tyre, as seen in Figure 1.17(b) [122]. Several other studies also incorporated the tyre-road contact in the ring model using radial and tangential displacement-related constraint equations at the footprint area. These have illustrated the two branches of symmetric and anti-symmetric mode shapes about the contact point [121]. Such physics-based approaches, however, necessitate prior tyre measurements for identifications of the equivalent mass, stiffness and damping constants.

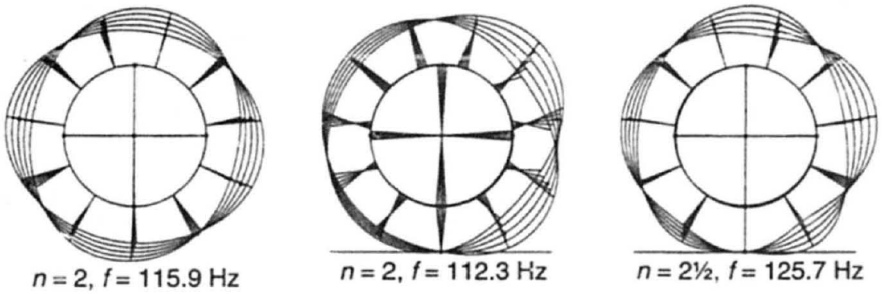

Figure 1.17: Comparing the shape and frequency of one of the vibration modes of (a) a free tyre with those of (b) a tyre standing on ground obtained from experimental modal analysis by Zegelaar [122]

The theoretical and experimental studies could detect only a few lower mode frequencies with limited accuracy. The structural tyre models, formulated using finite element methods, however, could provide more comprehensive deflection modes considering the material and geometric complexities of pneumatic tyres [12, 13, 109, 123, 124, 134, 135]. The majority of these have reported eigenvalue problem solutions for the non-contacting tyres and thus for the natural frequencies and the corresponding mode shapes [13, 136, 137]. Zhang et al. [13] performed modal analyses of a comprehensive finite element truck tyre model subjected to inflation pressure only. The study used ANSYS to present a detailed description for the multiple layers of the carcass and belt constructions, and could demonstrate the individual effects of the tyre inflation pressure as well as the anisotropy-related features upon the tyre natural frequencies. Figure 1.18 illustrates the 3-D mode shapes and the corresponding natural frequencies related to the first nine modes of the inflated tyre model. The study incorporated the contribution of the tyre internal pressure via prior determination of the stresses caused by inflation and applying them in the eigen-frequency calculations.

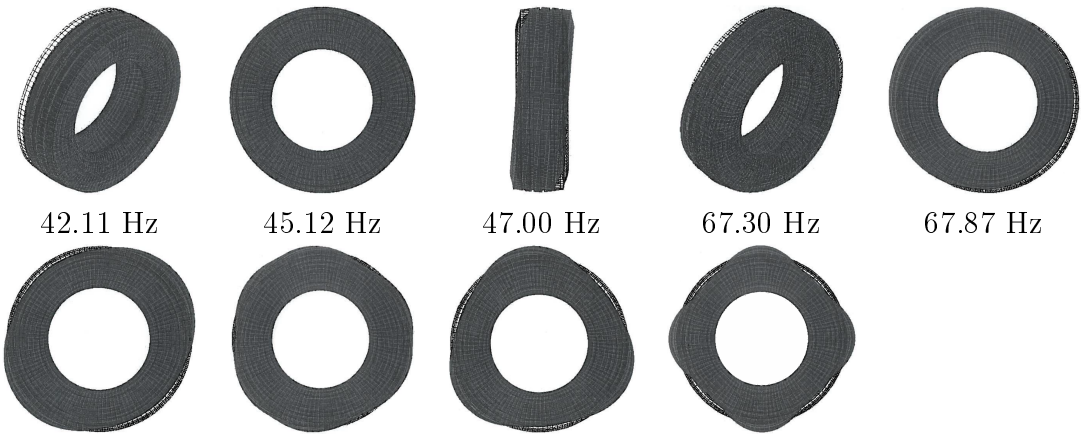

Figure 1.18: The first nine natural modes and frequencies predicted from modal analysis of an inflated non-contacting tyre model by Zhang et al. [13]

Extracting the tyre natural frequencies from *Fast Fourier Transformation (FFT)* analyses of the tyre transient responses to impact-like excitations has been also used in a number of studies as an alternative to eigenvalue solutions. The *drop* test has been widely used

to determine the fundamental frequency of a stationary tyre under static forces such as the inflation pressure and road contact load [12, 109]. Whereas the *cleat-drum* test has been applied to investigate the variations in the lowest natural frequency of a rolling tyre with rotational speed [12, 75, 77, 109, 124, 138]. Figure 1.19 exemplifies a cleat-drum test simulation performed by Kao et al. [75] using LS-DYNA. This approach could effectively demonstrate the effects of pre-loads and rotational speed on the fundamental natural frequency of a rolling tyre. The tyre mode shapes, however, could not be determined using this approach. Moreover, the application of this approach was limited to detecting only the natural frequencies that could be directly excited.

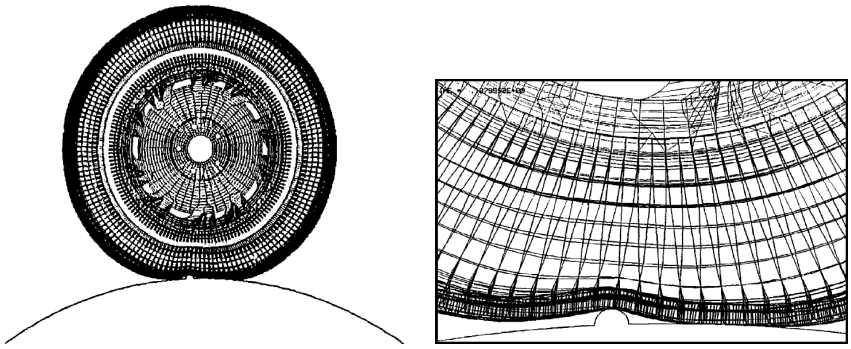

(a) (b)

Figure 1.19: (a) Side view, and (b) zoom view of the cleat-drum test simulation using LS-DYNA reported by Kao et al. [75]

Very few studies demonstrated the influences of tyre inflation, road contact and rotational speed on eigenvalues of the tyre. This is mostly due to nonlinearities caused by tyre stresses under multiple loadings and varying contact geometry, which necessitate prior explicit dynamic simulations [123, 134, 135, 139, 140]. Burke and Olatunbosun [123] applied MSC/NASTRAN to conduct modal analyses on a pre-loaded tyre for investigating the effects of air pressure, contact load and rolling speed upon the natural modes and frequencies of a passenger car tyre. The application range of the study, however, was limited only to a few basic modes such as lateral, longitudinal, radial and steer, as illustrates in Figure 1.20. This suggests that the individual contributions of the inflation pressure, contact load and rolling speed to the higher modes and frequencies need to be explored, particularly for the

truck tyres.

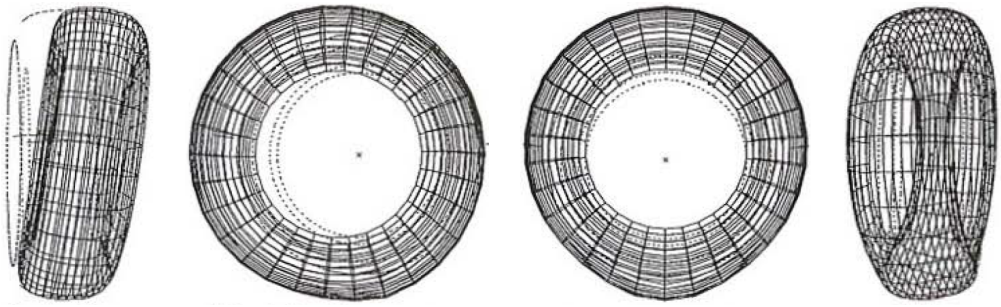

(a) Lateral (b) Longitudinal (c) Radial (d) Steer

Figure 1.20: Basic modes related to (a) lateral, (b) longitudinal, (c) radial, and (d) steer vibrations, as predicted by Burke et al. [123]

1.2.3 Tyre-soil interaction modeling

The vast majority of the reported tyre models are developed for rolling over rigid roads. The interactions between the pneumatic tyres and deformable terrains such as soft soils are presented in relatively fewer studies due to complexities associated with soil constitutive behavior when subjected to dynamic vehicular loads. Mobility performance characteristics of off-road vehicles are highly dependent on the applied forces/moments resulting from tyre-terrain interactions. Effective estimations of these force/moment properties are thus vital for off-road vehicle design and developments. Exploring dynamic properties of off-road vehicles in relation to terrains is known as the *Terramechanics* [141].

Terramechanics-based models and soil testing devices

The terramechanics-based models provide semi-empirical formulations to approximate the soil stresses at the contact interface as functions of the normal and shear deformations of soil beneath a rolling wheel. The tyre-soil interface forces and moments are estimated through integrating these stresses over the contact region [19, 20]. The terrain stresses are determined using regression-based formulations that contain model coefficients representing terrain material strength properties [141, 142] that need to be identified through

experiments. A number of test devices have been developed for measurements of material strength properties for different types of soils [143].

The *cone index* was initially used as a measure of soil strength for evaluating the tractive performance of off-road vehicles [144]. This property is defined as the soil resistance against a penetrating cone-shaped object, known as the *cone penetrometer*, as illustrated in Figure 1.21(a) [142]. Reece and Peca [145] stated that the cone index is inadequate for vehicle mobility analyses since it does not illustrate the individual effects of the normal and shearing strength of soils. Alternatively, the *bevameter* machine, developed by Bekker [16–18], is used for separately characterizing the normal and shearing characteristics of soils, as schematically illustrated in Figure 1.21(b). Bekker [16–18] formulated the pressure developed beneath a penetrating rigid plate, p, as a function of its sinkage into soil, z, such that:

$$p = \left(\frac{k_c}{b} + k_\phi\right) z^n \tag{1.1}$$

where n, k_c and k_ϕ are soil parameters to be determined via curve fitting of the pressure-sinkage data obtained from the bevameter machine. The shear stress of soil, τ, was also represented in terms of its shear deformation, j, using the following phenomenon-based equation [141]:

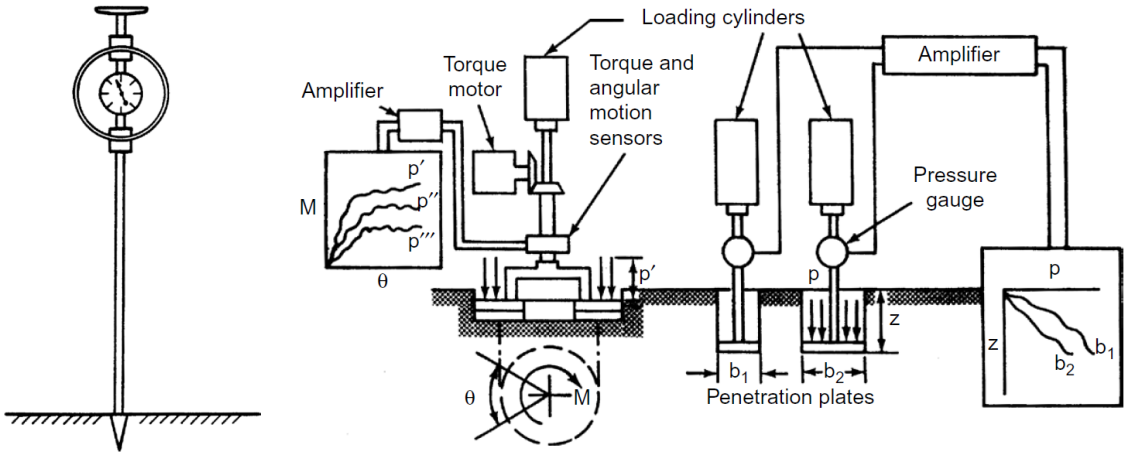

Figure 1.21: Schematic illustrations of (a) cone penetrometer, and (b) bevameter [141]

$$\tau = \tau_{max}\left[1 - \exp\left(\frac{-j}{K}\right)\right] \tag{1.2}$$

where K is the *shear displacement modulus*, and τ_{max} represents the shear strength of the soil, which depends on its confining pressure as characterized by the *Mohr-Coulomb failure criterion* [18]:

$$\tau_{max} = c + p\tan\phi \tag{1.3}$$

where c and ϕ are soil parameters known as *cohesion stress* and *angle of shearing resistance*, respectively, to be identified via the *shear ring* tests using the bevameter machine [18]. Besides these types of field tests, a number of laboratory tests are also commonly used in civil engineering for measurements of soil properties [141]. Figure 1.22(a) shows a simplified illustration of a *triaxial* apparatus, where a cylindrical specimen of soil is subjected to hydrostatic pressure and axial load. This device features a measurement feedback control system that can simulate idealized states such as hydrostatic and triaxial compressions as well as uniaxial strain loading/unloading, which are essential for characterizing compressibility, shear strength and unloading behavior of soil. Figure 1.22(b) illustrates the *direct shear-box*, which is used to identify the shear-related properties of soils under defined ranges of confining pressures.

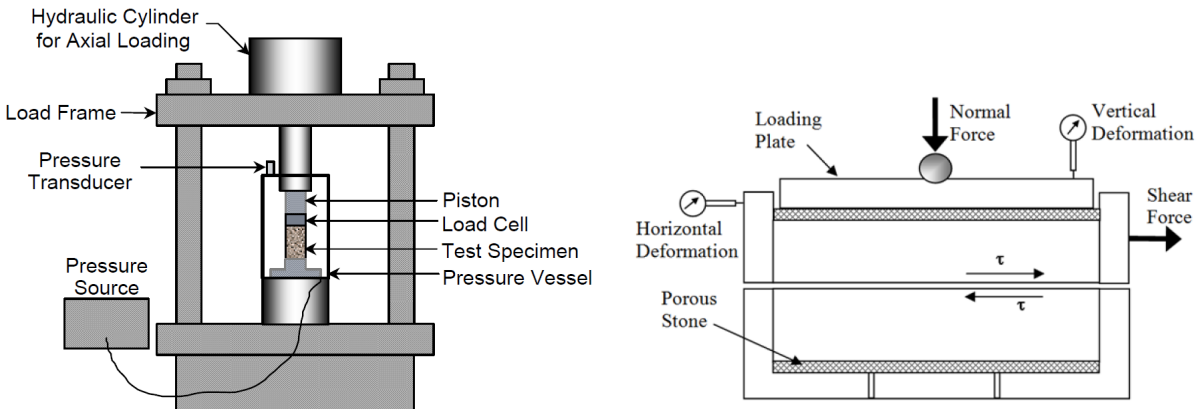

Figure 1.22: Schematic illustrations of (a) triaxial apparatus [146], and (b) shear-box [147]

Onafeko and Reece [148, 149] measured the radial and tangential stresses beneath a rolling rigid wheel under driven and towed conditions over a range of longitudinal slip/skid ratios. Figure 1.23 compares the distributions of the radial and tangential stresses beneath a driven rigid wheel with those of a towed wheel rolling on the sand. The measurements revealed the presence of a transition point in the contact region beneath a towed wheel, where the tangential stress changes its direction from opposite to wheel rotation (specified as positive) to a direction along the wheel rotation (negative). Whereas, for a driven wheel the direction of the tangential stress was consistent with the wheel rotation throughout the contact region. The study further showed that the position of the maximum radial stress as well as the location of the transition point for the tangential stress depend on the degree of slip or skid for a driven and towed wheel, respectively.

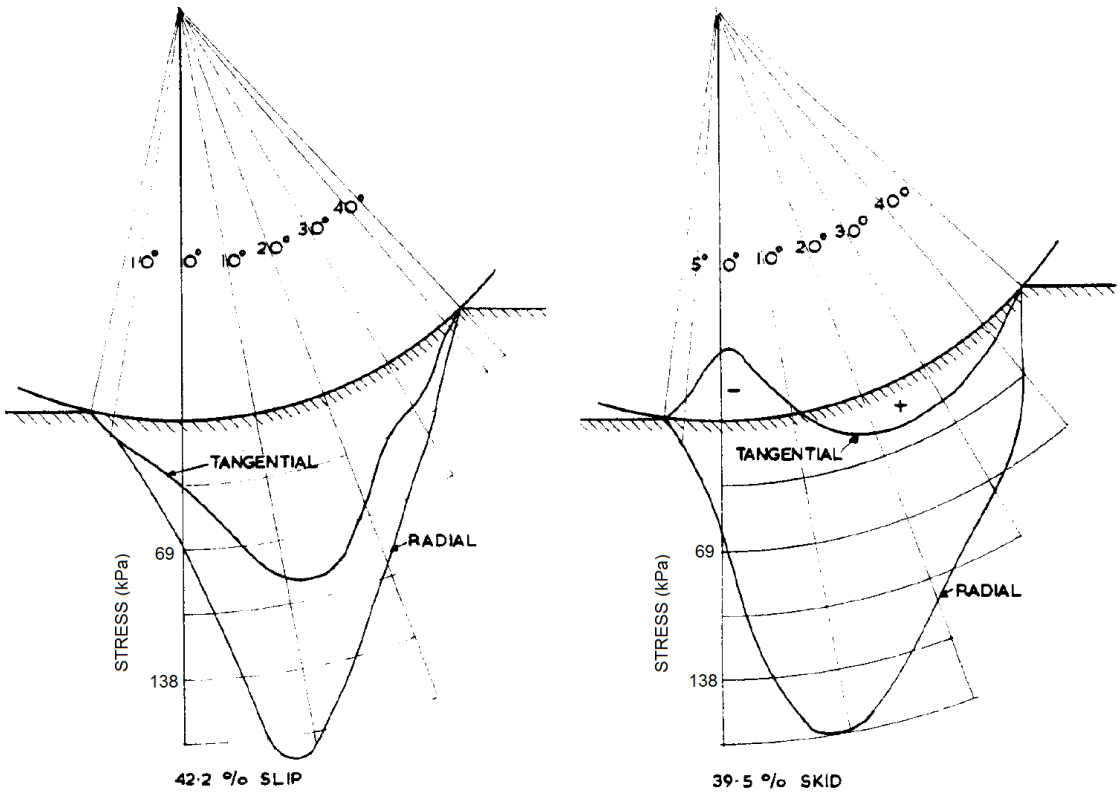

Figure 1.23: (a) Distributions of radial and tangential stresses for (a) a driven rigid wheel, and (b) a towed wheel rolling on sand, as measured by Onafeko and Reece [148, 149]

Wong and Reece [19, 20] formulated the radial and tangential stress distributions beneath a rolling tyre as functions of the tyre sinkage and slip/skid ratio. The radial stress distribution along the contact region was derived using the Bekker's pressure-sinkage relation [18] based on the assumption that the reaction of soil at the contact interface of a penetrating wheel is analogous with that underneath a plate penetrated to the same depth. Similarly, the tangential stress distribution was estimated using the Bekker's shear stress-shear displacement relation, while characterizing the shear strength dependence on pressure via the Mohr-Coulomb failure theory [141]. The study incorporated the effect of slip/skid in representing the radial and tangential deformations at the contact interface of a rolling rigid wheel, which resulted in deriving quite different formulations of stress distributions for the cases of driven and towed wheels [19, 20]. Figure 1.24(a) illustrates the measured [149] and predicted [19] distributions of radial and tangential stresses under a driven rigid wheel, while Figure 1.24(b) demonstrates those under a towed wheel [20]. The resulting contact forces and moments were thus approximated through integrating these stress distributions over the tyre-soil interface, such that [19]:

$$F_x = bR \int_{\theta_2}^{\theta_1} [-\sigma_r(\theta) \sin\theta + \tau_x(\theta) \cos\theta] \, d\theta \tag{1.4}$$

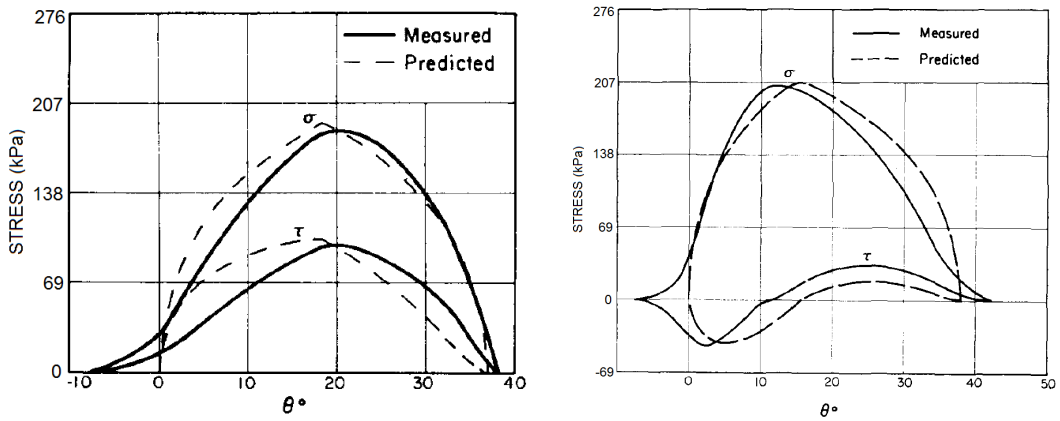

Figure 1.24: (a) Distributions of radial and tangential stresses for a driven rigid wheel on compact sand under 2000 lb axle load and 22.1% slip, and (b) that for a towed wheel at 21.6% skid, as measured by Onafeko [149], and predicted by Wong and Reece [19, 20]

$$F_z = bR \int_{\theta_2}^{\theta_1} [\sigma_r(\theta) \cos\theta + \tau_x(\theta) \sin\theta] \, d\theta \tag{1.5}$$

$$M_y = bR^2 \int_{\theta_2}^{\theta_1} \tau_x(\theta) \, d\theta \tag{1.6}$$

where σ_r and τ_x are the radial and tangential stresses, b, R, θ, θ_1 and θ_2 are the contact width, contact radius, angular position and boundaries of the contact interface, respectively, F_x and F_z are the contact forces along the longitudinal and vertical directions, and M_y is the driving/braking torque. As an example, Figure 1.25 illustrates the measured [149] and predicted [19] driving force and torque produced under a driven rigid wheel on compact sand for a range of slip ratios. Considering similar formulation for the shear stress along the lateral direction, a number of studies predicted the cornering force and aligning moment for use in simulations of steering maneuvers, such that [21, 150]:

$$F_y = bR \int_{\theta_2}^{\theta_1} \tau_y(\theta) \, d\theta \tag{1.7}$$

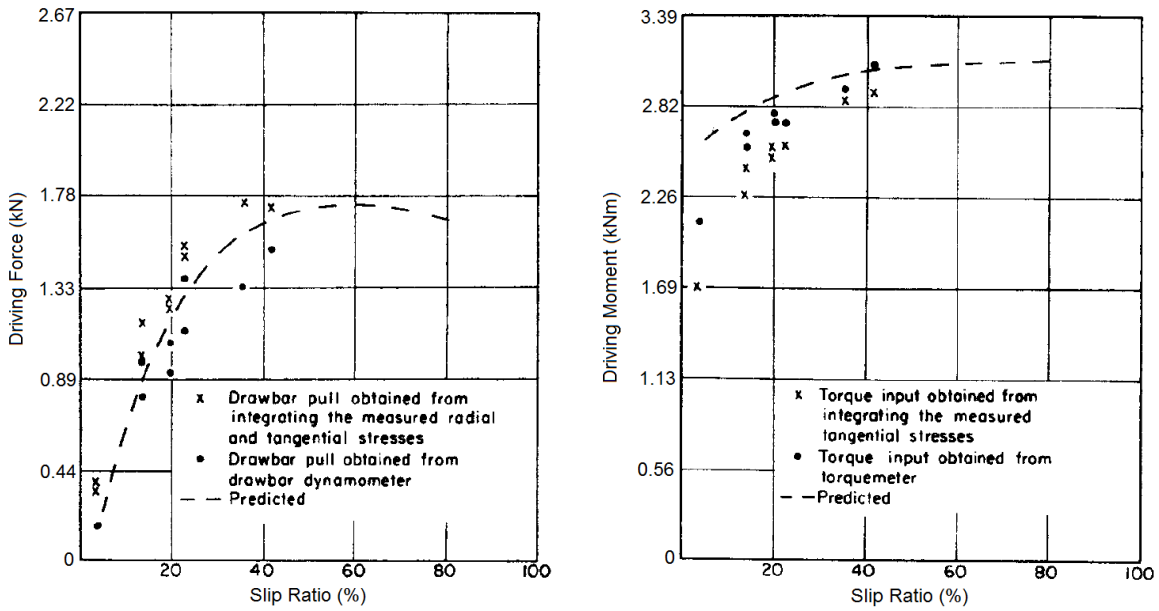

Figure 1.25: (a) Driving force, and (b) driving torque of a driven rigid wheel on compact sand under 2000 lb axle load for a range of slip ratios, as measured by Onafeko [149], and predicted by Wong and Reece [19]

$$M_z = bR^2 \int_{\theta_2}^{\theta_1} \tau_y(\theta) \sin\theta \; d\theta \tag{1.8}$$

where τ_y is the lateral shear stress, which is related to the side-slip angle through lateral shear displacement, and F_y and M_z are the side force and aligning moment, respectively. The reported studies have also considered different contact geometries, as seen in Figure 1.26.

The majority of the studies on terramechanics are based on rigid wheels assuming negligible contributions due to tyre compliance. A few studies have attempted to incorporate the tyre compliance in the tyre-terrain models by representing the contact arc by a larger radius than that of an unloaded tyre, as shown in Figure 1.26(b) [151]. Schmid et al. [152] approximated this contact radius (R) in terms of unloaded radius (r), tyre deflection (Δ) and sinkage depth (z), such that:

$$\sqrt{\frac{R}{r}} \approx \sqrt{1 + \frac{\Delta}{z}} + \sqrt{\frac{\Delta}{z}} \tag{1.9}$$

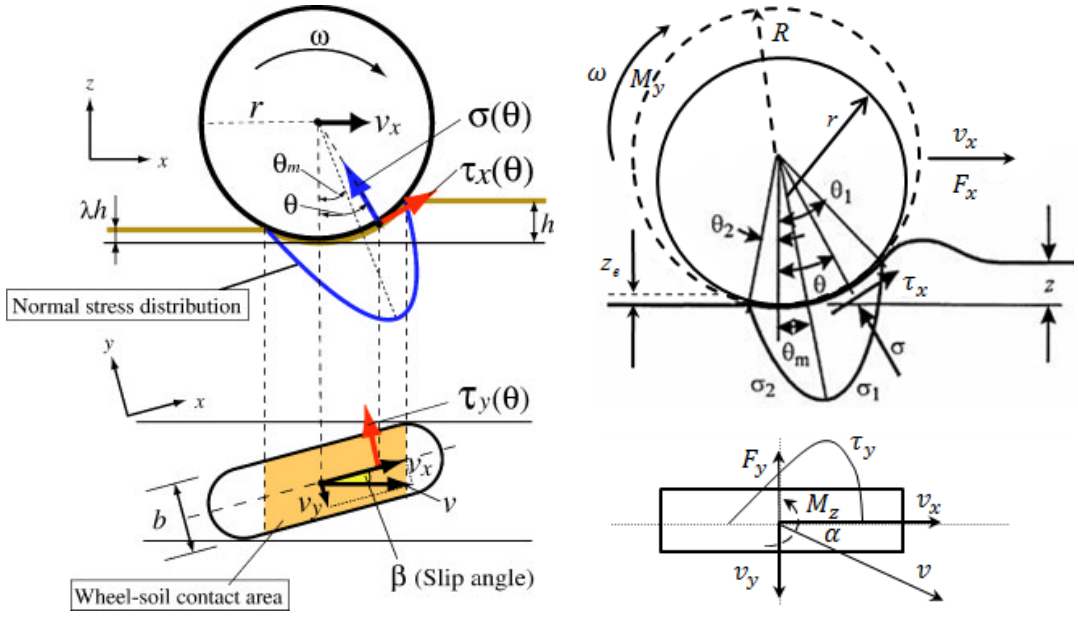

Figure 1.26: (a) Rigid wheel-soil interaction model for approximating side force and aligning moment [21], and (b) incorporating pneumatic tyre compliance via representing the contact arc using a larger radius than that of an unloaded tyre [151]

These terramechanics-based models have been widely used for approximating tyre-soil contact forces and moments as functions of tyre sinkage, longitudinal slip/skid ratio and side-slip angle for applications in multi-body system simulations of off-road vehicles [31, 111, 150, 153, 154] as well as planetary exploration rovers [21–23] on soft soils. As an example, Figure 1.27 illustrates an exploration rover as well as its dynamic model, which is developed using the terramechanics-based rigid wheel-soil interaction formulations for driving and steering simulations on loose sand [21].

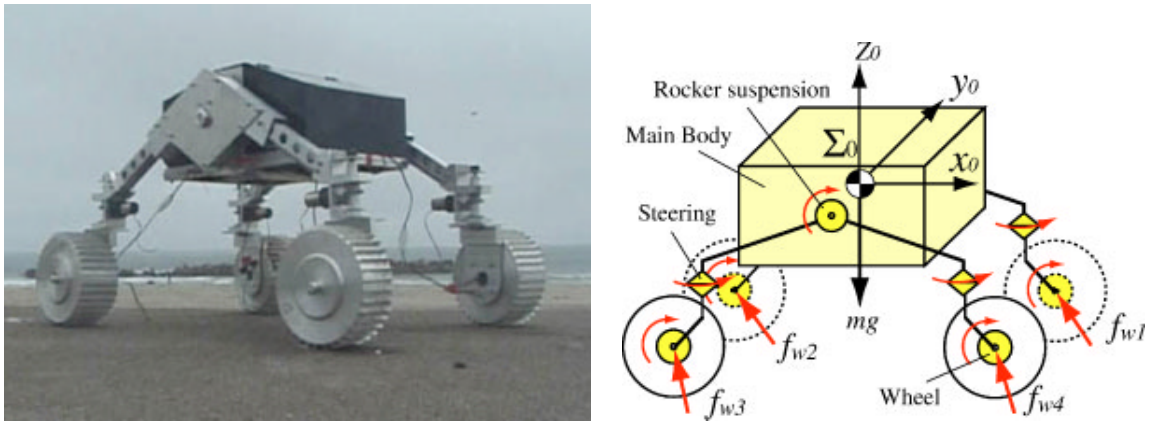

(a) (b)

Figure 1.27: (a) An exploration rover with rigid wheels, and (b) its dynamic model for driving and steering maneuvers on loose sand, developed by Ishigami et al. [21] using terramechanics-based formulations

The applications of these terramechanics-based models, however, necessitate prior identifications of the soil parameters used in characterizations of the normal and shearing behavior of the soil. These parameters are determined via curve fittings of the measured data [155] obtained from soil test devices [151, 156–158]. The reliabilities of the predicted forces and moments thus highly depend on the accuracy of these parameters for each particular type of soil.

Computational tyre-soil models using finite element methods

Terramechanics-based models could yield effective estimations of the overall stress distributions and force/moment characteristics for off-road vehicle simulations [111, 150,

153, 159]. The flow of the soil and its deformed shape under a rolling pneumatic tyre, however, were not addressed by these theoretical models. Therefore, a vast number of computational models were developed for simulating tyre-soil interactions in a more realistic manner. The *Finite Element (FE)* methods have been widely used in these models for accurate representations of soil material properties together with structural details of the pneumatic tyres. Some of these studies have attempted to predict of off-road tyre mobility and motion resistance [160, 161], tyre footprint and soil compaction [29, 30, 162], and soil flow and stress characterizations [24, 27, 28, 163]. In these studies, the soil is represented by different constitutive models and material properties. A number of studies have used the traditional plasticity theory and described the soil as an *elastic-plastic* material represented by a bi-linear stress-strain curve with a constant yield stress [24–26, 28, 29, 164, 165]. These studies require only minimal material properties including the Young's modulus, yield stress and tangent modulus. While the initial values for these material parameters are approximated from the reported measured data for the typical soils [166], final values are tuned by matching the simulation results with the reported experimental data in terms of pressure-sinkage characteristics [24, 95].

Hambleton et al. [28, 29] developed 2-D and 3-D finite element soil models in the ABAQUS platform for analyses of wheel-induced rutting in sand and clay for two cases of indentation and rolling. The tyre was simplified to a rigid cylindrical wheel, while the soil was modeled using an elastic-plastic material model consisting of a linear elastic part expressed by Young's modulus and Poisson's ratio, and a perfectly plastic part following the Mohr-Coulomb yield criterion described by cohesion stress and friction angle. The study investigated the influences of soil strength parameters and wheel geometry on the relationship between the indentation force and the wheel sinkage. The study showed only minor difference between the 2-D and 3-D simulation results for clays. The difference, however, were significant for sands. An analytical relation between the indentation force and the wheel sinkage was also approximated, which correlated qualitatively with experimental data [28]. The study further conducted 3-D simulations of a towed rigid wheel rolling and rutting in soil, as illustrated in Figure 1.28(a), and provided analytical formulations to estimate the wheel sinkage under steady-state rutting, which showed reasonably good

agreements with the numerical and experimental results [29].

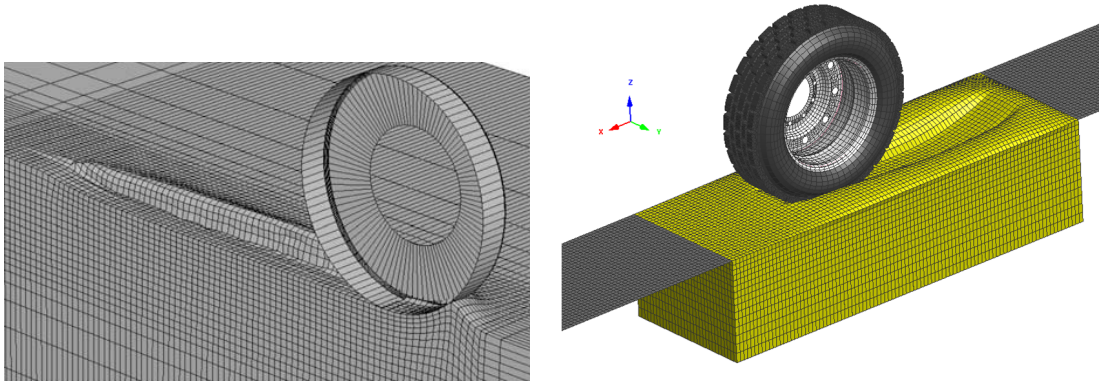

(a) (b)

Figure 1.28: FE soil models using elastic-plastic material properties, developed by (a) Hambleton et al. [28, 29], and (b) Slade et al. [24, 95]

Slade et al. [24, 95] developed a finite element soil model employing the elastic-plastic material model to simulate sandy loam using PAM-CRASH. The soil model was calibrated through comparisons with the Bekker's pressure-sinkage relationship [18], while the initial soil parameters were extracted from a study by Wong [142]. A detailed finite element model of an off-road truck tyre was also developed to be used for tyre tests on soft soils, as illustrated in Figure 1.28(b). The soil flows and the pressure distributions within the soil were qualitatively verified via comparisons with a reported study by Wong [142] for two cases of driven and towed rigid wheels, as shown in Figures 1.29(a) and 1.29(b), respectively. Using the validated tyre-soil model, a series of test simulations were conducted for identifications of the in-plane and out-of-plane parameters associated with an analytical off-road rigid ring tyre model, which was developed through modifications on a previous on-road rigid ring tyre model, reported by Chae [11, 12], so as to account for off-road tyres running over soft soils.

The traditional plasticity theory, however, could not sufficiently represent the soil compaction behavior and the resulting stress responses, since it was developed for metal-like materials. Unlike metals, soils are highly compressible with varying strength under compaction loading, particularly the non-cohesive soils such as sands [167]. Figure 1.30 illustrates the stress distributions within the soil domain in a pressure-sinkage test using

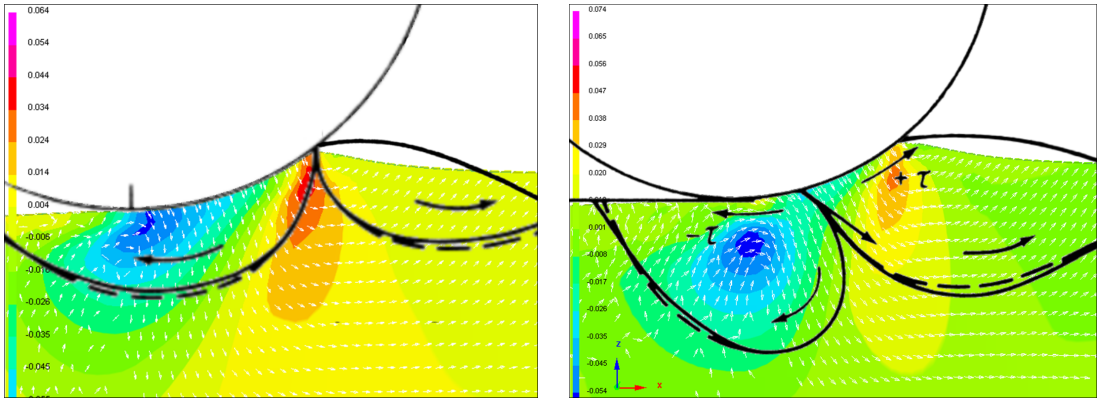

(a) (b)

Figure 1.29: Soil flow and pressure distributions under (a) driven, and (b) towed rigid wheel models using a finite element soil model with elastic-plastic material properties, developed by Slade et al. [24]

a bi-linear elastic-plastic material model with a constant yield stress [37]. The stress concentrations near the edges of the penetrating plate clearly show the metal-like behavior of the soil elements under compression.

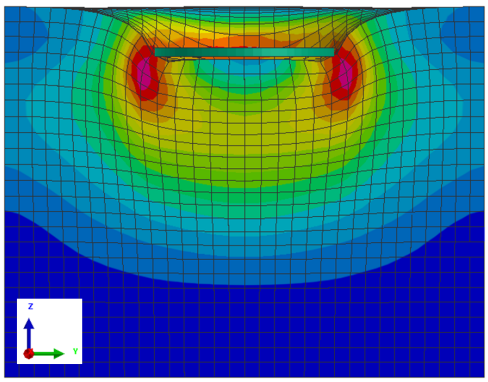

Figure 1.30: Stress concentrations near the edges of the plate in a pressure-sinkage test simulation using a finite element soil model with elastic-plastic material properties reported by Lescoe et al. [25]

In order to account for the compressible behavior of the soil, a number of studies have attempted to relate the soil volumetric deformation to the applied pressure via defining an *Equation Of State (EOS)*. Lescoe [25, 37] and Dhillon [26, 39, 40] applied a linear equation

of state in PAM-CRASH to relate the pressure and volumetric deformation of a soil through a constant bulk modulus. Although these studies could yield reasonable predictions of the contact pressure and the resulting forces and moments, idealizing the soil pressure-volume response by a linear equation of state could result in inaccurate representation of the material compressibility of soil. Moreover, the dependence of the soil shear strength on the applied pressure was not considered in these studies [37, 39, 95].

Alternatively, a number of studies have directly related the shear strength of a soil to its confining pressure via defining a failure criterion. These studies have mostly used the soil material models such as the *soil and foam* constitutive model from the LS-DYNA material library [38, 43, 45, 100, 168, 169] as well as the *Drucker-Prager* material model in ABAQUS [27, 150, 170–174]. The soil and foam constitutive model (material type 5 in LS-DYNA [104, 105, 168]) requires independent sets of input parameters to describe the compressibility and shearing characteristics of soil, being determined from triaxial tests [175]. A pressure-volumetric strain curve takes care of the compressibility of soil during loading, while a *bulk unloading modulus* specifies a linear behavior for unloading. These loading/unloading parameters are obtained from the *uniaxial strain* and *hydrostatic compression* tests, respectively. The shear strength is described via a yield surface, which defines the second invariant of the deviatoric stress tensor as a quadratic function of hydrostatic pressure with coefficients realized from a *triaxial compression* test [105, 168]. This material model has been widely used for simulations of tyre-soil interactions [38, 100], soil penetration tests [43, 45, 176], aircraft landing [169, 177], and road-side barrier impacts [178].

Wright [100] developed a finite element soil model using the soil and foam material model in LS-DYNA for analyses of tyre-soil interactions over different types of frictional and cohesive soils. The material model input parameters were determined from triaxial and direct shear-box tests using curve fitting methods. The soil models were assessed through comparisons of the simulation results predicted from quasi-static plate sinkage tests with those obtained from experiments for dry sand and sandy loam. The normal and tangential stress distributions beneath a towed rigid wheel were estimated, as illustrated in Figures 1.31(a) and 1.31(b), which correlated well with the experimental results reported

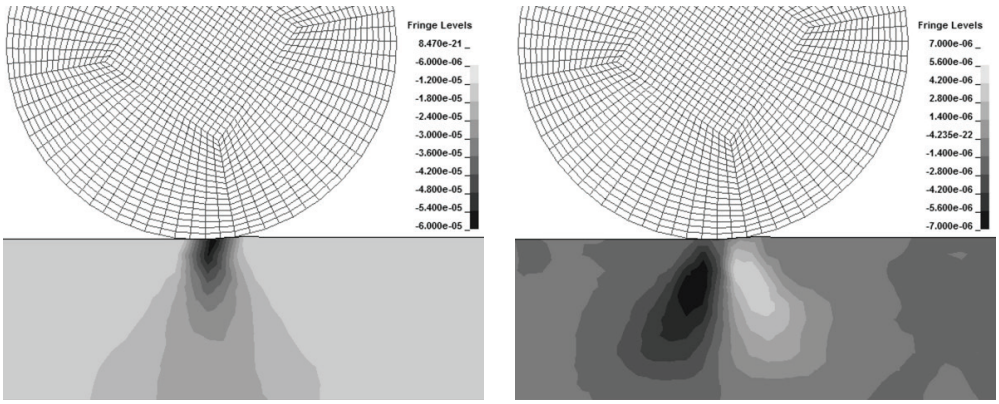

(a) (b)

Figure 1.31: (a) Normal and (b) shear stress distributions beneath a towed rigid wheel as predicted by Wright [100] using LS-DYNA

by Onafeko [149] and Reece [19, 20] in a qualitative manner in terms of the maximum normal stress location as well as the shear stress transition point at the boundary of the two failure zones. The study integrated the soil model to a simplified tyre model to predict performance characteristics of a pneumatic car tyre in terms of rolling resistance, drawbar pull and tractive efficiency on a deformable terrain, as shown in Figure 1.32.

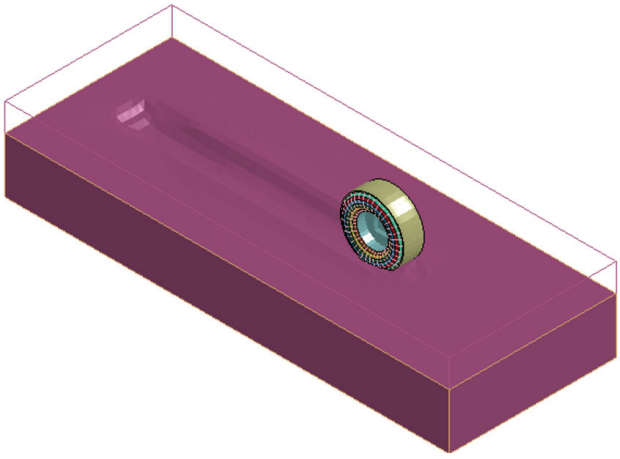

Figure 1.32: Tyre-soil interaction model developed by Wright [100] to predict rolling resistance of a towed tyre on soft soil

Fervers [27] developed a finite element soil model using the Drucker-Prager material

model in ABAQUS, which considers the dependence of soil shear strength on its plastic compaction. A 2-D finite element tyre model was used for analyses of a rolling tyre on deformable soils so as to avoid computationally demanding simulations associated with 3-D representations of the pneumatic tyres. Two different types of soils were considered including a wet loose loam as a cohesive soil with low compaction resistance, and a dry dense sand as a frictional soil with high compaction resistance. The tyre model was inflated at extremely low and high inflation pressures, and was vertically loaded while driven at zero slip. Figure 1.33 illustrates the tyre sinkage, soil compaction and pressure distributions in loam and sand for high and low inflation pressures. The tyre sinkage into the loam was much deeper for the high inflation pressure tyre compared to the low pressure tyre (Figure 1.33(a)). The sinkage of tyre into the sand, however, was nearly identical for both the inflation pressures (Figure 1.33(b)). Moreover, the loam was compacted more under a high-pressure tyre (Figure 1.33(a)), and the pressure contours were deeper, compared to a low-pressure tyre (Figure 1.33(c)). However, on the sand, for the low inflation pressure, the soil was compacted more, particularly in the upper layers (Figure 1.33(b)), and the reduction of pressure was not as effective as it was on the loam (Figure 1.33(d)). Further, on the

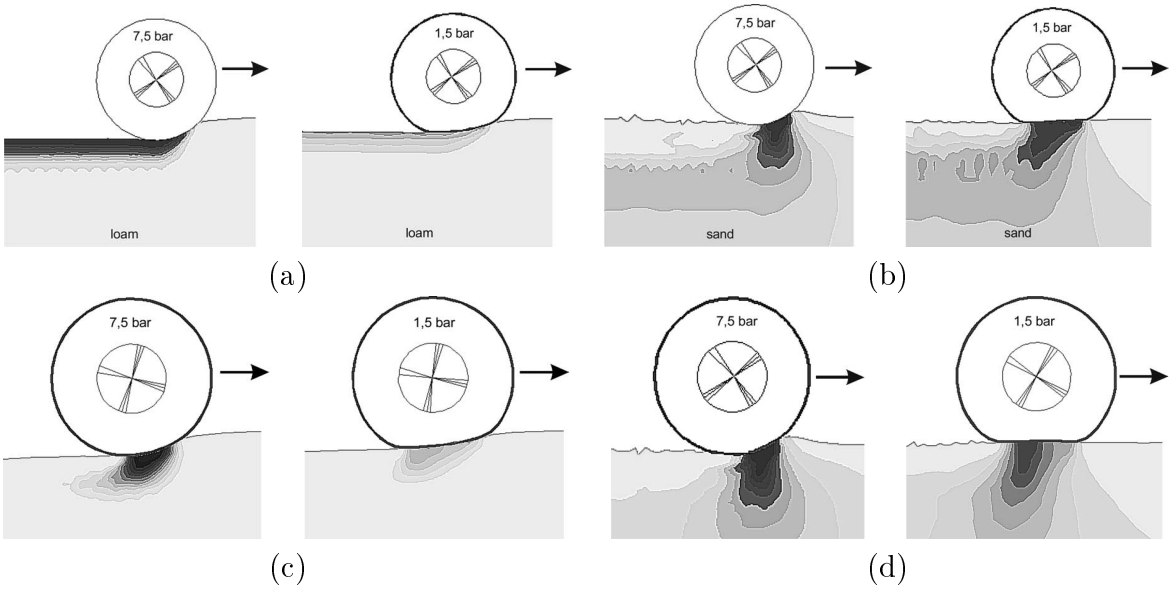

Figure 1.33: Soil compaction for (a) loam, and (b) sand; and pressure distributions in (c) loam, and (d) sand at high and low inflation pressures, reported by Fervers [27]

loam, the rolling resistance of high pressure tyre decreased significantly for the low inflation pressure (Figure 1.33(a)). The operation on sand, however, resulted in accumulation of soil in front of the tyre leading to a bulldozing wave (Figure 1.33(c)). This accumulation was not observed for the low pressure tyre, which contributed to significant reduction in the rolling resistance.

Li et al. [150, 151] also developed a finite element soil model using the Drucker-Prager constitutive model in ABAQUS with input material parameters determined from triaxial tests. An analytical tyre-soil interaction model was also developed based on terramechanics formulations for estimations of the normal and tangential stresses as well as the tyre-soil interface forces and moments to be used in off-road vehicle multi-body system simulations using ADAMS. Using the finite element soil model, a number of virtual tests were performed for identifications of the analytical model parameters. Figures 1.34(a) and 1.34(b) exemplify the pressure-sinkage and the direct shear-box simulations used for parametrization of the normal and tangential characteristics of soil in a limited range of sinkage depth and shear displacement. The soil model was integrated to a finite element model of an excavator tyre for investigating dynamic performance properties such as drawbar pull and cornering force at varying slip conditions. It was shown that the FE model overestimates the forces and moments developed at the interface compared to the analytical model.

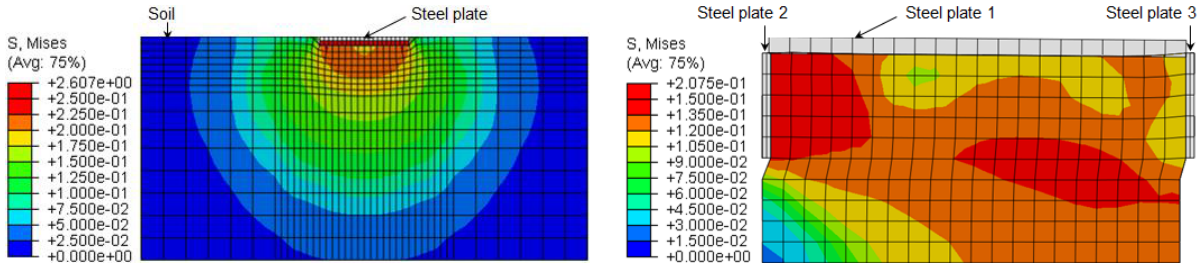

(a) (b)

Figure 1.34: Plate-sinkage and shear-box test simulations performed by Li et al. [150, 151] using finite element method

Xia [30] also used the Drucker-Prager material model in ABAQUS to develop a 3-D tyre-terrain system for predicting soil compaction and tyre mobility. While a few top

layers of the soil elements were represented using the Drucker-Prager model, the remaining elements at the bottom were described by a simple elastic model with stiffer material properties, as illustrated in Figure 1.35. A non-uniform mesh was used for the soil domain, being refined only at places undergoing large deformations. Using the computational model, the influences of the tyre inflation pressure, rolling speed and contact friction on effective rolling radius, hub acceleration, axle torque and traction performance were investigated. The study demonstrated that the finite element soil modeling can serve as a robust tool for predicting soil compaction and tyre traction properties as a replacement for tyre performance field tests.

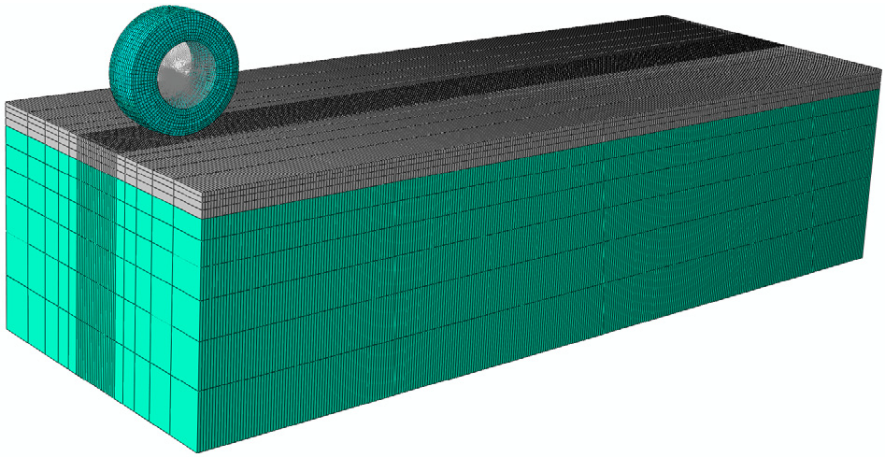

Figure 1.35: Tyre-soil interaction model developed by Xia [30] using finite element method

Computational tyre-soil models using mesh-less analysis methods

The vast majority of the studies have modeled the soil using the *Finite Element (FE)* methods [24, 27, 29, 100, 173, 179]. A number of those developed the soil models in the Pam-Crash platform [37, 39, 95] for predicting the contact pressure distributions as well as the forces and moments produced under a truck tyre when rolling on deformable terrains. These have found that the mesh-based nature of the finite element method is not appropriate for simulating the penetration of a flat plate into soil. In a finite element mesh, the soil elements are connected through shared nodes and thus can never be disintegrated

in response to the penetrating plate. This limitation makes the soil domain to deform in accordance with the mesh pattern and the soil acts like a piece of sponge, which is not representative of actual soil response. Figure 1.36 illustrates the sponge-like response of the soil domain in the plate-sinkage test, as reported by Lescoe [25, 37] and Dhillon [26, 39]. Dhillon [39] further observed that the penetrating plate is supported not only by the compacted soil elements, but also by the undesirable tension caused by the stretched soil elements that cannot be disconnected from each other, leading to inaccurate contact force predictions. Several other studies using the finite element methods for modeling large deformations of soils have also reported similar limitation for the FE method [38, 43].

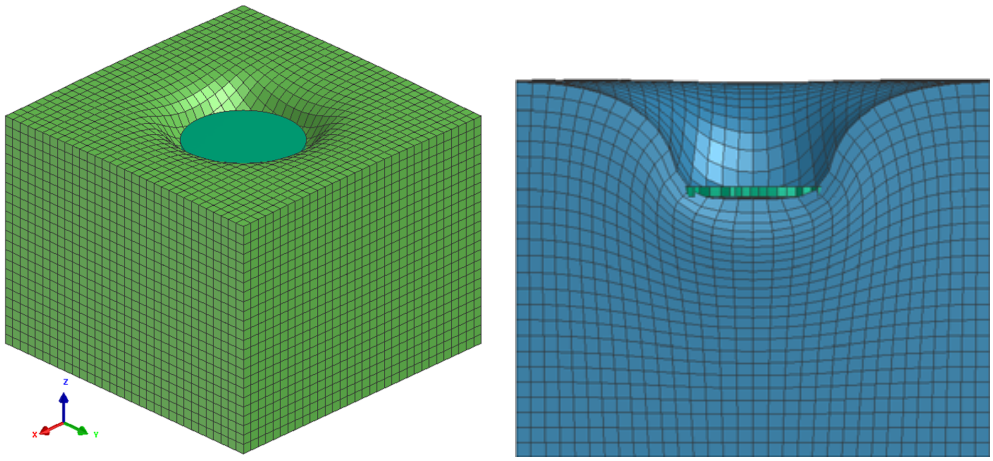

(a) (b)

Figure 1.36: Sponge-like deformed shape of the finite element soil mesh in the plate-sinkage test simulations reported by (a) Lescoe et al. [25, 37], and (b) Dhillon et al. [26, 39]

Alternatively, a few studies have used mesh-less methods such as the *Smoothed Particle Hydrodynamics (SPH)* method [26, 37, 40, 180], and the *Discrete Element (DE)* method [181–184]. The Smoothed Particle Hydrodynamics technique was invented by Lucy [185], Gingold and Monaghan [186] for simulating astrophysical processes, and has been widely used for analyses of viscous fluid flows [187, 188] as well as strength of materials [189]. This method of analysis uses finite particles (in place of finite elements), while each particle carries hydrodynamic filed variables that change on the basis of conservation laws. Each field variable is smoothed at a particle via averaging those of other neighboring particles

within a distance named *smoothing length*, while an averaging function *(kernel)*, gives weight to the contribution of every neighboring particle based on its closeness. Unlike mesh-based approaches such as the finite difference, finite element and finite volume methods, the spatial derivatives of the field variables in the mesh-less method are analytically calculated by differentiating these smoothing kernel functions.

Lescoe [25, 37] and Dhillon [26, 39, 40] applied the SPH technique for development of a computational soil model considering an hydrodynamic elastic-plastic constitutive model together with a linear pressure-volume equation of state in the Pam-Crash analysis platform. These studies conducted plate-sinkage test simulations, as illustrated in Figure 1.37, and observed that the mesh-less nature of the SPH method can more realistically model large deformations of the soil in response to the penetrating plate in comparison with the traditional FE method. The CPU time for the SPH soil model, however, was nearly 5.5 times longer than that of an identical FE soil model [37, 39]. Lescoe [37] further simulated the shear-box test using both the FE and SPH analysis methods, as illustrated in Figure 1.38, and reported that such extremely large shear deformations, which result in disintegration of the soil domain, could only be modeled using the SPH method.

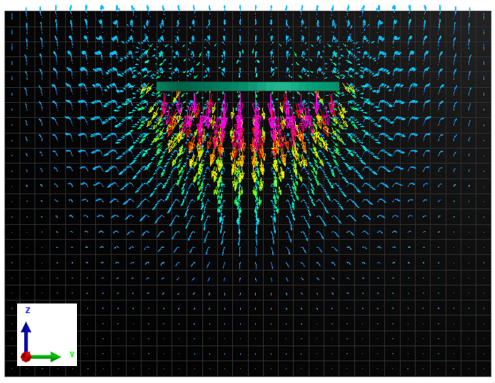

Figure 1.37: Plate-sinkage test simulations using SPH method with elastic-plastic material properties developed by Lescoe et al. [25]

Owing to excessive processing time required for the soil elements/particles, a rigid wheel model, derived from a previous truck tyre model [11] with tread removed, was used to study the tyre-soil interactions in a more efficient manner. The initial solver-related

(a) (b)

Figure 1.38: Shear-box test simulations using (a) FE, and (b) SPH soil models with elastic-plastic material properties developed by Lescoe et al. [25]

parameters in the SPH soil model, taken from previous studies [35, 36, 42], were fine-tuned through matching the SPH simulation results with those predicted by the FE soil model considering identical geometry, grid size and material properties. The SPH soil model could yield satisfactory results for the stress distributions beneath a stationary rigid wheel, while the computing time was 4 times longer than for the FE soil model [37]. A hybrid FE-SPH soil model was thus derived from the FE soil model via replacing few top layers of the FE elements, undergoing large deformations, with SPH particles [37], which could reduce the CPU time to nearly one-half. Figure 1.39 illustrates the hybrid soil model under a towed-rolling rigid wheel at constant speed, which was employed for evaluating the tyre rolling resistance on a soft terrain. It was observed that the depth filled with the SPH particles in the hybrid soil model highly affects the rolling resistance. Using a deeper amount of SPH

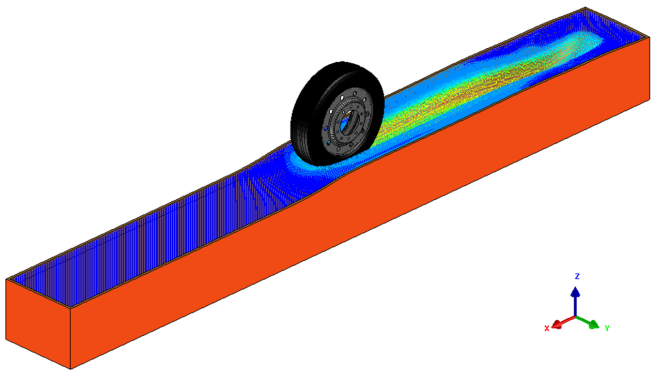

Figure 1.39: Hybrid FE-SPH soil model subjected to a towed-rolling rigid wheel, developed by Lescoe et al. [25, 37]

particles increased the rolling resistance coefficient. For a full SPH model this coefficient was 15% higher than that obtained from the FE model.

Barsotti [38] also compared the FE and SPH techniques for modeling a crushable foam aircraft arrestor bed in LS-DYNA. The arrestor bed was represented using the crushable foam material model (type 63 in LS-DYNA) in conjunction with an erosion model to allow element failure based on a strain criterion. Figure 1.40(a) illustrates the aircraft tyre model rolling through the FE arrestor model, while creating a rut of crushed material.

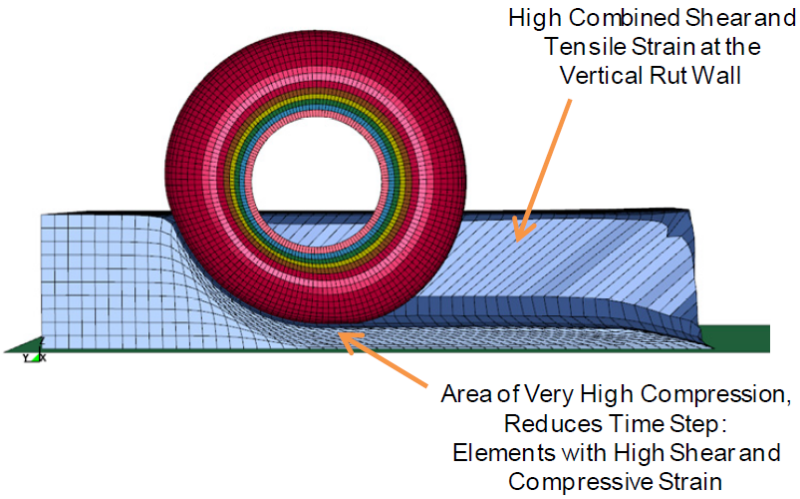

(a)

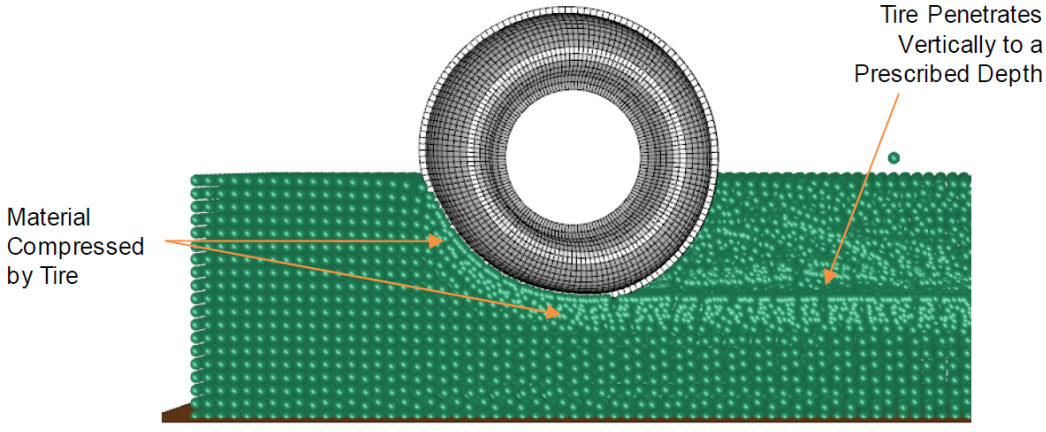

(b)

Figure 1.40: (a) FE, and (b) SPH aircraft arrestor bed models subjected to high compaction and rutting by an aircraft pneumatic tyre model, developed by Barsotti [38]

The study reported several shortcomings associated with the FE model including distortions of the elements due to large shear deformations, high hourglass energy produced by the compacted elements, and reduced integration time-step caused by highly compressed elements. The FE approach was also found inadequate for modeling the plowing action of the tyre in a deep material. On the other hand, the SPH particles, being inherently dissociative, could better represent the actual crushable foam material behavior, resulting in more robust performance of the model for such high compaction and dislocation applications. With the SPH model, the aircraft tyre revealed clear rut formation through the material, while shearing through the soil walls and compacting the bottom material, as illustrated in Figure 1.40(b). Moreover, adding an erosion criterion to eliminate the distorted FE elements was not needed in the SPH model, since the particles were free to dislocate and be separated from the domain. Further, unlike the FE model, the time-step remained constant throughout the SPH solution.

1.3 Research objectives and scope

From the review of the reported studies on analyses of rolling tyre interactions with rigid and soft terrains, it is evident that the vast majority of the structural tyre models have been developed for applications on rigid roads. Relatively fewer efforts have been made towards analyses of tyres on deformable terrains considering the complex behavior of soft soils under a rolling tyre. The reported structural models of tyres have been successfully employed for predicting in-plane and out-of-plane dynamic responses of the rolling and steered tyres. Modal properties of pneumatic tyres have also been reported in a number of studies, although the vast majority are limited to the free inflated tyres. The modal characteristics of a rolling tyre with ground contact have been addressed in only a few studies, which are limited to a few lower vibration modes.

The mesh-based nature of the finite element method, however, has shown poor performance in modeling the soil flow under rolling tyre loads. Alternatively, mesh-less methods such as the Smoothed Particle Hydrodynamics technique could permit modeling of large deformations and fragmentations of soils under moving vehicular loads. Both the finite

element structural models of the tyre and the mesh-less models of the soil, however, pose excessive computational demands, which would limit their applications for vehicle system simulations. The developments in computationally efficient models are thus vital for applications in vehicle dynamics simulations. Moreover, such models could serve as effective virtual simulation tools to substitute for costly laboratory tests that are required for parametrization of physics-based, phenomenological tyre models, and terramechanics-based soil models. Owing to the lack of a computationally efficient structural tyre model, the majority of the studies on tyre-soil interactions have been limited to rigid wheel representation of the pneumatic tyre. This approach is justifiable only for characterization of the soil properties but would yield considerable errors in forces and moments attributed to tyre-terrain interactions. The tyre interactions with deformable terrains are generally evaluated considering terramechanics-based soil models. These analytical models, however, necessitate prior identifications of several model parameters, which are obtained through costly experiments. The overall objective of the dissertation research is formulated to develop comprehensive tyre and tyre-soil models that could serve as a virtual test environment for both on-road and off-road tyres, and parametrization of terramechanics-based soil models. The specific goals of the study are summarized below:

1. Develop a 3-D finite element model of a truck tyre considering its multi-layered composite structure for predicting its dynamic responses on a rigid road at relatively higher speeds and validate the tyre model using available experimental data;
2. Develop a pre-processing algorithm to automate model reformulations for design sensitivity analyses;
3. Investigate the effects of inflation pressure, ground contact and rolling speed on natural modes and frequencies of the tyre model using the intermittent eigenvalue extraction approach;
4. Develop a simplified Part-Composite truck tyre model to improve computational efficiency of the model for developed coupled tyre-soil models;
5. Develop a soil model using the Finite Element and the Smoothed Particle Hydrodynamics techniques in conjunction with a pressure-dependent material constitutive

model and investigate the merits and limitations of the two analysis methods;

6. Illustrate effectiveness of the integrated tyre-soil model considering the theoretical estimations for the contact force/moment responses of the stationary, driven, towed and steered tyre obtained from terramechanics-based models;

1.4 Organization of dissertation (manuscript-based)

This dissertation is prepared according to the *manuscript-based* format defined in the *Student's Guide to Thesis Preparation, Examination Procedures and Regulations* booklet of the School of Graduate Studies at Concordia University. The dissertation is organized in seven chapters, five of which present three published journal articles and two submitted articles for peer-review. The first chapter present the review of relevant reported studies on different methodologies for modeling pneumatic tyres, soft soils and rolling tyre interactions with rigid and soft terrains. Different approaches for modeling pneumatic tyres in view of dynamic responses and vibration characteristics are initially classified and discussed. The chapter further reviews the constitutive models and testing devices used for describing soft soil behavior in response to rolling tyre loads. The research objectives and scope of the dissertation are also presented in this chapter.

Chapter 2 presents the following article, published in the *International Journal of Vehicle Systems Modelling and Testing*:

S. Shokouhfar, S. Rakheja, and M. El-Gindy. Development of a rolling truck tyre model using an automatic model regeneration algorithm. *International Journal of Vehicle Systems Modelling and Testing*, 11(1):68–95, 2016 [109]

The article presents development of a three-dimensional finite element model of a rolling radial-ply truck tyre in order to predict its vertical and cornering properties at relatively high speeds. The model includes a detailed representation of the tyre complex geometry and multi-layered composite structure including the carcass and belt plies, bead fillers and tread. An algorithm is developed for efficient formulation of the model for parametric analyses, while LS-DYNA, a nonlinear finite element code, is used as the simulation tool. The validity of the proposed tyre model is demonstrated by comparing the predicted

load-deflection, cornering and free vertical vibration characteristics with the reported experimental data. The simulation results show the robust behavior of the tyre model up to rolling speeds of 100 km/h. The verified tyre model is subsequently employed to study the influences of various operating parameters, namely, the inflation pressure, vertical load, rolling speed and road friction on the tyre vertical and cornering properties.

Chapter 3 presents the following article, published in the *International Journal of Vehicle Systems Modelling and Testing*:

S. Shokouhfar, S. Rakheja, and M. El-Gindy. Modal analysis of a rolling truck tyre subjected to inflation pressure and vertical deflection. *International Journal of Vehicle Systems Modelling and Testing*, 11(2):116–141, 2016 [190]

This article presents the modal analysis of a rolling truck tyre under inflation pressure and vertical deflection in order to determine its natural frequencies and mode shapes. The finite element truck tyre model developed in the previous chapter is used for the eigenvalue analyses. The nonlinear effects of the inflation pressure, vertical load and rolling speed are incorporated in the analysis through an explicit dynamic simulation to determine the stress state throughout the tyre at instants when the modal characteristics are desired. The eigenvalues are subsequently extracted at three key moments when the tyre reaches the steady state after application of the inflation pressure, vertical deflection and rolling speed. It is shown that for a deflected tyre, the conjugate mode frequencies, being identical for an inflated tyre, diverge to two different frequencies with one being lower and the other higher than the corresponding frequency of the free tyre under inflation alone. The influences of the inflation pressure, vertical load and rolling speed on tyre natural frequencies are obtained through the development of a computationally efficient algorithm to automate the tyre model reformulations for parametric studies.

Chapter 4 presents the following article, published in the *International Journal of Vehicle Systems Modelling and Testing*:

S. Shokouhfar, S. Rakheja, and M. El-Gindy. A simplified model for rolling tyre interactions with rigid surfaces using Part-Composite approach in LS-DYNA. *International Journal of Vehicle Systems Modelling and Testing*, 11(2):142–164, 2016 [191]

The article presents a computationally efficient structural model of a truck tyre in

rolling contact with a rigid road surface for predicting its dynamic responses. The multiple layers of the rubber matrix and fiber-reinforcements, being used in the comprehensive structural model presented in chapter 2, are now lumped together and represented as a composite layered configuration of shell elements using the Part-Composite approach in LS-DYNA. This approach facilitates definition of the integration rule through the thickness of the multi-layered element via defining stacks of plies with pertinent material properties, thicknesses and fiber orientations. The validity of the proposed simplified tyre model is subsequently demonstrated through comparisons of the simulation results with those obtained from the comprehensive tyre model presented in chapter 2 as well as with the reported experimental data in terms of vertical force-deflection, cornering force/moment and vibration characteristics. It is sown that the proposed methodology of integrating several single-layered elements of the tyre structure into one multi-layered element results in substantial reduction in the total number of elements in the model and thereby significant improvement in the computational efficiency.

Chapter 5 presents the following article, submitted to the *Journal of Terramechanics*:

S. Shokouhfar, S. Rakheja, and M. El-Gindy. A virtual test platform for analyses of rolling tyre-soil interactions: Part I – Parametrization of terramechanics models. *Journal of Terramechanics*, 2016. (submitted) [192]

The article presents a virtual testing environment for parametrization and evaluation of the terramechanics-based rolling tyre-soil interaction models. A computational soil model is implemented using the Finite Element and the Smoothed Particle Hydrodynamics methods in conjunction with a pressure-dependent strength material model using LS-DYNA. The input parameters to this constitutive model are provided for a few types of soils based on geotechnical laboratory test data. The soil model is initially validated in terms of the volumetric deformation behavior via comparisons with the experimental data. After demonstrating the merits and limitations of the two analysis methods, the SPH soil model is utilized for conducting a series of virtual tests for parametrization of the pressure-sinkage as well as the shear stress-shear displacement relations for the selected soils. The identified parameters are assessed through comparisons with those calibrated via actual tests using the bevameter machine as well as the triaxial device.

Chapter 6 presents the following article, submitted to the *Journal of Terramechanics*:

S. Shokouhfar, S. Rakheja, and M. El-Gindy. A virtual test platform for analyses of rolling tyre-soil interactions: Part II – Evaluations of terramechanics models. *Journal of Terramechanics*, 2016. (submitted) [193]

In this article, the parameterized terramechanics-based models are evaluated via comparisons of the theoretical estimations for the tyre-soil contact forces and moments with those predicted by the computational simulations. A pneumatic tyre model as well as a rigid wheel model are integrated to both the FE and SPH soil models for predicting the normal and tangential stress distributions beneath the tyre as well as the contact forces and moments arising from the stationary, rolling and steered tyres. It is shown that the theoretical estimations by the terramechanics-based models are quite comparable with those obtained from simulation models of tyre and wheel under driving, towing and steering on soft soils. While the FE model predicted relatively higher forces/moments compared to the SPH soil model, the theoretical estimations occurred in between the FE and SPH predictions.

Chapter 7 presents the highlights, major contributions and major conclusions of the dissertation research together with a number of recommendations for future works.

Chapter 2

Development of a Rolling Truck Tyre Model using an Automatic Model Regeneration Algorithm

2.1 Introduction

Dynamic performance of ground-vehicles are primarily determined by the forces/moments arising from interactions of the pneumatic tyres with the ground. These forces/moments are known to depend on a number of design and operating parameters in a highly complex manner. These parameters involve the tyre structure, material properties, inflation pressure, vertical load, speed, road friction, road profile and more. A vast number of tyre models of varying complexities have evolved over the past many decades for estimating tyre forces/moments using widely different methods. Considerable efforts in modeling of tyres, however, are continuing for accurate and computationally efficient predictions of forces/moments for applications in vehicle design and dynamic analyses.

The reported tyre models may be grouped into three broad categories on the basis of the modeling approach, namely, physics-based, phenomenological and structural models. The physics-based models generally employ mass-spring-damper elements to formulate dynamic tyre properties and could estimate tyre forces/moments analytically as functions of tyre deformations/slips, road profile, speed and other operating conditions. Early models

focused on vertical vibrations of a non-rolling tyre for applications in vehicle ride simulations [1, 47–50].

A number of models formulated the in-plane tyre behavior for vehicle ride and traction/braking simulations. In these models, the belt and tread components were assumed as a rigid or flexible ring supported on an elastic foundation representing tyre sidewalls [3, 51–54]. These models were employed in analyses of vehicle vibrations under road irregularities with low to mid-range frequencies [47, 54, 56, 57] and were further enhanced to higher frequency excitations by incorporating tyre slip and enveloping properties using the brush model [58], and effective road profile technique [5]. A number of studies considered the out-of-plane tyre behavior and predicted tyre cornering force/moment characteristics in terms of side-slip angle, normal load, road friction and tyre elastic properties [59]. Models for estimating both traction/braking and cornering characteristics under combined longitudinal/lateral slip deformations have also been reported [58, 60, 61]. Three-dimensional (3-D) rigid-ring tyre models have been formulated by integrating the out-of-plane tyre properties to the in-plane rigid-ring tyre model [4, 62].

A group of phenomenological tyre models have also evolved using regression-based formulations to describe tyre forces/moments under a defined set of operating conditions. Among the reported phenomenological models, the Magic Formula tyre model [2, 63], is most widely used for analyses of vehicle braking and steering responses under widely varying operating conditions [194]. This model is known to provide accurate estimations of the steady-state braking and cornering forces for a rolling tyre as functions of the longitudinal-slip ratio, side-slip angle, inflation pressure and normal load [2, 63]. A number of semi-empirical tyre models have also been reported that integrate both the physics- and phenomenon-based models [65–67]. The MF-SWIFT model [65] is among the advanced semi-empirical tyre models that combines the rigid-ring model [3–5] with the Magic Formula model [63].

The physical and phenomenological tyre models can yield computationally efficient predictions of the tyre forces/moments and are thus well-suited for multi-body vehicle system analyses. The reliability of these models, however, strongly depends on the accuracy of model parameters that must be identified through physical measurements [6–8, 71].

Owing to nonlinear dependence of tyre forces/moments on various operating factors, the validity of such parameters is limited to the vicinity of the operating conditions used in the identification tests. Furthermore, the physical and phenomenological tyre models provide effective estimations of global tyre properties, while such models cannot yield guidance towards design of pneumatic tyres due to lack of consideration of tyre geometric, structural, and material properties. Consequently, a large number of structural models have been proposed for the purpose of tyre design and developments. These, invariably, employ finite element (FE) methods, which permit consideration of the geometric, structural and material properties of pneumatic tyres.

Early FE tyre models were developed based on two-dimensional (2-D) axisymmetric element formulations considering the tyre subject to inflation pressure and centrifugal loading in order to limit the computational cost [72, 73]. With advances in computer hardware and numerical algorithms, a range of 3-D FE models have been developed that incorporate the tyre complex structure under realistic loading and boundary conditions [74–78]. The reported models have employed widely different methods to describe the tyre structure. A number of models represented the tyre as a simple inflated airbag using a single layer of membrane elements with orthotropic material. Such models permitted improved computational efficiency but could only approximate the global performance of the tyre for applications in durability [80, 81], cornering [82], and vehicle crash [79] simulations.

Zhang [83] reported a 3-D multi-layered truck tyre structure model using ANSYS. The carcass and belt plies were modeled using layered solid elements considering a number of orthotropic layers for the carcass and belt reinforcements along with isotropic layers for the rubber matrix. The approach permitted analyses of stresses between the individual layers of the carcass and belts, which lead to a set of tyre design parameters to minimize inter-ply shear stresses and thereby enhance tyre durability. A number of other studies have also reported similar multi-layered structural models [84–87]. These models, however, were limited to static analyses of non-rolling tyres subjected to inflation pressure and footprint loads, although they could provide effective estimates of static vertical stiffness, footprint size and contact pressure distribution of the stationary tyres [84–87].

Rolling tyre models have also been developed using a non-rolling mesh considering

rigid body rotation of the tyre in Eulerian manner and tyre deformations in Lagrangian framework. In this approach, the non-rolling mesh is refined only in the vicinity of the contact area, which helps improve the computational efficiency [88–90]. However, the applications of such models are limited only to the steady-state response analyses of rolling tyres. With advances in explicit finite element methods, a number of structural tyre models have been proposed to consider the transient behavior of a tyre in terms of its physical characteristics [10, 12, 91–93].

Chae [92] proposed a 3-D model of a rolling radial-ply truck tyre using PAM-CRASH. A single composite layer of membrane elements represented the carcass and belt plies, which comprised a single orthotropic material layer for the carcass with radial cords, and a single layer for the belt with circumferential cords. Another isotropic material layer was integrated within the composite layer, which represented the rubber matrix. This methodology of describing the tyre structure has been used in several studies focusing on transient dynamic responses of tyres in PAM-CRASH [12, 24–26, 94, 96]. This approach, however, does not permit analysis of stresses and deformations in individual layers, which may be essential for design purposes. Moreover, this approach cannot simulate the effects of belt cord angle, β, on the tyre responses since the belt layer assumes only circumferential cords. A minimum of two layers would be essential to describe the belt with $\pm\beta$ cord angles. Alternatively a number of studies modeled the carcass and belt plies using several independent layers so as to capture the inter-layer interactions and their effects on tyre responses. Hall [10] reported a 3-D rolling tyre model using LS-DYNA. The carcass and belt plies were modeled using the *discrete reinforcement* technique, where the rubber matrix was described by isotropic solid elements including discrete reinforcements represented by orthotropic shell elements. Such structure models, however, pose unreasonable computational demands. It has been reported that a 0.4 s real time simulation could take about 200 hours on a Sun Ultra 60, 360 MHz workstation [195].

Apart from the wide variations in the structure models, the tyre models have also employed different material models. Selecting material data for different components of a tyre model is indeed a challenging task partly due to difficulties associated with characterizations of tyre composite components, and in-part due to confidentiality of data by the

manufacturers. The reported tyre models have thus mostly used equivalent orthotropic material properties for the fiber-reinforced composite layers of the carcass and belts. Only a few studies have defined material properties that are directly derived from the geometric and material data of pure rubber and twisted cords [32]. Reid [98] modeled the fibers using beam elements attached to the isotropic shell elements describing rubber matrix in the carcass and belt plies. This approach would further increase the model complexity and computational demand.

The structural tyre models permit the analysis of influences of various design and operating parameters on static/dynamic tyre performance characteristics, and can thus be employed for tyre design and developments. Such models, however, are computationally demanding for applications in vehicle dynamics simulations compared to the physics-based or phenomenological models. Moreover, design sensitivity analyses generally involve model reformulations which lead to significantly higher demands on human as well as computing resources. The structural models, however, could serve as vital virtual tyre testing environments for conducting design sensitivity analyses, and identification tests required for parameterizations of physical and phenomenological tyre models. The primary motivation of the present study arises from the desire for a reliable tyre model with reasonable computing demand for model reformulations and for predicting nonlinear dynamic properties of a rolling truck tyre under a wide range of operating conditions. A 3-D finite element model of a rolling truck tyre is developed to study its vertical and cornering properties when traversing a rigid road at relatively high speeds. The model takes into account the multi-layered composite structure of the carcass and belt plies, considering isotropic solid elements for the rubber matrix and orthotropic shell elements for the reinforcements, while orthotropic material properties are directly determined from those of the rubber compound and twisted cords. LS-DYNA is used as the FE simulation tool. An algorithm is developed for efficient generation and reformulations of the model on the basis of the defined tyre cross-section, mesh size, structural and material properties, loading and boundary conditions, and solution method settings to facilitate parametric studies. The validity of the model is illustrated through comparing the load-deflection, cornering and free vertical vibration characteristics with the reported measured data. The robustness of the model

is demonstrated at speeds up to 100 km/h, and a wide range of inflation pressures and vertical loads. The validated model is subsequently used for investigating the influences of different operating conditions, namely, inflation pressure, vertical load, speed and road friction, on the tyre vertical and cornering characteristics.

2.2 Finite element tyre model

A 3-D finite element (FE) model of a rolling truck tyre is developed to predict its transient and steady-state vertical and cornering characteristics while traversing a rigid road. The model is formulated using different element types, material models, and contact algorithms available in LS-DYNA [104, 107]. The models of various constituents of the tyre are described below.

2.2.1 Tyre geometry and mesh

A radial-ply truck tyre (295/75R22.5) is selected for the FE modeling and analyses, although the proposed methodology is considered applicable for all tyres. The tyre structure model is formulated considering tyre geometry and multi-layered structure including the bead fillers, tread, carcass and belts. Figure 2.1(a) illustrates the tyre cross-section and the mesh. The carcass and belt plies are represented as composite materials containing different layers of shell and solid elements, while the tyre cross-section geometry is taken from [11], where only a single composite layer of membrane elements was used to represent the carcass and belt plies. The bead fillers and the tread are modeled using solid elements with rubber material. As illustrated in Figure 2.1(a), the two layers of solid elements (regions 1 to 9) represent the carcass rubber matrix in the sidewalls, reinforced by three layers of composite shell elements with radial cords (cord angle, $\beta = 90°$). Two layers of solid elements (regions 10 to 14) represent the belt layers, where the upper layer accounts for the belt rubber matrix sandwiched between two layers of composite shell elements reinforced by cords with $\beta = \pm 22°$. The lower solid layer represents the carcass rubber matrix below the belt, which is also reinforced by a layer of composite shell elements with radial cords.

The carcass and belt plies are modeled using the *discrete reinforcement* technique

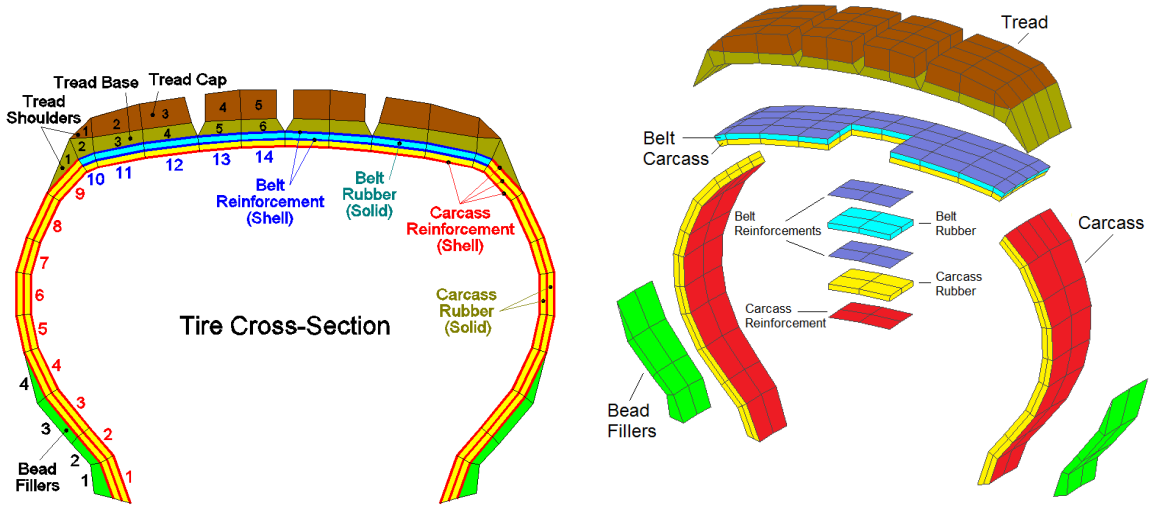

(a) (b)

Figure 2.1: (a) Tyre cross-section mesh; and (b) Multi-layered tyre structure

[10], where the rubber matrix is represented by solid elements and the reinforcements are discretely modeled using composite shell elements, as shown in Figure 2.1(b). This approach allows for stress/strain analyses for the individual matrix and the reinforcements. The matrix and the reinforcements are considered to be fully bonded by defining the shared nodes at the interface of the two layers. This assumption is considered valid since the study was not concerned with delamination of the plies, which rarely occurs in normal operating conditions.

The 3-D tyre mesh is made of equal sectors through copying and rotating the cross-section mesh about the tyre axis in equal increments. A refined mesh was used in the outer circumferential regions (9 to 14), including the tread, belt and partly carcass, by reducing the rotating increment, so as to accurately model large deformations of the rolling tyre in the contact area. Applying different number of circumferential divisions for the coarse and refined portions of the mesh, however, caused small gaps and thereby a number of free edges for the elements near the gaps, as shown in Figure 2.2(a). The initial positions of the nodes belonging to the free edges of refined elements are thus adjusted in order to obviate the gaps. A number of constraints are further defined to ensure continuous contact of free edges of the refined elements with those of the coarse elements during simulations.

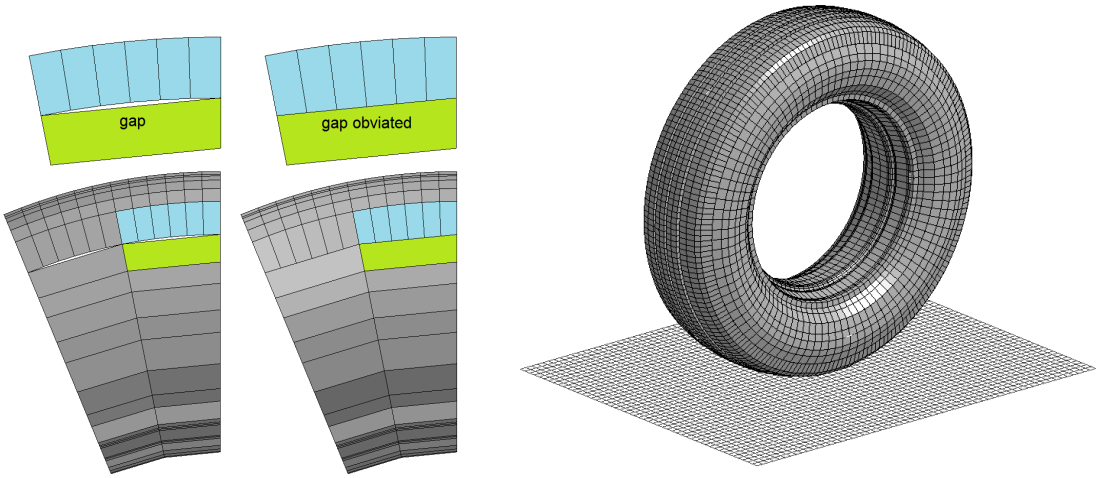

(a) (b)

Figure 2.2: (a) Gaps formed at the interface of the coarse and refined portions of a mesh with 32 and 192 divisions, respectively, and obviating them via adjusting nodal coordinates and defining constraints; and (b) 3-D tyre mesh, considering 96 and 192 circumferential divisions for the coarse and refined regions, respectively

The width and length of each solid rubber element is determined from the mesh increments defined for tyre cross-section mesh and the number of circumferential divisions, respectively. The thickness of the element is governed by the thickness of the respective layer. The number of circumferential divisions are chosen so as to achieve maximum element aspect ratio throughout the model close to unity. For a mesh of 96 sectors with refinement to 192 divisions for the outer circumferential regions (9 to 14), the model would yield a total of 17856 nodes and 24192 elements.

Figure 2.2(b) illustrates the 3-D tyre mesh, which is coupled with the wheel rim made of rigid shell elements through shared nodes so as to ensure tyre-rim force transmission during free-rolling and cornering force tests. The beads were thus not included in the model. The road was considered as an undeformable flat or drum surface made of shell elements of rigid material (4 mm thick). A large diameter (3 m) drum was chosen so as to perform simulations at relatively high speeds.

2.2.2 Material models and properties

The material properties of the carcass and belt composite plies were directly obtained from the geometric and material properties of pure rubber and twisted cords using the Halpin-Tsai equations [196, 197]. This approach permits study of influences of geometric and material properties of individual tyre constituents on the dynamic responses. Table 2.1 lists the isotropic material properties for the pure rubber and twisted cords, which were taken from the reported studies [32, 198] and slightly refined on the basis of the known load-deflection characteristics [11].

Table 2.1: Material properties of pure rubber, twisted cords, steel rim and rigid road

Material property	*Carcass rubber*	*Belt rubber*	*Carcass cord*	*Belt cord*	*Rigid rim*	*Rigid road*
Density (ρ, kg/m^3)	1190	1190	6677	6563	7860	9000
Young's Modulus (E, MPa)	11.032	13.79	63600	106000	200	10000
Poisson's Ratio (ν)	0.49	0.49	0.3	0.3	0.3	0.28
Shear Modulus (G, MPa)	3.702	4.627	45540	75900		

The solid elements representing rubber matrix in the carcass and belt plies are modeled using material type 1 (elastic) from the LS-DYNA material library [104]. The material properties described in Table 2.1 were used for the material model. The shell elements describing fiber-reinforced layers (Figure 2.3) are modeled using material type 22, which simulates an orthotropic composite material. Table 2.2 summarizes the geometric properties considered for the cord-rubber compounds, which include the cord diameter (d), the

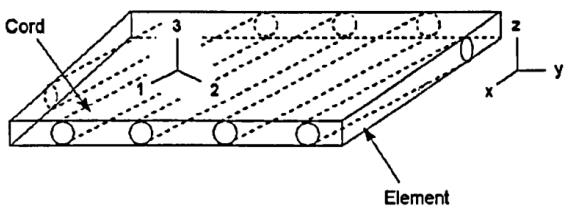

Figure 2.3: Fiber-reinforced composite shell element [10]

composite layer thickness (t) and cord-end-count (cec).

The volume fraction of the cord (f_v) is computed from geometry of the cords such that:

$$f_v = \frac{\pi d^2 cec}{4t} \tag{2.1}$$

The volume fraction of the cord generally ranges from 0.1 to 0.4 [197]. The material type 22 also requires the density of the cord-rubber compound, which is obtained from the *Rule of Mixtures*:

$$\rho = \rho_c f_v + \rho_r (1 - f_v) \tag{2.2}$$

where ρ_c and ρ_r are densities of the twisted cords and the pure rubber, respectively. The term $(1 - f_v)$ represents the rubber volume fraction.

The properties of composite material model are defined in terms of orthotropic elastic constants, namely, the Young's moduli (E_1, E_2, E_3), the Poisson's ratios (ν_{21}, ν_{31}, ν_{32}) and the shear moduli (G_{21}, G_{31}, G_{32}), defined in the cord axes system (1, 2, 3), as shown in Figure 2.3. The cord angle (β) is thus also required to define the orientation of the cords with respect to the element axes system (x, y, z), also shown in the Figure 2.3.

The orthotropic elastic constants E_1, E_2, ν_{12} were derived from the individual properties of the constituents (Table 2.1) as well as their volume fractions (Table 2.2) using Halpin-Tsai equations [197], such that:

$$E_1 = E_c f_v + E_r (1 - f_v) \tag{2.3}$$

$$\nu_{12} = \nu_c f_v + \nu_r (1 - f_v) \tag{2.4}$$

$$E_2 = \frac{E_r \left[E_c (1 + \zeta_1 f_v) + \zeta_1 E_r (1 - f_v) \right]}{E_c (1 - f_v) + \zeta_1 E_r \left(1 + \frac{f_v}{\zeta_1} \right)} \tag{2.5}$$

where E_c and E_r are the Young's moduli of the cord and rubber materials, respectively, and ζ_1 is a constant, taken as 2 [197]. The Young's modulus along axis 3, E_3, is identical to E_2, since both are in the transverse direction, normal to the cord axis. Similarly, the shear modulus G_{12}, which is identical to G_{13}, is computed from:

$$G_{12} = \frac{G_r [G_c (1 + \zeta_2 f_v) + \zeta_2 G_r (1 - f_v)]}{G_c (1 - f_v) + \zeta_2 G_r \left(1 + \frac{f_v}{\zeta_2} \right)} \tag{2.6}$$

where ζ_2 is taken as 1 [197]. The Poisson's ratio ν_{13} is also the same as ν_{12}. Furthermore, the Poisson's ratios ν_{21}, ν_{31}, ν_{32} are related to ν_{12}, ν_{13}, ν_{23} in the following manner:

$$\nu_{21} = \frac{E_2}{E_1}\nu_{12} \quad ; \quad \nu_{31} = \frac{E_3}{E_1}\nu_{13} \quad ; \quad \nu_{32} = \frac{E_3}{E_2}\nu_{23} \tag{2.7}$$

Table 2.2 also summarizes the orthotropic material properties of the cord-rubber compounds in the carcass and belt plies, which are computed using the aforementioned Halpin-Tsai equations [197].

Table 2.2: Geometric and orthotropic material properties of the cord-rubber compound in the carcass and belt plies

Geometric/material property	*Carcass compound*	*Belt compound*
Cord Diameter (d, mm)	0.6	0.8
Layer Thickness (t, mm)	1.0	1.5
Cord-End-Count (cec, /cm)	4	4
Cord Volume Fraction (f_v)	0.15	0.18
Density (ρ, kg/m^3)	1810	1910
Young's Modulus (E_1, MPa)	7202.77	14220.32
Young's Modulus (E_2, MPa)	15.25	20.19
Poisson's Ratio (ν_{12}, ν_{13})	0.4685	0.4645
Poisson's Ratio (ν_{23})	0.4217	0.4181
Shear Modulus (G_{12}, G_{13})	4.646	6.06
Shear Modulus (G_{23}, MPa)	3.577	4.61

The solid elements forming the bead fillers and the tread were described by the Mooney-Rivlin rubber material model (type 27). This constitutive model is considered to accurately describe the hyper-elastic behavior of the rubber in tyre models [10, 12, 32]. Table 2.3 summarizes the material model parameters for the different rubber compounds in the tyre structure, namely, the mass density, the Poisson's ratio, and the elastic constants C_{10} and C_{01} in the Mooney-Rivlin's strain energy function [11]. The table presents the material properties for the bead fillers, the tread base and tread cap, and the corresponding regions shown in Figure 2.1(a).

The shell elements representing the wheel rim and the road were described using material type 20 (rigid) since these are substantially stiffer than the tyre constituents. The

Table 2.3: Material properties of the solid elements of bead fillers and tread [11]

Component	*Bead fillers*		*Tread base*		*Tread cap*	
(regions)	*(1)*	*(2 to 4)*	*(1)*	*(2 to 6)*	*(1)*	*(2 to 5)*
Density ($\rho, \mathrm{kg/m^3}$)	882	881	869	596	693	693
Constant ($\mathrm{C_{10}}, \mathrm{MPa}$)	0.392	0.392	0.41	0.51	0.67	0.67
Constant ($\mathrm{C_{01}}, \mathrm{MPa}$)	1.268	1.268	1.44	1.86	2.46	2.46
Poisson's Ratio (ν)	0.499	0.499	0.499	0.499	0.499	0.499

input data to this material model are summarized in Table 2.1. Based on the geometric and mass properties defined for different components of the tyre model, the masses of the tyre and rim were computed as 46 and 32 kg, respectively, which are in good agreement with data reported for the 295/75R22.5 tyre [12].

2.2.3 Tyre inflation model

The tyre inflation pressure was modeled via applying a uniformly distributed normal load to the inner layer shell elements of the tyre. This approach yields uniform constant pressure independent of changes in the tyre volume resulting from the tyre deformations. It has been reported that the tyre normal deflection yields only small increase in the inflation pressure, in the order of 2%, which is also considered to be small compared to the estimation errors of typical FE tyre models [10].

2.2.4 Tyre-road contact model

The tyre-road contact is modeled using *automatic surface to surface* contact [107] between the tread elements and the road elements, together with the penalty stiffness approach [105]. In this approach, the penetration of the tread element nodes, considered as the slave nodes, into the road elements, treated as master segments, are resisted by a penalty stiffness factor. The friction between the tyre and road is modeled using the Coulomb formulation, while the transition between the static and dynamic coefficients of friction (μ_s and μ_d) is smoothed through an exponential decay based on a decay coefficient

(d_c) of 0.5 and the relative velocity (V_{rel}) between the slave nodes and the master segments, such that [105]:

$$\mu = \mu_d + (\mu_s - \mu_d)e^{-d_c|V_{rel}|} \tag{2.8}$$

where μ is tyre-road friction coefficient. Depending on the road surface condition, the static and dynamic coefficients of friction may vary from $\mu_s = 0.8$ and $\mu_d = 0.75$ (for dry asphalt) to $\mu_s = 0.2$ and $\mu_d = 0.15$ (for hard-packed snow) [142].

2.2.5 Method of solution

Automatic model regeneration

A high speed rolling tyre exhibits various nonlinear dynamic properties that may arise from large deformations of the elements under severe loading conditions, nonlinear behavior of the rubber and reinforcements, and changing boundary conditions due to variations in the tyre-road contact geometry. The LS-DYNA [107] was chosen as the FE solver to evaluate nonlinear dynamic properties of the rolling tyre. The solver, however, involves considerable efforts for sensitivity analyses and characterizations that require re-meshing and repetitive simulations. An algorithm is designed to perform the model regeneration within the preprocessor in an automated and efficient manner. The algorithm also permits repeated simulations for design sensitivity analyses and characterizations under a range of loads with minimal user efforts. The algorithm, developed using Visual-C#, formulates a command file for the LS-DYNA preprocessor to regenerate the model using the user input data. Figure 2.4 illustrates the interface of the proposed algorithm with the LS-DYNA

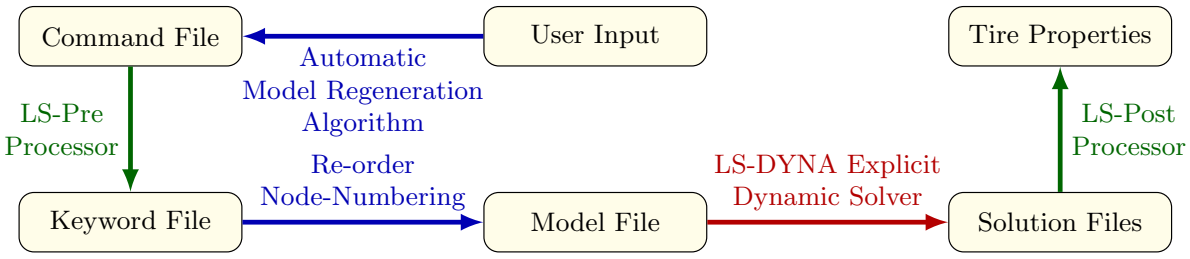

Figure 2.4: Re-modeling and analysis procedure

preprocessor and the re-modeling and analysis procedure. The algorithm initially converts the user-defined design and simulation parameters into a command file containing the list of commands to be executed by the preprocessor, denoted by LS-Pre Processor in Figure 2.4. These may include the tyre design data such as tyre cross-section, mesh size, geometric, material and damping properties; loading and boundary conditions, e.g., load curves for tyre inflation pressure, vertical load and speed; tyre-road friction and contact parameters. Solution settings such as integration step-size, elements formulations and hourglass control options are also incorporated. For simulations involving any changes in the tyre model input parameters, the command file can be regenerated in a highly efficient manner. The LS-DYNA preprocessor then executes the command file and generates the input file for the LS-DYNA solver, known as the *keyword* file. Depending on the type of elements chosen for the model, the user may need to re-order the default node numbering for generating the model file for the LS-DYNA solver. The algorithm is designed to reduce this user effort by modifying the keyword file with desired order of the nodes to generate the model file. The LS-DYNA solver subsequently reads the modified model file and performs the analysis. The simulation results obtained from the solver are visualized by the LS-DYNA post-processor, denoted as LS-Post Processor in Figure 2.4.

Required simulation scenarios

The explicit time integration method [107] was used for the transient dynamic analyses. The required simulation scenarios included the load-deflection test, drop test, free-rolling, cleat-drum test, and cornering force test at constant side-slip angles, which are briefly described here. The simulation is initiated by inflating the tyre to a nominal pressure, i.e., 758 kPa (110 psi). Following the tyre stabilization after inflation, a vertical load is applied to the rim center in a ramp manner up to the desired load, e.g., 26.7 kN (6000 lb). Although a damping ratio of 5% is commonly adopted for tyres [92], a critical damping is applied to dampen the oscillations following the tyre loading and thereby obtain rapid convergence to steady-state deformation. The critical damping is computed based on the natural frequency corresponding to the first vertical free vibration mode of the tyre, obtained from transient vertical oscillations of the tyre in the *drop test* [142]. The rolling

phase of the tyre is then initiated and the damping ratio is reduced to the typical value of 5%. A free-rolling condition was simulated by applying a prescribed velocity (up to 100 km/h) to the road along the tyre longitudinal axis, while the rim was only allowed to rotate about its axis after it was vertically loaded. The vertical loading was simulated by applying a prescribed vertical motion corresponding to the desired vertical load, e.g., 33.64 mm vertical displacement to represent 26.7 kN nominal operating load. A rigid drum of 3 m diameter with a small semicircular cleat of 1 cm radius was further used to vertically excite the tyre while rotating. The time-histories of the resulting tyre forces developed at the tyre spindle were evaluated to determine the dominant free vertical vibration frequencies of the tyre using the Fourier transformations of the vertical vibration response. A side-slip situation was also simulated by applying the road speed at a predefined angle, with respect to the tyre heading direction. This approach permitted characterization of the tyre cornering force/moment properties.

Elements formulations

The one-point integration shell element formulation (type 2) [199] was found sufficient for the rigid elements of the rim and the road. However, for the carcass and belt composite reinforcements, the fully-integrated shell element formulation (type 16) [199] was used, which applies a 2×2 Gaussian quadrature in the shell plane for integration.

As illustrated in Figure 2.5, the solid elements representing the rubber matrix in the carcass and belt plies yield aspect ratios well above the desired unity value due to their very small thickness. Such thin solid elements have been mostly modeled as 2-D shell elements assuming constant thickness [92]. 3-D solid elements are used in this study so as to capture the individual elements' deformations along the thickness axis. Applying the widely-used one-point integration formulation for such poor aspect ratio elements revealed poor convergence. Alternatively, fully-integrated element formulation was attempted, which provide stable solutions for rolling speeds up to 50 km/h. Extreme deformations leading to negative volume errors and instabilities, however, were observed at speeds above 50 km/h. The thick-shell element formulation available in LS-DYNA [107], was subsequently employed, which uses a solid element formulation with a strong

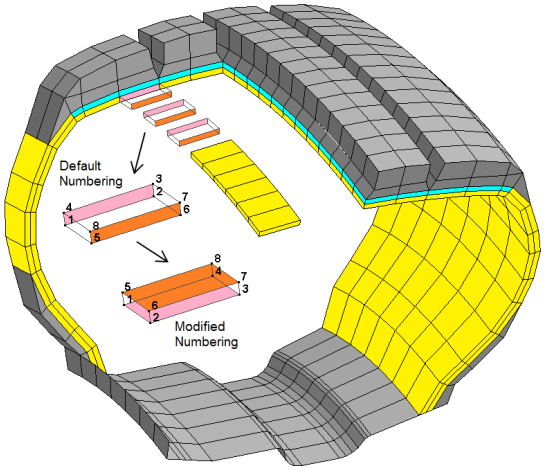

Figure 2.5: Modified order of node numbers in thick shell elements

emphasis on shell properties [105]. Owing to the 3-D constitutive law for such elements, the thickness changes could be easily deduced. As shown in Figure 2.1(a), a stack of two layers of such solid elements is considered to capture bending properties of the structure. This, however, involved re-ordering of node numbering for these thick shell elements. In this study, these elements are created through copying and rotating the tyre cross-section. Figure 2.5 illustrates default numbering of the nodes, which were subsequently modified to the correct order with nodes 1 to 4 on the bottom surface and 5 to 8 on the top surface of the thick shell element. The model simulations incorporating thick-shell elements revealed stable solutions up to rolling speeds of 100 km/h.

Furthermore, for the nearly-incompressible rubber materials in the tread and bead fillers (with ν near 0.5), the fully-integrated solid elements revealed highly stiff behavior leading to element locking and numerical instabilities. The one-point-integration formulation provided stable solutions and rapid convergence, although it required the control of hourglass energy modes. Owing to the limitation of viscous forms of the hourglass options in controlling the hourglass deformations in rolling tyres [15], one of the stiffness forms of the hourglass control (type 5) [107] was implemented for the one-point integration elements representing rubber material.

Mesh size selection

A grid convergence study was conducted to identify the desired mesh size so as to reduce the computational demand. For this purpose, the algorithm described in section 2.2.5 was used to automatically regenerate the tyre model for conducting repeated simulations considering different circumferential divisions (N_c) for the coarse mesh describing the carcass structure, ranging from $N_c = 12$ to $N_c = 192$. The mesh for the outer circumferential regions, comprising the composite belt layer and tread, however, was retained with 192 divisions so as to model the tyre-road contact accurately. Figure 2.6(a) illustrates the variations in vertical deflection of the non-rolling tyre with varying circumferential divisions (N_c). The variations in tyre cornering force corresponding to 6° side-slip angle at 5 km/h speed are also presented in Figure 2.6(b). In these simulations, the tyre was subject to 758 kPa inflation pressure and 26.7 kN vertical load. The results suggest reasonably good convergence for the grid with 96 circumferential divisions for the carcass structure.

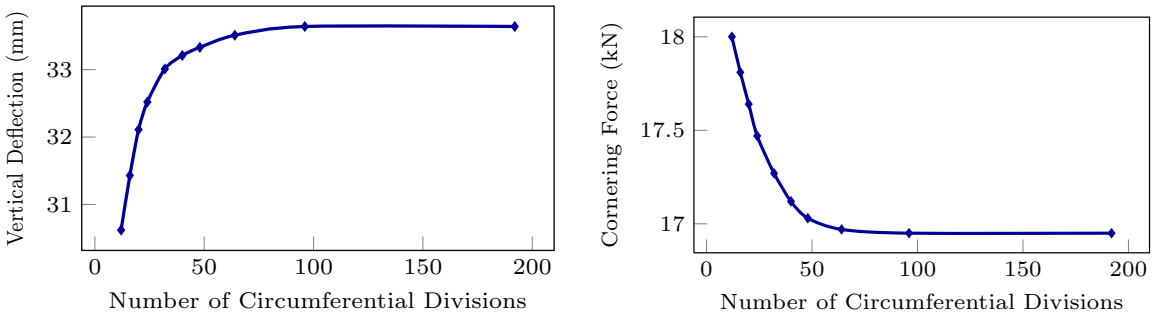

Figure 2.6: Variations in the tyre responses as a function of number of circumferential divisions: (a) vertical tyre deflection; and (b) cornering force

2.3 Tyre model validation tests

The validity of the tyre model was established through a series of static and dynamic tests involving comparisons of simulation results with the reported measured data considering nominal tyre inflation pressure of 758 kPa. These include: (i) static load-deflection

tests to verify the tyre vertical stiffness and the contact patch size; (ii) drop and cleat-drum tests to determine vertical mode fundamental frequency of the non-rolling and rolling tyres, respectively; and (iii) cornering force tests to evaluate tyre cornering characteristics under different vertical loads.

2.3.1 Load-deflection tests

The load-deflection tests were conducted to determine steady-state vertical deflection of the tyre under different loads up to 40 kN. In each loading case, the tyre was inflated to its nominal pressure of 758 kPa, which was followed by application of a vertical load, as described in section 2.2.5. The resulting vertical tyre deflection response was evaluated together with the contact patch size. As an example, Figure 2.7(a) illustrates the variations in tyre deflection response corresponding to the nominal load of 26.7 kN applied in a ramp manner, while Figure 2.7(b) shows the deformed shape of the tyre after application of the load.

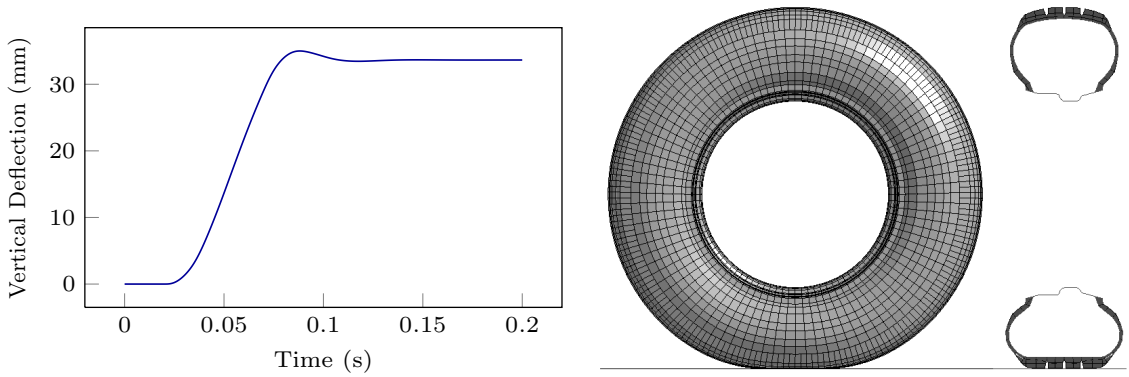

Figure 2.7: (a) Time history of the tyre deflection under 26.7 kN vertical load applied in a ramp manner; and (b) Deformed shape of the tyre after application of vertical load

Figure 2.8(a) compares the steady-state load-deflection response of the tyre with the measured data reported in [11]. The steady-state contact patch length and width responses of the tyre are also compared with the measured data in Figure 2.8(b). The comparisons in Figures 2.8(a) and 2.8(b) show reasonably good agreements of the steady-state tyre

deflection response with the measured data.

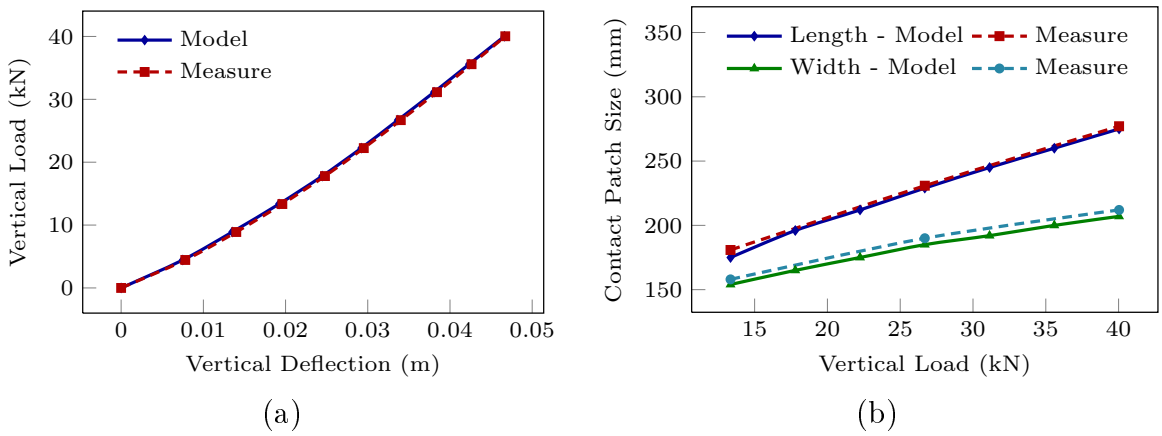

Figure 2.8: (a) Comparisons of steady-state load-deflection characteristics with measured data [11]; and (b) Comparisons of variations in steady-state contact patch length and width with measured data [11]

2.3.2 Drop and cleat-drum tests

The fundamental vertical mode frequency of the non-rolling tyre was estimated via the *drop test* [142]. In this test, the tyre was subjected to a vertical load of 26.7 kN. The fundamental frequency was subsequently obtained from the exponentially decaying oscillatory deflection response of the model, attributed to its light damping (5%), such that [200]:

$$f_n = \frac{1}{\tau_d}\left(1 - \frac{1}{1 + \left(\frac{2\pi}{\delta}\right)^2}\right)^{-\frac{1}{2}} \tag{2.9}$$

where τ_d is period of damped oscillations in the deflection response, f_n is the fundamental frequency and δ is logarithmic decrement. The fundamental frequency of the tyre was subsequently estimated as 19.6 Hz. This frequency was found to be comparable with those reported for different truck tyres. For instance, Ford [201] used the drop test to obtain fundamental frequency of the 285/75R24.5 truck tyre FE model as 16 Hz. Scavuzzo [202] measured the fundamental frequency of the 285/75R24.5 truck tyre as 17 Hz using a tyre modal test rig.

The vertical mode frequencies of the rolling tyre were subsequently evaluated using the cleat-drum test [142]. For this purpose, free-rolling tests were initially conducted to verify the angular wheel velocity, and to examine convergence and stability of the model at different rolling speeds. These tests were conducting at different constant longitudinal velocities of the road surface (up to 100 km/h), while permitting rotation of the loaded tyre about its axis. Tyre loading was achieved by applying vertical deflection of 33.64 mm, which corresponded to vertical load of 26.7 kN. The static and dynamic friction coefficients of the road surface (dry asphalt) were assumed as 0.8 and 0.75, respectively [142]. The longitudinal velocity of the road surface was gradually increased to the desired value for speeds ranging from 10 to 100 km/h. The angular speed of the tyre model also increased gradually and approached a steady-state value, as shown in Figure 2.9(a). The simulation results, however, revealed unstable tyre behavior at road speeds exceeding 100 km/h. This was evidenced from very large deformations of the solid elements of the carcass leading to negative volume due to some of deformed elements. The tyre effective rolling radius R_e was also estimated from the road speed V and the predicted steady-state angular velocity of the rim ω_y, as $R_e = V/\omega_y$. The results revealed nearly constant effective rolling radius for speeds up to 100 km/h, which could be attributed to application of constant vertical tyre deflection in the tests.

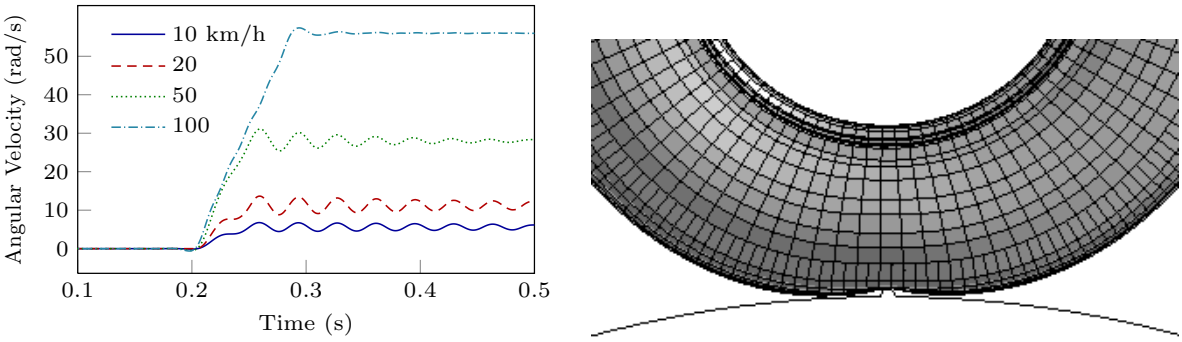

(a) (b)

Figure 2.9: (a) Time history of rim angular velocity in free-rolling simulations under 33.64 mm tyre deflection at different speeds up to 100 km/h; and (b) Tyre contact with cleat on a rotating drum

In the cleat-drum test, the tyre was permitted to roll at 50 km/h over a drum with a

1 cm radius semi-circular cleat, shown in Figure 2.9(b), while the wheel rim was subjected to 33.64 mm vertical motion, as in case of the free-rolling test. During this simulation, the typical damping ratio of 5% was used for the tyre constituents. Figures 2.10(a) and 2.10(b) illustrate time-history of the total tyre force and Fourier spectrum of the tyre force variations at the tyre spindle, respectively. The tyre force spectrum in Figure 2.10(b) exhibits a peak at 1.2 Hz which is related to the rotation of the drum corresponding to the linear velocity of 50 km/h. The spectrum also shows a peak near 19.8 Hz, and dominant peaks near 59.5, 72.3 and 93.3 Hz. Chae [12] also reported a dominant peak near 73 Hz, which was referred to as the first free-rolling natural frequency of the tyre. Kao [75] also conducted cleat-drum tests on a P205/65R15 passenger car tyre using LS-DYNA, and observed the vertical mode frequency of 85 Hz. The peak at the lower frequency of 19.8 Hz, however, is slightly higher than the fundamental vertical mode frequency observed from the drop test (19.6 Hz). This is due to the constraint imposed on the wheel during the cleat-drum test.

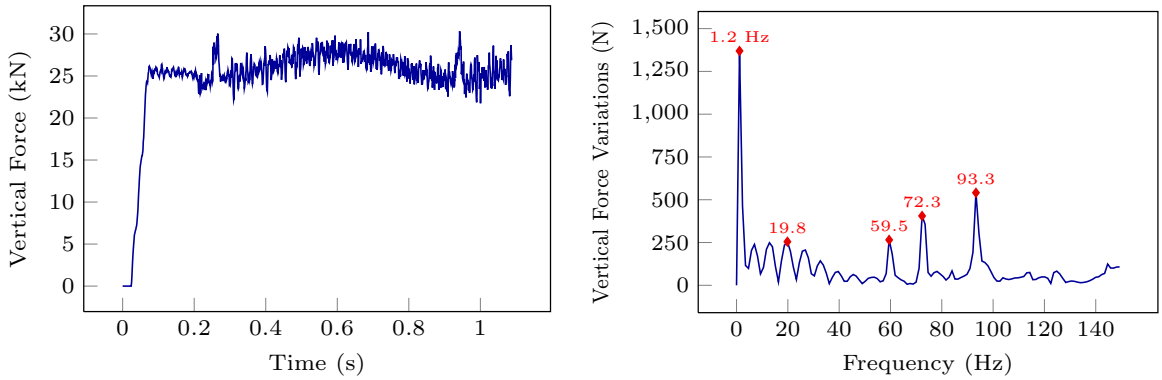

Figure 2.10: (a) Time history of vertical tyre force; and (b) Fourier spectrum of the tyre vertical force

2.3.3 Cornering force tests

The cornering characteristics of the tyre model were evaluated in terms of cornering force and aligning moment over a wide range of side-slip angles up to 12°. The tyre side-slip

deformation was produced by applying the road speed at a predefined angle with respect to the tyre heading direction. In these simulations, the tyre inflated at 758 kPa, was permitted to roll at a forward speed of 5 km/h, while the static and dynamic coefficients of friction were assumed as 0.8 and 0.75, respectively, to represent a dry asphalt road [142]. The simulations were repeated for three different vertical loads of 17.8, 26.7, and 35.6 kN. The cornering force and aligning moment responses of the tyre model are compared with the measured data and the simulation results reported by Chae [11] for the same tyre in Figure 2.11. The model results show good agreement with the measured data for the lower vertical load of 17.8 kN. Relatively good agreements in cornering force and

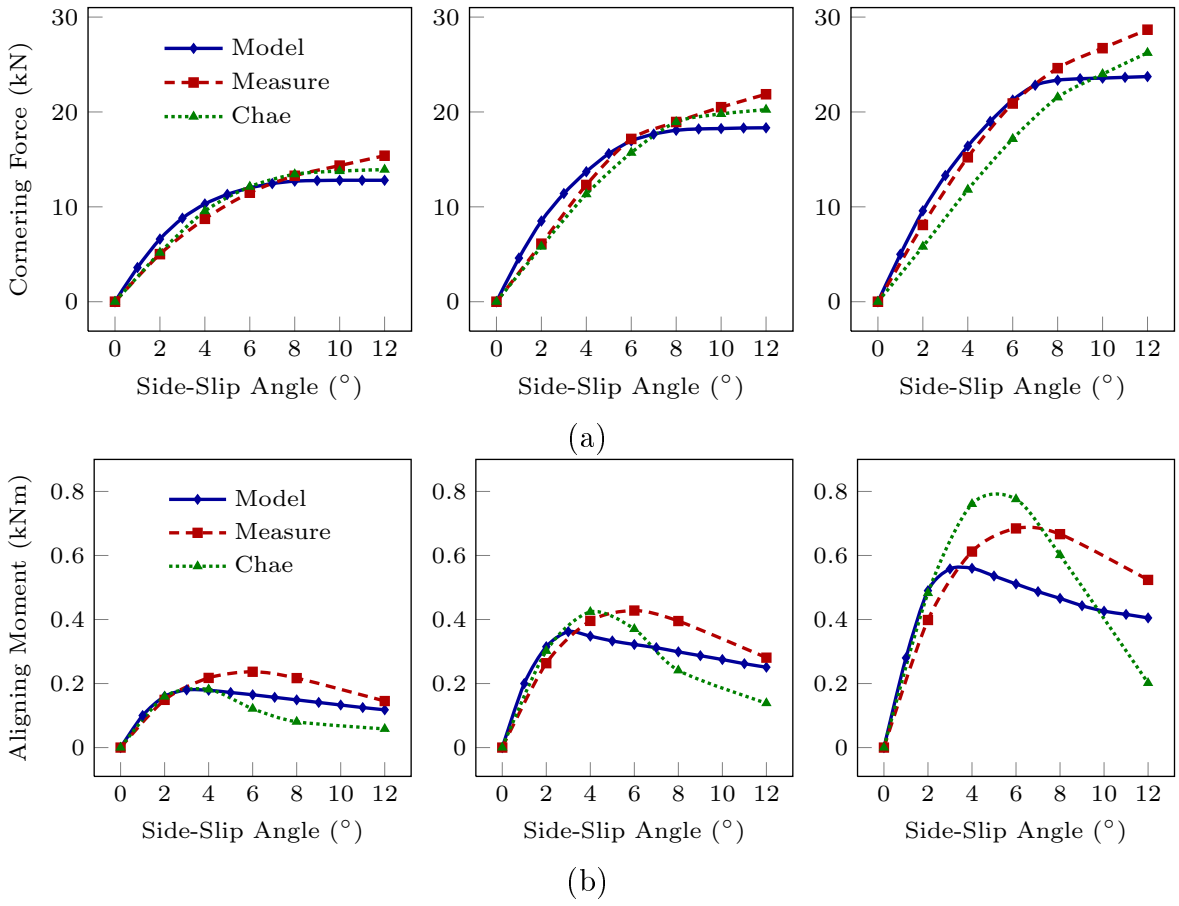

Figure 2.11: Comparisons of (a) cornering force; and (b) aligning moment responses of the tyre model at 5 km/h free-rolling speed in a range of side-slip angles up to 12° with reported measured data and simulation results [12] for different vertical loads of 17.8, 26.7 and 35.6 kN

aligning moment are also evident under higher loads up to side-slip angles of 8° and 4°, respectively. The cornering force responses of the tyre model under higher loads reveal saturation above side-slip angle of about 8°. The deviation between the measured data and the model response tends to increase with increasing side-slip in the saturation region, which is attributed to likely differences between the tread pattern in the real tyre and the simplified tread design considered in the model. The cornering force results presented by Chae [11], however, exhibit considerably large deviations from the measured data in the entire range of side-slip angles under higher vertical loads. Even greater deviations are observed in the aligning moment response, particularly under the higher vertical load of 35.6 kN.

2.4 Influences of operating parameters on vertical and cornering properties

The verified rolling tyre model may be used to study the influences of variations in design and operating parameters. In this study, the model is applied to investigate the influences of different operating parameters on vertical and cornering properties of a truck tyre. These include the variations in inflation pressure, normal load, speed and road friction. It needs to be noted that parametric study of such tyre models necessitates repeated model reformulations. The algorithm described in section 2.2.5 is utilized to realize model reformulations in an efficient manner.

2.4.1 Influences of inflation pressure and vertical load on static vertical stiffness

The static vertical tyre stiffness and contact area are strongly related to the inflation pressure. The influence of inflation pressure on the vertical stiffness is thus evaluated considering pressure variations in the 345 to 1172 kPa range. For each inflation pressure, a series of repeated simulations were performed to characterize the load-deflection properties of the tyre. Figure 2.12(a) illustrates the predicted load-deflection characteristics

of the non-rolling tyre for a range of loads up to 44.5 kN at different inflation pressures. The results suggest increase in vertical stiffness with increasing pressure, as expected and illustrated in Figure 2.12(b).

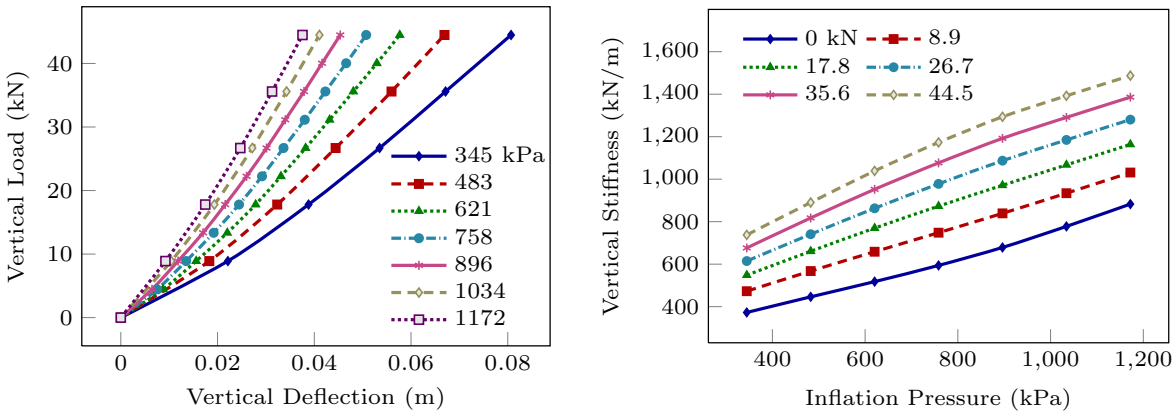

(a) (b)

Figure 2.12: Influence of inflation pressure on: (a) Load-deflection characteristics of the tyre; and (b) static vertical stiffness of the tyre

The pressure-dependent load-deflection properties of the tyre may be described by a second order polynomial in terms of the tyre deflection Δ:

$$F_z(\Delta, P) = A_2(P)\ \Delta^2 + A_1(P)\ \Delta \tag{2.10}$$

where the coefficients $A_1(P)$ and $A_2(P)$ were identified as quadratic and cubic polynomial functions of inflation pressure P, respectively, within the range of pressure considered:

$$\begin{cases} A_1(P) = 1.951 \times 10^{-4}\ P^2 + 0.314\ P + 244.897 \\ A_2(P) = -6.805 \times 10^{-6}\ P^3 + 1.225 \times 10^{-2}\ P^2 + 1.311\ P + 620.764 \end{cases} \tag{2.11}$$

In the above relations, the vertical force F_z is in kN, P is in kPa and Δ is in m. Moreover, these relations provided correlation coefficients in excess of 0.99 for the range of pressure considered. For a given inflation pressure P, the static vertical stiffness of the tyre K_s can be obtained as a function of the tyre deflection:

$$K_s(\Delta, P) = \frac{\partial F_z(\Delta, P)}{\partial \Delta} = 2\ A_2(P)\ \Delta + A_1(P) \tag{2.12}$$

The variations in the static stiffness characteristics of the tyre are illustrated in Figure 2.12(b) as a function of the inflation pressure and normal load. The results suggest that the static tyre stiffness increases with increase in both the normal load and the inflation pressure. Similar trends on the effects of inflation pressure and normal load on static vertical tyre stiffness have also been reported by Alkan [85].

2.4.2 Influence of speed on rolling dynamic stiffness

The influence of variations in speed on vertical stiffness of a rolling tyre is investigated through repeated simulations of the free-rolling tyre at different speeds considering the nominal inflation pressure (758 kPa) and tyre vertical deflection of 33.64 mm, corresponding to the nominal vertical load of 26.7 kN. The linear rolling dynamic stiffness is directly obtained from the vertical contact force of the tyre model for the given constant tyre deflection. Figure 2.13 illustrates variations in the resulting vertical stiffness of the rolling tyre with speed ranging from 0 to 100 km/h. The resulting rolling dynamic stiffness represents the constant linear stiffness corresponding to 0 km/h speed, which is lower than the nonlinear static stiffness presented in Figure 2.12(b). The results suggest approximately 5% decrease in the tyre stiffness with increase in speed up to about 20 km/h. The dynamic stiffness, however, approaches a nearly steady value at speeds above 40 km/h. This trend

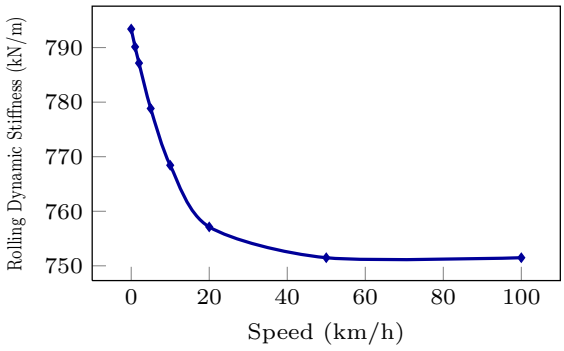

Figure 2.13: Influence of speed on the effective rolling dynamic stiffness of the tyre (inflation pressure = 758 kPa; vertical tyre deflection = 33.64 mm)

with increasing speed has also been reported by Taylor and Bashford [203] through measurements of the dynamic vertical stiffness of a 260/80R20 radial-ply agricultural vehicle drive tyre. The results further show that the tyre rolling at 50 km/h would yield a nearly 5.28% lower effective vertical stiffness compared to that at the speed of 0 km/h. Ford and Charles [201] also reported nearly 5% decrease in stiffness of heavy duty truck tyres when operating at normal speeds.

2.4.3 Influence of inflation pressure on tyre cornering force

The influence of tyre inflation pressure on cornering force response of the rolling tyre model is investigated through repeated simulations for different pressures ranging from 483 to 1034 kPa. The simulations were performed for two different tyre loads (17.8 and 26.7 kN) and three different values of side-slip angles (2°, 4° and 6°). The tyre is subjected to free-rolling at a speed of 5 km/h on a road surface with static and dynamic friction coefficients of 0.8 and 0.75, respectively. Figure 2.14 illustrates variations in the cornering force developed by the tyre as a function of the inflation pressure for the three different side-slip angles. The results show highly nonlinear dependence of the cornering force on both the inflation pressure and the normal load. For the nominal load (26.7 kN), decreasing the

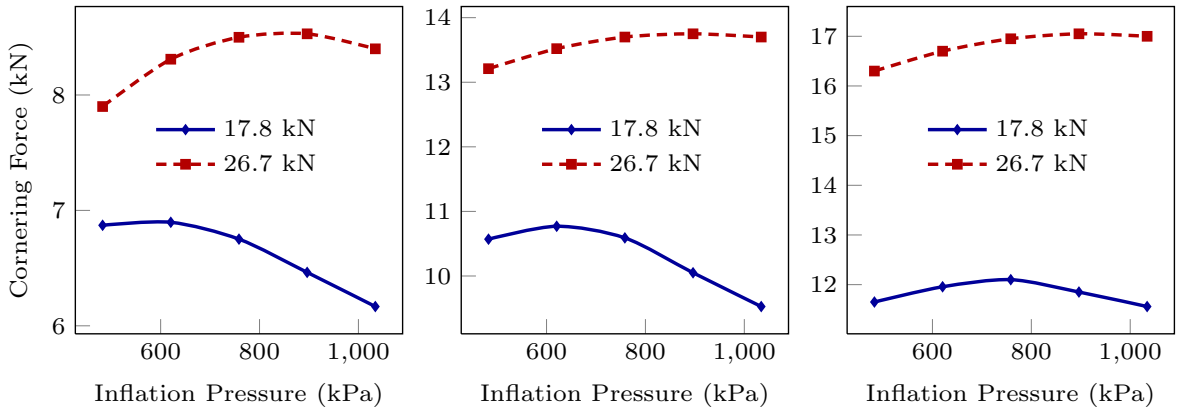

Figure 2.14: Influence of variations in inflation pressure on the cornering force developed by the tyre under two different loads and three different side-slip angles: (a) 2°, (b) 4° and (c) 6°

inflation pressure from the nominal pressure results in lower cornering force, irrespective of the side-slip angle considered in the study. An increase in the inflation pressure, on the other hand, resulted in only slight increase or decrease in the cornering force. This is primarily caused by variations in the contact patch area of the tyre with changes in the inflation pressure. An increase in the inflation pressure would yield higher stiffness of the sidewalls but lower contact patch area, while a lower inflation pressure causes lower stiffness but greater contact patch area.

Decreasing the tyre normal load to 17.8 kN, however, revealed somewhat different trends in the cornering force characteristics, which are likely due to reduced contact patch area. In this case, an increase in the inflation pressure above the nominal pressure, resulted in considerable reduction in the cornering force, irrespective of the side-slip angle. This is likely due to further reduction in the contact patch area. Decreasing the inflation pressure, however, resulted in only slightly variation in the cornering force for side-slip angles of 2° and 4°, when compared to that at the nominal pressure. The results for 6° side-slip angle, however, show relatively greater reduction in cornering force with decreasing inflation pressure, which is likely due to greater side-slippage of the tyre tread in the contact region. The observed trends are similar to those reported from the measured data for a radial-ply 12R22.5 heavy vehicle tyre [204].

2.4.4 Influence of vertical load and road friction on tyre cornering force

The results in Figure 2.14 revealed strongly nonlinear and coupled effects of inflation pressure and vertical load on cornering characteristics of the tyre. Figure 2.15 further illustrates influence of variations in normal load on the cornering force characteristics of the tyre model considering only the nominal inflation pressure. The results are obtained for a range of vertical loads up to 44.5 kN and side-slip angles up to 12°. For the given inflation pressure, the cornering force increases with increase in the normal load in the entire range of side-slip angles. At lower side-slip angles the cornering force increases rapidly with increase in the side-slip angle, which is attributed to greater adhesion of the contact patch

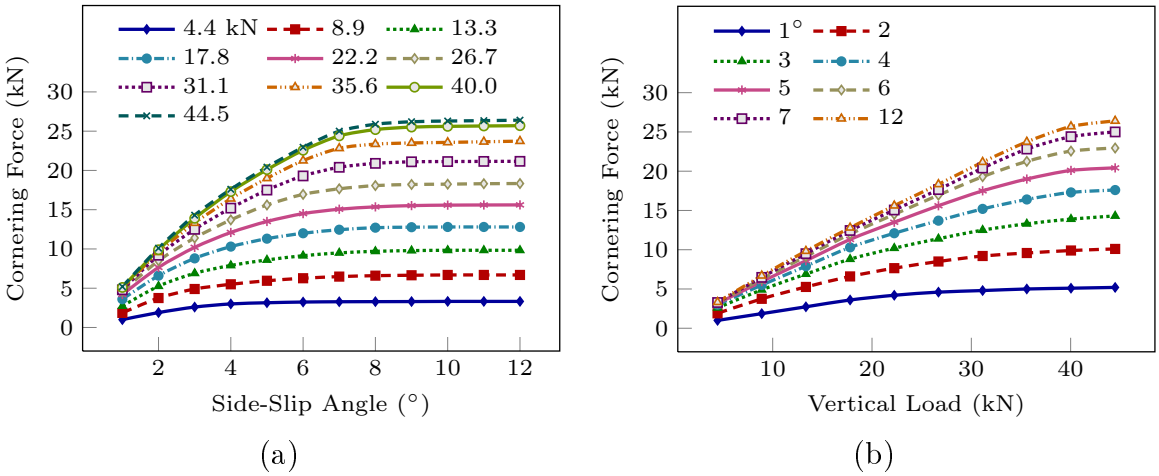

Figure 2.15: Influence of variations in normal load on cornering force characteristics at nominal inflation pressure and 5 km/h rolling speed

with the road. In this range of side-slip angles, the normal load has very little effect on the tyre cornering force. With further growth in the side-slip angle, the partial slippage of tyre tread in the contact patch increases and the cornering force tends to approach saturation.

Increasing the normal load yields significantly higher cornering force at higher slip angles, as shown in Figure 2.15(b). This is due to relatively high adhesion of the tyre with the road surface under higher normal loads. The measured cornering characteristics of a car tyre, reported by Van Eldik Thieme [205] also revealed similar trends. The cornering force saturation under higher tyre loads occurs at relatively larger side-slip angles compared to that at lower loads, which further demonstrates the significance of the normal load at large side-slip angles. Wei and Oertel [206] also evaluated cornering characteristics of a truck tyre under different normal loads through FE simulations and reported similar results on the influence of the normal load.

Figure 2.16(a) illustrates the influence of road fiction on the cornering force generated by the tyre model for a range of side-slip angles up to 12°. The results are presented for two different road surface conditions: (i) a dry asphalt road with $\mu_s = 0.8$ and $\mu_d = 0.75$; and (ii) a wet road surface with $\mu_s = 0.5$ and $\mu_d = 0.45$. The results suggest minimal effect of road surface friction on the cornering force at small side-slip angles. The effect of road friction, however, is more pronounced with increasing side-slip angle. At higher side-slip

angles, the cornering force developed on a wet surface is nearly 35% lower compared to that on the dry asphalt road. Baffet [207] measured the cornering forces generated by a car tyre due to a wide range of side-slip angles up to 16° for different road friction conditions and reported similar trends on the influence of the road friction on tyre cornering force.

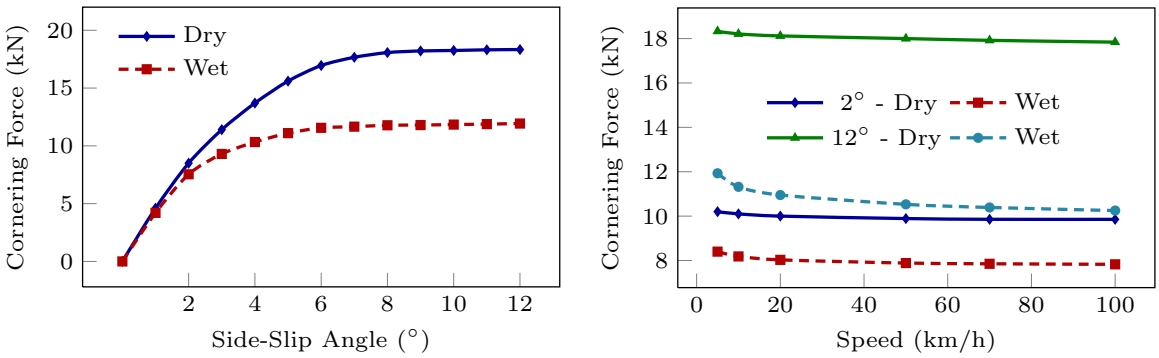

Figure 2.16: (a) Influence of variations in road friction (dry and wet asphalt roads) on tyre cornering force characteristics; and (b) Influence of variations in rolling speed on cornering force at 12° and 2° side-slip angles under different road surface conditions

2.4.5 Influence of rolling speed on tyre cornering force

The tyre rolling speed affects the relative slip between the tyre contact patch and the road, which could influence the tyre cornering force, particularly under large side-slip angles. Figure 2.16(b) illustrates the influence of speed on the cornering force generated by a freely rolling tyre on dry and wet road surfaces considered in section 2.4.4. The results are obtained for tyre speeds ranging from 5 to 100 km/h and two extreme values of the side-slip angle (2° and 12°) to highlight the effect of side-slip angle in conjunction with the tyre rolling speed. The simulations were limited to nominal inflation pressure and normal load. The results suggest only minimal effect of the rolling speed on the tyre cornering force developed on a dry asphalt road, particularly at the small side-slip angle of 2°. A reduction in the cornering force with increasing speed, however, is evident for the wet road condition. This reduction is more evident for the large side-slip angle of 12°. Longhouser [208] also reported similar trends for the effect of speed on the cornering force generated

by a military truck tyre on dry and wet pavements.

2.5 Conclusions

The 3-D finite element model of the multi-layered rolling truck tyre structure revealed reasonably good agreements with the reported measured tyre properties in terms of load-deflection, contact patch size, cornering force and free vertical vibration frequency characteristics. The aligning moment response of the model, however, showed agreement with the measured data for side-slip angles less than 4°, while the model revealed comparable trends at higher side-slip angles. The thick-shell element formulation selected for the poor-aspect-ratio solid elements of the rubber matrix in the carcass and belt plies provided stable model responses at high speeds up to 100 km/h. At speeds above 100 km/h, the tyre model revealed unstable behavior observed from extremely large deformations of the solid elements of the carcass.

The automated model regeneration algorithm developed in the study facilitated efficient model reformulations following changes in tyre cross-section, structural design parameters, and operating conditions. The proposed model together with the model regeneration algorithm could thus serve as an important tool for design sensitivity analyses involving geometric, structural and material properties of the tyre constituents. In particular, the model with automatic model regeneration algorithm could effectively be used as a virtual tool for parameter identifications for the physics-based and phenomenological tyre models.

Repeated model formulations and simulations were performed to study the influences of variations in operating parameters such as inflation pressure, vertical load, speed and road friction. The results showed that the static tyre vertical stiffness increased with increase in inflation pressure and normal load, while the dynamic stiffness of the rolling tyre was 5% lower than the static stiffness. Strongly nonlinear and coupled effects of normal load and inflation pressure on the cornering properties were evident. Reducing the road surface friction resulted in substantially lower cornering force at higher side-slip angles, while the effect was minimal at low side-slip angles. Increasing the speed reduced the cornering force on a wet road surface, particularly at higher side-slip angles, while the

effect was slight on a dry asphalt road.

Chapter 3

Modal Analysis of a Rolling Truck Tyre Subjected to Inflation Pressure and Vertical Deflection

3.1 Introduction

Vibration characteristics of a pneumatic tyre are known to play an important role in dynamic performance of ground vehicles, particularly in view of ride comfort and tyre noise. Vibration modes of a tyre can be potentially excited by road impacts, tyre non-uniformities, tread patterns, etc. The tyre natural modes and frequencies are also important considerations for designing and optimizing the tyre-vehicle systems and for identifying critical rolling speeds. Moreover, natural frequencies and mode shapes of a tyre are representative of its dynamic stiffness, and could facilitate analytical solutions for tyre dynamic responses to any arbitrary loading in vehicle dynamics simulations. Extensive studies of varying complexities have thus been reported on estimating vibration properties of pneumatic tyres using experimental [112–115], theoretical [116–122] and numerical [13, 75, 123–125] approaches.

It is customary to solve a linear eigenvalue problem to determine the natural modes and frequencies of a mechanical structure as a free system without attention to its probable stress state. However, in case of nonlinear systems, particularly those subjected to large deformations, the stiffness of the system and hence the modal characteristics are highly

dependent on the stresses induced from external loading and boundary conditions. Typical examples include tuning a guitar string by adjusting its tension, or variations in dynamic response of a bridge during day and night at regions with significant daily temperature fluctuations. A rolling tyre subjected to internal pressure, centrifugal forces, road contact and normal load also constitutes a complex nonlinear vibration system, whose natural frequencies are strongly affected by variations in loading and boundary conditions.

The modal properties of inflated non-contacting tyres have been extensively studied via experimental [112–114] and analytical [117–119] methods, while neglecting the contributions due to non-axisymmetry attributed to ground contact. The resonant frequencies of non-rolling tyres have been experimentally obtained through measurements of distributed vibration responses on the tyre perimeter [114, 122]. Optical methods have been employed to identify resonant frequencies and the corresponding mode shapes of the rotating tyres [112, 113]. These experimental methods could effectively identify a number of lower natural frequencies corresponding to radial, tangential and lateral deformations. Complex vibration patterns beyond the classical mode shapes, however, can rarely be triggered by modal testing devices due to restricted types of excitations of such devices [112, 114]. Moreover, the experimental methods cannot obtain the tyre mode shapes with adequate resolution, particularly the complex 3-D modes associated with higher natural frequencies, due to limited number of measurement points. Further, damping properties of tyres tend to attenuate the amplitudes of the higher modes and prevent them to be seen clearly in the measured frequency response curves [118].

A number of studies have considered the tyre as a thin shell of revolution [117, 126–128] or a toroidal membrane [119] to predict free vibration properties of an inflated non-contacting tyre, taking advantage of axisymmetry in tyre geometry to achieve computational efficiency. Hunckler [117] performed free vibration analysis on a steel belted radial tyre under inflation pressure considering the orthotropic material properties as well as the pre-stress effects due to internal pressure in the axisymmetric shell element formulation. Saigal [119] included the geometric nonlinearities due to large displacements in the membrane element formulation to determine free vibration response of a low-pressure tyre. The study could detect the symmetrical and twisting modes of vibration. Kung [118] studied

the effects of additional stresses due to centrifugal forces on natural modes and frequencies of a rotating but non-contacting tyre using the axisymmetric thin shell finite element of revolution.

Vibration characteristics of a rolling tyre in ground contact have been explored in fewer studies compared to the non-contacting tyre, likely due to computational complexities associated with changing contact geometry as well as losing the axisymmetry assumption leading to substantial computational demand. Soedel [129] reported dynamic response of a rolling tyre subjected to contact loading in terms of the natural frequencies and mode shapes of the inflated but non-contacting rotating tyre using the *modal expansion* approach. The study used the linear thin shell theory in conjunction with 3-D dynamic Green function, and could provide a general solution for tyre dynamic response to any type of contact loading due to pure rolling, traction/braking and cornering. The study also permitted predictions of the critical tyre speed causing *standing waves* formations. The linear thin shell type structure, however, cannot be considered valid under high frequency disturbances associated with road roughness. A thick shell element formulation would be essential in such situations to account for tread rubber effects. Several other studies also used the modal expansion approach to obtain analytical solutions for tyre vibration responses [122, 127, 130–132]. The accuracy of such mode-superposition solutions, however, strongly depends not only on the accuracy of the modes but also considerations of large number of natural modes, which suggests the need for measurement or computations of higher order modes of tyre vibrations [129].

A number of studies investigated the effect of ground contact on tyre natural modes and frequencies using theoretical approaches. Soedel and Prasad [126] presented an analytical approach to determine the natural modes and frequencies of a tyre in ground contact using the responses of the free inflated non-contacting tyre. The reported method, however, could effectively obtain the modes with dominant transverse deflection components at contact with a relatively small footprint area. Many theoretical studies have used the concept of *ring on elastic foundation* to predict modal characteristics of the contacting tyre [116, 120–122, 128, 133]. Huang [121] formulated a ring model and included the effect of ground contact by defining displacement constraints at the footprint along the radial

and tangential directions. The study observed that the mode shapes were divided into two branches, a symmetric and an anti-symmetric mode about the contact point, stemming from the radial and tangential constraints, respectively. This approach, however, involves identifications of equivalent parameters of the mass-spring-damper elements via physical measurements. Zegelaar [122] performed experimental modal analysis on a non-rotating car tyre and compared the in-plane natural modes and frequencies of a free tyre with those of a tyre contacting the road under a preload. The study observed that owing to the symmetry of the free tyre, each natural frequency corresponded to two identical mode shapes with an offset in the angular position of the anti-nodes. This symmetry, however, could not be preserved in the presence of the ground contact, where the initially identical modes split into symmetric and anti-symmetric modes at two different frequencies.

Comprehensive finite element models of tyres have been formulated for predictions of tyre vibration characteristics considering the complex tyre geometry and material properties [12, 13, 109, 123, 124, 134, 135], which could not be adequately represented in the aforementioned mathematical models. The natural modes and frequencies of free non-contacting tyres have been widely obtained via solving the finite element model eigenvalue problem [13, 136, 137]. Zhang et al. [13] proposed a detailed finite element model of a free non-contacting truck tyre considering its multi-layered composite structure using ANSYS, and investigated the effects of inflation pressure together with the anisotropy-related parameters on the tyre natural modes and frequencies. In such studies, the effect of inflation pressure is considered through analysis of the stress state of the tyre elements, which is subsequently used to update the element stiffness matrices in the eigenvalue problem solution.

Alternatively, a number of studies conducted explicit dynamic simulations to predict natural frequencies of a tyre through Fast Fourier Transformation of the tyre response to an impact excitation. The *drop* [12, 109] and the *cleat-drum* [12, 75, 77, 109, 124, 138] tests have been commonly used in order to extract the fundamental frequencies of the stationary and rolling tyres, respectively, under contact loading. Unlike the direct eigenvalue analysis, this approach can only detect the natural frequencies corresponding to those vibration modes being triggered by the input excitations. Furthermore, these methods cannot yield

the mode shapes of the tyre.

Considering the effects of ground contact and rotation in eigenvalue analysis of a rolling tyre, however, has been reported in only a few studies [123, 134, 135, 139, 140]. This is due to complexities associated with the geometric nonlinearities involved in determination of the stress state of the tyre structure under multiple loading conditions and changing contact geometry, which requires prior explicit dynamic simulations. Burke and Olatunbosun [123] performed such analysis on an inflated/deflected rolling tyre modeled in MSC/NASTRAN and attempted to investigate the influences of the tyre inflation pressure, hub load and speed on the natural frequencies of a passenger car tyre. The reported results, however, were only limited to a few basic modes, namely, lateral, longitudinal, radial and steer. The effects of these operating parameters on the natural frequencies corresponding to the complex vibration modes, beyond the classical modes documented for tyres, have not yet been notably reported, particularly for the truck tyres.

In this study, a three-dimensional finite element model of a radial-ply rolling truck tyre is employed to predict its natural frequencies and the corresponding mode shapes with particular focus on the effects of inflation pressure, road contact, normal load and the rotational speed. The proposed model comprises detailed representations of the multi-layered composite structure of a truck tyre and is developed using the material and element library of the nonlinear dynamic simulation platform, LS-DYNA. In order to estimate the natural frequencies of an inflated and deflected rolling tyre, an explicit dynamic simulation is initially conducted to determine the stress state throughout the tyre. The validity of the explicit dynamic simulation results is demonstrated through comparisons with the reported physical measurements. The modal analysis is subsequently performed to extract natural frequencies and the corresponding mode shapes of the rolling and contacting tyre, while the nonlinear large-deformation finite element theory is applied to include the contribution of the stresses in the element stiffness matrices. Parametric studies are performed to investigate the influences of different operating parameters on tyre natural frequencies. A model reformulation algorithm is used to conduct repeated simulations in a computationally efficient manner.

3.2 Finite element model of the rolling truck tyre

3.2.1 Tyre structure model

A 3-D finite element model of a rolling truck tyre developed in LS-DYNA is used to perform modal analyses for predicting the tyre natural frequencies and the corresponding mode shapes. The tyre model formulation has been described in a recent study by the authors together with model validations in view of vertical force-deflection, cornering characteristics, and the fundamental frequency [109]. Figure 3.1(a) illustrates the structure model, created based on a 295/75R22.5 radial-ply truck tyre. The model contains the carcass and belt composite plies, tread, and bead fillers. The tyre sidewalls are modeled by two layers of solid elements representing rubber matrix, and three layers of orthotropic shell elements with radial cords accounting for reinforcements. The tyre crown area includes two layers of solid elements: (i) an upper layer representing the belt rubber matrix, sandwiched between two layers of shell elements reinforced by cords with $\pm 22^{\circ}$ angle with respect to the tyre circumferential centerline; and (ii) a lower solid layer representing the carcass rubber matrix below the belt, which is also reinforced by a layer of shell elements with radial cords. The bead fillers, tread shoulders, tread base and tread cap are modeled

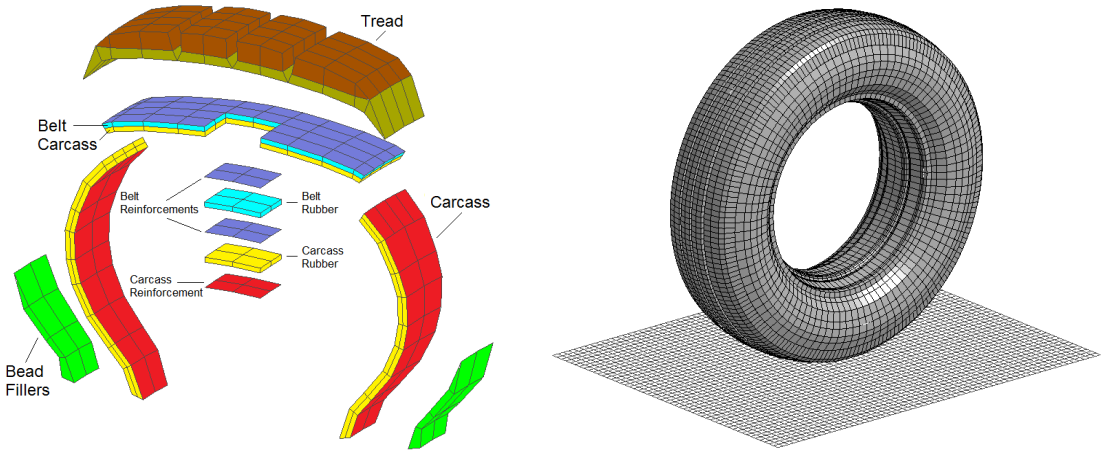

(a) (b)

Figure 3.1: (a) Tyre structure mode; and (b) Tyre mesh with 96 and 192 circumferential divisions for the coarse and refined regions, respectively [109]

using solid elements with hyper-elastic rubber materials.

Figure 3.1(b) illustrates the 3-D tyre mesh with 17856 nodes and 24192 elements, being made of 96 equal sectors, which is refined to 192 divisions for the outer circumferential regions so as to accurately model large displacements of the rolling tyre in the contact area. The tyre mesh is coupled with a wheel rim made of rigid shell elements through shared nodes. The road is considered as a flat surface made of rigid shell elements, while a drum of 3 m diameter is used to perform simulations at high speeds. The tyre-road contact is modeled using the *automatic surface to surface* contact algorithm [105, 107] in conjunction with Coulomb friction with smooth exponential transition between the static and dynamic coefficients of friction [105].

3.2.2 Material constitutive types and properties

The solid elements representing rubber matrix in the carcass and belt plies are modeled using the elastic material model (type 1) from the LS-DYNA material library [104], while the elastic properties of rubber are taken from the reported data [198], which have been presented in [109]. The shell elements describing fiber-reinforced layers are modeled using the composite material model (type 22) [104]. The orthotropic material properties of the cord-rubber compounds in the carcass and belt plies were obtained considering the geometric and material properties of the pure rubber and twisted cords using the Halpin-Tsai equations [196, 197] and reported in [109]. These properties are defined in the cord axes system, and a cord angle will thus be required to define the orientation of the cords with respect to the element axes system. The solid elements forming the bead fillers and the tread are described by the Mooney-Rivlin rubber material model (type 27), which is considered to accurately represent the hyper-elastic behavior of the rubber in tyre models [10, 12, 32]. The material parameters for the different rubber compounds in the tyre structure, namely, the bead fillers, the tread base and tread cap were taken from reported data [109]. The shell elements representing the wheel rim and the road are described using rigid material model (type 20) as these are substantially stiffer than the tyre constituents.

3.2.3 Method of solution

Modal analysis of a tyre as a pre-stressed structure

In order to incorporate the influences of the tyre inflation pressure, normal load, rolling speed, and contact boundary condition on the natural frequencies and mode shapes of a rolling tyre, it must be considered as a pre-stressed structure [209, 210]. For this purpose, a transient dynamic simulation is initially conducted, where the tyre, subjected to desired pressure and normal loading, is permitted to roll freely at a constant speed. The resulting stress field throughout the rolling tyre model is subsequently used in the modal analysis of the rolling tyre to include the effects of loading and boundary conditions. Modal analysis of the tyre model is basically carried out using the classical undamped free-vibration analysis problem [200]:

$$\left([K] - \omega_i^2[M]\right)\{\Phi_i\} = 0 \tag{3.1}$$

where $[M]$ and $[K]$ are the assembled mass and stiffness matrices, and ω_i and $\{\Phi_i\}$ are the natural circular frequency (eigenvalue) and the mode shape vector (eigenvector) corresponding to vibration mode i. In the linear infinitesimal-deformation theory of finite element, the stiffness matrix formulation for each element only includes the constitutive response of the element material. In this theory, all the pre-stresses and pre-strains might only participate in the element force vector, and are thus excluded from the above eigenvalue analysis formulation. Applying the large-deformation finite element theory, however, the influences of stresses arising from the loading conditions also contribute to the stiffness matrix formulation, such that [105]:

$$[K]^{(e)} = [K_{mat}] + [K_{geo}] = \int_{V^{(e)}} [B]^T[D][B]dV + \int_{V^{(e)}} [G]^T[\sigma][G]dV \tag{3.2}$$

In the above formulation, $[K]^{(e)}$ is the stiffness matrix of element (e), of volume $V^{(e)}$, which is used by the eigensolver in the modal analysis. The first term, $[K_{mat}]$, is the *material stiffness matrix*, which reflects the material constitutive response, and depends on the stress-strain matrix, $[D]$, and the strain-displacement matrix, $[B]$. The second term, $[K_{geo}]$, is the *geometric stiffness matrix* and accounts for the geometric nonlinearities associated with rotation of the stress with the motion. This term is also called the *initial stress*

stiffness matrix as it reflects the contribution of the existing stresses, and depends on the current state of stress, $[\sigma]$, and the matrix of shape-function derivatives, $[G]$ [211]. The tyre-road contact may also contribute as a boundary condition when assembling the total stiffness matrix of the system. It constrains the relative motions of the nodes within the contact region such that the relative normal displacement remains zero, while the tangential motion is governed by the stick/slip condition. In the stick mode, the relative tangential displacement is set to zero, and is unconstrained in the slip mode [105].

LS-DYNA [107], a nonlinear transient dynamic finite element solver, was selected as the simulation tool for performing both the transient dynamic and modal analyses in this study. The pre-and-post processor of LS-DYNA, known as the LS-PrePost, was also used for both providing the input model file, and visualizing the output simulation results. Providing the input model file using the LS-Pre processor, however, involves considerable user efforts, particularly when performing repetitive simulations for parametric studies that may necessitate frequent model reformulations. In order to facilitate this re-modeling process, a computationally efficient model regeneration algorithm, reported in [109], was used in LS-Pre processor.

Figure 3.2 illustrates the simulation procedure used for parametric modeling, model reformulations and modal analysis of the rolling tyre. The procedure sets up the model based on the user-defined inputs using the automated model regeneration algorithm, which creates a command file containing nearly 12000 command lines to be executed by the LS-Pre processor. These parameters may include the tyre design data such as tyre cross-section,

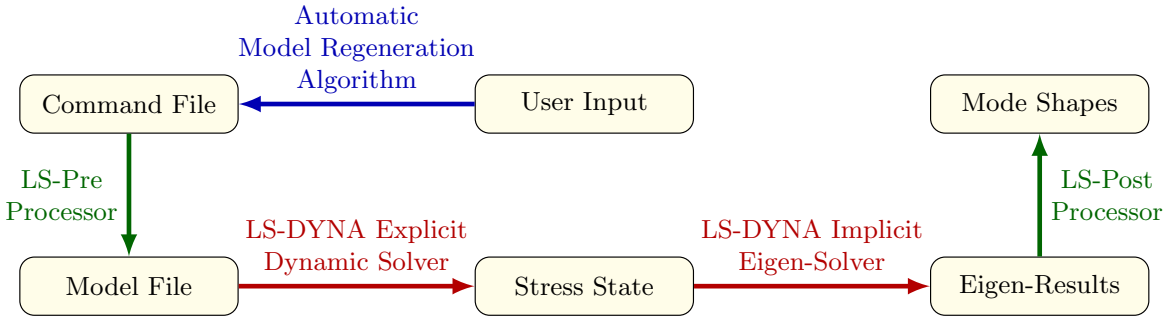

Figure 3.2: Procedure of parametric modeling and modal analysis of the rolling tyre

mesh size, geometric, material and damping properties; loading and boundary conditions (e.g., load curves for tyre inflation pressure, vertical load and speed); tyre-road friction and contact parameters. Solution settings such as integration step-size, elements formulations and hourglass control options are also incorporated. For simulations involving changes in the tyre model input parameters, the command file can be regenerated in a highly efficient manner [109]. The execution of the pre-defined command file by LS-Pre processor yields mesh generation, assignment of material properties and elements formulations, and definition of the pertinent loading and boundary conditions, together with the required solution settings (model file).

Two different types of analyses are performed in the LS-DYNA platform, which include an explicit dynamic simulation to realize the stress field due to the applied loading and boundary conditions, following by an implicit eigenvalue analysis for computations of modal characteristics, as shown in Figure 3.2. In the explicit dynamic simulation, the tyre is initially inflated to a desired pressure through applying a uniformly distributed normal load to the inner layer shell elements of the tyre. Following the tyre stabilization after inflation, the vertical load is applied in a ramp manner up to a desired level. It must be mentioned that the normal load is directly applied to the center of the wheel rim without increasing the total mass of the system. The rolling phase is initiated when the tyre oscillations due to applied vertical load subside and steady-state tyre deflection is attained. The free-rolling condition is simulated through applying a ramp-like velocity to the road along the tyre longitudinal axis until the angular velocity of the rim approaches a desired steady value. The rim is permitted to rotate only about its axis. Throughout this explicit dynamic simulation, the nodal displacements as well as the stresses and strains within all elements of the tyre structure model are computed at each time-step.

The modal analyses of the tyre model are carried out using the LS-DYNA implicit eigensolver [105] by selecting the *intermittent eigenvalue extraction* option. Using this option, eigenvalues are extracted intermittently at particular instants during the simulation, taking into account the effects of changes in geometry, material, stress state and contact condition. The effects of inflation pressure, vertical load and rolling speed on the tyre natural frequencies are investigated at three key instants. These are chosen as the instants:

(i) when tyre deflection approaches steady-state following a desired inflation; (ii) when the tyre deflection approaches steady-state following the application of a vertical load; and (iii) when the angular speed of the free-rolling tyre becomes steady corresponding to the selected rolling speed. The vibration analyses of the model are performed at these three instants considering the corresponding instantaneous geometry and stress state of the model. Finally, the eigen-solution files are viewed in the LS-Post processor to scale and animate the deformation mode shapes corresponding to the tyre natural frequencies.

Solution method settings for implicit eigenvalue analysis

The settings of the implicit solver in LS-DYNA are defined to extract the solutions corresponding to the above-stated three instants. For this purpose, intermittent eigenvalue extraction option is chosen by defining IMFLAG in the keyword CONTROL_IMPLICIT_GENERAL as 6. The default value for this flag is zero for a standard explicit analysis. The variable IGS in the same keyword is defined as 1 to include the geometric (initial stress) stiffness matrix in the eigenvalue problem. The instants of eigenvalues extractions are defined via the variable NEIG in the keyword CONTROL_IMPLICIT_EIGENVALUE. The variable also defines the number of modes to be extracted [107]. Finally, the *Block Shift and Invert Lanczos* algorithm is selected as the eigenvalue extraction method by setting the variable EIGMTH as 2. This method uses a very robust iterative algorithm in conjunction with the *sparse matrix solver* to achieve rapid convergence, which is considered suitable for efficient computations of the desired number of eigenvalues and eigenvectors for a large-scaled vibration system with large degrees-of-freedom [105].

Selection of appropriate elements formulations

The one-point integration shell element formulation (type 2) [199] was found sufficient for the rigid elements of the rim and the road. For the carcass and belt composite reinforcements, however, the fully-integrated shell element formulation (type 16) [199] was used to achieve improved accuracy. Applying the default one-point integration solid element formulation for the 3-D solid elements representing the rubber matrix in the carcass

and belt plies revealed poor convergence owing to their poor element aspect ratios originated from their small thicknesses compared to their other dimensions. The thick-shell element formulation [107] was thus employed, which uses a solid element formulation with a strong emphasis on the shell properties [105]. For the hyper-elastic rubber materials in the tread and bead fillers, the one-point-integration solid element formulation [107] in conjunction with one of the stiffness forms of the hourglass energy control (type 5) [107] provided stable solutions and rapid convergence for the explicit dynamic simulations. For the eigenvalue analyses, however, this method of element integration exhibited hourglass effects, particularly in the mode shapes related to the higher modes of vibration (above 20). The fully-integrated solid element formulation was thus found to be essential to obtain accurate eigenvalues and mode shapes related to higher vibration modes.

3.3 Validation of explicit dynamic simulation results (pre-stresses)

The validity of the tyre model proposed in [109] was extensively examined by comparing the responses obtained from explicit dynamic simulations with the reported measured data for the same truck tyre type in terms of static vertical force-deflection, cornering and vertical free vibration characteristics. A grid convergence study was also conducted, and a mesh with 96 circumferential divisions for the sidewall structure, and 192 divisions for the outer circumferential regions, as illustrated in Figure 3.1(b), was selected as the minimal requirement for convergence of the load-deflection as well as the cornering force results [109].

The load-deflection and contact patch area characteristics of the tyre model at 758 kPa inflation pressure demonstrated good agreements with the measured data [11], as reported in [109]. The lateral behavior of the rolling tyre model at 5 km/h was also evaluated in terms of the cornering force/moment responses to a range of side-slip angles up to 12°. The lateral contact force as well as the self-aligning moment responses of the tyre model showed reasonable agreements with the measured data reported in [11] in the range of lower

side-slip angles, while the deviation between the measured data and the model response at higher side-slip angles was likely attributed to the difference between the tread pattern in the real tyre and the tread design considered in the model [109].

The validity of the tyre model was further examined in terms of its vertical free vibration properties under non-rolling and rolling situations using *drop* and *cleat-drum* tests, respectively [109]. The fundamental frequency of the non-rolling tyre was estimated from the drop test at 19.6 Hz [109], which is comparable with the frequency reported by Ford [201] at 16 Hz for a 285/75R24.5 truck tyre via drop test; measured by Scavuzzo [202] at 17 Hz for a 285/75R24.5 truck tyre using a tyre modal test rig; and measured by Burke [123] at 19.4 Hz for a 195/65R15 car tyre.

The dominant vertical free vibration frequencies of the free-rolling tyre at 50 km/h were also determined from the cleat-drum test. Figures 3.3(a) and 3.3(b) illustrate the time-history of the vertical component of the force at the tyre spindle and the Fourier spectrum of its variations, respectively. Apart from the peak near 1.2 Hz, which is related to the rotational motion of the drum at 50 km/h, the spectrum also shows a peak near 19.8 Hz, and dominant peaks near 59.5, 72.3 and 93.3 Hz [109]. The peak at the lower frequency of 19.8 Hz is close to the fundamental vertical mode frequency observed from the drop test at 19.6 Hz. This frequency is also comparable to that obtained by Kerchman [135] at 19.5

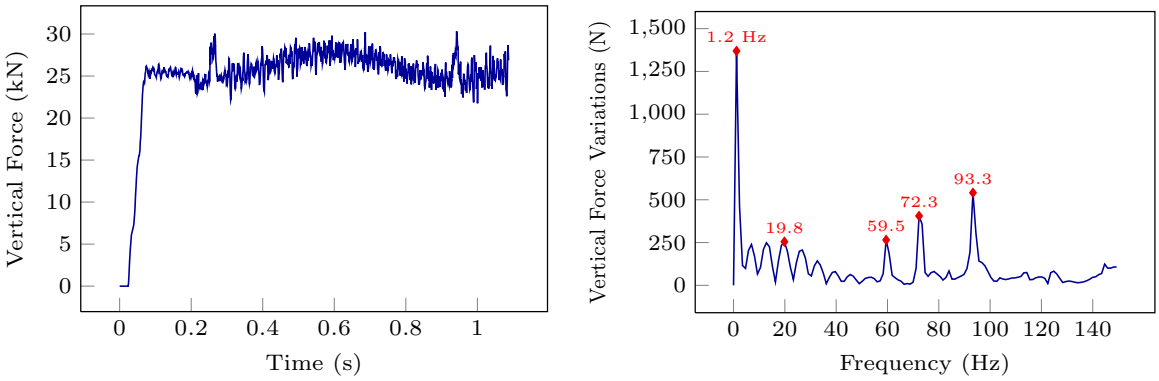

Figure 3.3: (a) Time history of tyre vertical force; and (b) Fourier spectrum of the tyre vertical force, as reported in [109]

Hz via a cleat impact test using ABAQUS for a P205/75R15 car tyre rolling at 50 km/h on a flat road. The peak near 59.5 Hz is close to the natural frequency of 61.54 Hz obtained from the modal analysis of the rolling tyre at 50 km/h, which is later discussed in section 3.4. The dominant peak near 72.3 is comparable to the natural frequency of 73 Hz observed by Chae [12] in a cleat-drum simulation for a 295/75R22.5 truck tyre using PAM-CRASH. Finally, the higher frequency of 93.3 Hz is comparable to the resonant frequencies observed by Palmer [124] at 81.1 and 94.7 Hz for a truck tyre using LS-DYNA, and is further comparable to the vertical mode at 85 Hz obtained by Kao [75] in a cleat-drum test for a P205/65R15 car tyre rolling at 48.28 km/h using LS-DYNA. These dominant frequencies are also comparable to the natural frequencies achieved from the modal analyses in this study, and will be later discussed in section 3.4.

3.4 Modal properties of the inflated and loaded rolling tyre

Modal analyses of the tyre model were performed using the intermittent eigenvalue extraction at three chosen instants described in section 3.2.3. The eigenvalue analysis was initially performed for the inflated tyre when the tyre deformation stabilized after application of the inflation pressure. The rigid wheel rim was fixed, and the tyre was not in contact with the road. Subsequent eigenvalue extraction was conducted at the instant when tyre approached steady-state deflection following application of the vertical load to obtain natural frequencies of the loaded tyre. Finally, the eigen-frequencies of the rolling tyre were obtained through execution of the third eigenvalue extraction, when the loaded tyre was freely rolling at a steady-state angular speed. In these analyses, the inflation pressure, vertical load and rolling speed were chosen as 758 kPa, 26.7 kN and 50 km/h, respectively. The static and dynamic friction coefficients were assumed as 0.8 and 0.75, respectively, and a damping ratio of 5% was considered. The predicted natural frequencies and the corresponding mode shapes are presented and discussed in this section, while the similar mode shapes obtained for the inflated, deflected and rolling cases, whenever

observed, are compared together.

Figure 3.4(a) illustrates the first (lowest) vertical vibration mode extracted from the deflected tyre (denoted as Hop) at 17.85 Hz, which reflects hopping motions of the tyre along the vertical direction. This frequency is comparable to the frequency of 19.6 Hz observed from the drop test simulation. This mode was not detected from the inflated tyre model responses due to lack of contact with the road. Ford and Charles [201] predicted this vibration mode for a non-rolling 285/75R24.5 truck tyre near 16 Hz from the drop test simulation using NASTRAN. Kao [212] predicted this mode at 20 Hz for a non-rolling P215/70R15 car tyre under 207 kPa inflation pressure and 3.45 kN vertical load using NASTRAN. The rolling tyre, however, exhibited this mode at a relatively lower frequency of 15.83 Hz, as shown in Figure 3.4(b). This can be justified by the fact that the rolling dynamic stiffness of tyres is somewhat (nearly 5%) lower than their static (non-rolling) stiffness along the vertical direction, as reported by Ford and Charles [201]. Moreover, Scavuzzo [202] used a tyre test rig to conduct modal analysis on a P205/70R14 car tyre under 207 kPa inflation pressure and 4.89 kN normal load and observed a reduction in natural frequency from 19 Hz to 18 Hz between the stationary tyre and the rolling tyre at 8 km/h speed. Burke [123] also conducted modal analysis on a 195/65R15 car tyre subjected to 193 kPa inflation pressure and 3.33 kN hub load using MSC/NASTRAN and reported a drop in frequency from 17.75 Hz to 15.7 Hz between the static and the rolling

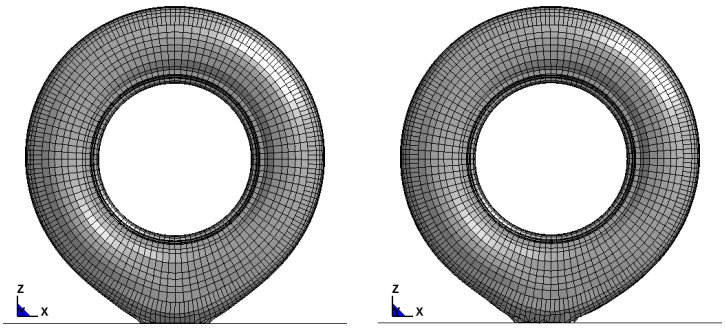

(a) Loaded: 17.85 Hz (b) Rolling: 15.83 Hz

Figure 3.4: First vertical mode (Hop) observed for the (a) loaded tyre; and (b) loaded and rolling tyre, suggesting hop motion of the tyre along the vertical direction

tyre at 10 km/h speed.

The first lateral deflection mode of the inflated tyre model (denoted as Tran-Y) is observed at the natural frequency of 42.39 Hz, which reveals translational motion of the tyre along the transverse direction (designated as Y-axis), as shown in Figure 3.5(a). Such an out-of-plane mode can only be detected by a 3-D tyre model, and would be ignored by the physical in-plane tyre models using the *ring on elastic foundation* concept [121, 122, 128]. This natural frequency is in agreement with that predicted by Zhang [13] at 42.11 Hz via modal analysis of a 12.5R22.5 truck tyre inflated at 690.3 kPa using ANSYS. The loaded tyre, however, showed this lateral mode shape at a slightly higher frequency of 45.21 Hz, as illustrated in Figure 3.5(b), which is attributed to an increase in the lateral stiffness of the loaded tyre model promoting the frictional contact force in the lateral direction. Scavuzzo [202] measured the same vibration mode for a 285/75R24.5 truck tyre as 48 Hz. Further, Burke [123] predicted this deflection mode at 43.76 Hz for a 195/65R15 car tyre subjected to 193 kPa inflation pressure and 3.33 kN normal load. The same for the rolling tyre was obtained at 44.93 Hz (Figure 3.5(c)), which is similar to that of the loaded tyre, suggesting that rolling has only minimal effect on the lateral stiffness.

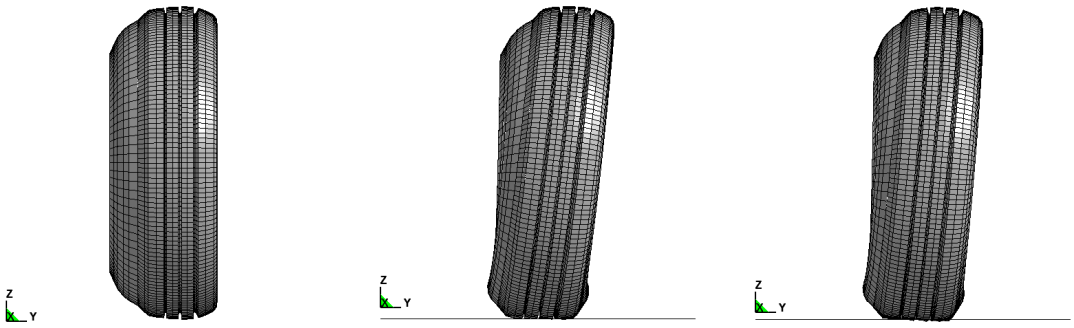

(a) Inflated: 42.39 Hz (b) Loaded: 45.21 Hz (c) Rolling: 44.93 Hz

Figure 3.5: First lateral mode (Tran-Y) of the (a) inflated tyre; (b) loaded tyre; and (c) rolling tyre, revealing translational motion of the tyre along the transverse direction

The first torsional deflection mode of the inflated tyre (denoted as Rot-Y) was observed at 43.83 Hz, while revealed rotational oscillations of the tyre about the wheel axle, as illustrated in Figure 3.6(a). This natural frequency is in agreement with the torsional

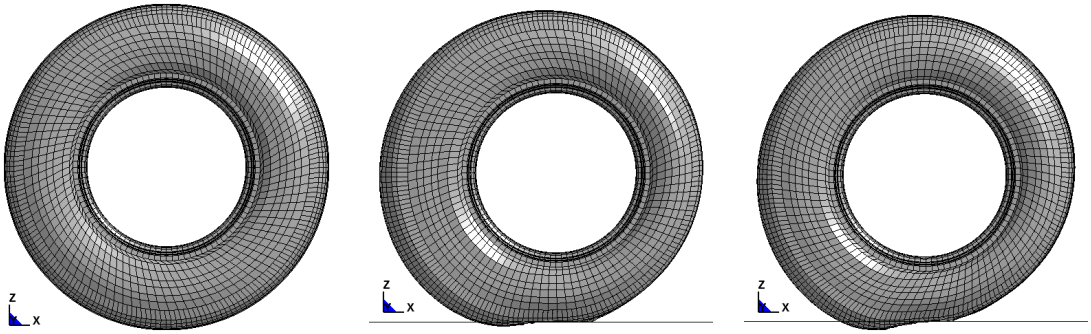

(a) Inflated: 43.83 Hz (b) Loaded: 49.47 Hz (c) Rolling: 26.35 Hz

Figure 3.6: First torsional mode (Rot-Y) of the (a) inflated tyre; (b) loaded tyre; and (c) rolling tyre, revealing rotational oscillations of the tyre about the wheel axle

mode frequencies reported by Ford and Charles [201], Palmer [124] and Zhang [13] at 43, 44 and 45.12 Hz, respectively, although the studies employed different simulation platforms and different truck tyres subjected to nominal operating inflation pressures. This frequency, however, increased to 49.47 Hz for loaded tyre due to increase in the vertical tyre stiffness, as shown in Figure 3.6(b). Kerchman [135] extracted this vibration mode at 47.8 Hz from modal analysis of a non-rolling P205/75R15 car tyre subjected to 240 kPa inflation pressure and 4.45 kN normal load using ABAQUS. This mode for the rolling tyre at 50 km/h, shown in Figure 3.6(c), was observed at a substantially lower frequency of 26.35 Hz, which is largest change observed between the deflected (static) and rolling cases among all the extracted vibration modes. Such a large reduction in the natural frequency can be attributed to relaxation in stresses in the contact patch of the rotating tyre leading to considerable decline in tyre dynamic stiffness. Burke [123] also reported a considerable reduction in this mode frequency from 56.3 Hz for the static case to 49.3 Hz for the rolling tyre at a speed of 40 km/h for a 195/65R15 car tyre.

The rotational vibration modes about the Z-axis (denoted as Rot-Z) were observed at 49.50, 50.84 and 49.88 Hz for the inflated, deflected and rolling cases, respectively, which revealed dominant rotational oscillations of the tyre about the vertical axis, as shown in Figure 3.7. Zhang [13] predicted this mode at 47 Hz for a free non-contacting truck tyre inflated at 690.3 kPa.

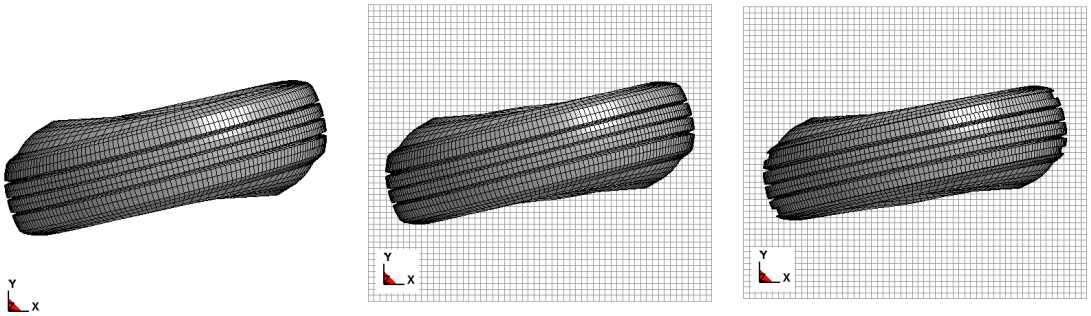

(a) Inflated: 49.50 Hz (b) Loaded: 50.84 Hz (c) Rolling: 49.88 Hz

Figure 3.7: Twisting mode (Rot-Z) obtained for the (a) inflated tyre; (b) loaded tyre; and (c) rolling tyre, revealing rotational oscillations about the vertical (Z) axis

Figure 3.8 depicts mode shapes (denoted as Expan-Comp) at 54.91, 62.93 and 61.54 Hz for the inflated, deflected and rolling tyres, respectively, which reflects a vibrational motion causing the expansion of nearly one half of the tyre and compression of the other half. These frequencies are comparable to the dominant frequency of 59.5 Hz derived from the cleat-drum test. Zhang [13] predicted this natural frequency for an inflated non-contacting truck tyre at 57.6 Hz, while Palmer [124] predicted it as 67.87 Hz for an inflated and deflected but non-rolling truck tyre.

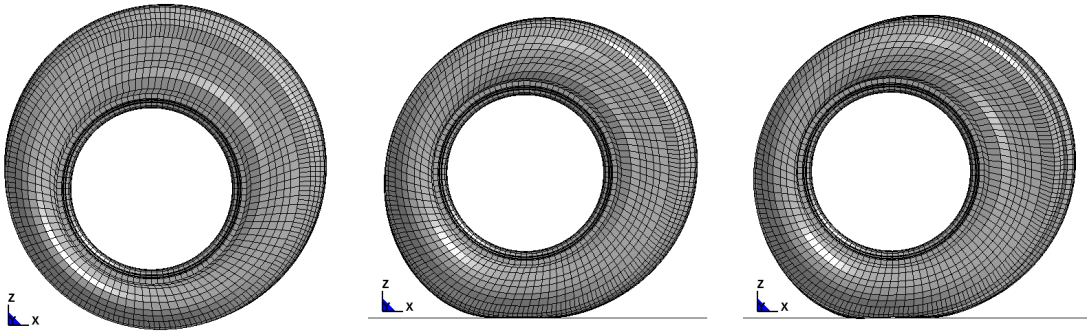

(a) Inflated: 54.91 Hz (b) Loaded: 62.93 Hz (c) Rolling: 61.54 Hz

Figure 3.8: Expansion/compression (Expan-Comp) mode obtained for the (a) inflated tyre; (b) deflected tyre; and (c) rolling tyre, revealing expansion of one half of the tyre and compression of the other half

The results showed presence of conjugate pair modes at the higher frequencies. These

were observed at 72.15 Hz for the inflated tyre, as shown in Figure 3.9(a) and 3.9(d). The resulting in-plane modes (denoted as Oval-Diag and Oval) revealed an oval form resulting from extensions in opposite directions along a central axis in the wheel plane and compressions along the perpendicular axis. The loaded tyre, however, reflected these modes at two different frequencies of 70.11 and 76.97 Hz, one being lower and the other greater than 72.15 Hz, as shown in Figures 3.9(b) and 3.9(e). The difference in the natural frequencies of these two vibration patterns is attributed to the effect of contact boundary condition in conjunction with application of the vertical load which likely causes different degrees of variations in the stiffness and hence the natural frequency for the tyre vibrations along vertical and diagonal directions. Shiraishi [125] also observed similar conjugate pair modes for a 195/65R15 car tyre inflated at 200 kPa and deflected under a 4.41 kN normal

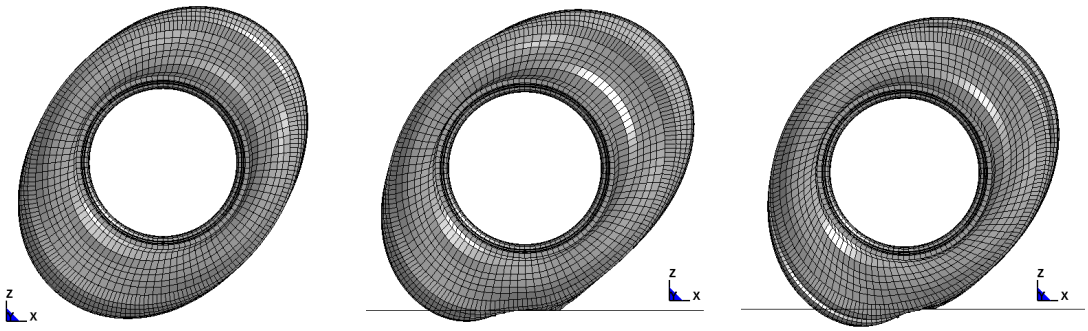

(a) Inflated: 72.15 Hz (b) Loaded: 70.11 Hz (c) Rolling: 69.86 Hz

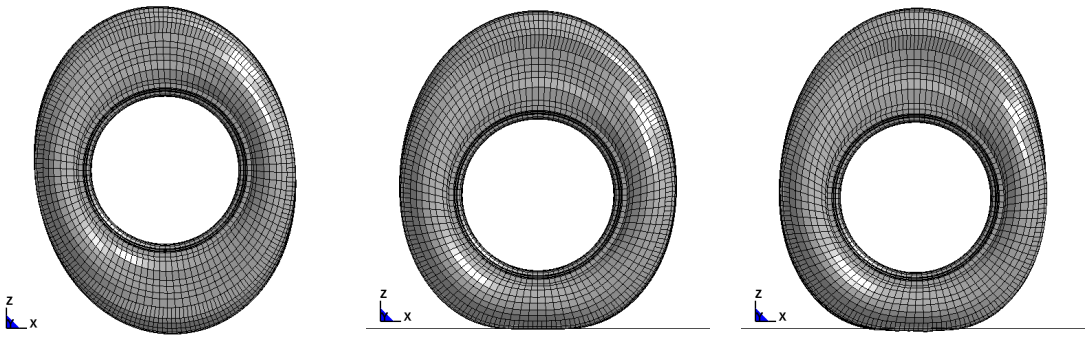

(d) Inflated: 72.15 Hz (e) Loaded: 76.97 Hz (f) Rolling: 76.79 Hz

Figure 3.9: Oval mode shapes (Oval-Diag and Oval) observed for the (a,d) inflated tyre; (b,e) deflected tyre; and (c,f) rolling tyre, revealing extensions in opposite directions along a central axis and compressions along the orthogonal directions

load using LS-DYNA. The study revealed vertical and diagonal oval mode shapes at two different frequencies of 78.5 and 72.2 Hz, respectively. Natural frequencies of 69.86 and 76.79 Hz were also extracted for this pair of conjugate modes for the case of the rolling tyre, as demonstrated in Figures 3.9(c) and 3.9(f), which are slightly lower than those of the deflected tyre. These frequencies are comparable to the dominant frequency of 72.3 Hz derived from the cleat-drum test as the second free vertical vibration mode of the tyre. Chae [12] also observed a dominant frequency at 73 Hz for a 295/75R22.5 truck tyre rolling at 50 km/h via a cleat-drum test simulation using PAM-CRASH. Moreover, Burke [123] obtained this mode shape at 75.01 Hz for a 195/65R15 car tyre deflected under 3.33 kN normal load. Further, Kao [212] obtained this vertical vibration mode at 69.71 Hz using a FE model of a P205/65R15 car tyre subjected to 207 kPa inflation pressure.

As shown in Figures 3.10(a) and 3.10(d), a pair of conjugate mode shapes with a complex out-of-plane deformation pattern (denoted as Twist and Twist-Diag) were observed for the inflated tyre at the natural frequency of 75.75 Hz. Whereas, the loaded tyre revealed these modes at different frequencies of 66.60 and 78.03 Hz, as seen in Figures 3.10(b) and 3.10(e). In these modes, the tyre exhibited a twisting vibrational motion, where the two opposite halves of the tyre moved outwards from the tyre plane and the other two opposite halves displaced backwards out of the tyre plane. The rolling tyre, however, exhibited these modes at the natural frequencies of 63.02 and 75.94 Hz, as shown in Figures 3.10(c) and 3.10(f), which are lower than those related to the deflected tyre. Zhang [13] predicted the natural frequency corresponding to this out-of-plane mode shape as 67.3 Hz for a non-rolling truck tyre inflated at 690.3 kPa.

As shown in Figure 3.11(a), an additional vertical mode (denoted as Oval-Extra) at frequency of 82.33 was observed for the deflected tyre. This mode was not observed for the inflated tyre, due to lack of contact with the road. This mode for the rolling tyre was observed at the natural frequency of 79.19 Hz, which is lower than that of the deflected tyre, as demonstrated in Figure 3.11(b). Scavuzzo [202] also measured the natural frequency corresponding to this mode for a P205/70R14 car tyre subjected to 207 kPa inflation pressure and 4.89 kN vertical load, and reported a reduction from 84 to 80 Hz between the deflected tyre (static) and the rolling tyre at a speed of 8 km/h. These frequencies are

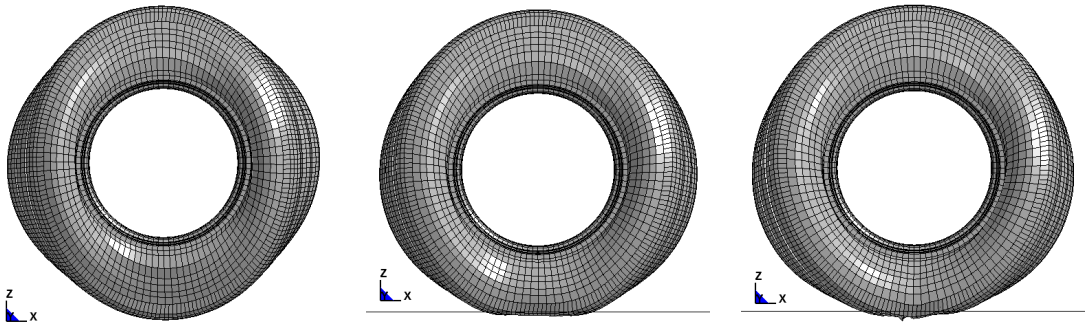

(a) Inflated: 75.75 Hz (b) Loaded: 66.60 Hz (c) Rolling: 63.02 Hz

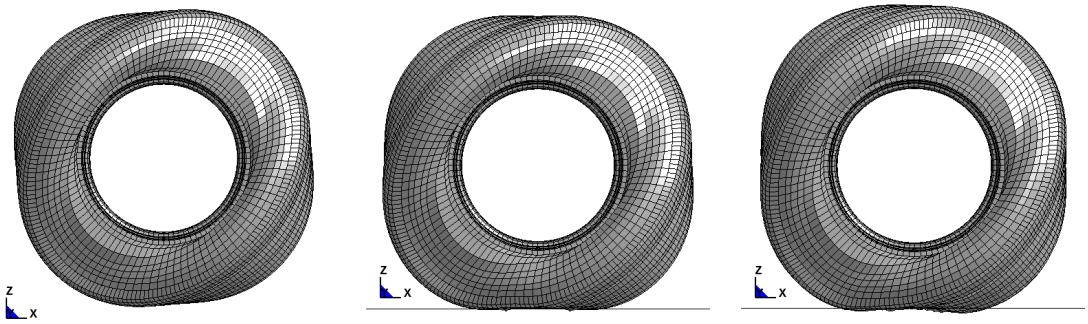

(d) Inflated: 75.75 Hz (e) Loaded: 78.03 Hz (f) Rolling: 75.94 Hz

Figure 3.10: Twisting mode shapes (Twist and Twist-Diag) observed for the (a,d) inflated tyre; (b,e) deflected tyre; and (c,f) rolling tyre, resulting from a complex out-of-plane twisting motion

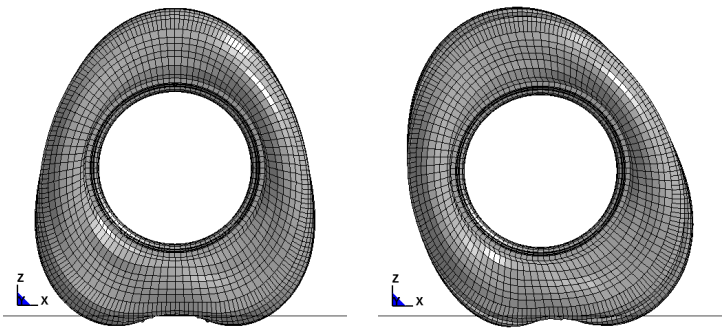

(a) Loaded: 82.33 Hz (b) Rolling: 79.19 Hz

Figure 3.11: An additional vertical mode (Oval-Extra) observed for the (a) deflected tyre; and (b) rolling tyre

comparable to the dominant frequency of 93.3 Hz derived from the FFT analysis in the cleat-drum test, and are considered as the third free vertical vibration mode of the tyre. Moreover, Palmer [124] computed vertical vibration modes at 81.1 and 94.7 Hz for a truck tyre using LS-DYNA. Similarly, Ford and Charles [201] reported this mode at 83 Hz for a 285/75R24.5 truck tyre. Kao [75] obtained this mode at 85 Hz for a P205/65R15 car tyre under 220 kPa inflation pressure, 4 kN load and 48.28 km/h rotational speed using LS-DYNA.

At the frequency of 91.69 Hz, the inflated tyre revealed a pair of conjugate modes with corner-rounded triangular shapes (denoted as Tri-Diag and Tri), as illustrated in Figures 3.12(a) and 3.12(d). Whereas, for the loaded tyre, these in-plane vibration modes were obtained at different frequencies of 90.59 and 102.25 Hz, as seen in Figures 3.12(b) and 3.12(e). The rolling tyre, however, revealed this pair of conjugate modes at lower

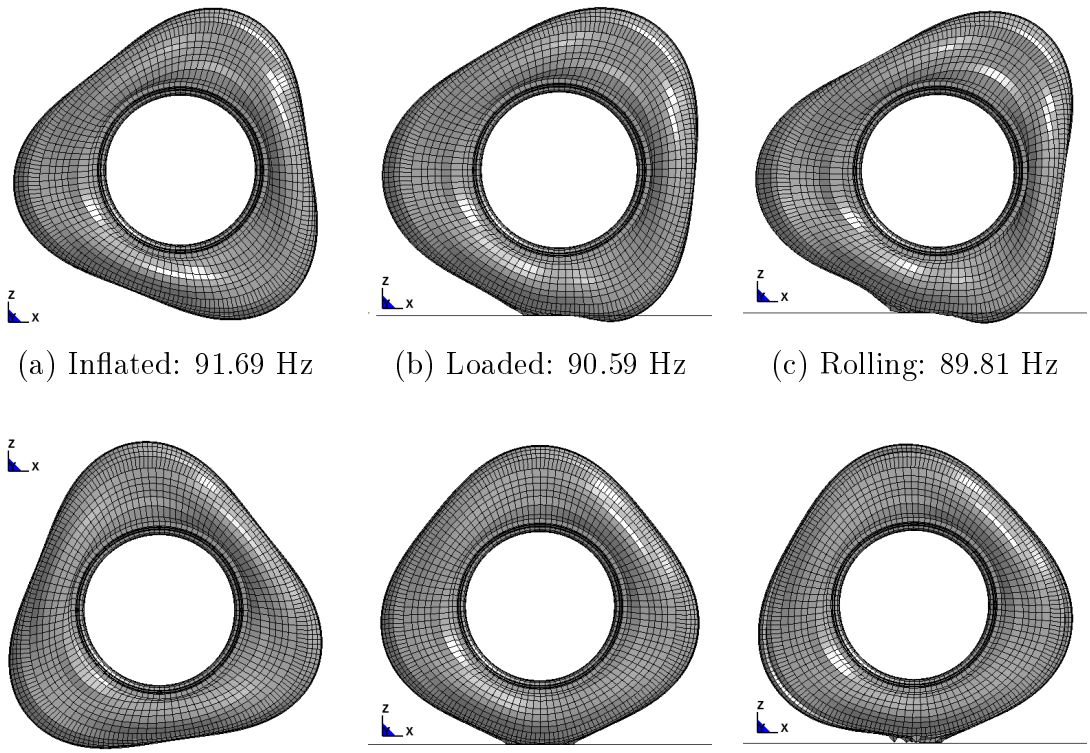

(a) Inflated: 91.69 Hz (b) Loaded: 90.59 Hz (c) Rolling: 89.81 Hz

(d) Inflated: 91.69 Hz (e) Loaded: 102.25 Hz (f) Rolling: 99.09 Hz

Figure 3.12: Triangular deflection modes (Tri-Diag and Tri) of the (a,d) inflated tyre; (b,e) deflected tyre; and (c,f) rolling tyre

frequencies of 89.81 and 99.09 Hz compared to those of the deflected tyre, as demonstrated in Figures 3.12(c) and 3.12(f). Zhang [13] and Palmer [124] predicted the natural frequency related to this triangular mode shape as 98.94 and 113.3 Hz, respectively, for a non-rolling truck tyre. Burke [123] also obtained this vibration mode at 97.55, 94.78 and 91.85 Hz for a 195/65R15 car tyre while rolling at 10, 40 and 70 km/h, respectively.

At the frequency of 110.29 Hz, the inflated tyre revealed a complex out-of-plane deflection mode (denoted as Toroidal and Toroidal-Diag), causing twisting oscillations of the tyre along the toroidal centerline, as shown in Figures 3.13(a) and 3.13(d). While, the loaded tyre experienced the same deflection pattern at frequencies of 100.93 and 112.20 Hz. Relatively lower frequencies of 90.98 and 109.93 Hz of this pair of modes were observed for the rolling tyre. Zhang [13] estimated the frequency of this mode at 97.62 Hz

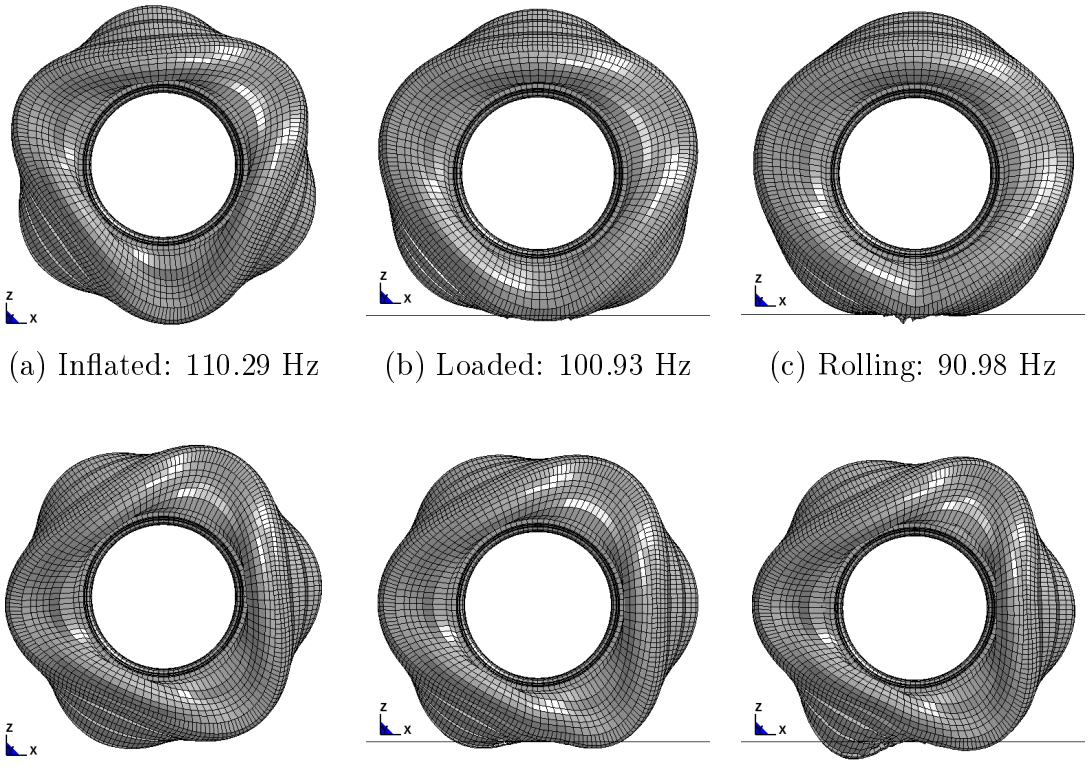

(a) Inflated: 110.29 Hz (b) Loaded: 100.93 Hz (c) Rolling: 90.98 Hz

(d) Inflated: 110.29 Hz (e) Loaded: 112.20 Hz (f) Rolling: 109.93 Hz

Figure 3.13: Complex out-of-plane deflection modes (Toroidal and Toroidal-Diag), of the (a,d) inflated tyre; (b,e) deflected tyre; and (c,f) rolling tyre, showing twisting oscillations of the tyre along the toroidal centerline

and reported it as the most complicated mode shape among all the modes they considered.

Figures 3.14(a) and 3.14(d) illustrate a pair of conjugate modes with quadric shapes of the inflated tyre (denoted as Quad and Quad-Diag) at the frequency of 112.65 Hz. The loaded tyre, however, revealed the quadric modes at frequencies of 110.25 and 122.26 Hz, as illustrated in Figures 3.14(b) and 3.14(e). Relatively lower frequencies of 106.14 and 110.27 Hz were observed for the rolling tyre, as demonstrated in Figures 3.14(c) and 3.14(f). Zhang [13] and Palmer [124] predicted the natural frequency related to this quadric mode as 110.86 and 128.9 Hz, respectively, for non-rolling truck tyres. Zegelaar [122] measured this quadric mode for a normally inflated car tyre at 115.9 Hz. Adding ground contact, however, this frequency was diverged into two distinctive frequencies of 112.3 and 125.7 Hz for the deflected tyre under 4 kN load.

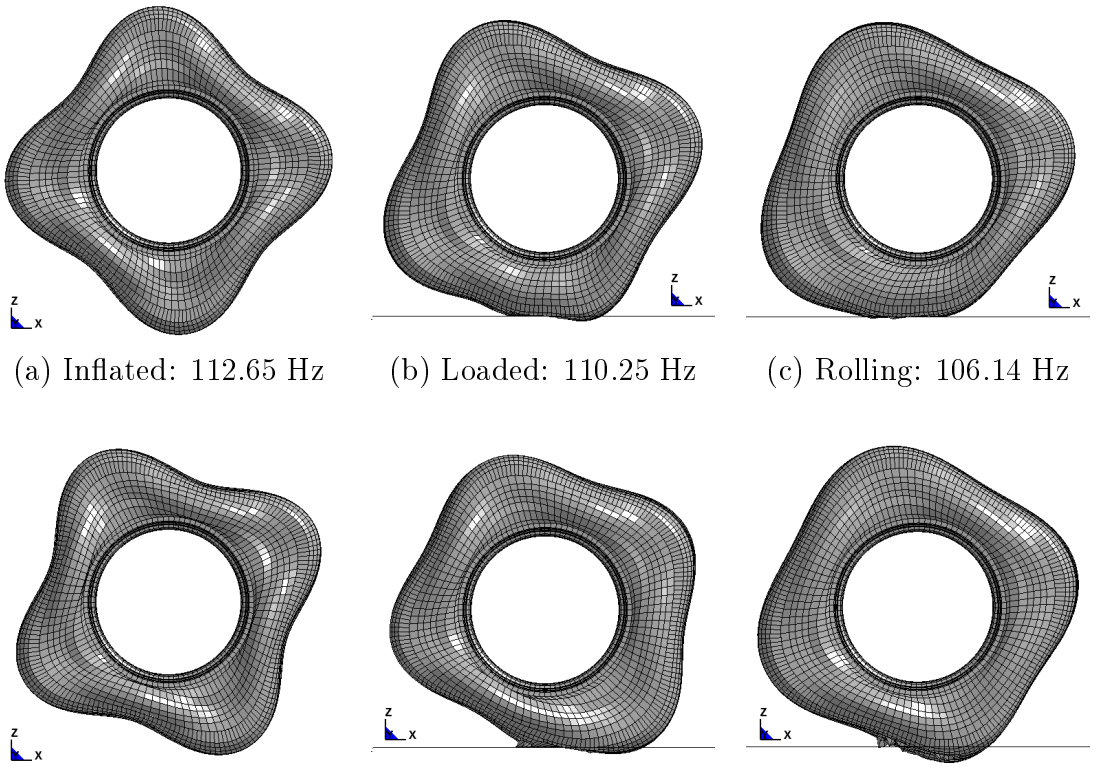

(a) Inflated: 112.65 Hz (b) Loaded: 110.25 Hz (c) Rolling: 106.14 Hz

(d) Inflated: 112.65 Hz (e) Loaded: 122.26 Hz (f) Rolling: 110.27 Hz

Figure 3.14: Quadric mode shapes (Quad and Quad-Diag) of the (a,d) inflated tyre; (b,e) deflected tyre; and (c,f) rolling tyre

3.5 Influences of operating parameters on tyre modal properties

The deflection modes of the tyre are strongly affected by a number of operating and design parameters. In this study, the influences of variations in inflation pressure, normal load, and rolling speed on the natural frequencies and deflection modes are evaluated considering the three cases: inflated, deflected and rolling tyre models.

3.5.1 Inflation pressure

The eigenvalue analyses were repeated for the inflated tyre model considering different inflation pressures, ranging from 483 to 1034 kPa (70 to 150 psi). The results revealed significant effects of inflation pressure on the natural frequencies corresponding to the in-plane and out-of-plane modes of the inflated tyre, as seen in Figures 3.15(a) and 3.15(b). It is seen that all the in-plane and out-of-plane mode frequencies increase with increase in the inflation pressure. The observed changes are attributed to the strong dependence of the tyre stiffness and hence the natural frequencies on the inflation pressure. The results also suggest nearly linear variations in the natural frequencies with the inflation pressure within the range considered in the study. The rate of changes of the natural frequencies

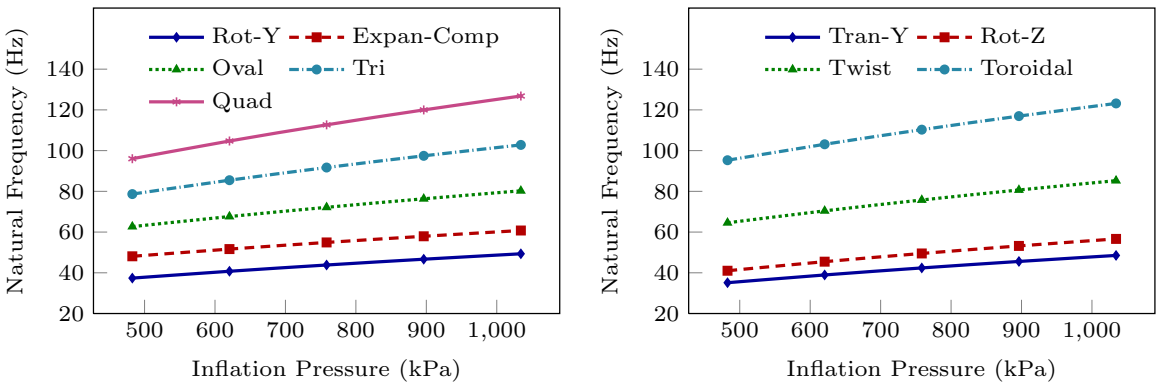

Figure 3.15: Influences of inflation pressure on natural frequencies corresponding to (a) in-plane; and (b) out-of-plane modes

with respect to the inflation pressure, however, tend to be higher for the higher modes than the lower modes. For instance, increasing the inflation pressure from 483 to 1034 kPa, revealed an increase in the highest mode natural frequency, denoted as Quad, of 30.8 Hz, which is substantially higher than 13.4 Hz observed for the lowest mode (Tran-Y). Burke [123] also investigated the effect of inflation pressure on natural frequencies of a 195/65R15 car tyre via experiments and simulations, and reported a dramatic increase in the natural frequencies with increase in the inflation pressure.

3.5.2 Normal load

The influences of normal load on the natural frequencies corresponding to the in-plane and out-of-plane modes are evaluated considering load variations in the range of 8.9 to 44.5 kN (2000 to 10000 lb), while the inflation pressure was held as 758 kPa. The vertical load was applied directly as an external force to the center of the wheel rim without adding any extra mass to the system. Figures 3.16(a) and 3.16(b) illustrate the influence of variations in the normal load on different in-plane and out-of-plane natural frequencies of the deflected

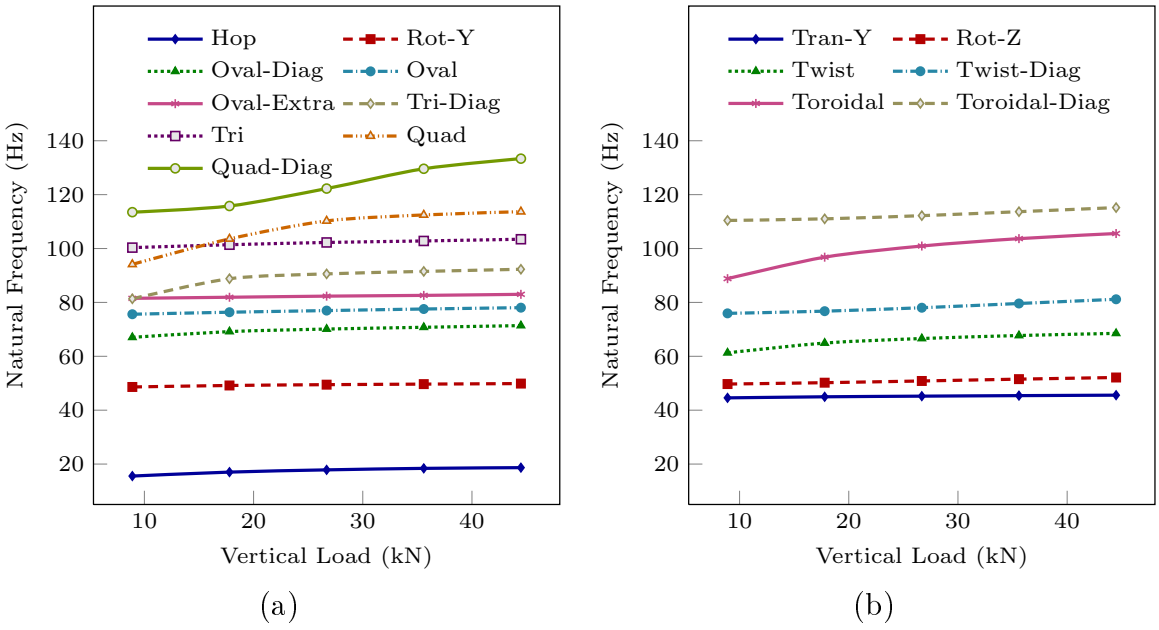

Figure 3.16: Influences of vertical load on natural frequencies corresponding to (a) in-plane; and (b) out-of-plane modes of a deflected tyre under 758 kPa inflation pressure

tyre. The results suggest varying effects of normal load on deflection modes. For the in-plane modes denoted as Tri-Diag and Quad as well as for the out-of-plane modes denoted as Twist and Toroidal, the natural frequencies tend to increase with increase in the vertical load in the lower range but saturate with further growth in the vertical load. The highest in-plane mode frequency (denotes as Quad-Diag) increased significantly and nonlinearly with increasing normal load. It can be concluded that the tyre deflection can affect the tyre natural frequencies related to higher modes of vibration, while the effect on most of the natural frequencies is very small, particularly those related to the lower modes. Burke [123] also reported slight increase in the frequencies with increase in the hub load for a stationary car tyre under 193 kPa inflation pressure. Huang [120] investigated the effect of ground contact on tyre vibrations using a theoretical approach based on the ring on elastic foundation concept and showed that the tyre natural frequencies in ground contact were higher than those of the non-contacting tyre.

3.5.3 Rolling speed

The influence of rolling speed on the in-plane and out-of-plane mode frequencies are evaluated for the rolling tyre. The inflation pressure and the normal load are held to their respective nominal values, 758 kPa and 26.7 kN. All the in-plane and out-of-plane natural frequencies, in general, decreased with increase in the rolling speed, as shown by Figures 3.17(a) and 3.17(b). This is due to reduction in the dynamic tyre stiffness with increase in the speed. The most substantial change is observed in the frequency corresponding to the in-plane mode, denoted as Rot-Y, as seen in Figure 3.17(a), which is perhaps the most important deflection mode shape concerning tyre rotation about its axle. The natural frequency corresponding to this mode decreased sharply by 41.2% from the static case, when the speed increased to 5 km/h. A further increase in the speed resulted in additional reduction in the natural frequency, but very small. For example, increasing the speed from 5 to 10 km/h resulted in only 2.4% further reduction in this mode frequency. Such a substantial reduction at the onset of rolling is attributed to the fact that dynamic motion of the tyre enables it to relieve the stresses developed in the footprint, which results in a rapid drop in the tyre stiffness and hence the natural frequency corresponding to the rotational

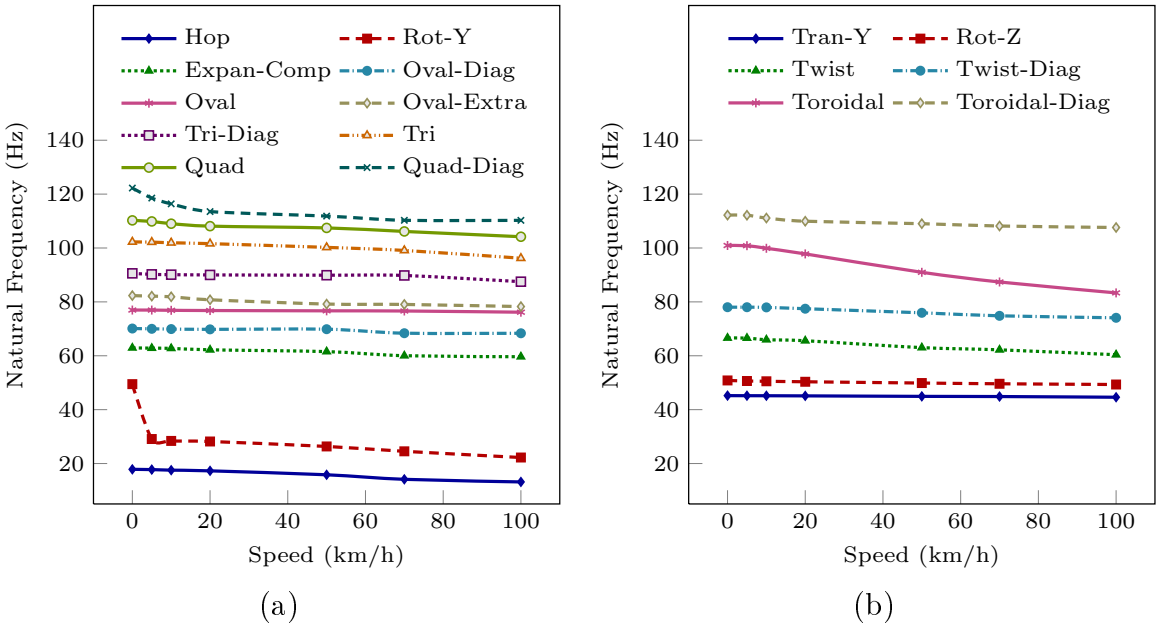

Figure 3.17: Influences of speed on natural frequencies corresponding to (a) in-plane; and (b) out-of-plane modes of a rolling tyre under 758 kPa inflation pressure and 26.7 kN load

mode shape (Rot-Y). This suggests that the rotational motion of the tyre is the key factor in reducing the dynamic stiffness of the tyre, while the magnitude of the rotational speed is the secondary factor. Burke and Olatunbosun [123], also performed modal analyses on a 195/65R15 car tyre over a range of speeds and observed that the tyre rotation caused a considerable decline in the natural frequency from 56.3 Hz for the static case to 50.35 Hz for the rolling tyre at 10 km/h speed. Further increase in the speed to 70 km/h resulted in only a slight reduction in the frequency to 49.3 Hz. Kindt [115] measured the vibration responses of a rolling 205/55R16 tyre using a laser Doppler vibrometer in a tyre-on-tyre test set-up and observed a significant drop in the tyre response frequencies at the onset of rolling. The in-plane mode Quad-Diag as well as the out-of-plane mode Toroidal also exhibited considerable reductions in the corresponding natural frequency with increase in the speed compared to those observed for the other lower modes of vibration, which showed only slight decrease.

3.6 Conclusions

A virtual tyre simulation platform was developed to investigate vibration modes of a rolling truck tyre subjected to inflation pressure and vertical deflection due to normal load. The study of the effects of loading and boundary conditions on the vibration modes necessitated consideration of the inflated and deflected rolling tyre as a pre-stressed structure. The stress field of the rolling tyre under inflation pressure and vertical load could be effectively evaluated through explicit dynamic analyses. The implicit eigensolver could then be employed to conduct modal analyses of the pre-stressed tyre due to applied inflation, normal load and the speed. It is shown that modal behavior of the tyre subjected to inflation, normal load and the rolling speed could be evaluated in a sequential manner at instants the tyre approaches steady responses under each loading. The results showed that increasing the tyre inflation pressure substantially increases its natural frequencies, which suggests the importance of the inflation pressure as a key factor governing the stiffness of a pneumatic tyre and hence its dynamic performance. It was observed that the identical conjugate mode natural frequencies extracted for the inflated tyre diverged to two different frequencies for the deflected tyre, with one being lower and the other higher than the identical frequencies of the inflated tyre. The rolling tyre also revealed same phenomenon with somewhat lower frequencies. It was demonstrated that for a deflected tyre under direct application of an external vertical hub load, increasing the amount of load resulted in slight increase in most of the natural frequencies except for a few higher modes. The natural frequencies corresponding to these higher modes increased with increasing load but approached saturation with further increase in the load. The rotational motion of the tyre resulted in a most dramatic reduction in the tyre stiffness and hence the natural frequencies compared to those of the non-rolling tyre. Increasing the rolling speed, however, caused only smaller further reductions in the natural frequencies.

Chapter 4

Development of a Computationally Efficient Rolling Truck Tyre Model using Part-Composite Approach and its Verification

4.1 Introduction

Developments in reliable and computationally efficient tyre modeling continues to be of significant importance for design and developments of vehicle systems. Widely different mathematical and structural models with varying complexities have evolved for predicting dynamic responses of pneumatic tyres. Mathematical tyre models employ either phenomenon-based [2, 63–65] or physics-based [1, 3, 51, 62, 67, 213–219] approaches to formulate contact forces and moments in terms of tyre deformations/slips, ground surface profile, axle load, speed and other operating parameters. These models could provide efficient predictions of tyre dynamic responses for applications in multi-body simulation models for vehicle ride [65, 214, 218] and handling [63, 67, 215, 217] performance evaluations. The accuracy of these models, however, strongly relies on a number of regression coefficients or physical parameters describing equivalent inertia, stiffness and damping properties, which are generally identified through experiments [6, 7]. Such mathematical models, however, do not directly consider the contributions due to tyre complex structure

and material properties, and thus cannot provide guidance towards design of pneumatic tyres.

Alternatively, a vast number of structural models have been proposed for the purpose of tyre design and developments. Structural tyre models, developed using finite element methods, permit consideration of the complex geometric details in tyre structure as well as anisotropies and nonlinearities associated with tyre material properties. In these studies, the multi-layered composite structure of the tyre has been described using widely different methods. Earlier studies have taken advantage of axisymmetry in tyre geometry and simplified the tyre construction as a thin shell of revolution [117, 127] or a toroidal membrane [119] to achieve greater computational efficiency. Although these studies could take into account the contributions due to geometric nonlinearities [119] and material anisotropies [117] of the tyre structure, their applications were limited to approximations of the tyre dynamic responses under axisymmetric loading situations such as inflation pressure and centrifugal forces.

Three-dimensional (3-D) representations of the tyre structure, however, are vital for analyses considering ground contact loading, rolling and side-slip. A number of studies have considered the tyre as an inflated 3-D airbag made of a single layer of membrane elements with equivalent orthotropic material properties. These models have been employed for durability [80], cornering [82] and vehicle crash simulations [79] with moderate computational demand. A number of comprehensive tyre models have been developed considering the multi-layered composite structure of the tyre using different methods [10, 32, 78, 92, 96, 108, 109, 190, 206]. The *discrete reinforcement* technique has been commonly adopted in many structural tyre models [10, 12, 32, 109]. In this technique, the multiple layers of the carcass and belt structures are described such that the rubber matrix is represented using 3-D solid elements with hyper-elastic rubber material properties, while the reinforcements are discretely modeled via shell elements with orthotropic material properties [10]. The approach permits analyses of stresses within and between different layers for fatigue life and durability enhancements via minimizing the inter-layer stresses [10, 14, 83]. Moreover, the geometric and material properties of the rubber compound and twisted cords can be incorporated in the equivalent orthotropic material properties of the

fiber-reinforced layers using the *rule of mixtures* for composite materials [10, 32, 196, 197]. Alternatively, the reinforcing fibers in the carcass and belt layers may be independently modeled using beam elements coupled to the isotropic elastic shell elements representing the rubber matrix via shared nodes [98]. This method thus permits consideration of material properties of fibers and analyses of stresses/strains developed within the fibers apart from the rubber matrix [98].

The detailed structure models yield reliable predictions of tyre dynamic responses, but impose excessive computational demands. The application of such models thus pose complex computational challenges in situations involving repeated simulations such as design parameter analyses, particularly for the rolling tyre [97]. Moreover, the majority of the structural tyre models have been limited to static analyses of stationary tyres subjected to inflation and footprint loads [85–87]. Hall et al. [15, 195] reported CPU time of nearly 8 days for a 0.4 s real time force-deflection simulation in LS-DYNA on a Sun Ultra 60, 360 MHz workstation. The simulation time could exceed 70 days for a 10 s free-rolling simulation of the tyre model on a Sun Blade 1000, 750 MHz workstation. Such unreasonable computational demands limit the applications of comprehensive structural tyre models in vehicle dynamics analyses, and tyre design and optimization. Considerable efforts are thus being attempted for development of computationally efficient yet accurate tyre models.

Chae et al. [11, 92] proposed an efficient approach for modeling the carcass and belt structures in a truck tyre using a three-layered membrane element in PAM-CRASH. The carcass and belt plies with radial and circumferential cords, respectively, were described by two layers with orthotropic material properties, while the rubber matrix with isotropic properties was represented by a third layer. The three-layered membrane element, however, is not sufficient for simulating the effect of belt cord angle, β, on the tyre responses. While a single layer could effectively represent the belt with circumferential cords, a minimum of two layers would be essential to represent the belt plies with $\pm\beta$ cord angles. This methodology, however, has been commonly utilized in several studies focusing on transient response analyses of truck tyres using PAM-CRASH [12, 24–26, 94, 96]. Slade [95] used this approach for simulating the responses of a truck tyre rolling on deformable terrains, which could serve as a virtual test platform for parameterization of an off-road rigid-ring

tyre model. Lescoe [37] enhanced the soil model proposed by Slade [95] using meshless methods in PAM-CRASH and investigated the tyre interactions with soft terrains. Owing to additional computational demand imposed by the soil model, the majority of the studies on tyre-soil interactions have considered the tyre as a rigid body so as to limit the computing time [25, 28, 29, 110, 111]. The aforementioned studies suggest the desire for a simplified but representative tyre model that can be effectively integrated into the design and development process of truck tyres with reasonable computational demand, and for analyses of tyre-soil interactions.

In this study, a simplified model of a rolling truck tyre is proposed in order to achieve enhanced computational efficiency, while maintaining sufficient accuracy for predicting the dynamic responses of the tyre in a virtual testing system. The simplified model is developed on the basis of a comprehensive validated tyre model, where the rubber matrix and the composite reinforcements in the carcass and belt structures are represented using individual solid and shell elements. Using the Part-Composite approach in LS-DYNA, all the layers in the carcass and belt structures are lumped together as a single composite part made of shell elements with multi-layered configuration, which resulted in considerable reduction in the total number of elements in the tyre model. The reduced model employed material properties, thicknesses and fiber orientations identical to those specified for the individual layers of the comprehensive model. The vertical force-deflection, cornering force/moment and modal characteristics of the reduced model are compared with those predicted by the comprehensive tyre model as well as with the reported experimental data to demonstrate its validity.

4.2 Simplified finite element tyre model

4.2.1 Tyre structure model

A finite element model of a rolling truck tyre is implemented based on simplifications of a recently reported comprehensive tyre model using LS-DYNA, which was thoroughly validated considering the reported experimental data [109, 190]. Figure 4.1(a) illustrates

the finite element mesh considered for the cross-section of the comprehensive tyre model representing a 295/75R22.5 radial-ply truck tyre. The model contains a detailed representation of the multi-layered tyre structure including the carcass, belts, tread and bead fillers [109]. The tread and bead fillers are represented by solid elements with hyper-elastic rubber material properties. The rubber matrix and the reinforcing fibers in the carcass and belts are separately modeled via multiple individual layers of isotropic solid and orthotropic shell elements, respectively, which are fully bonded through shared nodes. Figure 4.1(b) shows the carcass and belt layers in the comprehensive tyre model. The sidewalls, denoted by regions 1 to 9 in Figure 4.1(a), are formulated by two layers of solid rubber elements, which are reinforced by three layers of orthotropic shell elements with radial cords. The crown area, denoted as regions 10 to 14 in Figure 4.1(a), consists of two layers of solid rubber elements. The upper layer accounts for the belt rubber matrix, which is enclosed by two layers of reinforcing shell elements of orthotropic materials with $\pm 22^{\circ}$ cord angles with respect to the tyre circumferential centerline. The lower layer represents the carcass rubber matrix below the belt, which is reinforced by a layer of orthotropic shell elements with radial cords [109]. The comprehensive model could yield accurate predictions for the dynamic responses of the truck tyre as compared to the reported experimental

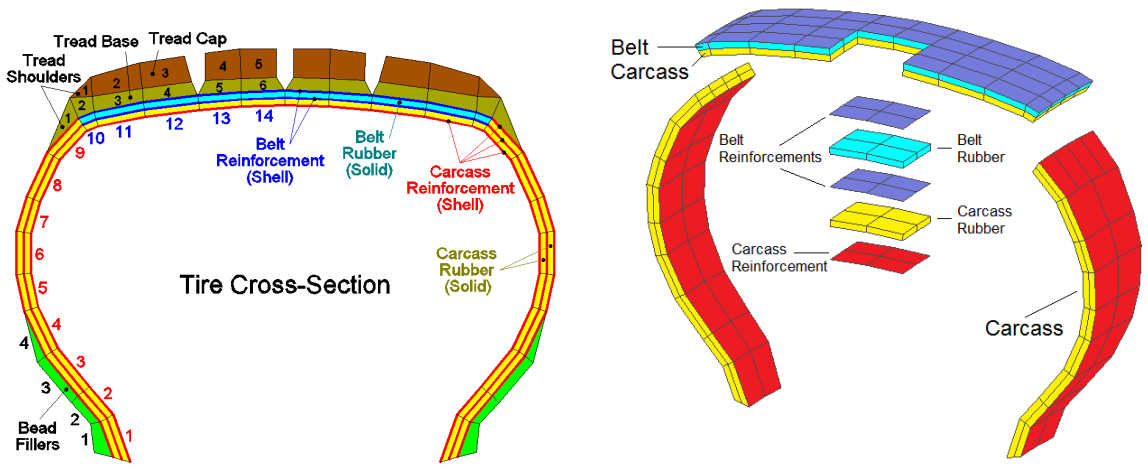

Figure 4.1: (a) The tyre cross-section; and (b) the multi-layered composite structures of the carcass and belt in the comprehensive tyre model [109]

data [109, 190]. However, modeling different layers in the carcass and belt constructions with individual finite elements resulted in a large number of elements and thus substantial computational demand. For instance, a computing time of nearly 4 hours was measured for a 0.2 s real-time force-deflection test simulation, which exceeded 16 hours for a 1.0 s cornering force test simulation using an Intel Xenon processor of 3.2 GHz speed. Such computational demands would likely make the comprehensive model inefficient to be used in a virtual tyre testing environment. The simplification of such a tyre model is thus desirable, while still representing the multi-layered structure of the carcass and belts with sufficient accuracy.

The proposed simplification is based on reducing the number of finite elements via condensing the stack of individual solid and shell elements representing the carcass and belts into a single shell element with multi-layered composite configuration. This is achieved using the Part-Composite approach in LS-DYNA. Figure 4.2(a) shows the reduced cross-section mesh assumed for the simplified tyre model. Only the carcass and belts, having multi-layered composite structures, are involved in this simplification, while the tread and bead fillers are again represented by solid elements of rubber materials identical to that in the comprehensive model. Figure 4.2(b) illustrates the proposed structure for the simplified

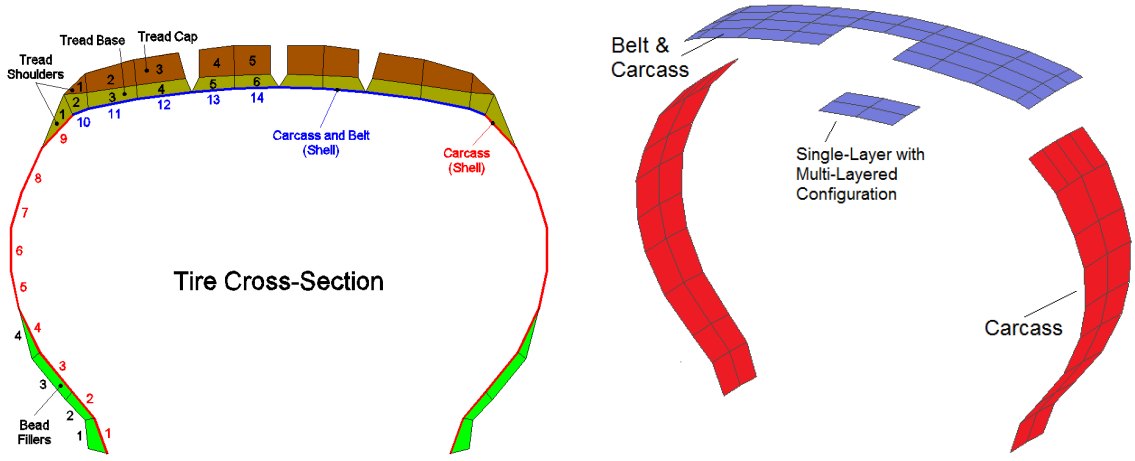

(a) (b)

Figure 4.2: (a) The tyre cross-section; and (b) the reduced structure proposed for the carcass and belts in the simplified tyre model

tyre model, where all the individual layers of solid and shell elements representing the belt and carcass structures are reduced into a single part made of shell elements with layered configuration using the PART_COMPOSITE approach in LS-DYNA [107]. In this approach, a stack of plies can be configured within a single shell element, while the effects of changes in material, thickness and cord angle properties in different layers are incorporated via selecting pertinent integration points through the thickness of the layered element.

Table 4.1 summarizes the material models, thicknesses and fiber orientations defined for different layers of the carcass and belt structures in the simplified model, which are identical to those defined for the comprehensive tyre model so as to facilitate assessments of validity of the simplified model. Regions 1 to 9 in Figure 4.2(a), representing the tyre sidewall structure, are described by a single layer of shell elements with a layered configuration comprising two layers of isotropic elastic material for the rubber matrix mixed with three layers of orthotropic material for the fiber-composite reinforcements with radial cords. Similarly, the regions 10 to 14 in Figure 4.2(a), representing the tyre crown, are considered as a single layer of shell elements with a layered composition consisting of two layers of isotropic material for the rubber matrix, one for the carcass and the other for the belt. The belt rubber matrix is reinforced by two layers of orthotropic materials with $\pm 22^{\circ}$ cord angles with respect to the tyre circumferential centerline, while the carcass rubber matrix is also reinforced by a layer of orthotropic material with radial cords.

Similar to the detailed tyre model [109], the 3-D mesh for the simplified model is generated by spinning the cross-section mesh about the tyre axis in equal increments. By reducing the spinning increment, a finer mesh is formed for the outer circumferential regions, directly subjected to ground contact. Table 4.2 compares the number of elements used in different components of the simplified tyre model with the comprehensive tyre model, while considering a finite element mesh of 96 sectors with 192 divisions for the refined circumferential region. It is evident that the reduced model comprises fewer elements (80% reduction) in the carcass and belt structures. The number of solid elements representing the tread and bead fillers, however, remains the same as these parts have no layered composite nature and thus are not included in the simplification process. This resulted in 63.5% reduction in the total number of elements for the simplified tyre model

Table 4.1: Multi-layered configuration considered in the simplified tyre model

Sidewall structure (regions 1 to 9 in Figure 4.2(a))			
Layer	*Material*	*Thickness*	*Cord angle*
Carcass Reinforcement	Orthotropic	0.33 mm	90°
Carcass Rubber	Isotropic	4.00 mm	—
Carcass Reinforcement	Orthotropic	0.33 mm	90°
Carcass Rubber	Isotropic	4.00 mm	—
Carcass Reinforcement	Orthotropic	0.33 mm	90°
Belt structure (regions 10 to 14 in Figure 4.2(a))			
Layer	*Material*	*Thickness*	*Cord angle*
Belt Reinforcement	Orthotropic	1.50 mm	+22°
Belt Rubber	Isotropic	4.00 mm	—
Belt Reinforcement	Orthotropic	1.50 mm	−22°
Carcass Rubber	Isotropic	4.00 mm	—
Carcass Reinforcement	Orthotropic	1.00 mm	90°

compared to the comprehensive tyre model having a total of 24192 elements. The tyre mesh is subsequently coupled to the rigid rim via shared nodes as in the case of the comprehensive model. The beads are thus not necessary to be included in the model. Further, the road is assumed as a flat surface made of rigid shell elements.

Table 4.2: Comparisons of the number of elements used in the simplified and comprehensive [109] truck tyre models

Component	*Comprehensive model [109]*	*Simplified model*	*Reduction*
Carcass and belt	11520 (shell) and 7680 (solid)	3840 (shell)	80.0%
Tread and bead fillers	4992 (solid)	4992 (solid)	—
Total	24192 (element)	8832 (element)	63.5%

4.2.2 Material constitutive models and properties

The material constitutive types and properties of the simplified tyre model are chosen identical to those defined for the comprehensive model [109]. The elastic material model is selected for solid elements representing the rubber matrix in the carcass and belt structures,

which is available in the LS-DYNA material library (type 1) [104]. The elastic properties of rubber are chosen from the data reported in [198]. The composite material model (type 22) [104] is used for the shell elements describing the fiber-reinforced layers. The orthotropic material properties of the cord-rubber compounds are derived based on the geometric and material properties of the rubber and twisted cords using the Halpin-Tsai equations [196, 197], and reported in [109]. These properties are defined in the cord axes system, and the orientation of the cords with respect to the element axes system is specified via defining a cord angle. The Mooney-Rivlin rubber material model (type 27) is used for the solid elements of the tread and bead fillers, while the material constants for the different rubber compounds are extracted from the reported data [11, 109]. Considering the chosen geometric and material properties, the total mass of the simplified tyre model (78 kg) was comparable with that of the comprehensive tyre model [109]. Finally, the rigid material model (type 20) is used for the shell elements representing the wheel rim and the road surface, as these are substantially stiffer than the tyre constituents.

4.2.3 Tyre-road contact model

The contact between the simplified tyre model and the rigid surface road is modeled using the surface-to-surface contact algorithm in LS-DYNA [105, 107]. In the contact model definition, the solid elements of the tyre tread are defined as the slave, while the shell elements of the rigid surface are designated as the master elements. The Coulomb formulation is used to model the friction between the tyre and the rigid surface, while the static and dynamic coefficients of friction are specified as 0.8 and 0.75, respectively, to represent a dry asphalt road [142].

4.2.4 Method of analysis

Part-Composite definitions and settings

Multiple layers of the carcass and belt structures are defined using the PART_COMPOSITE keyword in LS-DYNA [107]. This permits an efficient way to input the layout and material properties for composite parts, since it obviates the need for using the SECTION_SHELL

keyword for element formulation selection as well as the INTEGRATION_SHELL keyword for user-defined integration rules [107]. For each layer i, the material constitutive model, the thickness associated with the integration point i, and the angle specifying the fiber orientation for integration point i, are defined using the data in Table 4.1. The material properties of the rubber matrix and the reinforcements are defined using the MAT_ELASTIC and MAT_COMPOSITE_DAMAGE keywords, respectively. Owing to the substantial dissimilarities in material properties of the rubber matrix and the orthotropic reinforcements, the consideration of default constant transverse shear strain through the thickness of the composite shell makes it too stiff. The *laminated shell theory* is thus applied to correctly describe the stiffness of the shell elements. This option is activated via selecting the variable LAMSHT as 1 in the CONTROL_SHELL keyword. The integration rule through the thickness of the composite part, which includes the integration points and the corresponding weights, are determined such that each integration point i is located at the center of the respective layer thickness. The total thickness of the composite shell is then obtained from summation the thickness of the individual layers.

The cord angle is defined for each orthotropic layer in order to specify the orientation of cords with respect to the element coordinate system. Using the axis option AOPT in the MAT_COMPOSITE_DAMAGE keyword, the element coordinate system was adjusted via element nodes such that the x-direction is from node 1 to node 2, and the y-direction is orthogonal to the x-direction, while it lies in the plane formed by nodes 1, 2 and 4 [104]. The nodes in the element definition were numbered counterclockwise, as required for the AOPT option. Such a local element coordinate system is constantly subject to change as the solution progresses, particularly under large element deformations and rotations. This strongly affects the definition of cord angles, and thus the responses of orthotropic shells. By activating the *invariant node numbering* via selecting the variable INN as 2 in the CONTROL_ACCURACY keyword, the element coordinate system is modified so as to minimize the sensitivity of the orthotropic shell responses to element distortions. Further details regarding formulations and steps to modify the local element coordinate system can be found in [107].

Finite element formulations

The fully-integrated Belytschko-Tsay shell element formulation (type 16) [199] in conjunction with the hourglass energy control type 8 is selected for the shell elements in the composite part. This hourglass option activates the full projection warping stiffness in order to achieve accurate solutions for shell element type 16 with a reasonable additional computational cost [107]. Similar to the comprehensive tyre model, the nearly-incompressible rubber materials in the tread and bead fillers are formulated using the one-point-integration solid elements together with the hourglass energy control type 5, which resulted in stable and accurate simulations with significant computational cost saving compared to the fully-integrated solid element formulations [107].

Simulation scenarios

The explicit dynamic solver in LS-DYNA [107] is used to predict the tyre dynamic responses in vertical force-deflection and free-rolling cornering force tests. The static vertical stiffness of the tyre model is verified through virtual load-deflection tests, where the tyre is firstly inflated by a uniform and constant internal pressure, and is subsequently loaded in vertical direction with a desired load. The cornering force as well as the aligning moment characteristics of the tyre model are also evaluated via virtual cornering force tests, where the inflated/deflected tyre is permitted to roll freely with a constant side-slip angle with respect to the longitudinal axis of the rigid road surface.

The natural frequencies and mode shapes of the simplified tyre model are also evaluated using the implicit eigensolver in LS-DYNA [107]. In order to incorporate the effects of the internal pressure, ground contact, normal load and rotational motion of the tyre on its natural modes and frequencies, an explicit dynamic simulation is initially performed to determine the stress state through the tyre elements. The stress state is then introduced to the eigensolver to account for its contributions in the stiffness matrix of the inflated/deflected tyre [190]. Using the *intermittent eigenvalue extraction* in LS-DYNA [107], the eigen-frequencies of the tyre are extracted in three instants during the explicit dynamic simulation, which include: (i) modal properties of the free tyre, when the tyre

inflation stabilizes following a desired pressure; (ii) modal properties of the deflected tyre in contact with the road, when the tyre deflection approaches steady-state after application of a vertical load; and (iii) modal properties of the deflected rolling tyre, when the angular speed of the free-rolling tyre becomes steady corresponding to a desired rolling speed.

4.3 Verification of the simplified tyre model

The validity of the proposed simplified tyre model is examined by comparing its static and dynamic results with the reported experimental data as well as with those obtained from the comprehensive tyre model [109, 190]. The results are compared in terms of vertical force-deflection, cornering force/moment and modal characteristics. A grid convergence study was initially performed to determine the minimal required mesh for convergence of the simulation results so as to achieve good computational efficiency.

4.3.1 Grid convergence study

The virtual force-deflection and cornering force tests were repeated using different grids of varying densities ranging from 12 to 192 circumferential divisions. The mesh related to the outer circumferential regions, however, remained fine at 192 divisions so as to eliminate the errors and instabilities, which may be caused by the contact algorithm

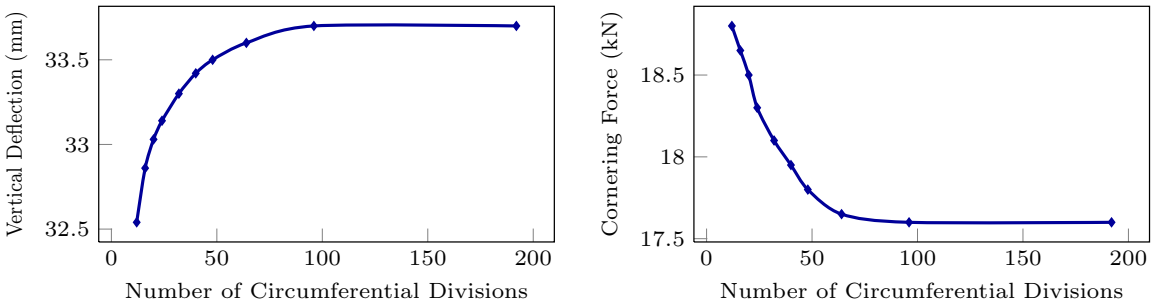

Figure 4.3: Grid convergence study illustrating the simulation results as a function of the circumferential divisions: (a) the vertical tyre deflection; and (b) the cornering force at 5 km/h speed and 6° side-slip angle (inflation pressure = 758 kPa; normal load = 26.7 kN)

during explicit dynamic simulations. Figure 4.3(a) illustrates the vertical tyre deflection response as a function of the mesh refinement in terms of circumferential divisions. The results were obtained considering nominal tyre inflation pressure of 758 kPa, and normal load of 26.7 kN. Figure 4.3(b) shows the convergence of the cornering force developed by the tyre at a free-rolling speed of 5 km/h and constant 6° side-slip angle. The results suggest that a mesh with 96 sectors together with 192 divisions for the outer regions is the minimal required mesh to achieve convergence. Subsequent simulations to obtain the load-deflection, cornering and modal properties of the tyre are thus performed considering this optimal mesh size.

4.3.2 Load-deflection characteristics

The validity of the proposed simplified tyre model is initially evaluated by comparing the virtual load-deflection test results with the reported experimental data and those predicted by the comprehensive tyre model under a range of normal loads at three different inflation pressures. The load-deflection responses of the comprehensive tyre model have been reported in [109]. Figure 4.4(a) illustrates the deformed shape of the simplified

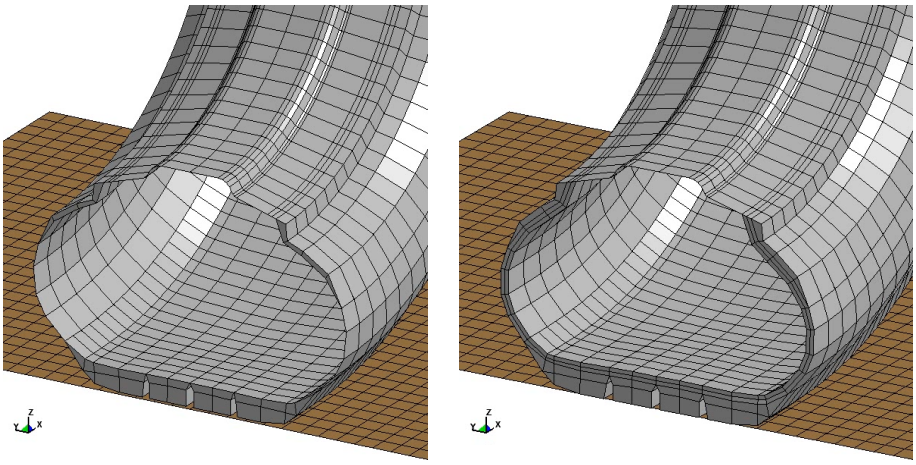

(a) (b)

Figure 4.4: Deformed shapes of: (a) the simplified tyre model; and (b) the comprehensive tyre model (inflation pressure = 758 kPa; normal load = 26.7 kN)

tyre model under 758 kPa internal pressure and 26.7 kN normal load, which is qualitatively similar to that for the comprehensive tyre model shown in Figure 4.4(b). Virtual load-deflection tests were repeated for varying normal loads ranging from 4.448 to 44.48 kN (1000 to 10000 lb) considering three different inflation pressures of 621 kPa, 758 kPa (nominal) and 896 kPa. Figure 4.5 illustrates comparisons of the load-deflection responses of the simplified tyre model with those obtained from the comprehensive tyre model [109] and the experimental data reported for 758 kPa inflation pressure [11]. The comparisons show very good agreements in the responses of the simplified model with those of the comprehensive model and the reported data under the ranges of inflation pressure and normal load considered in the study.

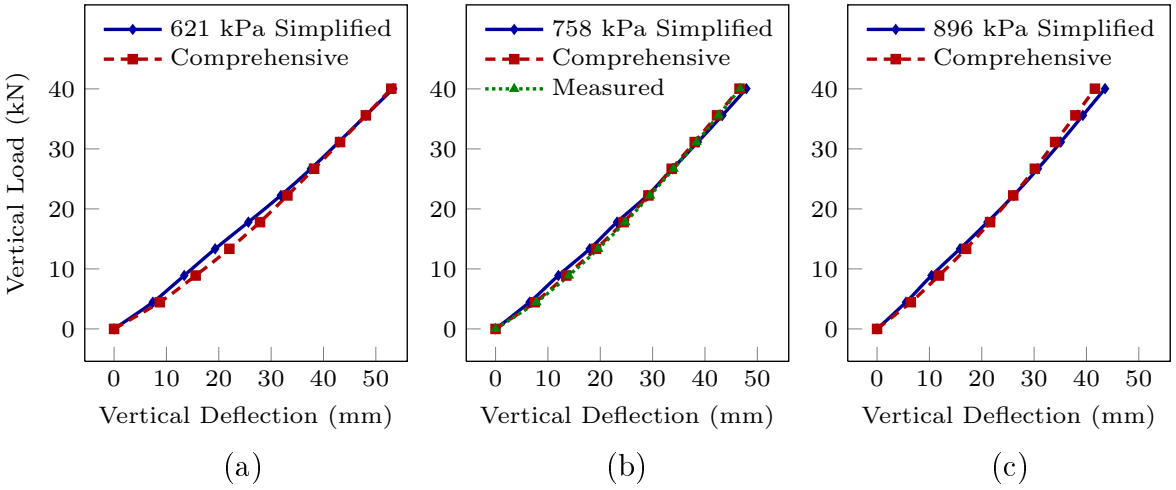

Figure 4.5: Comparisons of load-deflection characteristics predicted by the simplified tyre model with those obtained from the comprehensive tyre model [109], and the reported experimental data [11] under different inflation pressures: (a) 621 kPa; (b) 758 kPa; and (c) 896 kPa

4.3.3 Cornering characteristics

The lateral force prediction performance of the simplified tyre model is evaluated by comparing its cornering force/moment characteristics with the reported experimental data [11] and with those of the comprehensive tyre model [109]. The cornering force tests were performed for a wide range of constant side-slip angles up to 12°, while the

inflated/deflected tyre was freely rolling at a 5 km/h speed on a dry asphalt road with 0.8 and 0.75 static and dynamic coefficients of friction, respectively. The tyre internal pressure and normal load in these simulations were maintained at their nominal values of 758 kPa and 26.7 kN, respectively. Figure 4.6(a) illustrates the deformed shape of the simplified tyre model corresponding to 6° side-slip angle, which is qualitatively similar to that obtained from the comprehensive tyre model shown in Figure 4.6(b).

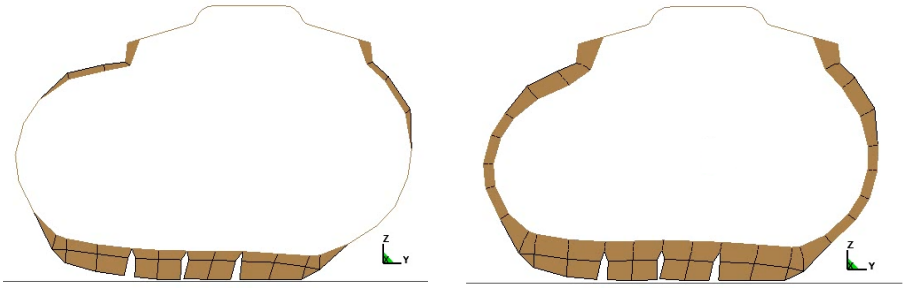

(a) (b)

Figure 4.6: Deformed shapes of: (a) the simplified model; and (b) the comprehensive model subjected to 6° side-slip angle and 5 km/h rolling speed (inflation pressure = 758 kPa; normal load = 26.7 kN)

Figures 4.7(a) and 4.7(b) compare the cornering force and aligning moment responses of the simplified tyre model with the reported experimental data [11] as well as with those obtained from the comprehensive tyre model [109] under three different vertical loads: 17.8, 26.7 and 35.6 kN. The cornering force and aligning moment results predicted by the two models show reasonably good agreements in ranges of side-slip angle and normal load considered in the study. The cornering force characteristics predictions by both the tyre models, however, show some discrepancies with the reported experimental results, specifically at higher side-slip angles. At lower side-slip angles (less than 6°), both the tyre models tend to overestimate the cornering force, while they underestimate the force at higher side-slip angles in the saturation region. The aligning moment predictions by the two models exhibit trends similar to those in the experimental data but show notable differences from the experimental data at side-slip angles above 4°. Despite the observed differences, both the comprehensive as well as reduced models show comparable cornering

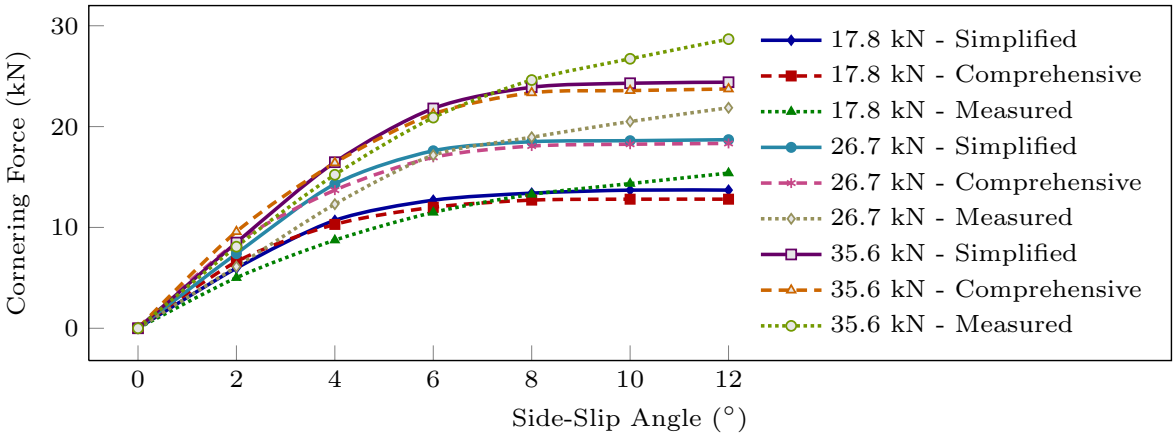

(a)

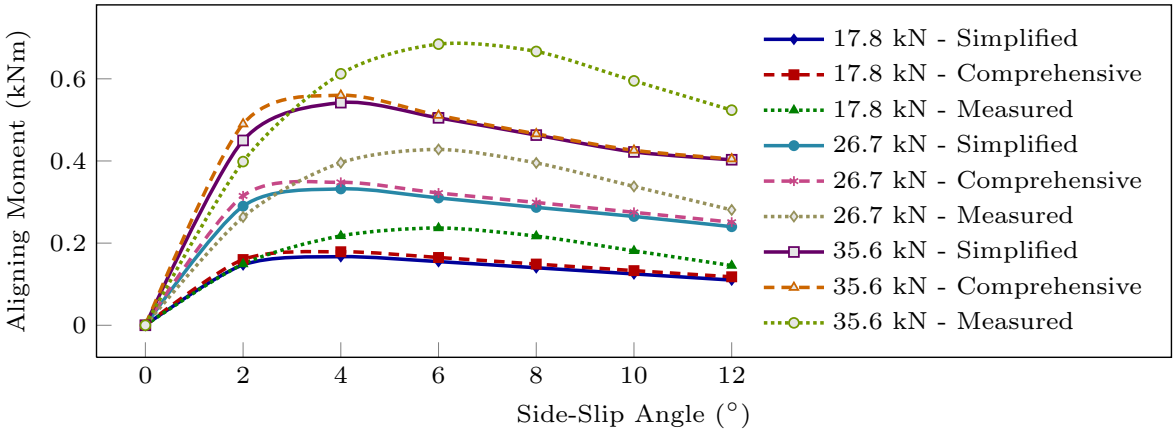

(b)

Figure 4.7: Comparisons of: (a) the cornering force; and (b) the aligning moment characteristics predicted by the simplified and comprehensive [109] tyre models, and the reported experimental data [11] under three different vertical loads

responses.

4.3.4 Modal characteristics

The validity of the simplified tyre model is further evaluated by comparing its natural frequencies with those of the comprehensive tyre model, whose validity has been demonstrated in [190]. Using the intermittent eigenvalue extraction in LS-DYNA [107], the natural modes and frequencies of the simplified tyre model are obtained at three different instants: (i) inflated tyre, representing modal properties of the unloaded tyre in the

static condition; (ii) inflated and loaded, representing modal properties of the deflected tyre in contact with the road; and (iii) inflated, loaded and rolling, representing modal properties of the rolling tyre operating at a given speed. The method of extracting eigenvalues and modal vectors corresponding to the three instants has been described in [190]. In this method, an explicit dynamic simulation is initially performed to realize the stress state throughout the tyre at instants when the modal characteristics are desired. The eigenvalues are subsequently extracted at the desired instants, while the nonlinear large-deformation finite element formulation is applied to include the contribution of the stress state in the eigenvalue analyses. The method permits consideration of the influences of the tyre internal pressure, ground contact, normal load and rotational speed on the tyre modal properties. In these analyses, the tyre inflation pressure, normal load and speed are chosen as 758 kPa, 26.7 kN and 50 km/h, respectively.

The reduced model revealed natural frequencies and mode shapes comparable to those of the comprehensive tyre model [190]. Similar to the comprehensive model, the simplified model presented a number of in-plane and out-of-plane modes of vibration. Figures 4.8 and 4.9 present comparisons of the natural frequencies corresponding to the in-plane and out-of-plane modes, respectively, of the reduced and comprehensive models for the inflated, deflected and rolling states, together with the mode shapes of the deflected tyre. The in-plane modes, shown in Figure 4.8, include: (a) the hopping motion along vertical direction (denoted as Hop); (b) rotational oscillations about wheel axle (Rotate Y); (c) an oval form resulting from extensions in opposite directions along a central axis in the wheel plane and compressions along the perpendicular axis (In-Plane Oval); (d) a reuleaux triangle-like deflection shape (In-Plane Triangle); and (e) a corner-rounded quadric shape (In-Plane Quadric). The out-of-plane modes, presented in Figure 4.9, include: (f) the translational motion along the transverse direction (Translate Y); (g) rotational oscillations about the vertical axis (Rotate Z); (h) a twisting vibrational motion, where the two opposite halves of the tyre move outwards from the tyre plane and the other two opposite halves displaced backwards out of the tyre plane (Out-of-Plane Oval); (i) twisting oscillations along the toroidal centerline (Out-of-Plane Triangle); and (j) an out-of-plane corner-rounded quadric shape (Out-of-Plane Quadric).

Simplified tyre model		*Comprehensive tyre model [190]*	
(a) Hop Inflated: — Deflected: 17.76 Rolling: 17.70	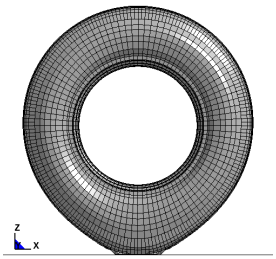	— 17.85 Hz 15.83 Hz	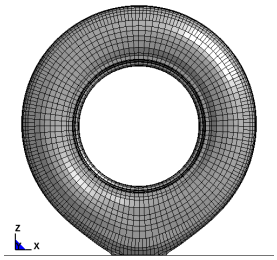
(b) Rotate Y Inflated: 48.46 Deflected: 49.79 Rolling: 32.15	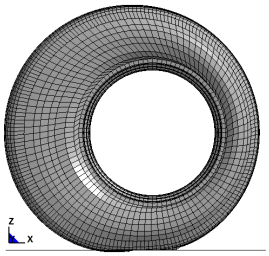	43.83 Hz 49.47 Hz 26.35 Hz	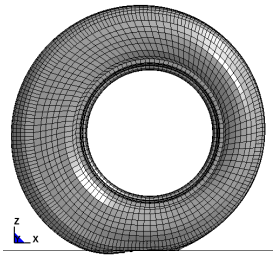
(c) Oval Inflated: 64.55 Deflected: 77.70 Rolling: 77.36	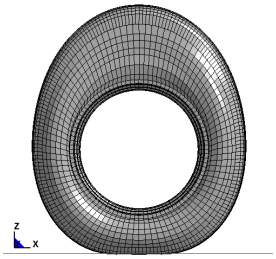	72.15 Hz 76.97 Hz 76.79 Hz	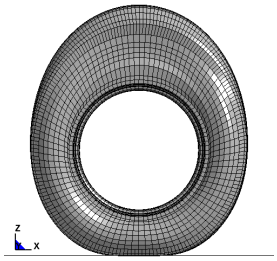
(d) Triangle Inflated: 88.91 Deflected: 101.71 Rolling: 101.60	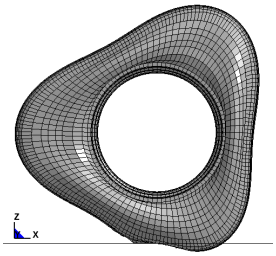	91.69 Hz 102.25 Hz 99.09 Hz	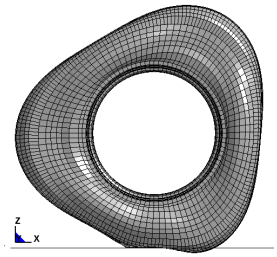
(e) Quadric Inflated: 109.57 Deflected: 123.71 Rolling: 123.28	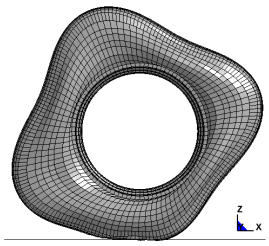	112.65 Hz 122.26 Hz 110.27 Hz	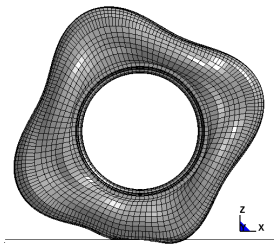

Figure 4.8: Comparisons of in-plane mode shapes of the simplified and comprehensive [190] tyre models corresponding to the inflated, deflected and rolling states

Simplified tyre model		*Comprehensive tyre model [190]*	
(f) Translate Y Inflated: 38.82 Deflected: 42.86 Rolling: 42.58	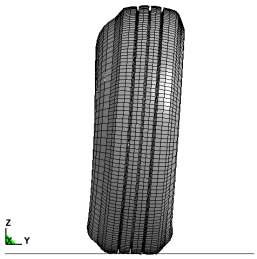	42.39 Hz 45.21 Hz 44.93 Hz	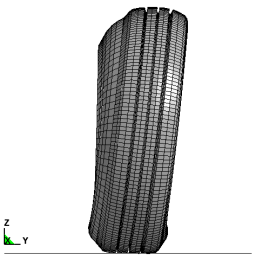
(g) Rotate Z Inflated: 48.91 Deflected: 50.05 Rolling: 49.85	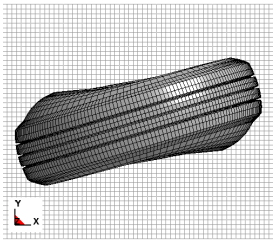	49.50 Hz 50.84 Hz 49.88 Hz	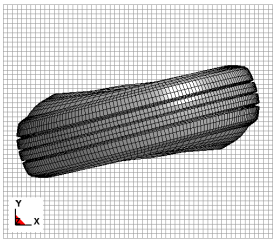
(h) Oval Inflated: 80.94 Deflected: 82.19 Rolling: 82.07	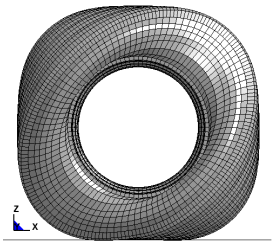	75.75 Hz 78.03 Hz 75.94 Hz	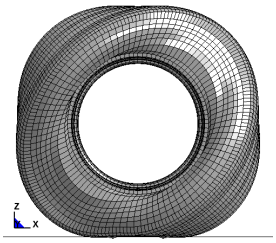
(i) Triangle Inflated: 118.72 Deflected: 119.80 Rolling: 119.52	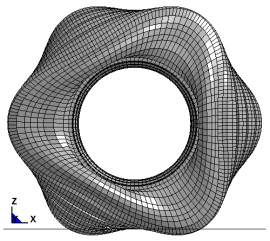	110.29 Hz 112.20 Hz 103.93 Hz	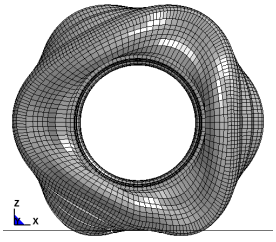
(j) Quadric Inflated: 137.27 Deflected: 138.53 Rolling: 138.12	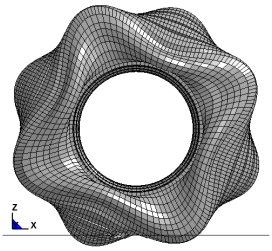	135.90 Hz 138.01 Hz 137.51 Hz	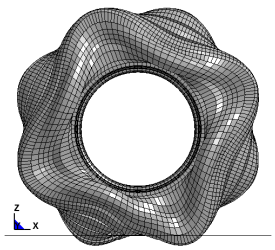

Figure 4.9: Comparisons of out-of-plane mode shapes of the simplified and comprehensive [190] tyre models corresponding to the inflated, deflected and rolling states

Both the simplified and comprehensive tyre models resulted in slightly higher natural frequencies corresponding to the deflected state when compared to those of the inflated state. This tendency has also been reported in a few studies [120, 122, 123], and is attributed to an increase in the tyre stiffness due to additional stresses arising form ground contact along with application of the normal compressive load. Moreover, the natural frequencies in the rolling state decreased to some extent with reference to the deflected state, which is attributed to the fact that the rolling dynamic stiffness of tyres is somewhat lower than the static stiffness, as reported by Ford and Charles [201]. The comprehensive model, however, showed relatively larger decrease in the natural frequency due to rolling compared to the simplified model, particularly in the fundamental vertical model (Hop) and the most relevant mode to the tyre rotation (Rotate Y). This suggested that the comprehensive model, involving substantially higher number of elements, can more accurately describe the decline in tyre stiffness caused by relaxation of stresses in the contact patch in the rolling state.

While the two models resulted in very similar in-plane and out-of-plane deflection shapes, some differences in the natural frequencies were evident. These are attributable to simplifications in the tyre structure considered for the reduced model. Table 4.3 summarizes the percentage differences in the natural frequencies obtained from the simplified tyre model with reference to those predicted by the comprehensive tyre model corresponding to the inflated, deflected and rolling states. The simplified model in the inflated state predicted the natural frequency corresponding to the mode denoted as Rotate Y as 48.46 Hz, which is nearly 13% higher than that extracted from the comprehensive model (43.83 Hz). This is likely due to relatively higher sidewall stiffness caused by the Part-Composite approach compared to the comprehensive model, particularly in the circumferential direction. The stiffer sidewall structure of the simplified model also resulted in relatively higher frequencies for the higher out-of-plane modes, denoted as Oval, Triangle and Quadric, in the inflated state (Table 4.3). The lower frequencies corresponding to the out-of-plane modes, denoted as Translate Y and Rotate Z in the inflated state, however, suggest relatively lower stiffness of the sidewall structure along the radial direction. Moreover, the higher in-plane mode frequencies related to Oval, Triangle and Quadric mode shapes are observed at somewhat

Table 4.3: Percent differences in natural frequencies predicted by the simplified tyre model relative to those obtained from the comprehensive tyre model [109] corresponding to the inflated, deflected and rolling states

In-plane mode	*Inflated*	*Deflected*	*Rolling*
(a) Hop	—	-0.5%	11.8%
(b) Rotate Y	12.9%	0.6%	22.0%
(c) Oval	-10.5%	0.9%	0.7%
(d) Triangle	-3.0%	-0.5%	2.5%
(e) Quadric	-2.7%	1.2%	11.8%
Out-of-plane mode	*Inflated*	*Deflected*	*Rolling*
(f) Translate Y	-8.4%	-5.2%	-5.2%
(g) Rotate Z	-1.2%	-1.6%	-0.1%
(h) Oval	6.9%	5.3%	8.1%
(i) Triangle	7.6%	6.8%	15.0%
(j) Quadric	1.0%	0.4%	0.4%

lower frequencies for the simplified model in comparison to the comprehensive model. This suggests that the simplified model comprises a relatively softer belt structure than the comprehensive model. In the deflected state, the two models demonstrated reasonably good agreements in the in-plane and out-of-plane mode frequencies with maximum deviation being 1.2%, and 6.8%, respectively. In the free-rolling state, the two models also show relatively good agreements in the natural frequencies (less than 10% deviation), with the exception of in-plane modes Hop, Rotate Y and Quadric, and out-of-plane Triangle mode. The relatively greater differences in these mode frequencies are likely due to deficiency of the simplified model for relief of stresses in the elements so as to adequately represent relaxation of a rolling tyre.

4.3.5 Computational performance

The simplified tyre model was developed to achieve greater computational efficiency while preserving the model accuracy compared to the comprehensive tyre model [109]. The computational efficiency of the model is assessed in terms of the CPU time required by the two models considering identical simulation scenarios. A 0.2 s real time load-deflection

simulation as well as a 1.0 s cornering force test were considered to be executed using a 3.2 GHz Intel Xenon processor with 8 cores and 14 GB memory. A mesh of 96 sectors with 192 divisions for the outer regions was used for both models, which resulted in 24192 and 8832 elements for the comprehensive and simplified models, respectively. Table 4.4 compares the process times required by the simplified and comprehensive models for different computing tasks involving the carcass/belt, tread/bead fillers, and other processes. The comparisons show that the simplified model can yield nearly 85% reduction in the CPU time required for processing the carcass and belt elements compared to the comprehensive model. This substantial reduction in the CPU time is attributed to the Part-Composite approach, which results in substantially lower number of elements associated with the carcass and belt structures compared to the comprehensive model.

The simplified model, however, yields identical CPU times for the elements forming the tread and bead fillers compared to the comprehensive model. This is due to the fact that the tread and bead fillers in the reduced model are formulated using the same approach as in the comprehensive model. The two models thus comprise identical number of elements for the tread and bead fillers. The reported times for other processes such as initialization, contact algorithm, rigid body motion and database also show CPU time reductions in the

Table 4.4: Comparisons of total and individual process times required by the simplified and comprehensive [109] tyre models

	Load-deflection test (0.2 s)		
Process time (hours)	*Comprehensive*	*Simplified*	*Reduction (%)*
Carcass and belt	2.31	0.35	85.05%
Tread and bead fillers	0.03	0.03	0.000%
Other processes	1.63	0.48	70.48%
Total	3.97	0.83	79.14%
	Cornering force test (1.0 s)		
Process time (hours)	*Comprehensive*	*Simplified*	*Reduction (%)*
Carcass and belt	10.81	1.54	85.75%
Tread and bead fillers	0.15	0.15	0.000%
Other processes	5.94	1.25	78.90%
Total	16.75	2.79	83.32%

order of 70% for the load-deflection simulations and 79% for the cornering force tests, which is again attributed to the reduced number of elements in the simplified model. The table also compares the total computing times for both the models for 0.2 s load-deflection and 1.0 s cornering force test simulations. For the load-deflection simulations, the total computing time for the comprehensive model is nearly 4 hours, which reduces to about 50 minutes for the simplified model, resulting in nearly 79% reduction. In the case of cornering force test, the total computing time for the comprehensive model of about 16.75 hours reduces to about 2.79 hours for the simplified model, resulting in about 83% reduction.

4.4 Conclusions

A computationally efficient simplified model of a rolling truck tyre was implemented and verified in terms of its effectiveness in predicting vertical force-deflection, cornering force/moment and modal characteristics through comparisons with the reported experimental data as well as those obtained from a comprehensive tyre model. The Part-Composite approach used for formulating the simplified model resulted in nearly 80% reduction in the number of elements used for describing the carcass and belt structures, which shortened the required computing time by 79.14% for a load-deflection simulation and by 83.3% for a cornering force test. The load-deflection results obtained from the simplified tyre model were in very good agreement with the experimental data and those predicted by the comprehensive tyre model, which verifies the static vertical behavior of the simplified model. The simplified model also demonstrated good correlations with the comprehensive model in both the lateral force and the aligning moment characteristics. Both, the simplified and comprehensive tyre models, however, showed some deviations with respect to the measured cornering properties of the tyre. The deviation was particularly higher in the aligning moment. The modal characteristics of the simplified tyre model, including the in-plane and out-of-plane deflection modes, were also in good agreements with those obtained from the comprehensive tyre model. Generally good agreements were obtained in the natural frequencies corresponding to the three states of tyre considered, namely, inflated, deflected under a vertical load and in contact with the road, and deflected

and rolling at a speed of 50 km/h. Similar to the comprehensive model, the natural frequencies of the simplified model subjected to deflection increased slightly compared to the inflated state, and somewhat decreased under free-rolling. From the results, it is concluded that proposed simplified model formulated using the Part-Composite approach could yield accurate predictions of static and dynamic properties in substantially efficient manner compared to a comprehensive structural tyre model. The proposed computationally efficient model could thus serve as an effective virtual tyre simulation platform for identifications of parameters of phenomenon-based tyre models.

Chapter 5

A Virtual Test Platform for Analyses of Rolling Tyre-Soil Interactions: Part I – Parametrization of Terramechanics Models

5.1 Introduction

Dynamic properties of ground vehicles strongly rely on the tyre-terrain interaction forces and moments applied to the vehicle body. Considerable efforts are thus continuing to develop reliable models of tyre-terrain interactions for vehicle dynamics simulations and tyre design. The analysis of tyre-terrain interactions is known to be challenging, especially for off-road vehicle applications involving deformable terrains. A number of terramechanics-based models have been developed for estimating the forces and moments generated at the tyre-terrain interface, which are generally derived from integration of the normal and shear stresses developed over the contact area [19, 20, 141]. The stresses are often represented in terms of the normal and shear deformations considering terrain material properties, which are generally determined through measurements such as cone index, a measure of soil supporting stress [141, 143, 144]. The *cone index*, however, has been judged to be insufficient, particularly for non-cohesive soils such as sands, since it does not account for individual contributions of the compressive and shear resistances of the soil [145]. Bekker

[18] formulated the pressure-sinkage and the shear stress-shear displacement characteristics of soils in conjunction with the Mohr-Coulomb failure criterion. The normal and shear properties of soils have been widely characterized through plate-sinkage and shear ring tests using *bevameter* techniques [18]. The shear strength of soil and its dependence on confining pressure have also been experimentally characterized using *shear-box* and *triaxial* tests [141].

A number of analytical formulations have evolved to estimate tyre-soil contact forces and soil stresses. Wong and Reece [19, 20] developed theoretical formulations for estimating the radial and tangential stress distributions beneath a rolling tyre using the Bekker and Mohr-Coulomb theories [18, 141], which could yield estimates of tyre-soil contact forces and moments. Such terramechanics-based models have served the essential basis for developing tyre-terrain interaction models for applications in multi-body system simulations of off-road vehicles [31, 111, 150, 153, 154] as well as planetary exploration rovers [21–23] on soft soils. The reliability of such models, however, strongly relies on the accuracy of normal and shear properties of the specific soils under study, which are generally obtained from the measured soil properties using regression-based methods [151, 155–158].

The theoretical terramechanics-based models could yield reasonably accurate estimations of tyre-soil contact forces and moments in different maneuvers of off-road vehicles including ride [159], traction/braking [153] and cornering [111, 150]. These theoretical models, however, are not suited for determinations of deformed shape, stress distributions and soil flows under a rolling pneumatic tyre. A number of computational models based on *Finite Element (FE)* methods have evolved for accurate modeling of both the pneumatic tyre and soft soil considering structural details and material properties. Such models have been reported for analyses of soil compaction and tyre footprint [29, 30, 162], stress distributions and soil flows [24, 27, 28, 163], and tyre mobility and motion resistance [160, 161] of off-road tyres. The computational tyre-soil interaction models, however, generally consider the soil as an *elastic-plastic* material, described via a bi-linear stress-strain curve with constant yield stress based on the traditional plasticity theory [24–26, 28, 29]. The material properties such as Young's modulus, tangent modulus and yield stress are often extracted from available reported data and adjusted to match the experimental data in terms of

pressure-sinkage behavior [24, 166]. The traditional plasticity theory, however, does not accurately account for stresses attributed to soil compaction [25, 167]. Linear pressure-volumetric deformation relation have been employed to account for the soil compressibility [25, 26]. These have provided reasonably good estimations of normal stress distributions and resulting forces underneath a tyre. The linear pressure-volume relationship, however, does not accurately describe material compressibility as well as shear behavior of soils [24–26]. Moreover, the relation cannot account for progressively increasing strength of soils with compaction.

Alternatively, a number of studies described the soil using a pressure-dependent strength constitutive model such as the *soil and foam* material model family in LS-DYNA [38, 43, 45, 100, 168, 169] and the *Drucker-Prager* material model in ABAQUS [27, 150, 170–174]. The soil and foam material model (type 5 in LS-DYNA) [104, 105] has been widely used for simulations of tyre-soil interactions [38, 100], soil penetration tests [43, 45, 176], earth landing [169, 177], and road-side safety [178]. This material model separately accounts for compressibility and shear strength characteristics of soil, while the input material parameters are provided through geotechnical laboratory test data obtained from the triaxial apparatus [175]. The compressibility is defined through pressure-volumetric strain curves during loading and unloading, while the shear strength is described via a yield surface, which defines the second invariant of deviatoric stress tensor as a quadratic function of hydrostatic pressure with coefficients identified from the *triaxial compression* test data [105, 168].

Slade [24] and Lescoe [25] developed tyre-soil models using Pam-Crash finite element platform to predict contact force/moment properties of truck tyres on soft soils. These and many other studies have shown that the FE method could not adequately model the penetration of an object such as a tyre or a plate into soil due to the mesh-based nature of the method [24, 27, 29, 100, 173, 179]. Furthermore, penetrating object is not only resisted by the compacted soil but also by the tension caused by the elongated elements that cannot be separated from adjacent elements within the deformed soil domain, which may yield inaccurate estimations of contact forces [38, 43].

Alternatively, a few studies have employed mesh-less *Smoothed Particle Hydrodynamics (SPH)* [25, 26, 180] and *Discrete Element (DE)* [181–184] methods for modeling tyre-soil interactions. Lescoe [25] and Dhillon [26] applied the SPH method to develop a soil model in the Pam-Crash platform for conducting plate-sinkage and shear-box test simulations using an elastic-plastic-hydrodynamic material type in conjunction with a linear pressure-volume equation of state. These have shown that the mesh-less nature of the SPH method can describe the soil deformations more accurately compared to the FE method, particularly under large deformations and soil fragmentations, as encountered in the shear-box test. A SPH soil model, however, imposes substantially higher computational demands compared to a similar FE model [25, 26].

The computational soil models can yield reasonably accurate predictions of soil deformations, stress distributions and reaction forces. Their applications for analyses of vehicle-terrain interactions, however, are limited due to excessive computational demands. Alternatively, the computationally efficient terramechanics-based tyre-soil models may be used for vehicle-terrain analyses. The reliability of such models strongly depends on the accuracy of their parameters, which are identified through costly measurements.

In this study, a computational soil model is developed to be employed as a virtual test laboratory to perform a set of soil test simulations for identifications of parameters of the terramechanics-based tyre-soil interaction models. The validity of the virtual simulation model is illustrated using the pressure-sinkage and shear-box tests for characterizations of the normal and shear properties of different selected soils. The computational soil models are formulated using FE and SPH techniques in the LS-DYNA platform, considering a pressure-dependent strength constitutive model with input parameters derived from the reported triaxial tests. The material model parameters are identified using the available measured data. The validity of the material model is subsequently assessed by comparing computed soil properties with reported test data. The relative merits and limitations of the FE and SPH soil models are discussed through comparisons of the model results under pressure-sinkage tests. The models are used to simulate pressure-sinkage and shear-box

tests to determine the compressive strength and shear stress-shear displacement characteristics. These are subsequently applied for parameterization of the phenomenological terramechanics soil models for analyses of tyre-soil interactions considering stationary, driven, towed and steered tyres. The latter part involving applications of the terramechanics models is presented in the second part of the study.

5.2 Soil Model

5.2.1 Soil constitutive model and material parameters

Strength of a soil strongly depends on its confining pressure, particularly for a soil with low cohesion. A pressure dependent material model is thus vital for accurate characterization of soil constitutive behavior. Material model type 5 (MAT_SOIL_AND_FOAM), available in the LS-DYNA material library [104], is used for describing different types of soils in this study. Among the several soil constitutive models available in LS-DYNA, this model is the most basic pressure dependent strength model requiring simple input parameters, which can be readily identified from the reported laboratory test data [43, 45, 146, 169]. The loading and unloading behaviors of the soils, however, differ due to plastic deformations. In this model, the shear deformations of the soil during initial loading are described by the elastic shear modulus, G, while the soil relaxation during unloading can be adequately described by the bulk modulus, K_u. The compressibility of the soil is represented through a pressure-volumetric deformation relation. The strength of soil is described by a shear failure surface by defining the second invariant of the stress deviator as a function of the pressure [168].

The constitutive model is formulated for four types of soils for which geotechnical laboratory test data are accessible [146, 220]. These include: a high density clayey sand, also referred to as *unwashed sand*, and three distinct coastal sand conditions, namely, *low density dry sand*, *high density wet sand* and *high density flooded sand*, all containing common material constituents and grain size distribution. The input parameters for the constitutive model are determined from the *triaxial* tests involving compressibility, unloading and yield

surface characteristics of the soils.

The *uniaxial strain* test is used to characterize the compressibility (volumetric deformation behavior) of the soil. The volumetric strain, ϵ_v, is defined as the ratio of change in volume of the soil specimen, ΔV, to its initial volume, $V_\circ$. For the material type 5 in LS-DYNA [104], this strain is defined in terms of logarithmic volume strain, $\epsilon_{\log}$, also known as *natural strain*. The $\epsilon_{\log}$ is defined by natural logarithm of the relative volume, ratio of final volume V to the initial volume $V_\circ$, and is negative under compression. The natural strain $\epsilon_{\log}$ can be related to the volumetric strain ϵ_v, such that [105]:

$$\epsilon_{\log} = \log \frac{V}{V_\circ} = \log \frac{V_\circ - \Delta V}{V_\circ} = \log (1 - \epsilon_v) \tag{5.1}$$

Figure 5.1 shows the pressure-logarithmic volume strain curve obtained using the uniaxial strain test data for the selected soils [146]. The reported data were idealized by a set of 10 discrete input data points for the LS-DYNA material model. Other elastic properties such as the Young's modulus, E, Poisson's ratio, ν, and shear modulus, G, are also determined from the uniaxial strain test data and summarized in Table 5.1.

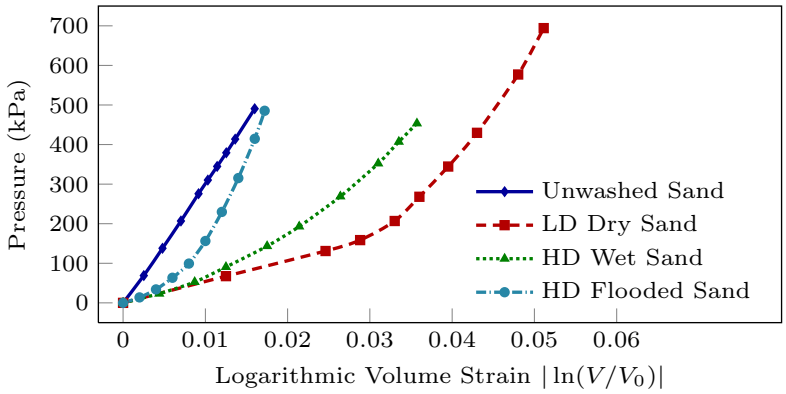

Figure 5.1: Pressure-logarithmic volume strain curves obtained from uniaxial strain tests of selected soils [146] (LD: Low Density; HD: High Density)

The unloading bulk modulus is determined from data acquired from the *hydrostatic compression* tests involving axial as well as radial deformations of the soil. The unloading bulk modulus, K_u, is estimated from the slope of the pressure-volumetric strain curve during unloading, which is also presented in Table 5.1 for selected soils.

Table 5.1: Material parameters for selected soils derived from the geotechnical laboratory test data reported in [146]

Material parameter	*Unwashed sand*	*Low density dry sand*	*High density wet sand*	*High density flooded sand*
Moisture content (%)	12	2	16	30
Mass density ($\rho, \mathrm{kg/m^3}$)	2094.63	1282.43	1603.03	1442.73
Young's modulus (E, MPa)	54.94	7.68	12.49	8.41
Poisson's ratio (ν)	0.193	0.298	0.279	0.286
Shear modulus (G, MPa)	23.03	1.39	3.25	3.62
Bulk unloading ($\mathrm{K_u}$, MPa)	133.55	224.01	110.87	131.52
Coefficient $\mathrm{a_\circ (kPa)^2}$	300.72	0	65.17	6.68
Coefficient $\mathrm{a_1}$(kPa)	25.56	0	12.89	3.72
Coefficient $\mathrm{a_2}$	0.5432	0.5042	0.6368	0.518

The identification of shear strength of soil in the material model involves the derivation of a yield surface by expressing the second invariant of the stress deviator, J_2', as a quadratic function of pressure, p, such that [168]:

$$J_2' = a_\circ + a_1 p + a_2 p^2 \tag{5.2}$$

where p is the average of principal stresses, known as *mean stress*, being positive in compression. The *triaxial compression* test data is used to determine the yield surface parameters, $a_\circ$, a_1 and a_2. In this test, the soil specimen is initially loaded to a desired confining pressure σ_c, and a compressive axial strain is applied, while the confining pressure is held constant, which results in an axial stress σ_a. The increment of axial stress above the confining pressure, $\sigma_a - \sigma_c$, known as *stress difference* (σ_Δ), is then measured. Considering the principal stresses $(\sigma_a, \sigma_c, \sigma_c)$ along the axial and transverse directions, and p as the mean stress, the deviatoric stress tensor, s_{ij} $(i, j = 1, 2, 3)$, is defined as [146]:

$$s_{ij} = \begin{bmatrix} \sigma_a - p & 0 & 0 \\ 0 & \sigma_c - p & 0 \\ 0 & 0 & \sigma_c - p \end{bmatrix} \quad ; \quad p = \frac{1}{3}(\sigma_a + \sigma_c + \sigma_c) \tag{5.3}$$

The second invariant of the stress deviator, J_2', is subsequently obtained in terms of the

stress difference, σ_Δ, such that [146]:

$$J_2' = \frac{1}{2} s_{ij} s_{ij} = \frac{1}{2}\left(s_{11}^2 + s_{22}^2 + s_{33}^2\right) = \frac{\sigma_\Delta^2}{3} \tag{5.4}$$

The tests are repeated for a range of confining pressures and the data are used to define J_2'. The resulting (p, J_2') data are used to construct the strength envelops of a soil by curve fitting using Equation (5.2). Figure 5.2 illustrates the (p, J_2') functions together with the test sample points for selected soils. The yield surface coefficients $a_\circ$, a_1 and a_2 for the selected soils are presented in Table 5.1.

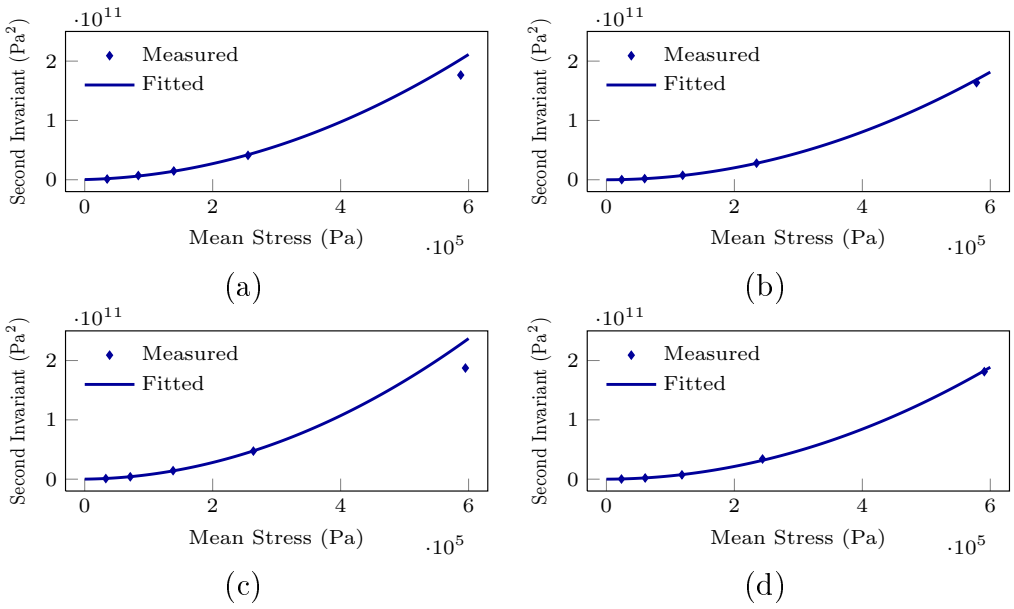

Figure 5.2: Yield surface fit of the triaxial test data reported in [146] for: (a) unwashed sand; (b) low density dry sand; (c) high density wet sand; and (d) high density flooded sand

5.2.2 Simulation scenarios and method of solution

A computational soil model is formulated in the LS-DYNA platform to characterize the soil behavior under normal and shear loads arising from either a plate or a stationary/rolling tyre. The validity of the material model and properties chosen for the selected

soils is initially examined using the reported experimental data. The soil model is subsequently employed as a virtual test environment to perform a set of standard tests for identifications of soil parameters for the terramechanics-based tyre-soil interaction models. The simulations are performed using the *Finite Element (FE)* as well as the *Smoothed Particle Hydrodynamics (SPH)* analysis approaches. The results obtained from the two approaches are compared, and relative merits and limitations of the two methods are discussed. The computational models are subsequently used to determine tyre-soil interface forces and moments, which are described in Part II of this article. A modal analysis is initially conducted for characterizing the fundamental frequency and effective damping property of the soil model employing the constitutive soil material model. The results are used to estimate global damping characteristics required for dampening of the unwarranted oscillations of the soil elements during loadings. The method of analysis is described in the following subsections.

Simulation scenarios

The computational models are formulated to address two different simulation objectives. These include validations of the computational soil models and simulations of typical virtual testing scenarios for parametrization of terramechanics models of the selected soils. Simulation scenarios are briefly described below.

1. **Pressure-volumetric deformation test**: This test is performed on a rectangular soil domain, made of either solid elements or SPH particles. The soil domain is subjected to a range of pressures applied directly to the top surface, while all other boundaries of the soil domain are held considering frictionless contact with the constraining rigid walls. The volumetric strain ratio ($\Delta V/V_\circ$) of the soil domain is evaluated corresponding to each applied pressure and compared with the reported uniaxial strain test data [146] to examine validity of the computational models. The comparisons permitted verifications of the compressibility behaviors of the material models for the selected soils.
2. **Pressure-sinkage test**: In this test, a rectangular soil domain is subjected to a

range of sinkages applied by a rigid circular plate, as in case of the bevameter machine [141]. Taking advantage of the symmetry, only a quarter of the soil box and the plate is meshed in both the FE and SPH models, as illustrated in Figures 5.3(a) and 5.3(b). The top surface of the soil is unconstrained and the two sides of symmetry are defined as symmetric planes. The remaining three sides are in contact with rigid walls representing the adjacent soil. The penetration is applied in a ramp manner and the resulting pressure developed in the soil is determined. The simulation results yield pressure-sinkage relations for selected soils, which are used to identify the terramechanics model parameters using the Bekker's pressure-sinkage relation through curve fitting.

3. **Shear-box test**: A rectangular block of soil, made of SPH particles, is confined within a shear-box, as illustrated in Figure 5.4(a). This test was not attempted with the FE model. The shear-box designed in this study comprises three parts: the top plate and upper and bottom halves, as described in [141]. The test is performed in two stages. A desired pressure is initially applied via the top plate, which is allowed to move only in the vertical direction. While the upper half of the box is fixed, the pressurized soil is subsequently subjected to a shear displacement via horizontal motion of the bottom half, as illustrated in Figure 5.4(b). Due to symmetry of the model in the x-z plane, only one-half of the box is considered for simulations. The shear stress corresponding to the applied shear displacement is computed from the shear force developed at the interface of the two halves and the cross-sectional area of the box in the x-y plane. The resulting shear stress-shear displacement characteristics corresponding to different confining pressures are used for parametrization of the terramechanics model using Bekker's shear stress-shear displacement relation through curve fitting.

Soil domain and analysis methods

The pressure-sinkage test simulations are performed considering one-quarter of the soil domain ($600 \times 600 \times 600\ mm$) using both methods: Finite Element (FE) and Smoothed Particle Hydrodynamics (SPH). Figure 5.3(a) illustrates the FE soil model, which is meshed

with 20700 ($30 \times 30 \times 23$) solid elements. The elements are distributed uniformly until half of the depth, while the size of elements over the remaining depth is increased along the z-axis in an increasing rate in order to enhance computational efficiency. Figure 5.3(a) illustrates the SPH soil model made of 27000 ($30 \times 30 \times 30$) uniformly distributed particles. The plate-sinkage test in both the models is conducted by applying a 100 mm vertical displacement via a 150 mm radius circular rigid plate.

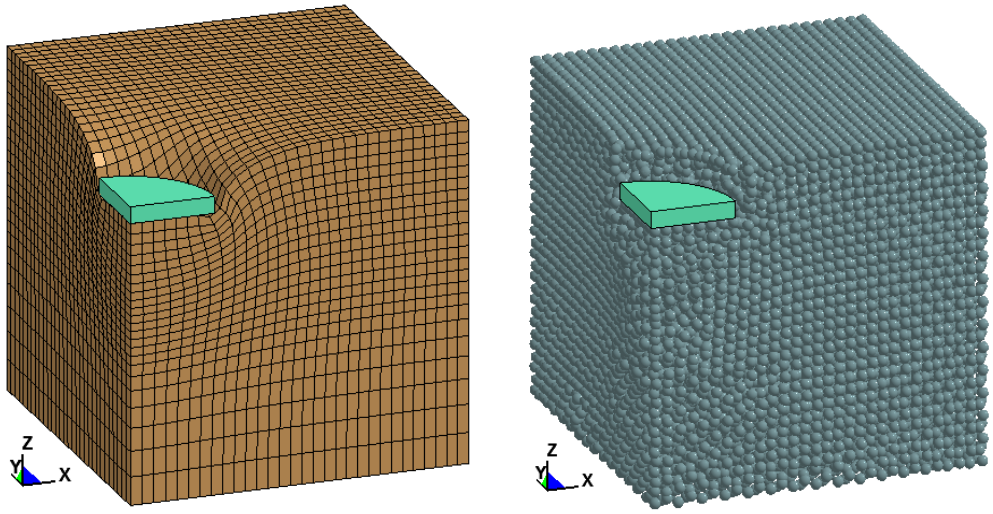

(a) (b)

Figure 5.3: (a) FE, and (b) SPH soil models (quarter) under 100 mm plate sinkage for the unwashed sand

The shear-box test simulations are performed considering only one-half of the box due to symmetry in the x-z plane. The ($400 \times 200 \times 240$ mm) soil block is represented by 19200 ($40 \times 20 \times 24$) SPH particles, as shown in Figure 5.4(a). The shear-box is made of solid elements of rigid materials. The soil block is confined by the top and bottom plates, side walls, and front/rear face walls of the shear-box. The side and front/rear face walls comprise two halves, where the upper half is fixed and the bottom half is permitted to move with the bottom plate along the x-axis. The pressure is applied via direct loading of the top plate, while the shear displacement is imposed by moving the bottom half along the x-axis, as illustrated in Figure 5.4(b).

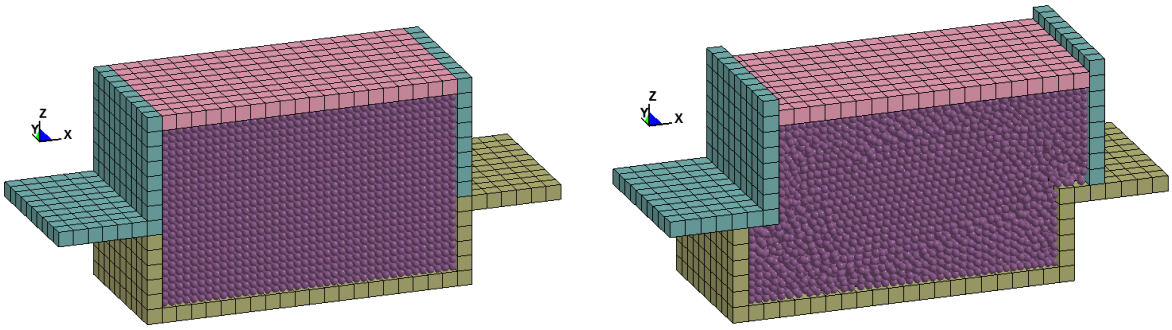

(a) (b)

Figure 5.4: Illustration of the shear-box test of the high density wet sand: (a) before, and (b) after applying 700 kPa pressure and 40 mm shear displacement

Element formulations

In the FE soil model, the one-point integration solid element formulation is used in conjunction with one of the stiffness forms (type 5) of the hourglass energy control options. During the FE soil model simulations, the hourglass energy was constantly monitored and it was not permitted to exceed 10% of the internal energy. For the soil particles in the SPH model, the particle approximation theory [105] is applied, while selecting the *cubic B-spline kernel* as the smoothing function. In the SPH formulation, the field variables at a point are approximated by *weighted averaging* (smoothing) of field variables of particles in a neighboring distance specified by the so-called *smoothing length*. The role of the kernel function is to provide weighting to the influence of neighboring particles depending on their distances. The smoothing length for each particle, $h(t)$, is adapted automatically by the SPH processor at each time step according to the soil flow so as to keep the same number of particles in the neighborhood. The user-defined scale factors CSLH, HMIN and HMAX are adjusted as 1.2, 0.2 and 2, respectively, to limit the range of the smoothing length, such that [107]:

$$\text{HMIN} \times h_\circ < \text{CSLH}\ h(t) < \text{HMAX} \times h_\circ \tag{5.5}$$

where $h_\circ$ is the initial smoothing length, defined as maxima of minimum distances between the particles at the beginning of the simulation. CSLH is a constant applied to the smoothing

length of the particles, and HMIN and HMAX are scale factors describing the minimum and maximum smoothing lengths. For further details on the SPH formulations and solution control settings, we refer to Chapter 20 of the LS-DYNA theory manual [105].

Contact models and parameters

The *automatic surface to surface contact* algorithm in LS-DYNA [105, 107] is used to model the contact between rigid plate/tyre and the elements of the soil. The static and dynamic coefficients of friction are assumed as 0.55 and 0.5, respectively, to mimic an earth road surface [142]. In order to maintain a smooth and stable contact in the soil model simulations, the *pinball segment base contact* algorithm (SOFT=2) is used. The contact viscous damping ratio of 10% is applied perpendicular to the contacting surfaces to avoid undesirable oscillations in the solutions. The contact between the SPH particles of soil and the elements of rigid plate (tyre), however, is modeled using the *automatic nodes to surface contact* algorithm in conjunction with the *soft constraint formulation* (SOFT=1). The SPH particles are defined as the *slave* part, while the elements of the rigid plate (tyre) are defined as the *master* part. Every particle in the SPH model represents a small sphere-shaped piece of soil with radius equal to half the distance between two consecutive particles. Since (by default) the center of the sphere is considered as the slave node in the contact algorithm, an offset thickness is used via the variable SST (slave surface thickness) to incorporate the radius of the sphere in the contact calculations.

Damping properties

A global damping is defined for the soil elements so as to limit undesirable oscillations in the solutions and to maintain more stable simulations. Considering a desired damping ratio ζ_s, the mass-weighted damping coefficient α_s is defined in terms of the fundamental frequency f_n, such that:

$$\alpha_s = 4\pi\zeta_s f_n \tag{5.6}$$

The fundamental frequencies of the selected soils are initially estimated from eigen analyses of the FE model considering material properties presented in Table 5.1. For this purpose,

the ($1200 \times 1200 \times 600$ mm) soil block is meshed using 108000 ($60 \times 60 \times 30$) uniformly distributed cubic elements of 20 mm side. The top side of the soil box is unconstrained, while all other boundaries are in contact with rigid walls representing adjacent soils. The fundamental frequencies of the soil models are summarized in Table 5.2. The mass-weighted damping coefficients of the soil models were subsequently estimated using Equation (5.6) assuming 5% global damping ratio, which are also summarized in Table 5.2. The chosen damping ratio revealed negligible oscillations in the deformation responses. The subsequent simulations were thus performed using 5% global damping ratio.

Table 5.2: Fundamental frequencies and mass-weighted damping coefficients of the soil models assuming 5% global damping ratio

Soil model parameter	*Unwashed sand*	*Low density dry sand*	*High density wet sand*	*High density flooded sand*
Fundamental frequency (Hz)	61.76	19.36	26.54	29.51
Mass-weighted damping (Hz)	38.81	12.17	16.68	18.54

Convergence study

A convergence test was conducted in order to exclude the effects of the element size and the soil box height on the resulting pressure developed beneath the plate in response to 60 mm sinkage. The sensitivity of the response was investigated considering four element sizes (100, 40, 20 and 10 mm) and four different domain heights (0.4, 0.5, 0.6 and 0.8 m). As an example, Figures 5.5(a) and 5.5(b) illustrate variations in the pressure obtained from the FE and SPH models of the high density wet sand considering variations in the number of elements per unit length and the height of the soil grid, respectively. The results suggest satisfactory convergence of both the methods for element sizes less than 20 mm (50 elements per unit length) and soil depth above 0.6 m. Similar trend were also observed for the other soil models. As a result, the grid with the element size of 20 mm and the height of 0.6 m was selected for both the FE and SPH parametrization tests. Lescoe [25] and Dhillon [26] also conducted such grid convergence tests and proposed a mesh of 25 mm element size for the FE and SPH soil model simulations.

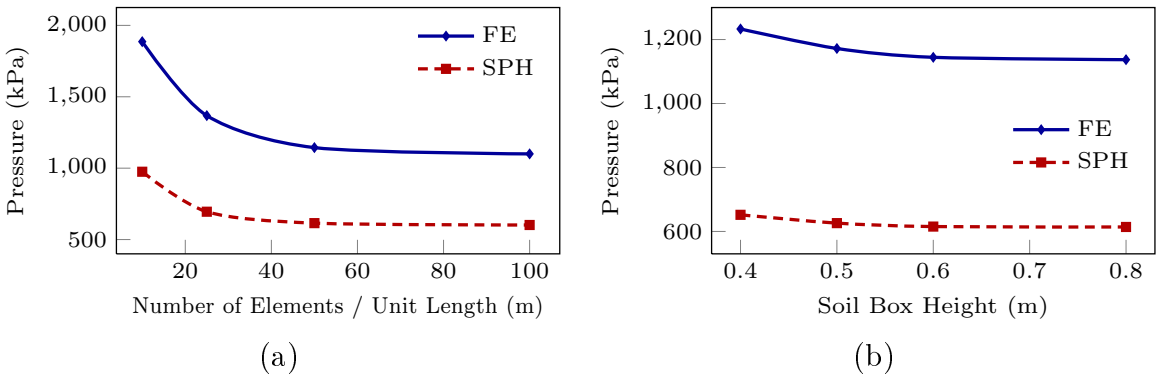

Figure 5.5: Variations in the pressure obtained from the FE and SPH methods for the high density wet sand in response to 60 *mm* plate sinkage as a function of: (a) number of elements per unit length; and (b) soil box height

5.3 Results and discussions

5.3.1 Model verification: Pressure-volumetric deformation test

The pressure-volumetric deformation characteristics of the selected soils are evaluated via the volumetric deformation test simulations. In these simulations, 600 *mm* of the soil, meshed with 20 *mm* cubic elements, is subjected to a range of pressures (up to 1000 kPa)

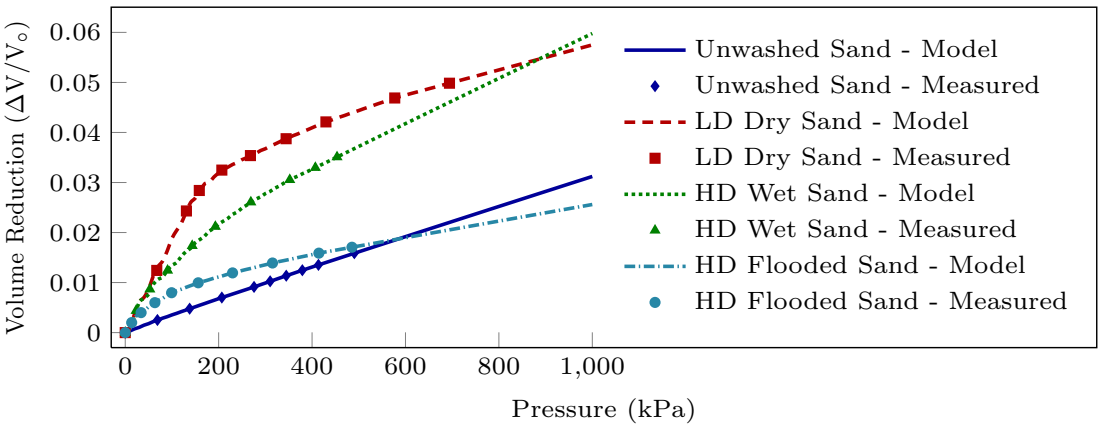

Figure 5.6: Comparisons of volume reduction-pressure characteristics predicted from the computational models with the reported measured data for selected soils [146] (LD: Low Density; HD: High Density)

applied to the top surface, while all the other boundaries of the soil are held in frictionless contact with rigid walls. The volume reduction ratios $\Delta V/V_\circ$ of each soil are obtained as a function of the applied pressure, as shown in Figure 5.6. In the figure, the simulation results are compared with reported measured data [146]. For the purpose of comparisons with the measured data, the hydrostatic state was maintained during simulations by letting $a_\circ = a_1 = a_2 = 0$ in Equation (5.2). This permitted to exclude the influence of soil shear strength in the simulations. The comparisons show very good correlations between the predicted volume reductions (continuous lines) with the reported measured data (symbols) obtained from the uniaxial strain tests over a range of applied pressures. The material constitutive model is thus considered valid for predicting the volume reduction characteristics of selected soils under pressure loading.

5.3.2 Comparisons of the FE and SPH soil models

Figures 5.3(a) and 5.3(b) show deformed shapes of the FE and SPH soil models for the unwashed sand, which suggest considerable differences between the two analysis methods. In the FE model, the rigid plate cannot truly penetrate into the soil due to constraints imposed by common shared nodes of the adjacent solid elements. The entire block of soil thus behaves like a sponge, which cannot be considered to represent the actual soil behavior in response to the plate sinkage. In the SPH model, the rigid plate sinks into the soil by shearing the coupling between the affected soil particles. Moreover, in the FE model, the affected elements couple only with immediate neighboring elements, and must constantly comply with the mesh pattern while displacing. On the other hand, the deformations of SPH particles are not constrained by any pattern, and the particles coupling occurs over wider regions compared to the finite elements. This feature of SPH permits the soil particles to envelop the plate (or any penetrating object) as it sinks into the soil. This tendency represents actual soil sinkage more closely. The SPH method, however, is computationally more demanding compared to the FE method. For a 10 s real-time pressure-sinkage simulation, the computation time for the SPH model was nearly 4.4 times that of the FE model.

The pressure distributions obtained from the FE and SPH models of the unwashed

sand under a 60 mm plate sinkage are shown in Figures 5.7(a) and 5.7(b). The comparisons show that the FE model overestimates the pressures and thus the contact forces compared to the SPH model. The observed differences are attributed to differences between the two analysis methods. In the SPH soil model, the contact force is produced by compacted soil particles underneath the plate in response to the penetration loading. In the FE soil model, the tensile resistance of the stretched elements located near the edges of the plate yield additional force apart from that caused by the compressed elements. This additional force does not occur in the SPH model since the motion of particles is not constrained by the meshing as in the FE model.

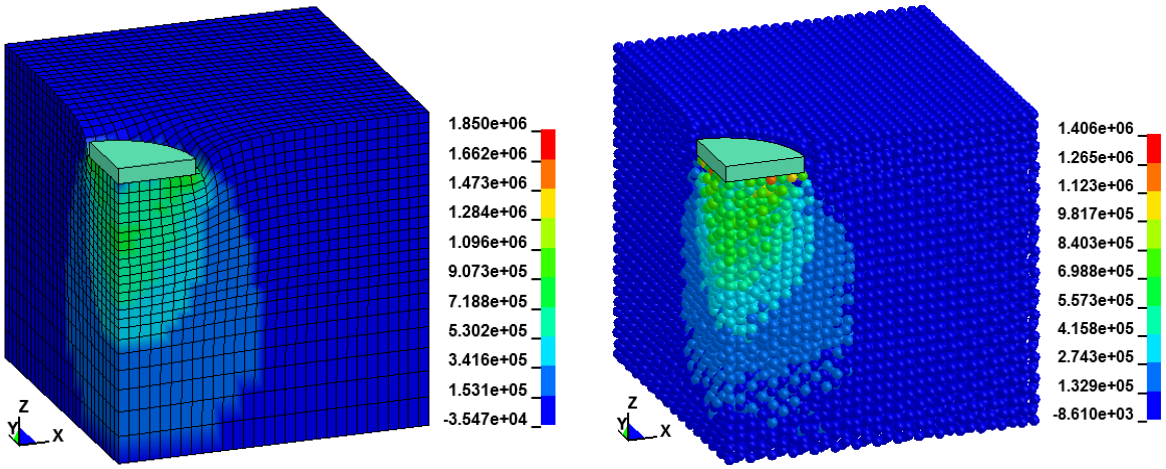

(a) (b)

Figure 5.7: Pressure distributions obtained from (a) FE and (b) SPH soil models (quarter) under 60 mm plate sinkage for the unwashed sand

Notable differences are evident between the pressure-sinkage characteristics of selected soils obtained from the FE and SPH soil models, as seen in Figure 5.8. The results from the FE model of the unwashed sand exhibits a steep increase in the pressure during the initial 20 mm sinkage and near saturation of pressure under sinkage above 20 mm. This is likely due to failure of this type of sand, leading to only small increase in pressure with further sinkage. The SPH model for this soil, however, exhibits rapid increase in pressure only under initial sinkage up to about 1.5 mm, which is followed by nearly linear increase in pressure. As expected, the FE method overestimates the pressure compared to the SPH

method, as stated above. Similar trends are also evident from the results obtained for other types of soils.

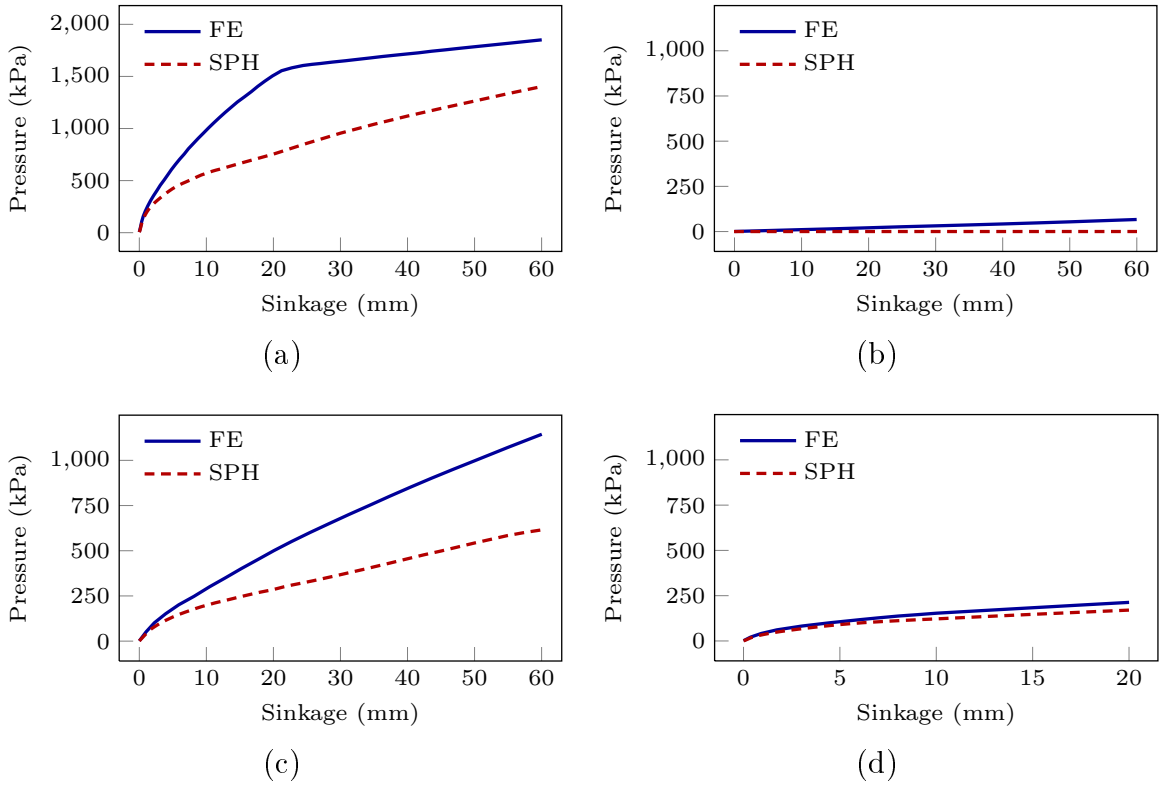

Figure 5.8: Pressure-sinkage properties obtained from the plate-sinkage test simulations with a circular 150 *mm* radius plate using FE and SPH models of different soils: (a) unwashed sand, (b) low density dry sand, (c) high density wet sand, and (d) high density flooded sand

The results obtained from the flooded sand model simulations, however, are somewhat comparable for both methods under sinkages not exceeding 20 *mm*. The results obtained for higher sinkage could not be considered valid due to instability problems. Owing to the lack of moisture content, the results for the dry sand revealed negligible pressure from both the methods under unconfined pressure-sinkage test. This is also evident from the yield surface coefficients for this soil ($a_\circ = a_1 = 0$), as seen in Table 5.1, suggesting that the strength is proportional to the square of its confining pressure. The unconfined pressure-sinkage simulation thus yields negligible strength. This suggests that the type 5 material model in LS-DYNA [104] is not suited for pressure-sinkage analysis of the dry

sand. Wright [100] also showed very low pressure beneath the plate for dry sand through pressure-sinkage test simulations in LS-DYNA using the same material model. Further, Hambleton [28] performed sinkage tests with a non-rolling wheel using a pressure-dependent strength constitutive model (Drucker-Prager) in ABAQUS. It was stated that for a purely frictional soil ($c = 0$), nearly zero resisting pressure is obtained in response to the wheel indentation. This resulted in very large deformations of the soil elements and solution failures.

Figure 5.4(a) illustrates the half-model of the shear-box before loading, while Figure 5.4(b) shows the deformed shape of the SPH soil particles after application of pressure and shear displacement. In this test, the block of soil is subjected to a shear deformation of up to 100 mm, which leads to fragmentations of soil. Such extremely large deformations distort the elements in a corresponding FE model of the shear-box test and invalidate the simulation. The shear-box tests of the selected soils are thus limited only to the SPH method.

The average processing times required for the FE and SPH soil models in different simulations together with the size of the soil domain and the number of elements in the FE model as well as the number of particles in the SPH model are summarized in Table 5.3. The simulations are performed using a 3.2 GHz Intel Xenon processor with 8 cores and 14 GB memory. For volumetric deformation and plate-sinkage simulations, the CPU time of the SPH method was nearly 4.4 times that of the FE method. Bojanowski et al. [43] also conducted virtual plate-sinkage tests comparing different analysis methods, and reported that the SPH plate-sinkage model takes 4.18 times that of the corresponding FE model.

Table 5.3: Comparisons of processing times of the FE and SPH soil models together with soil domain size and number of elements/particles

Simulation type	*Simulation time (s)*	*CPU time (h)*		*Soil domain size (mm)*	*Soil elements/particles*	
		FE	*SPH*		*FE*	*SPH*
Volumetric deformation	1	0.12	0.53	$600 \times 600 \times 600$	20700	27000
Plate-sinkage	6	0.83	3.65	$600 \times 600 \times 600$	20700	27000
Shear-box	10	—	8.5	$400 \times 200 \times 240$	—	19200

For the shear-box test, considering 19200 SPH particles, the CPU time for a 10 s real-time simulation was 8.5 hours. While the FE model is relatively more computationally efficient than the SPH model, the FE model exhibits notable deficiencies, namely, the sponge effect and unwarranted tensile forces leading to overestimation of the plate-soil interface force. The particle-based nature of the SPH method, on the other hand, is able to more accurately represent the soft soil, particularly under large deformations. As a result, the SPH method is chosen for the repeated virtual plate-sinkage test simulations for parametrization of the terramechanics-based tyre-soil interaction models.

5.3.3 Terramechanics-based model parametrization

The verified virtual soil test simulation platform is applied for parametrization of the terramechanics-based tyre-soil interaction models. The simulation results are used to identify model parameters describing the pressure-sinkage as well as the shear stress-shear displacement relations for the selected soils.

Pressure-sinkage relation

The pressure p developed in soil due to sinkage z of a circular plate of radius b is expressed using Bekker's relation as [18]:

$$p = \left(\frac{k_c}{b} + k_\phi \right) z^n \tag{5.7}$$

where k_c, k_ϕ and n are soil parameters, known as *cohesive* and *frictional* moduli and *exponent*, respectively. These soil parameters are generally identified through repeated *pressure-sinkage* tests using a *bevameter* [141]. In this study, these parameters are identified using a virtual environment involving the pressure-sinkage test simulations. The plate radius, b, in Equation (5.7), determines the size of the contact region and its contributions to the pressure. The pressure-sinkage relation in Equation (5.7) can be rewritten as [221]:

$$p = k_b \; z^n \quad ; \quad k_b = \frac{k_c}{b} + k_\phi \tag{5.8}$$

The above power relation yields a linear relation between $\log p$ and $\log z$, as:

$$\log p = \log k_b + n \log z \tag{5.9}$$

The slope n and the intercept $\log k_b$ are subsequently identified through linear regression of a set of $(\log z, \log p)$ data obtained from the pressure-sinkage test simulations. The SPH soil

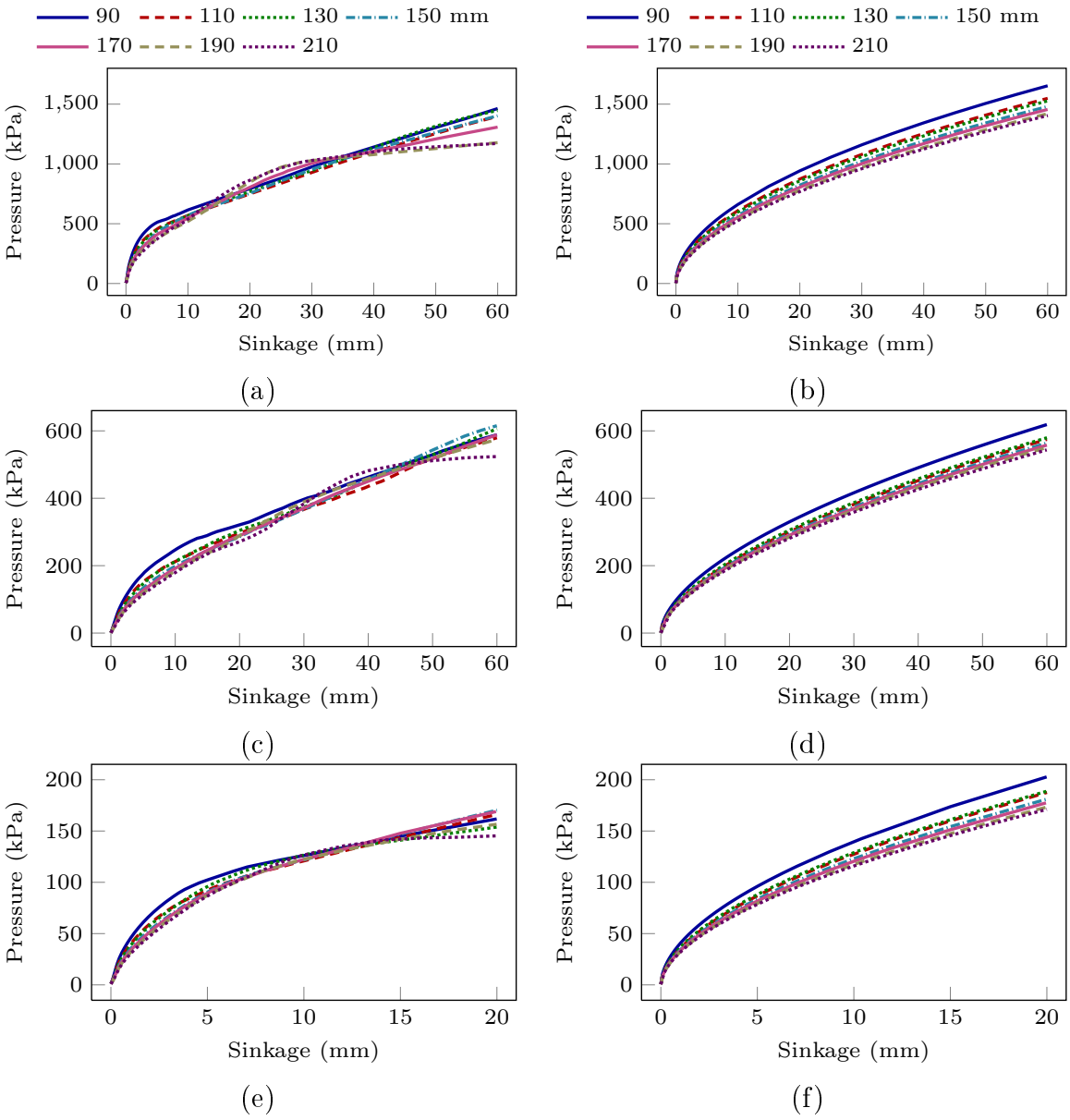

Figure 5.9: Pressure-sinkage characteristics obtained from virtual test simulations (right column) of different soils and plate radii, and the corresponding fitted curves (left column) for: (a,b) unwashed sand; (c,d) high density wet sand; and (e,f) high density flooded sand

model is employed to perform the pressure-sinkage test simulations. Figure 5.9 illustrates the pressure-sinkage characteristics of selected soils obtained from the simulations together with the fitted curves for different plate sizes. It should be noted that the pressure-sinkage relation for the dry sand was not attempted due to its very low cohesion. Considering different plate radii, ranging from 90 to 210 mm, the logarithmic pressure-sinkage data, obtained corresponding to different plate radii, invariably revealed linear relations for the selected soils with correlation coefficient (r^2) in excess of 0.97. Table 5.4 presents the model parameters (n and k_b), identified for different soils considering varying plate radii. The results show that constant k_b for a given soil is strongly dependent on the plate radius, while the variations in exponent n are very small. The mean value of n is thus considered adequate to describe the pressure-sinkage relation in Equation (5.7).

Table 5.4: Model parameters, k_b and n, obtained from the virtual pressure-sinkage tests of selected soils considering different plate radii

Radius	*Unwashed sand*		*High density wet sand*		*High density flooded sand*	
b (mm)	n	k_b (kN/m^{n+2})	n	k_b (kN/m^{n+2})	n	k_b (kN/m^{n+2})
90	0.5120	6981.495	0.5718	3090.985	0.5390	1670.391
110	0.5206	6699.779	0.5900	3022.367	0.5561	1651.977
130	0.5242	6674.028	0.5829	2987.260	0.5505	1626.694
150	0.5340	6649.794	0.5909	2971.881	0.5577	1605.139
170	0.5397	6645.766	0.5942	2967.058	0.5599	1587.607
190	0.5470	6619.206	0.5968	2951.082	0.5626	1566.089
210	0.5489	6578.169	0.5998	2939.078	0.5618	1541.031

From Equation (5.8), the parameter k_b can be considered as a linear function of plate curvature ($1/b$) with slope k_c and intercept k_ϕ. The regression analysis of the simulation data was thus performed to obtain linear relationship between k_b and $1/b$, and thereby the constants k_c and k_ϕ for each soil (Table 5.5). Figure 5.10 illustrates the goodness of fit of the simulation data (b, k_b) for each soil with correlation coefficient, r^2, greater than 0.90 in all cases.

Table 5.5: Model parameters n, k_c and k_ϕ identified from the pressure-sinkage test simulations for selected soils

Soil type	*Exponent n*	k_c (kN/m^{n+1})	k_ϕ (kN/m^{n+2})	*Goodness of fit* (r^2)
Unwashed sand	0.5324	53.195	6309.082	0.91
HD wet sand	0.5895	22.518	2827.607	0.98
HD flooded sand	0.5554	19.763	1464.505	0.97

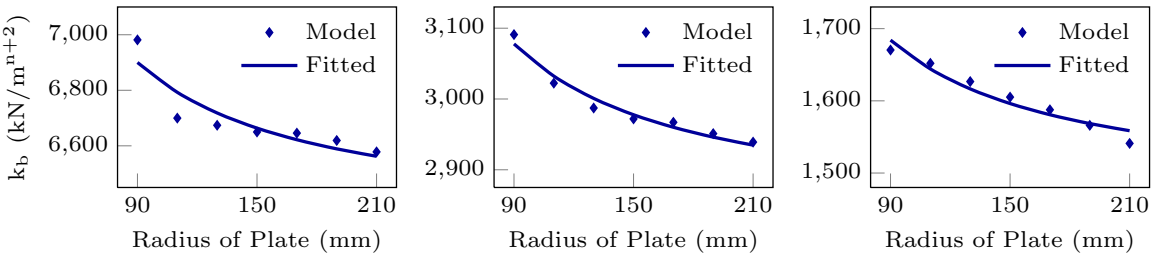

(a) (b) (c)

Figure 5.10: Pressure-sinkage simulation results illustrating variations in k_b with plate radius for selected soils: (a) unwashed sand; (b) high density wet sand; and (c) high density flooded sand

Evaluations of the identified pressure-sinkage model parameters

The pressure-sinkage test data as well as the curve-fitting-based values for the soil parameters n, k_c and k_ϕ are available for a broad range of soils, as reported in [141]. Such experimental data, however, could not be found for the soils considered for virtual tests and model characterizations. The effectiveness of the identified parameters for the selected soils are thus evaluated in a qualitative sense through comparisons of pressure-sinkage tendencies with those of the reported experimental properties of different soils. Figure 5.11 compares the pressure-sinkage characteristics of the three selected soils with those of several other types of soils reported in [141]. The results are presented for plate radius of 150 mm. The plots for the selected soils are based on the parameters identified from the computational tests (Table 5.5), whereas the plots for the other soils are based on the parameters identified through curve fitting of the experimental results obtained from the bevameter machine (Table 5.6), as reported in [141]. The soils in Table 5.6 are arranged in the order of their

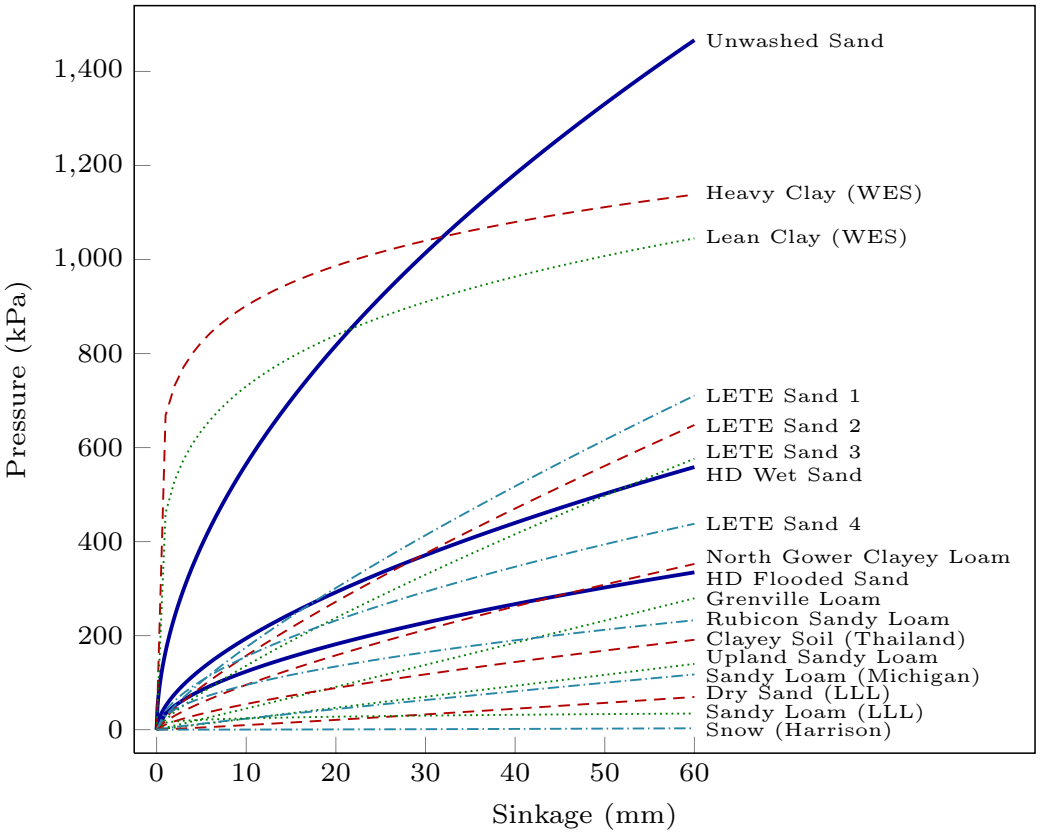

Figure 5.11: Comparisons of the theoretical pressure-sinkage curves for the soil types parameterized in this study with those of other types of soils being experimentally parameterized as reported in [141]

pressure corresponding to 60 mm sinkage. The comparisons suggest highest strength of the unwashed sand as the sinkage exceeds 30 mm. Although the strength of the heavy clay of the US Army Waterways Experiment Station (WES) is somewhat close to that of the unwashed sand, the pressure-sinkage trends are not comparable. The data for WES heavy clay exhibits substantial higher rate of pressure development than the unwashed sand under very low sinkage, which is clearly due to their large difference in the value of the exponent n (0.13 versus 0.53). With increasing the sinkage, however, the pressure tends to saturate for the heavy clay, while it continues to increase for the unwashed sand. This can be attributed to the parameter k_ϕ of the unwashed sand (6309 kN/m^{n+2}), which is much higher than that for the heavy clay (1556 kN/m^{n+2}). The parameter k_c and k_ϕ of the reported LETE sands (1, 2, 3) are comparable with those of the unwashed sand, as seen

in Tables 5.5 and 5.6. The rate of change of pressure for the unwashed sand, however, is substantially higher than the LETE sands, which is due to its relatively smaller exponent (0.53) compared to the LETE sands (0.781 to 0.806).

Table 5.6: Comparisons of the identified pressure-sinkage parameters with those of other soils being experimentally parameterized as reported in [141]

Soil type (moisture %)	*Exponent n*	k_c (kN/m^{n+1})	k_ϕ (kN/m^{n+2})
Unwashed sand (12%)	0.5324	53.195	6309.082
Heavy clay (WES) (25%)	0.13	12.7	1555.95
Lean clay (WES) (22%)	0.2	16.43	1724.69
LETE sand 1	0.781	47.8	6076
LETE sand 2	0.79	102	5301
LETE sand 3	0.806	155.9	4526
High density wet sand (16%)	0.5895	22.518	2827.607
LETE sand 4	0.578	9.08	2166
North Gower clayey loam (46%)	0.73	41.6	2471
High density flooded sand (30%)	0.5554	19.763	1464.505
Grenville loam (18.2%)	1.02	66	4486
Rubicon sandy loam (44%)	0.5	10.5	880
Clayey soil (Thailand) (55%)	0.7	16.03	1262.53
Upland sandy loam (49%)	1.00	5.7	2293
Sandy loam (Michigan) (11%)	0.9	52.53	1127.97
Dry sand (LLL)	1.1	0.99	1528.43
Sandy loam (LLL) (22%)	0.2	2.56	43.12
Snow (Harrison)	1.6	2.49	245.9

The results show that the pressures developed for the other two selected soils (high density wet and flooded sands) are considerably lower than the unwashed sand. The high density wet sand resembles the properties of the LETE sands enumerated as 1, 2 and 3 at lower, middle and higher levels of sinkage, respectively. At lower sinkages, the pressure is developed in the high density wet sand at a relatively higher rate than that observed for the three LETE sands. This is due to lower exponent n of the high density wet sand (0.58) compared to those of the three LETE sands (0.781 to 0.806). The high density wet sand model formulated in the present study, however, exhibits relatively lower pressure corresponding to the highest sinkage of 60 mm, when compared to those of the LETE sands. This can be attributed to lower k_c and k_ϕ values of the high density wet sand than

the LETE sands. The results also show that the strength of the high density flooded sand considered in the study is comparable to that of the North Gower clayey loam, reported in [141]. The high density flooded sand, however, shows a higher rate of pressure under lower sinkage and a lower final pressure compared to the North Gower clayey loam. This is due to the higher exponent n of the high density flooded sand together with its lower k_c and k_ϕ values compared to the North Gower clayey loam.

Shear stress-shear displacement characteristics

The shear stress τ developed in soil in response to a shear-displacement j is expressed as [18]:

$$\tau = \tau_{max}\left[1 - \exp\left(\frac{-j}{K}\right)\right] \tag{5.10}$$

where K is a soil parameter known as the *shear displacement modulus*, and τ_{max} represents the shear strength of soil, which depends on its confining pressure, p, through the *Mohr-Coulomb failure criterion*, such that:

$$\tau_{max} = c + p\tan\phi \tag{5.11}$$

where c and ϕ are soil parameters known as *cohesion stress* and *angle of shear resistance*, respectively. These parameters are generally determined from data obtained through *shear ring* tests using the bevameter machine [18]. In this study, the SPH soil model is used to perform virtual shear-box test simulations, and the results are used to identify the shear model parameters. In the shear-box test simulations, a pre-selected pressure p is initially applied to the soil particles through the top plate, which is free to move in the vertical direction, as illustrated in Figure 5.4(b). Subsequently, a desired shear displacement is applied in a ramp manner by gradually moving the bottom half of the shear-box in the horizontal direction, as shown in Figure 5.4(b). The resulting shear force is used to estimate the shear stress of the soil as a function of the applied shear displacement. The simulations are repeated considering different applied pressures, ranging from 0 to 700 kPa, and for each pressure, the shear stress is plotted versus shear displacement.

Figure 5.12 illustrates the shear stress versus shear displacement characteristics obtained from the shear-box test simulations for the four selected soils under different applied pressures. It is observed that the shear stress initially increases in a nonlinear manner with increase in the shear displacement, and tends to saturate at certain shear displacement depending on the applied confining pressure. The shear strength of each soil corresponding to a given applied pressure, $\tau_{max}(p)$, is then identified as the saturation level (maximum) of the shear stress. The shear displacement modulus K in Equation (5.10) is also identified from the simulation results, considering rate of change of shear stress with respect to the shear displacement. Differentiating Equation (5.10) with respect to the shear displacement

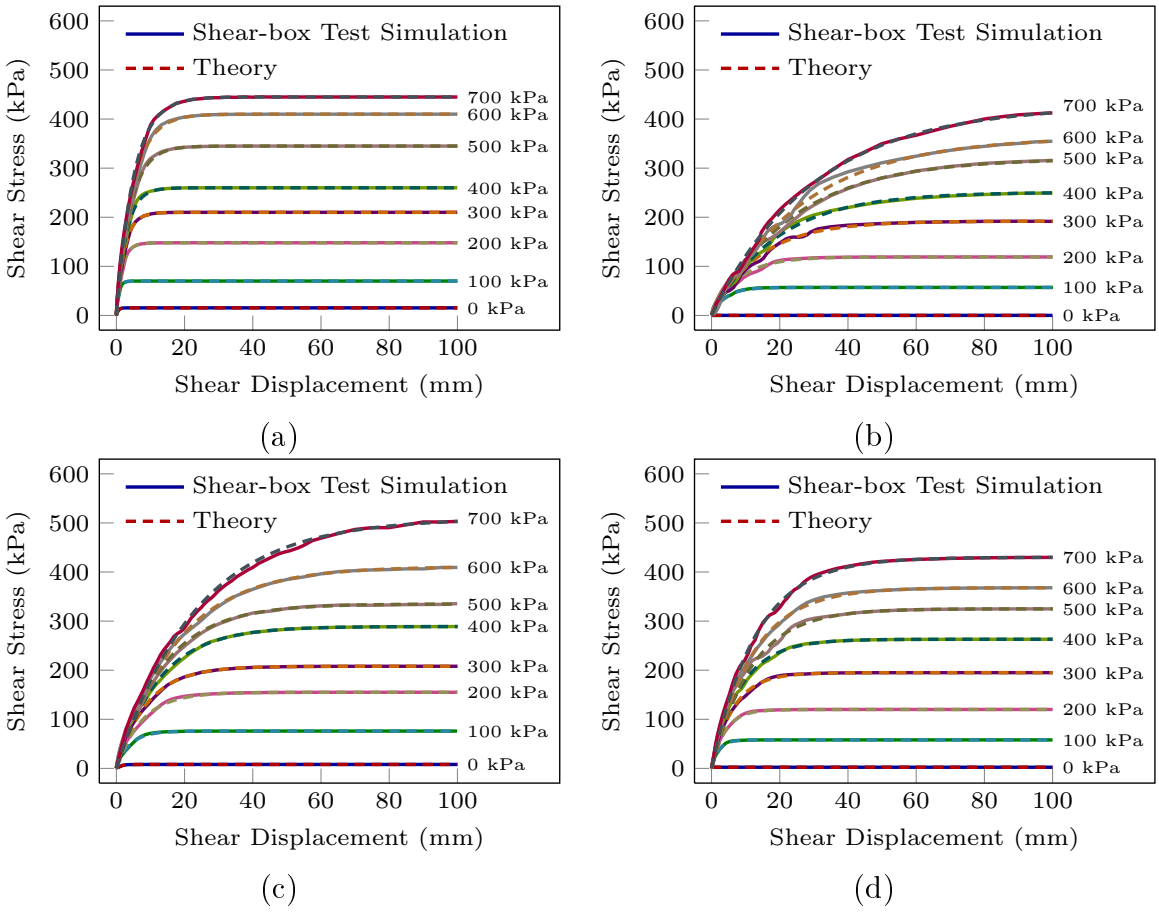

Figure 5.12: Shear stress-shear displacement curves obtained from shear-box test simulations using SPH method and the theoretical relation (Equation (5.10)) considering varying confining pressures and selected soils: (a) unwashed sand; (b) low density dry sand; (c) high density wet sand; and (d) high density flooded sand

j, yields:

$$\frac{d\tau}{dj} = \frac{\tau_{max}}{K} \exp\left(\frac{-j}{K}\right) \tag{5.12}$$

The above suggests that slope of the stress-displacement curve in the vicinity of zero displacement is inversely related to K (τ_{max}/K). The slope of the shear stress-displacement curve corresponding to each confining pressure is thus computed for deriving the value of K. Table 5.7 summarizes the identified soil shear parameters K and τ_{max} for a range of confining pressures up to 700 kPa for the selected soils. The identified model parameters are further used to predict shear stress-shear displacement properties of selected soils using Equation (5.10). The shear stress-shear displacement characteristics obtained from the shear-box test simulations are compared with those estimated from Equation (5.10), as presented in Figure 5.12 for different pressures.

Table 5.7: Identified values for the soil shear properties K and τ_{max}, obtained from virtual shear-box tests at varying confining pressures for selected soils

Pressure	*Unwashed sand*		*LD dry sand*		*HD wet sand*		*HD flooded sand*	
(kPa)	*K (mm)*	τ_{max} *(kPa)*	*K*	τ_{max}	*K*	τ_{max}	*K*	τ_{max}
0	0.55	15.4	0.01	0.04	1.5	8	0.19	2.3
100	0.76	70	4	57	4	76	2.1	58
200	1.72	148	8	119	7.55	155	4	120
300	2.4	210	14	192	8.9	208	6.4	195
400	2.9	260	19	251	12.6	289	8.6	263
500	4.1	345	24	320	14	335	11.5	325
600	4.8	410	27	364	18	411	12	368
700	5	445	30	428	23.2	510	13	430

The Mohr-Coulomb failure criterion, Equation (5.11), characterizes the soil strength τ_{max} as a linear function of the confining pressure p with slope of $\tan\phi$ and intercept of c. The constants c and $\tan\phi$ are thus identified through linear regression analysis of the (p, τ_{max}) data obtained from the simulations (Table 5.7). Table 5.8 summarizes the identified shear parameters c and ϕ. Figure 5.13 further illustrates variations in maximum shear stress with applied pressure obtained from the shear-box test simulations together

with the goodness of fit with correlation coefficient (r^2) in excess of 0.99 for all the selected soils.

Table 5.8: Soil shear model parameters K, c and ϕ identified from the shear-box test simulations for selected soils

Soil type	$K_\circ$ *(mm)*	γ *(mm/kPa)*	*c (kPa)*	ϕ°
Unwashed sand	0.3208	0.007	15.083	32.49
LD dry sand	0.0042	0.045	0.017	31.72
HD wet sand	1.0125	0.0292	6.917	34.67
HD flooded sand	0.3958	0.0195	2.375	31.89

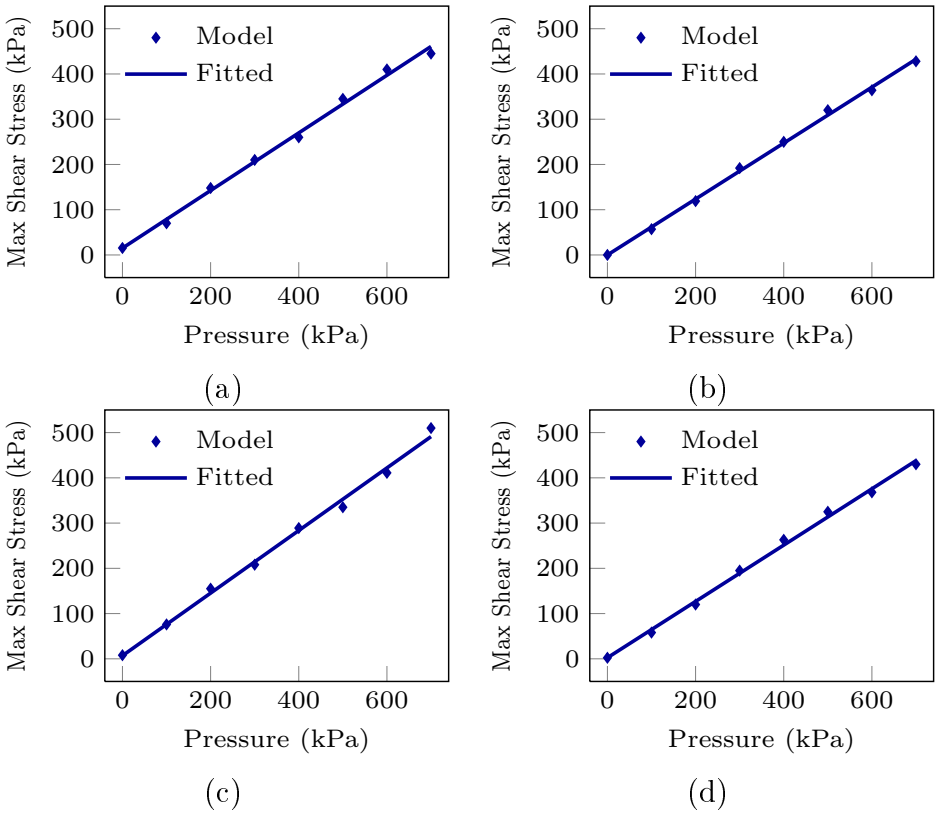

Figure 5.13: Variations in maximum shear stress with varying confined pressure, obtained from the shear-box test simulations of selected soils and the linear regression curves: (a) unwashed sand; (b) low density dry sand; (c) high density wet sand; and (d) high density flooded sand

The results in Table 5.7 show that the shear displacement modulus K varies considerably with the confining pressure. Reported studies generally consider mean value of K for a given soil [31], which may yield notable errors in the shear stress-shear displacement properties of the soil. Figure 5.14 illustrates variations in the shear displacement modulus K over the range of confining pressures considered in the study, which show linear variations in K with correlation coefficient (r^2) in excess of 0.98 for all the selected soils. Considering $K(p) = K_\circ + \gamma p$, the constants $K_\circ$ and γ for the selected soils are summarized in Table 5.8.

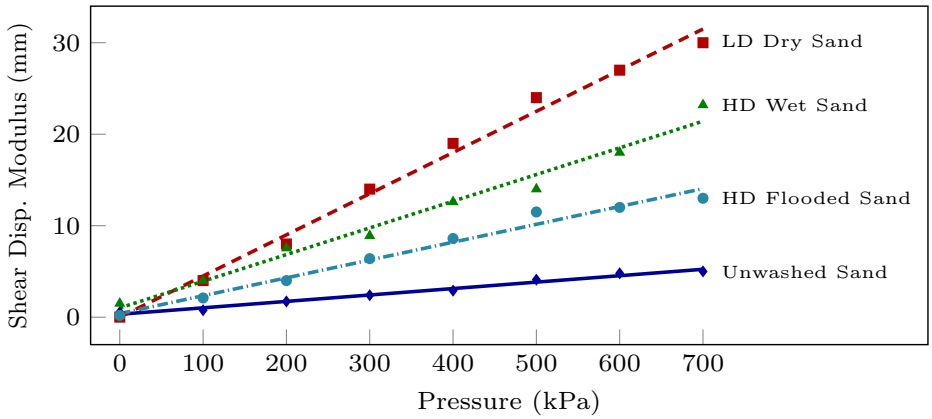

Figure 5.14: Variations in shear displacement modulus (K) with varying confined pressure (p), obtained from the shear-box test simulations and the linear regression curves for unwashed sand, low density dry sand, high density wet sand and high density flooded sand

Evaluations of the identified shear parameters

The validity of the identified values for the soil shear parameters c and ϕ is evaluated through comparisons with those identified via actual experiments performed by the triaxial machine [146] for the selected soils, as summarized in Table 5.9. The results for the angle of shear resistance, ϕ, show very good agreements with the experimental data. The peak deviation between the predicted and measured values is below 2.3%, which is observed for the low density dry sand and high density wet sand. The identified values for the cohesive stress, c, are also found to be comparable with the experimental results for the low density dry sand and the high density wet sand. However, the values obtained for

the unwashed sand and the high density flooded sand are overestimated compared to the experimental data. These overestimations can be attributed to the simplicity of the shear-box test, where during application of the shear displacement, the confining pressure cannot be held constant and tends to increases slightly. In a triaxial test, the confining pressure is controlled to be constant and under hydrostatic state. Wright [100] also identified soil shear parameters for a sample of sandy loam via performing both the shear-box and the triaxial compression tests. The study showed overestimation of the cohesive stress from the shear-box test (2.67 kPa) compared to that obtained from the triaxial compression test (1.33 kPa).

Table 5.9: Comparisons of the soil shear model parameters (c and ϕ) obtained from the shear-box test simulations with the reported data [146]

	Virtual shear-box test		*Actual experiment*		*Percentage error*	
Soil type	*c (kPa)*	ϕ°	*c (kPa)*	ϕ°	*c (%)*	*ϕ (%)*
Unwashed sand	15.083	32.49	11.721	32.9	22.29	-1.26
LD dry sand	0.017	31.72	0	31	—	2.27
HD wet sand	6.917	34.67	6.895	33.9	0.32	2.22
HD flooded sand	2.375	31.89	1.724	32.2	27.41	-0.97

5.4 Conclusions

The effectiveness of the computational soil model is demonstrated to serve as a virtual test platform for identifying terramechanics-based tyre-soil interaction models. The soil models formulated using the FE and SPH methods revealed considerable differences in the pressure-sinkage test simulations, while the computing time for the SPH model was nearly 4.4 times longer than the FE model. Comparisons of the deformed shapes of the two soil models suggested that the SPH model can more realistically represent the penetration of the plate into the soil and soil fragmentations. In the FE method, the body of soil behaves like a unit of sponge, while the particle-based nature of the SPH method permits the soil particles to envelop the plate as it sinks into the soil. Moreover, the FE model yields

relatively higher contact force due to tensile force of the stretched elements near the edges of the plate. The SPH method is more suited for the shear-box test since it permits soil disintegration under large shear deformations.

From the pressure-sinkage test simulations, it is shown that the pressure-dependent material model can accurately predict the pressure-sinkage characteristics of all the selected soils except for the dry sand due to its non-cohesive feature. The effectiveness of the pressure-sinkage simulation tests and the identified Bekker's relations is demonstrated through comparisons with those of several other soils parameterized using the bevameter technique. The results obtained from shear-box test simulations provided convenient mean for parametrization of Bekker's shear stress-shear displacement relations for the selected soils. These revealed good agreements with those determined from the triaxial compression tests for the selected soils. In Part II of the work, the proposed parametrization methodology is further assessed through evaluations of the terramechanics-based tyre-soil interaction models for predicting stress distributions as well as the contact forces and moments for the stationary, rolling and steered tyres.

Chapter 6

A Virtual Test Platform for Analyses of Rolling Tyre-Soil Interactions: Part II – Evaluations of Terramechanics Models

6.1 Introduction

Dynamic performance of off-road vehicles is directly related to forces and moments generated by interactions of the rolling tyres with deformable terrains. Dynamics performance simulations of off-road wheeled vehicles, however, involve considerable challenges related to modeling of the sub-system describing the tyre-terrain interactions. The modeling of tyre-terrain interactions has been the subject of many reported studies. The models describing the tyre-terrain interactions may be grouped into two broad categories: (i) theoretical models describing the phenomenological behavior of the soil under a penetrating, rolling or steered wheel; (ii) Computational models based on Finite Element (FE) and Smoothed Particle Hydrodynamics (SPH) formulations of the soils.

Wong and Reece [19, 20] proposed a phenomenon-based model for estimating contact forces developed underneath a rolling wheel through integration of the radial and shear stresses developed at the contact interface. The stresses were estimated as functions of the normal and shear displacements of the soil using the phenomenological formulations proposed by Bekker [18]. For a rolling tyre, apart from the sinkage and shear deformations of soil, the arising stresses are also highly affected by the degree of slip (or skid). The

forces generated beneath the driven and towed wheels thus require different formulations [19, 20].

The terramechanics-based models have been widely used in dynamic simulations of off-road vehicles [111, 150, 153] as well as planetary exploration rovers [21–23] for estimating forces/moments developed at the wheel-soil interface. The majority of these studies, however, neglect the contributions due to flexibility of the pneumatic tyre in the interest of focusing on modeling the soft soil characteristics [19, 21, 149, 155, 222–224]. A vast number of analytical pneumatic tyre models have also been reported using semi-empirical [63, 64] and physics-based [1, 3, 65, 218, 225, 226] approaches. These studies, however, have mostly assumed the terrain undeformable so as to focus on tyre responses to terrain irregularities, and relatively fewer studies have considered both the tyre and soil deformable [152–154, 227].

Although phenomenological formulations permit wheel-soil interactions analysis in a highly efficient manner when compared to the computational models, these require calibrations for every individual soil. The phenomenological models are invariably identified from measured data obtained using different test devices such as the bevameter machine, the shear-box and the triaxial apparatus [141]. The reported tyre-soil models employing semi-empirical or phenomenological formulations of soils facilitate simulations of dynamic performance of off-road vehicles in an efficient manner, while these provide only limited understanding of the physics of the soil behavior under a rolling pneumatic tyre. Moreover, these provide only limited guidance towards design of tyres operating on deformable terrains. This is due to lack of consideration of structural details and elastic properties of a pneumatic tyre as well as the plastic characteristics of the soils under the tyre loads [153, 154]. Alternatively, numerical approaches such as the finite element methods have been applied for accurate modeling of tyre-soil interactions with focus on physical properties of both the pneumatic tyre and the soil as deformable structures [24, 27, 29, 30, 150, 161, 163]. A large number of finite element structural tyre models have been developed with widely different levels of complexity ranging from a simple inflated airbag of membrane elements [79, 80, 82] to detailed structural models representing the multi-layered composite structure of a pneumatic tyre [10, 12, 32, 108, 109, 206]. These models have provided accurate

predictions of the tyre dynamic responses in different vehicle maneuvers on rigid roads [12, 15, 82, 87, 98, 206]. Such tyre models, however, are not suited for vehicle dynamics analyses due to their high computational demands. Applications of such comprehensive tyre models to deformable terrains pose far more computational demands. Consequently, the vast majority of the tyre-soil interaction studies have used either simplified pneumatic tyre models [24, 26, 27, 30, 100] or rigid wheel models [25, 29, 110, 228] to achieve a compromise between the accuracy of the simulation results and the computational efficiency of the tyre-soil model.

The reported computational tyre-soil models have established that the Finite Element (FE) methods are well suited for modeling the composite structure of the pneumatic tyre [10, 12, 109]. The FE methods, however, have shown limitations for modeling the soft soils, which are mostly associated with the mesh-based nature of the FE method [25, 38, 43]. The soil mesh in a FE model tends to deform like a sponge, which is not representative of the soil behavior. The elements in a soil mesh are defined via shared nodes, which cannot be disconnected from the adjacent elements in order to accommodate and envelop the penetrating object [25, 26, 43]. This sponge effect also tends to yield inaccurate estimations of contact forces due to the undesirable contributions of tension actions by the stretched elements [25, 26, 38]. Alternatively, the mesh-less methods such as the Smoothed Particle Hydrodynamics (SPH) techniques could overcome the above-stated mesh-related limitations [25, 26, 36, 180]. The reported studies have shown that the mesh-less SPH methods can provide more realistic soil behavior than the traditional FE methods, particularly when large deformations and fragmentations of soil materials are encountered [25, 40, 180].

This study is aimed at analysis of contact forces developed at the interface of a rolling tyre with the soil. The soil models established from the virtual testing platform, developed in Part I, are used to describe the pressure-sinkage and shear stress-shear displacement relations for two different soils. A FE model of a pneumatic tyre is subsequently integrated to the soil model to create a virtual simulation tool for analyses of tyre-soft soil interactions. Owing to the excessive computing demands of both the FE tyre and SPH soil models, a computationally efficient pneumatic tyre model, developed using the Part-Composite approach in LS-DYNA, is employed. The simulations are performed for two different tyre

models: a low-pressure tyre model to study the interactions of a compliant wheel with the soil; and a rigid tyre model representing high pressure wheel penetrating the soil. The coupled tyre-soil model is further used to assess effectiveness of the terramechanics-based tyre-soil models formulated using the virtual test simulations environment in Part I of this work. The assessments are based on the responses in terms of radial and tangential stresses as well as the contact forces and moments developed underneath the tyre under different maneuvers involving penetrations of the stationary, driven, towed and steered tyre into the soft soil.

6.2 Terramechanics-based wheel-soil interaction models

The terramechanics-based pressure-sinkage and the shear stress-displacement characteristics were parameterized using virtual test simulations for a number of selected soils in Part I of this study. The effectiveness of the identified parameters are evaluated via comparisons of the stress distributions and contact forces/moments obtained from the terramechanics-related formulations with those predicted from the virtual tyre-soil test platform. These comparison involve the stresses and forces/moments developed under a penetrating tyre/wheel into the soil in stationary, rolling and steering maneuvers. The terramechanics-related formulations for estimating the tyre/wheel-soil contact forces and moments are briefly presented below.

Figure 6.1 illustrates the schematic of the terramechanics-based tyre/wheel-soil model. The contact interface is represented by an arc of radius R, which is larger than the free tyre radius r, to account for the deformed tyre geometry effect [152]. The angular position along the contact patch is defined by the angle θ, while its boundaries, θ_1 and θ_2, define the contact patch. These are related to sinkage z and the rut recovery ηz, such that [19]:

$$\theta_1 = \cos^{-1}\left(1 - \frac{z}{R}\right) \quad ; \quad \theta_2 = \cos^{-1}\left(1 - \frac{\eta z}{R}\right) \tag{6.1}$$

The rut recovery ηz is considered proportional to the sinkage z using a sinkage ratio η [19].

The vertical contact force F_z generated due to sinkage z of a stationary pneumatic tyre is estimated from integration of the normal component of the radial stress σ_r throughout

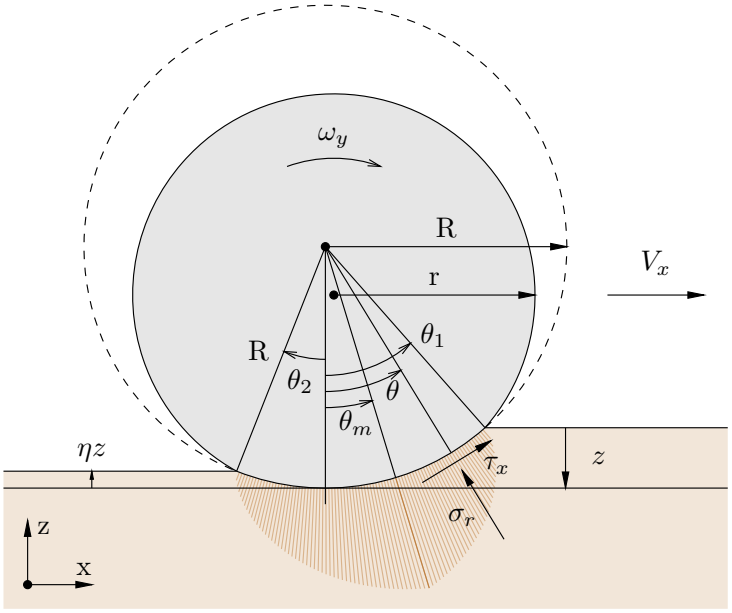

Figure 6.1: Terramechanics-based tyre-soil interaction model

the contact interface, such that [19]:

$$F_z = bR \int_{\theta_2}^{\theta_1} \sigma_r(\theta) \cos\theta \; d\theta \tag{6.2}$$

where b is the width of the contact interface. Assuming that the radial reaction stress over a small element of the tyre is equal to the pressure beneath a plate penetrating to the same depth, the radial stress distribution along the contact interface, $\sigma_r(\theta)$, is formulated in terms of the local sinkage $\zeta(\theta)$:

$$\sigma_r(\theta) = \left(\frac{k_c}{b} + k_\phi \right) [\zeta(\theta)]^n \tag{6.3}$$

where k_c, k_ϕ and n are the Bekker's pressure-sinkage relation parameters [18]. For a stationary tyre, with a sinkage ratio $\eta = 1$, the maximum radial stress occurs at a point beneath the wheel with angular position $\theta_m = 0$. Assuming similar distributions for the radial stress in the front and rear portions of the contact region, coordinates of the contact points within the front (θ_f) and rear (θ_r) portions possessing identical radial stress are related as [19]:

$$\theta_f = \theta_1 - (\theta_1 - \theta_m)\frac{\theta_r - \theta_2}{\theta_m - \theta_2} \tag{6.4}$$

The distribution of the local sinkage $\zeta(\theta)$ is subsequently formulated as:

$$\zeta(\theta) = \begin{cases} R(\cos\theta - \cos\theta_1) & (\theta_m \leqslant \theta \leqslant \theta_1) \\ R\left[\cos\left(\theta_1 - (\theta_1 - \theta_m)\dfrac{\theta - \theta_2}{\theta_m - \theta_2}\right) - \cos\theta_1\right] & (\theta_2 \leqslant \theta < \theta_m) \end{cases} \tag{6.5}$$

6.2.1 Forces and moments developed under a rolling wheel

The longitudinal (F_x) and normal (F_z) contact forces developed beneath a rolling wheel, and the rolling moment (M_y) are attributed to the shear stress τ_x in addition of the radial stress σ_r of the soil, such that [19]:

$$F_x = bR\int_{\theta_2}^{\theta_1} \left[-\sigma_r(\theta)\sin\theta + \tau_x(\theta)\cos\theta\right] d\theta \tag{6.6}$$

$$F_z = bR\int_{\theta_2}^{\theta_1} \left[\sigma_r(\theta)\cos\theta + \tau_x(\theta)\sin\theta\right] d\theta \tag{6.7}$$

$$M_y = bR^2\int_{\theta_2}^{\theta_1} \tau_x(\theta)\ d\theta \tag{6.8}$$

The shear stress distribution along the contact region, $\tau_x(\theta)$, is estimated as a function of the shear displacement $j_x(\theta)$ using the Bekker's relation in conjunction with the Mohr-Coulomb failure criterion [18], such that:

$$\tau_x(\theta) = \left[c + \sigma_r(\theta)\tan\phi\right]\left[1 - \exp\left(\frac{-j_x(\theta)}{K}\right)\right] \tag{6.9}$$

where c, ϕ and K are soil shearing parameters, which have been identified from the virtual shear-box test simulations presented in Part I of this study.

Driven wheel

From Equations (6.3) and (6.5), it is evident that the position of the maximum radial stress, θ_m, influences the local sinkage $\zeta(\theta)$ and thus the radial stress distribution $\sigma_r(\theta)$. For a stationary tyre, the maximum radial stress occurs beneath the wheel center ($\theta_m = 0$).

Reported experimental studies on different sands [19, 149] have shown that the radial stress distribution under a rolling wheel is a function of the longitudinal slip. For a driven wheel, the maximum radial stress occurs in front of the wheel center, such that:

$$\theta_m = (c_1 + c_2\ i)\ \theta_1 \tag{6.10}$$

where c_1 and c_2 are parameters characterizing the relative position of the maximum radial stress and its dependence on the slip ratio. Experimental studies [19, 149] have further shown that the shear stress beneath a driven wheel is rearward throughout the contact region. The local shear displacement $j_x(\theta)$ for a driven wheel is formulated via integrating the relative velocity of a point on the wheel with respect to the velocity of the rearward soil flow in the $[\theta, \theta_1]$ range, and is related to the longitudinal slip ratio i in the following manner [19]:

$$j_x(\theta) = \int_{\theta}^{\theta_1} R\left[1 - (1-i)\cos\theta\right] d\theta = R\left[(\theta_1 - \theta) - (1-i)(\sin\theta_1 - \sin\theta)\right] \tag{6.11}$$

Towed wheel

Experimental studies [20, 149] have shown that under a towed wheel, there exists a transition point, where the tangential stress changes its direction from opposite to wheel rotation (positive) to the direction of wheel rotation. The radial stress at this transition point $\theta_\circ$ is thus considered as the principal stress. Furthermore, $\theta_\circ$ can be considered as the point of maximum radial stress, θ_m. Unlike the driven wheel, the front contact zone of shear stress with positive sign (forward) is considerably large for the towed wheel. The shear stress developed due to the towed wheel thus necessitates consideration of the relatively large front zone of shear stress ($\theta_\circ \leqslant \theta \leqslant \theta_1$), particularly at high degrees of skid. The location of this transition point, $\theta_\circ$, is determined based on the theory of plastic equilibrium for soils from solving the following equation [20]:

$$\tan\left(\frac{\pi}{4} - \frac{\phi}{2}\right) = \frac{\cos\theta_\circ - (1+i)}{\sin\theta_\circ} \tag{6.12}$$

where i is the wheel skid ratio, and ϕ is the angle of shearing resistance for soil. Considering the transition in the shear stress distribution, the distribution of the shear displacement $j_x(\theta)$ in the two zones is obtained from [20]:

$$j_x(\theta) = \begin{cases} R(1-i)\left[\dfrac{\sin\theta_1 - \sin\theta_\circ}{\left(\dfrac{\theta_1-\theta_\circ}{\theta_1-\theta}\right)} - (\sin\theta_1 - \sin\theta)\right] & (\theta_\circ \leqslant \theta \leqslant \theta_1) \\ \\ R[(\theta_\circ - \theta) - (1-i)(\sin\theta_\circ - \sin\theta)] & (\theta_2 \leqslant \theta < \theta_\circ) \end{cases} \tag{6.13}$$

It should be noted that shear displacement distribution in rear zone ($\theta_2 \leqslant \theta < \theta_\circ$) is same as that for a driven wheel, as seen in Equation (6.11). The shear displacement $j_x(\theta)$ in the front zone ($\theta_\circ \leqslant \theta \leqslant \theta_1$) is formulated via integrating the relative velocity of a point on the wheel with respect to the velocity of the upward soil flow.

6.2.2 Forces and moments developed under a steered wheel

The lateral contact force F_y and self-aligning moment M_z developed by a driven steered wheel due to the side-slip angle α is estimated through integrating the lateral shear stress τ_y along the contact region, such that [31]:

$$F_y = bR \int_{\theta_2}^{\theta_1} \tau_y(\theta)\ d\theta \tag{6.14}$$

$$M_z = bR^2 \int_{\theta_2}^{\theta_1} \tau_y(\theta)\sin\theta\ d\theta \tag{6.15}$$

The lateral shear stress distribution $\tau_y(\theta)$ is estimated as a function of the lateral shear displacement $j_y(\theta)$ using the Bekker's relation in conjunction with the Mohr-Coulomb failure criterion [18], such that:

$$\tau_y(\theta) = [c + \sigma_r(\theta)\tan\phi]\left[1 - \exp\left(\frac{-j_y(\theta)}{K}\right)\right] \tag{6.16}$$

where c, ϕ and K are soil shearing parameters. For a steered rolling (driven) wheel, the lateral shear displacement $j_y(\theta)$ is formulated via integrating the lateral component of the slip velocity of a point on the wheel in the $[\theta, \theta_1]$ range, such that [162]:

$$j_y(\theta) = \int_{\theta}^{\theta_1} R(1-i)\tan\alpha \; d\theta = R(1-i)(\theta_1 - \theta)\tan\alpha \tag{6.17}$$

6.3 Computational tyre/wheel-soil models

The virtual soil test and simulation platform, developed in first part of this study, is further enhanced by integrating both the FE and SPH soil models to the finite element model of a stationary as well as rolling pneumatic tyre. The integrated test platform is formulated so as to simulate the tyre-soil interactions in the stationary, rolling and steered tyre maneuvers. Two different FE models of the tyre are considered in the study. These include a low-pressure tyre model to study the effect of tyre compliance on the tyre-soil interactions, and a rigid wheel model characterizing a high pressure wheel penetrating/compacting the soft soil.

6.3.1 Finite element model of the pneumatic tyre

A wide range of structural tyre models using FE modeling techniques have been reported [10, 12, 32, 79, 98, 108]. Some of these models have been developed considering the multi-layered composite structure of the pneumatic tyre [10, 32, 108], while others have represented the tyre via a single layer with equivalent orthotropic properties [12, 79, 98]. The validity of such tyre models for predicting vertical responses, modal properties, traction/braking and cornering forces has also been demonstrated in a few studies on the basis of experimental data [12, 108]. Such tyre models, however, pose considerable demands on computing tyre dynamic responses. Integration of such tyre models to the FE or SPH soil models may pose further challenges in view of the computational complexities. A computationally efficient structural model of a radial-ply truck tyre (295/75R22.5), reported in [191], is thus selected in this study. This tyre model was formulated based upon simplification of a comprehensive structural tyre model [109], considering the carcass and belts as multiple individual layers of solid and shell elements so as to separately account for the rubber matrix and the reinforcing fibers. The comprehensive model was simplified by compressing the stack of individual solid and shell elements into single-layered elements

with multi-layered configuration using the Part-Composite approach in LS-DYNA [107]. The approach permits representation of multiple plies by a single composite element and thereby yields substantial reduction in the number of elements. The influences of the material, thickness and cord angle properties of different plies are incorporated in each composite element by automatically arranging the pertinent integration points through the thickness of the layered element. Using this method, the individual elements that separately account for the rubber matrix and the reinforcing fibers could be lumped together and represented as a single layer of shell elements with multi-layered definition. This simplification resulted in 63.5 % reduction in the number of elements compared to the comprehensive tyre model [109], and thus enhanced the computational efficiency. The method of simplification is described in details in [191]. The study also demonstrated validity of the simplified tyre model in terms of vertical force-deflection, cornering force/moment and vibration characteristics through comparisons of the results with the available experimental data [12] as well as with those obtained from the comprehensive tyre model on a rigid surface [109, 190].

Figure 6.2(a) illustrates the exploded view of the simplified tyre model structure, which includes the major components of a pneumatic tyre, namely, carcass, belts, tread and bead fillers. The sidewalls are represented via a single layer of composite shell elements containing two plies of elastic materials for the rubber matrix together with three plies of the orthotropic material and radial cords reinforcements. The crown region is also modeled using a layered composition made of two plies of elastic materials accounting for the rubber matrix in the carcass and belt, respectively. The belt rubber matrix is reinforced by two orthotropic plies with cords aligned at angles of $\pm 22^{\circ}$, while the rubber matrix of the carcass comprises an orthotropic ply of radial cords. The tread and bead fillers are represented by solid elements with hyper-elastic rubber material properties. The mesh of the tread was modified such that the grooves are entirely omitted so as to reduce the processing time for the contact algorithm at the interface of the tread elements with the soil particles in the SPH model.

Figure 6.2(b) illustrates the three-dimensional finite element mesh of the simplified tyre model, which is created via revolving the tyre cross-section about the tyre axis at equal increments. After a grid study, a finite element mesh with 96 equal sectors, being

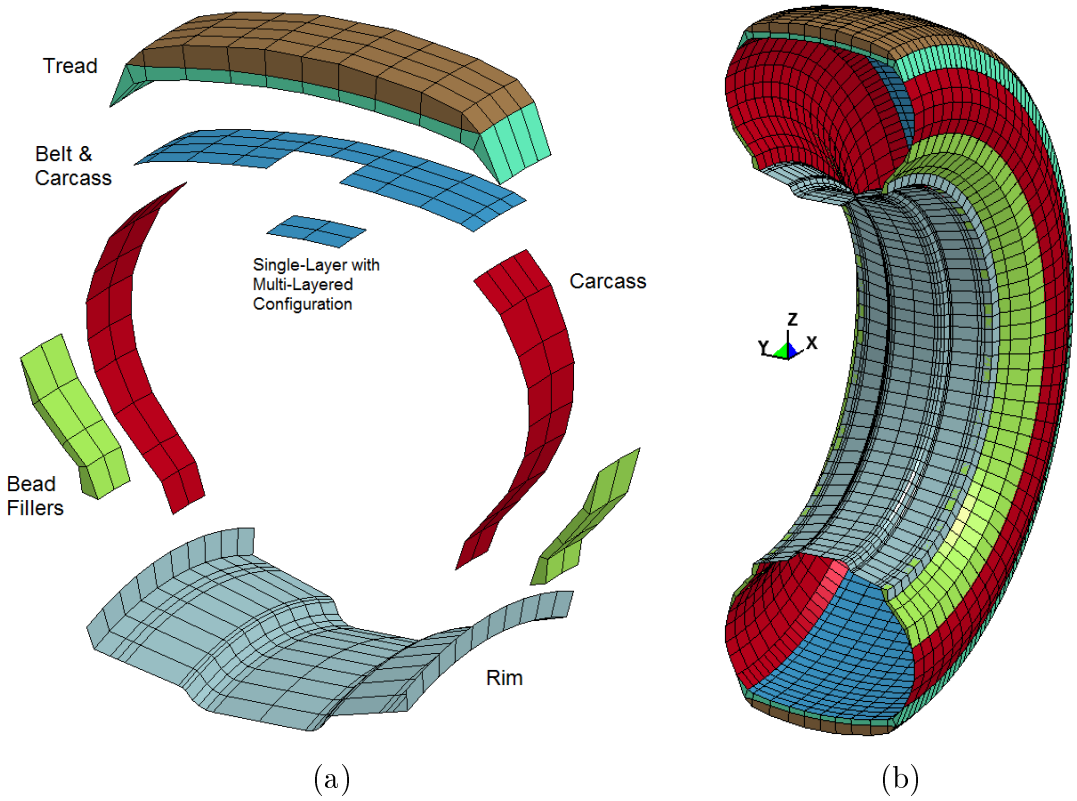

Figure 6.2: (a) Exploded view of the simplified tyre model structure, and (b) three-dimensional finite element mesh considered for both the pneumatic tyre and the rigid wheel models, chosen from a previous study [191]

refined to 192 subdivisions for smoothing the outer circumferential regions, was selected for the tyre dynamics simulations, as described in [191]. Considering the above-mentioned number of divisions and subdivisions, the tyre model includes 4992 solid rubber elements as well as 3840 composite shell elements. The tyre mesh is subsequently coupled with a wheel rim, made of 2304 rigid shell elements, using shared nodes.

The material models applied to the simplified tyre model together with the element formulations used for different components of the tyre structure model have been described in details in [109, 191]. Briefly, the elastic material model (type 1), available in the LS-DYNA material library [104], was used to describe the rubber matrix, while the material data were taken from [198]. The fiber-reinforced plies were described using the composite

material model (type 22) [104], with orthotropic properties derived from those of pure rubber and twisted cords. Multiple plies of the rubber matrix and the reinforcing fibers with pertinent material properties, thicknesses and fiber orientations were combined and represented by composite shell elements. These multi-layered elements were formulated using the fully-integrated shell element (type 16) [199] in conjunction with the hourglass energy control type 8, which activates warping stiffness for the shell type 16 to enhance solution accuracy. The solid elements representing the tread and bead fillers were modeled using the Mooney-Rivlin material model (type 27) [104], with material parameters extracted from [12]. These elements were formulated using the one-point-integration solid elements (type 1) together with the hourglass energy control type 5 [107]. The wheel rim was modeled as a rigid body using the rigid material model (type 20) [104]. The tyre inflation pressure was modeled via applying a uniformly distributed normal load to the inner layer of the carcass elements.

6.3.2 Finite element model of the rigid wheel

An alternate rigid wheel model is also constructed to study its interactions with the soil. The model is formulated with geometry identical to that of the simplified tyre model, as seen in Figure 6.2(b). The constitutive models, however, are changed to the rigid material model (type 20). Both the pneumatic tyre and rigid wheel models were employed in the stationary tyre sinkage test simulations to investigate the tyre-soil contact interface characteristics in the presence/absence of the tyre compliance property. The simulation results were used to determine the radius and angular boundaries of the contact interface, the penetration depth and the tyre vertical deflection. A relatively lower inflation pressure of 483 kPa (70 psi) is used for the pneumatic tyre model in the sinkage test simulations so as to study the influence of the tyre compliance on the contact interface characteristics. The rigid wheel model was also found to be useful in the rolling tyre test simulations, particularly for characterizing the radial and tangential stress distributions in the FE and SPH soil models. The characterization of the tyre-soil contact properties under a rolling tyre poses considerably higher computational demand due to requirement of a relatively lengthy route of soil elements (or particles). In this situation, the rigid wheel model can

facilitate simulations with greater computational efficiency as it eliminates the excessive processing time associated with the tyre elements, and permits more thorough analysis of soil elements. The computing efficiency of the wheel model is further enhanced by taking advantage of the symmetry in the tyre geometry. Three different mesh constructions are thus considered for different tests: (i) a quarter tyre mesh for the stationary tyre sinkage test simulations; (ii) a half mesh for the rolling tyre simulations; and (iii) a full mesh for the steered tyre simulations.

6.3.3 Integrated tyre/wheel-soil models

Both the FE and SPH soil models, described in Part I of the study, are integrated to the simplified FE tyre model to formulate a virtual tyre-soil interaction platform. The integrated model is formulated for two different types of soils, namely: a high density clayey sand, referred to as the *unwashed sand*, and a coastal sand, known as the *high density wet sand*, whose properties have also been described in Part I. Similar to the case of rigid plate-soil contact, the contact between the tyre/wheel elements and the FE soil elements is described using the *automatic surface to surface contact* algorithm in LS-DYNA [105, 107]. The Coulomb friction is considered to account for the tyre-soil frictional contact, while the static and dynamic coefficients of friction are selected as 0.55 and 0.5, respectively, to simulate a deformable surface [142]. The *pinball segment base contact* algorithm (SOFT=2) is activated in conjunction with applying 10% viscous damping perpendicular to the contacting surfaces so as to smooth the tyre-soil contact and maintain stable rolling wheel simulations. The contact between the tyre/wheel elements and the SPH soil particles, however, is modeled using the *automatic nodes to surface contact* algorithm in conjunction with the *soft constraint formulation* (SOFT=1), while the soil and tyre are considered as the slave and master parts, respectively. An offset thickness is defined for the SPH soil particles in the contact model to consider the radius of the soil particle spheres in the contact solution.

Soil domains and simulation scenarios

Soil domains for the couple tyre-soil simulation models are defined considering three different simulation scenarios, namely: (i) stationary tyre/wheel sinkage test; (ii) rolling wheel test; and (iii) steered wheel test. Owing to the excessive computational demand of the rolling tyre-soil model, the simulations in scenario (ii) and (iii) are limited only to the rigid wheel model.

The stationary tyre-sinkage test simulation is conducted to evaluate tyre/wheel penetration into a ($600 \times 600 \times 600\ mm$) rectangular soil domain. Taking advantage of symmetry of the tyre and the soil sample, only a quarter of the soil box and the tyre is modeled. The soil box is meshed with ($30 \times 30 \times 23 = 20700$) elements in the FE model, and ($30 \times 30 \times 30 = 27000$) particles in the SPH model. The depth of the FE soil model is meshed with 23 elements, which includes 15 uniformly-distributed elements of 20 mm size up to the half-depth and 8 non-uniformly-distributed elements with growing increments of 5 mm toward the end of the soil depth. The simulations are performed using the rigid wheel model, representing a high inflation pressure tyre, and a pneumatic tyre model with low inflation pressure to study the effect of the tyre compliance. In this simulation, the tyre/wheel is subjected to 60 mm vertical displacement inward the soil over a duration of 6 s in a ramp manner. The simulation results are used to characterize the radius and the angular boundaries of the contact interface (Figure 6.1) as well as the vertical deflection of the tyre and depth of penetration into the soil, which are subsequently used in the terramechanics-based tyre-soil models. The stress distributions along the contact region and thereby the vertical contact force obtained from the terramechanics-based models are compared with those predicted by the couple tyre-soil simulation model in order to evaluate the effectiveness of the identified soil parameters and terramechanics models.

For the rolling wheel test simulations, a route of soil, made of either elements or particles, is subjected to the rolling wheel. The test is conducted in two sequential stages. The wheel initially penetrates into the soil to a certain depth (60 mm) in 1 s. In the second stage, the wheel is permitted to roll at a defined speed (5 km/h) for 2 s, while its sinkage is held constant. Owing to symmetry of the wheel and soil geometries in the x-z plane, a half

soil model ($3980 \times 600 \times 600\ mm$) is used for the rolling wheel simulations, which is meshed with ($199 \times 30 \times 23 = 137310$) elements in the FE model, and ($199 \times 30 \times 30 = 179100$) particles in the SPH model. The length of the route was taken as 3980 mm so as to provide 2 s rolling simulation in addition of approximately 600 mm bounds on either side of the route. The radial and tangential stress distributions, and the longitudinal contact force and the resulting moment obtained from the terramechanics-based formulations are compared with those predicted from the rolling wheel-soil simulation model to examine the effectiveness of the identified terramechanics-based models. Two maneuvers are considered: a driven wheel and a towed wheel, since the normal and shear stress distributions for the two conditions differ considerably, as described in section 6.2.1.

In the steered wheel test simulations, a route of soil is subjected to a steered rolling wheel with a constant side-slip angle. This test is conducted in three stages involving penetration, rolling and steering of the wheel. Similar to the rolling wheel test, the wheel is initially penetrated 60 mm into soil in 1 s. While the sinkage is held constant, the wheel is driven to reach 5 km/h speed in 1 s in a ramp manner. In the final stage, the rolling wheel is subjected to steering, after it achieves the steady speed, by increasing the side-slip angle to a predefined constant value (6°) in a ramp-step manner in 2 s. For this purpose, a ($5380 \times 1200 \times 600\ mm$) soil domain is defined, which is meshed with ($269 \times 60 \times 23 = 371220$) elements in the FE model, and ($269 \times 60 \times 30 = 484200$) particles in the SPH model. The domain length of 5380 mm is selected so as to provide the required route for a rolling wheel at a speed of 5 km/h and duration of 3 s. The lateral force and the aligning moment in response to a constant side-slip angle obtained from the terramechanics-based formulations are compared with those predicted from the steered wheel-soil simulation models in order to evaluate the effectiveness of the identified terramechanics models.

6.4 Results and discussions

The effectiveness of the terramechanics-based models identified from the virtual soil test simulation platform is assessed by comparing model responses in terms of the forces/moments with those predicted from the computational tyre/wheel-soil interactions model. The radial

and tangential stresses, and the forces/moments developed at tyre/wheel-soil interface are thus evaluated from both the terramechanics formulations, denoted as *theoretical* thereafter, and the computational tyre/wheel-soil model, denoted as *computational*. The evaluations are performed for the stationary, rolling and steered tyre/wheel using the simulation scenarios described in section 6.3.3.

6.4.1 Stationary tyre/wheel sinkage

The pressure-sinkage model, identified from the virtual soil test simulations, is used to determine the radial stress and normal force developed due to penetration of a stationary tyre. The results are obtained for both a rigid wheel and a compliant tyre considering two different soils (unwashed sand and high density (HD) wet sand). The soil material model parameters identified on the basis of laboratory test data for the virtual soil test platform in Part I are used. The radial stress and normal force responses are also obtained from the coupled tyre-soil computational model employing both the FE and SPH soil models. The simulations are initially performed using a rigid wheel model representing a high inflation pressure pneumatic tyre, assuming negligible tyre deflection compared to that of the soft soil. The simulations are then repeated for the pneumatic tyre model with inflation pressure of 483 kPa (70 psi) to investigate the contribution of the tyre deflection in the vertical tyre-soil interactions.

Figures 6.3(a) and 6.3(c) illustrate the deformed shapes as well as the pressure distributions within the two soils when subjected to a 60 mm vertical displacement of the rigid wheel model. The simulation results are obtained using the FE soil model coupled with models of the rigid wheel and the pneumatic tyre. The results revealed 60 mm penetration of the rigid wheel model into both the soils. The contact arc was observed to be symmetric about wheel center ($\theta_{2,1} = \mp 28.16^{\circ}$) with contact arc radius $R = 507\ mm$, identical to the radius of the wheel. For the pneumatic tyre, however, as exemplified in Figure 6.3(b), the applied displacement produced only 13.8 mm penetration in the unwashed sand together with 46.2 mm deflection of the tyre, while the steady-state or maximum contact arc was observed within $\theta_{2,1} = \mp 8.45^{\circ}$ with arc radius $R_{max} = 1270\ mm$. For the relatively softer high density wet sand, the maximum sinkage and tyre deflection were 35.2 and 24.8 mm,

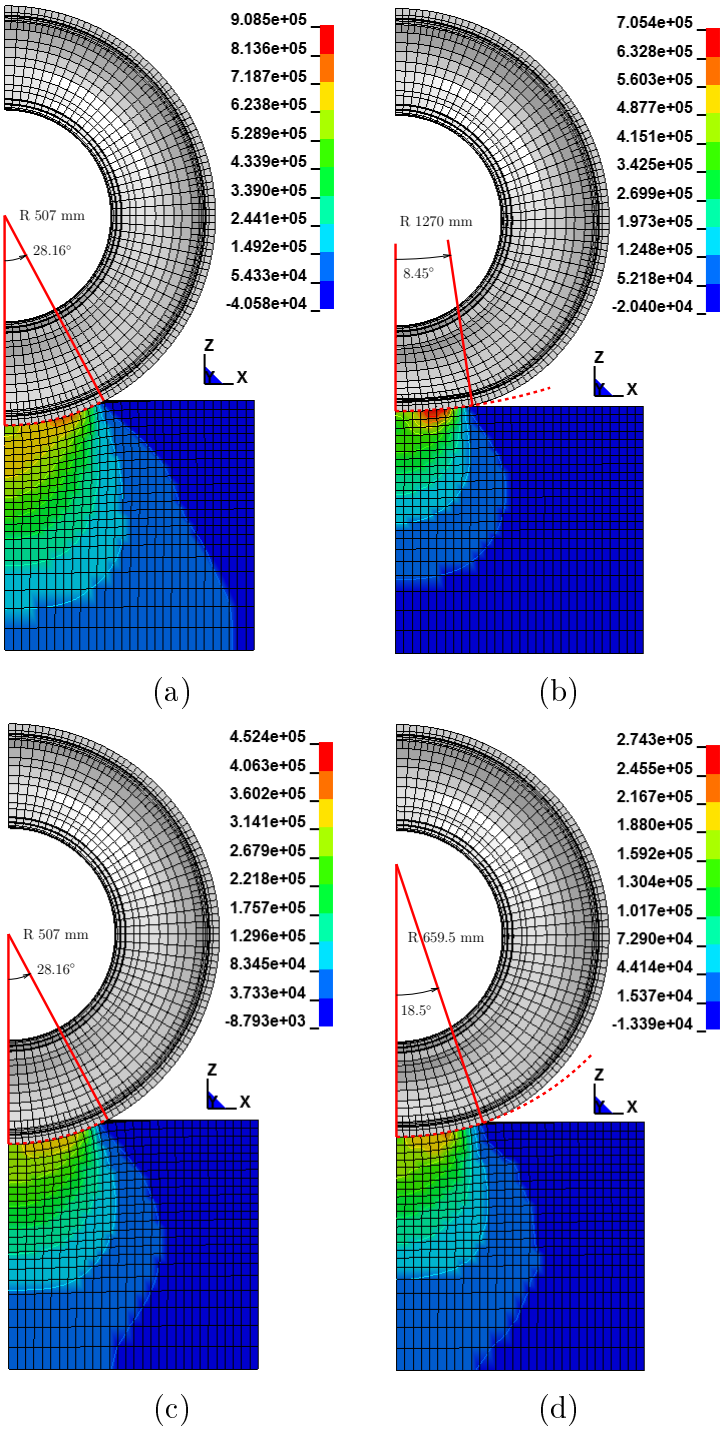

Figure 6.3: Comparisons of deformed shapes and pressure distributions for (a,b) unwashed sand, and (c,d) high density wet sand under a 60 mm vertical displacement imposed by (a,c) a rigid wheel, and (b,d) a pneumatic tyre

respectively. The contact arc occurred within $\theta_{2,1} = \mp 18.5°$ with $R_{max} = 659.5\ mm$, as seen in Figure 6.3(d). These values, which describe the contact geometry of the rigid wheel and the pneumatic tyre models when penetrating in the two soils are summarized in Table 6.1. For the pneumatic tyre, the radius of the contact arc is greater than the wheel radius for both the soils. The radius of the contact arc (R) is directly related to sinkage z during penetration. Assuming linear variation in R with z, yields following relationship:

$$R(z) = r + \frac{z}{z_{max}}(R_{max} - r) \tag{6.18}$$

where z_{max} is the maximum sinkage of the tyre into soil and r is the free tyre radius. The above equation is applied to determine the distribution of tyre/wheel sinkage into the two soils using Equation (6.5), and thereby the distribution of the radial stress from Equation (6.3).

Figure 6.4(a) illustrates the distributions of the tyre/wheel sinkage $\zeta(\theta)$ into the two soils obtained from Equation (6.5). The results show that the changes in the penetration depth z directly affect the size of the contact region. The rigid wheel yields identical sinkage distributions for both soils, as expected. The compliant tyre, on the other hand,

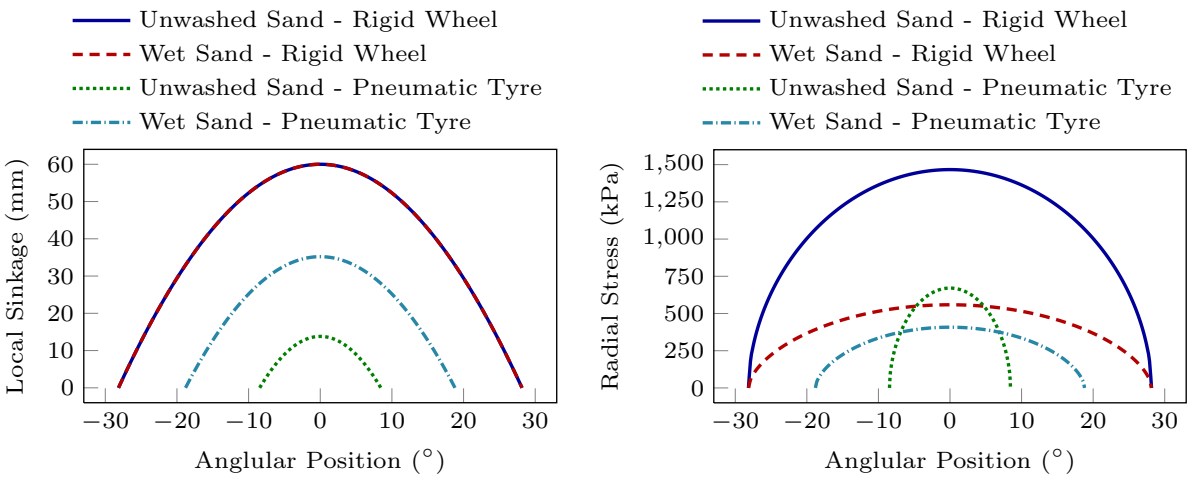

Figure 6.4: Distributions of (a) sinkage, and (b) radial stress along the contact region obtained from the theory for the rigid wheel and the pneumatic tyre on two soils

reveals significantly smaller sinkage and contact length on both soils compared to the rigid wheel. Furthermore, the maximum sinkage and the contact length are substantially lower for the relatively stiffer unwashed sand compared to the high density wet sand.

Figure 6.4(b) illustrates the distribution of the radial stress $\sigma_r(\theta)$ obtained from Equation (6.3) using the pressure-sinkage model parameters k_c, k_ϕ and n identified from the virtual soil test simulations. The distribution of radial stress along the contact patch is also significantly influenced by the tyre and soil properties, as seen in Figure 6.4(b). The peak radial stress $\sigma_r(\theta_m)$ obtained from the theory are compared with those observed from the computational FE model in Table 6.1. The rigid wheel yields significantly higher peak stress for the relatively stiffer unwashed sand (1466 kPa) compared to the high density wet sand (558 kPa), although the contact lengths are identical for both soils. The results for the rigid wheel with 60 mm sinkage revealed that the theory overestimates the maximum radial stress by 38.1% for the unwashed sand and by 19% for the HD wet sand compared to the computational FE model. This suggests that for the HD wet sand, the theory better correlates the simulation results within the range of applied sinkage compared to the unwashed sand. The deviation for the unwashed sand, however, may be attributed to the fact that the material model used in the computational soil model undergoes failure in response to such a high penetration (60 mm), which results in developing lower pressure

Table 6.1: Comparisons of contact geometry of the rigid wheel and pneumatic tyre models penetrating into the two soils together with maximum radial stress obtained from the theoretical and computational FE models

	Rigid wheel		*Pneumatic tyre*	
Quantity	*Unwashed*	*HD wet*	*Unwashed*	*HD wet*
Contact angles $\theta_{2,1}(^\circ)$	$\mp$28.16	$\mp$28.16	$\mp$8.45	$\mp$18.5
Contact radius R_{max} (mm)	507	507	1270	659.5
Tyre sinkage z_{max} (mm)	60	60	13.8	35.2
Tyre deflection (mm)	0	0	46.2	24.8
Theoretical $\sigma_r(\theta_m)$ (kPa)	1466	558	670	407
Computational $\sigma_r(\theta_m)$ (kPa)	908	452	705	274
Percentage error $\sigma_r(\theta_m)$ (%)	38.1	19	-5.2	32.7

compared to the theory. The radial stress developed by the pneumatic tyre for both the soils are substantially lower compared to the rigid wheel, which is due to lower sinkage of the pneumatic tyre into the soils. The results for the pneumatic tyre show that the deviations between the theoretical and computational results are -5.2% and 32.7% for the unwashed sand and HD wet sand, respectively. The better correlation of the theory with simulation for the unwashed sand is attributed to its lower sinkage when subjected to a penetrating pneumatic tyre compared to the HD wet sand.

Figure 6.5 compares the deformed shapes as well as the pressure distributions obtained from the FE and SPH models of the two soils under the 60 mm penetration by a rigid wheel. The results show slightly higher levels of pressure of the FE soil models compared to the SPH soil models throughout the contact region. Both the FE and SPH soil models, however, yield similar pressure distribution patterns for both types of the soils. The differences between the peak pressure predicted by the FE and SPH soil models is considerably smaller than that obtained under the plate sinkage test presented in Part I. For example, in the plate sinkage test for the unwashed sand under 60 mm sinkage, the FE model overestimated the peak pressure by 31.5% compared to the SPH model. In the wheel sinkage test, however, for the unwashed sand under 60 mm sinkage, the FE and SPH models yield very close peak pressures, as seen in Figures 6.5(a) and 6.5(b). This is attributed to difference in the geometry of the plate and wheel. The soil in the vicinity of the plate edges is more likely to experience greater shear compared to the wheel, particularly under higher penetration. The two simulation methods (FE and SPH) thus exhibit relatively smaller differences when subject to loading by the wheel/tyre geometry.

Figure 6.6(a) compares the normal contact force F_z estimated from the theory with those predicted by the computational models employing FE and SPH methods. The variations in normal force are presented for both soils as a function of the wheel sinkage. The theoretical value of F_z is obtained from the identified pressure-sinkage model and Equation (6.2). Although the theory tends to overestimate the maximum radial stress under a rigid wheel compared to the simulation results (Table 6.1), relatively better correlations are observed between the forces obtained from the theory and the computational models. This is likely due to integration of the radial stress. As expected, the FE soil models yield

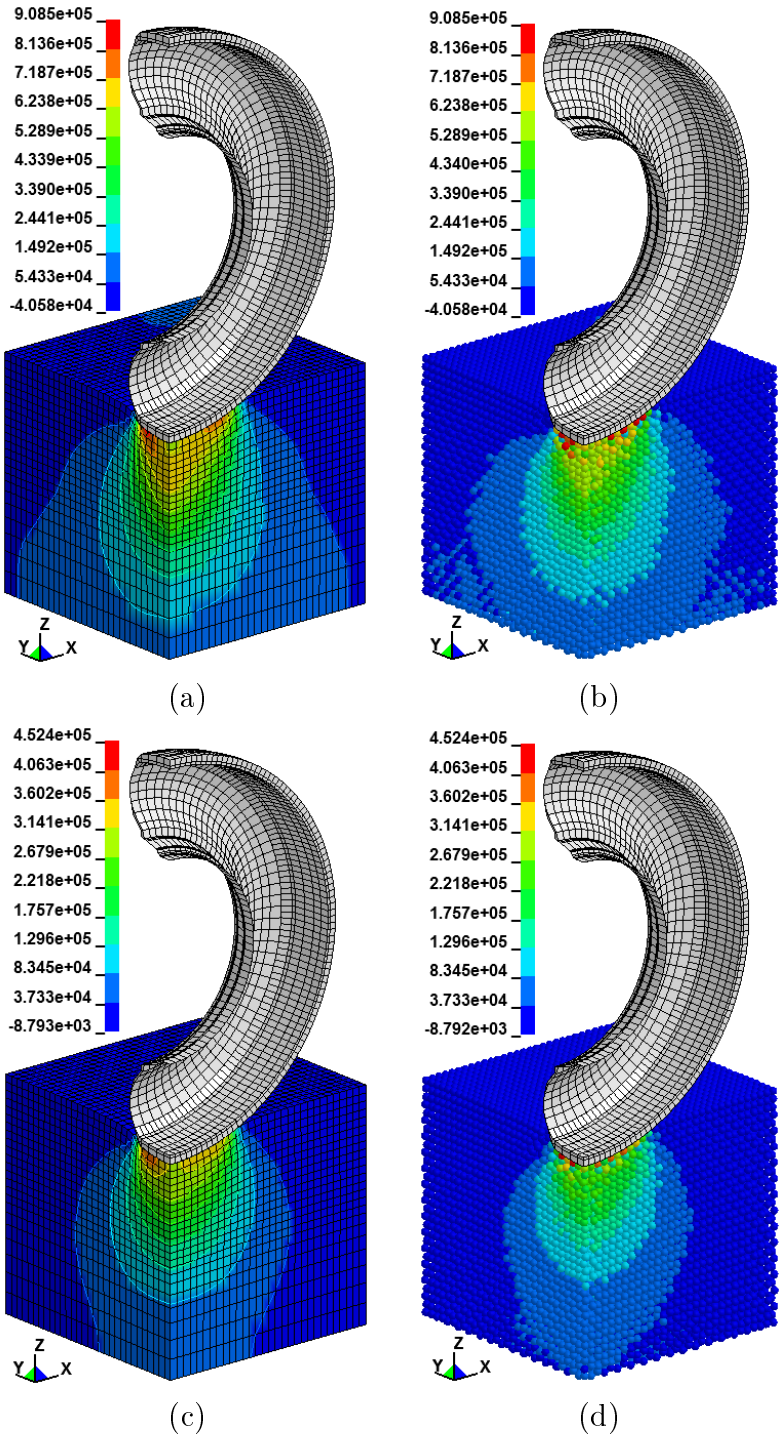

Figure 6.5: Comparisons of deformed shapes and pressure distributions in the FE and SPH soil models under 60 mm sinkage of a rigid wheel for (a,b) unwashed sand and (c,d) high density wet sand

higher magnitudes of F_z compared to the SPH soil models over the entire range of sinkage for both the soils. Reasonably good agreements between the forces estimated from the theoretical and the computational models are evident under lower sinkage. The theoretical estimations tend to lie between those obtained from the FE and SPH soil models under higher sinkage.

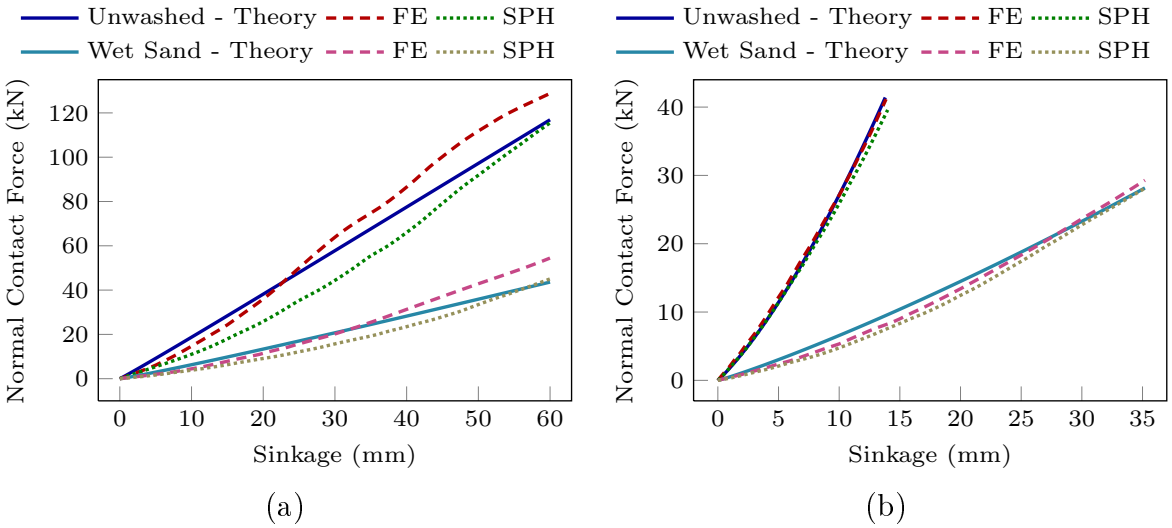

Figure 6.6: Comparisons of normal contact force estimated by the theory (identified pressure-sinkage model) for (a) the rigid wheel and (b) the pneumatic tyre as a function of sinkage with those obtained using the FE and SPH soil models for two soils

Figure 6.6(b) compares the normal forces due to penetration of the pneumatic tyre into the two soils. Unlike the rigid wheel, the theoretical forces are in good agreement with those predicted from the computational models employing FE and SPH soil models. This is due to relatively lower penetration of the pneumatic tyre compared to the rigid wheel. The results in Figure 6.6 and Table 6.1 suggest reasonably good validation of the pressure-sinkage terramechanics models of the soils, identified from the virtual soil tests. The identified model can thus be applied to obtain accurate estimations of the radial stress and normal force developed at the tyre-soil interface in an efficient manner.

6.4.2 Rolling wheel

The effectiveness of the terramechanics model, describing the shear stress-displacement characteristics of the soils, is evaluated considering interactions of the rolling wheel (driven and towed) with the soil. For this purpose, the computational model simulations are performed to obtain tangential stress distribution over the contact region. The contact force F_x and the moment M_y are subsequently obtained through integration of the tangential stress over the contact region. The simulations are performed for the rolling angular speed of 2.74 rad/s (theoretical forward speed=5 km/h).

Driven wheel

The contact force F_x and the moment M_y are estimated from the theoretical formulations in Equations (6.6) and (6.8) to evaluate the terramechanics model identified from the virtual soil test simulations. For the driven wheel, the sinkage distribution and the coordinates of the maximum radial stress (θ_m) are initially determined using Equation (6.10). The constants c_1 and c_2 are chosen from the reported values for comparable soils [19, 21]. The coefficient c_1 is selected as 0.38 and 0.43 for the unwashed sand and the high density wet sand, respectively, while c_2 is chosen as 0.32 for both the soils. Figures 6.7(a) and 6.7(b) present the deformed shapes as well as the radial stress distributions in the FE and SPH models of the high density wet sand coupled with the rigid wheel driven at 2.74 rad/s after 60 mm penetration. The results show nearly negligible rut recovery suggesting sinkage ratio $\eta = 0$. Considering the sinkage of 60 mm, the angles θ_1 and θ_2, defining the contact length, are obtained as 28.16° and 0°, respectively, using Equation (6.1). The simulation results also revealed longitudinal speed of the wheel as 1.11 m/s, and thereby the slip ratio of 20%. For the 20% slip ratio, the location of θ_m for the high density wet sand is subsequently obtained as 13.91° from Equation (6.10), which is indicated by dashed lines in Figures 6.7(a) and 6.7(b) for the FE and SPH soil models, respectively. These also coincide with the position of maximum radial stress predicted by the FE and SPH soil models, as seen in Figures 6.7(a) and 6.7(b). This verifies the appropriateness of the coefficients c_1 and c_2 chosen for the high density wet sand in Equation (6.10).

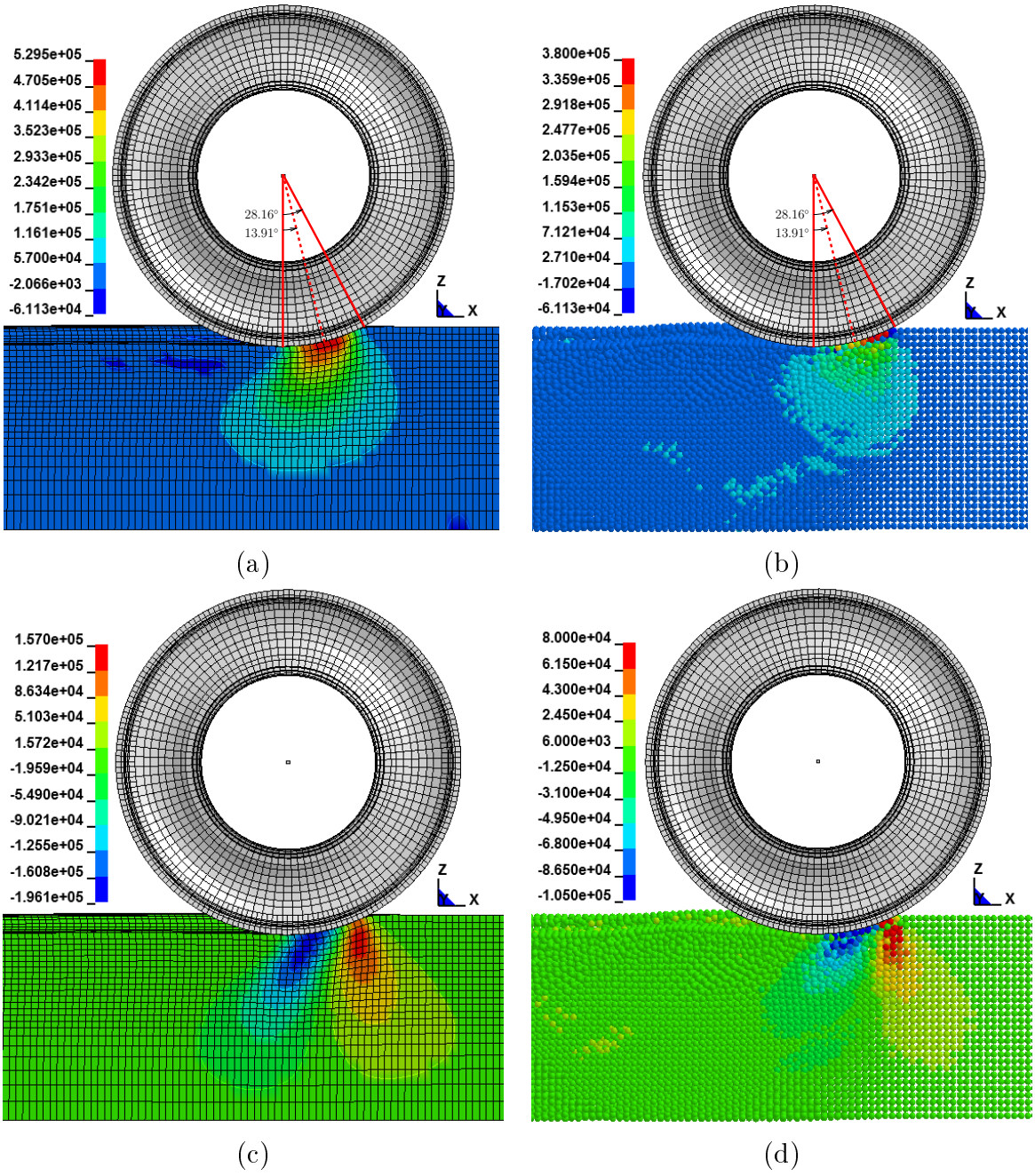

Figure 6.7: Comparisons of (a,b) pressure distributions and (c,d) shear stress distributions predicted from FE and SPH models of the high density wet sand under a driven wheel

For evaluations of the driving force F_x and the driving moment M_y, the radial and tangential stresses are initially characterized, which necessitate the local sinkage and shear displacement properties. The distributions of the sinkage and the radial stress are evaluated

considering three different slip ratios (0, 20 and 40%) to study the effect of slip ratio on the resulting F_x and M_y. Figures 6.8(a) and 6.8(b) illustrate the local sinkage $\zeta(\theta)$ and radial stress $\sigma_r(\theta)$ distributions, respectively, under the 60 mm penetration for different slip ratios. The results are obtained using the identified parameters for the two selected soils. The results show that the location of θ_m shifts forward with increasing slip ratio for both the soils. The maximum radial stress corresponding to 20% slip is estimated as 470 kPa from the theory for the high density wet sand, as shown in Figure 6.8(b). Compared to the theoretical peak radial stress, the FE soil model revealed higher value of peak stress (529 kPa), while the SPH soil model exhibited lower value (380 kPa), as seen in Figures 6.7(a) and 6.7(b), respectively.

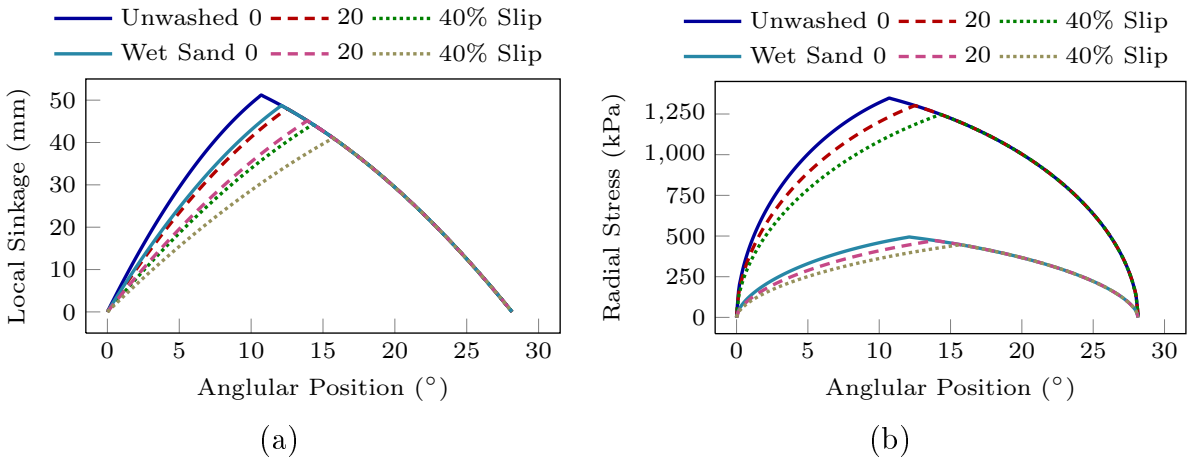

Figure 6.8: Theoretical (a) sinkage and (b) radial stress distributions along the contact region for a rigid wheel driven at varying slip ratios under 60 mm sinkage on two soils

Figures 6.7(c) and 6.7(d) illustrate the shear stress distributions obtained from the FE and SPH models for the high density wet sand. The stress contours exhibit two distinct zones of shear stress with opposite signs, suggesting the existence of a transition point in the contact region, where the shear stress changes its direction. The shear stress distributions also show that the rear zone with negative shear stress primarily contributes the contact patch. While the soil slides backward towards the rear zone due to negative shear stress, it tends to slide upward along the wheel within the smaller front zone with positive shear stress. In the SPH soil model, the front zone is even smaller than that in the FE model since

the particles possess greater degree of flexibility for sliding along the wheel. Experimental studies [19, 20] have also shown that the front zone beneath a driven wheel is very small compared with the rear zone, particularly at higher slip ratios. As a result, this zone has been considered negligible in the theory for the driven wheel [19].

Figures 6.9(a) and 6.9(b) illustrate the distributions of the shear displacement $j_x(\theta)$ and the shear stress $\tau_x(\theta)$ along the contact region for both the soils at varying slips, which are obtained from Equations (6.11) and (6.9), respectively. The shear displacement and stress are in the rearward direction, while the peak shear displacement occurs at the rear end of the contact region ($\theta_2 = 0$). The theoretical formulation considers only the rear zone of tangential stress assuming rearward shear direction and maximum shear stress occurring at θ_m, as in the case of radial stress [19]. This is evident from Equation (6.9), which suggest direct effect of radial stress on the soil strength and thus the resulting shear stress. The peak shear stress for the high density wet sand at 20% slip is estimated as 314 kPa (rearward), which is considerably higher compared to the corresponding estimates of -196 and -105 kPa from the FE and SPH model simulations. Such overestimation of the shear stress is likely caused by neglecting the front zone of shear stress in the theory for the driven wheel.

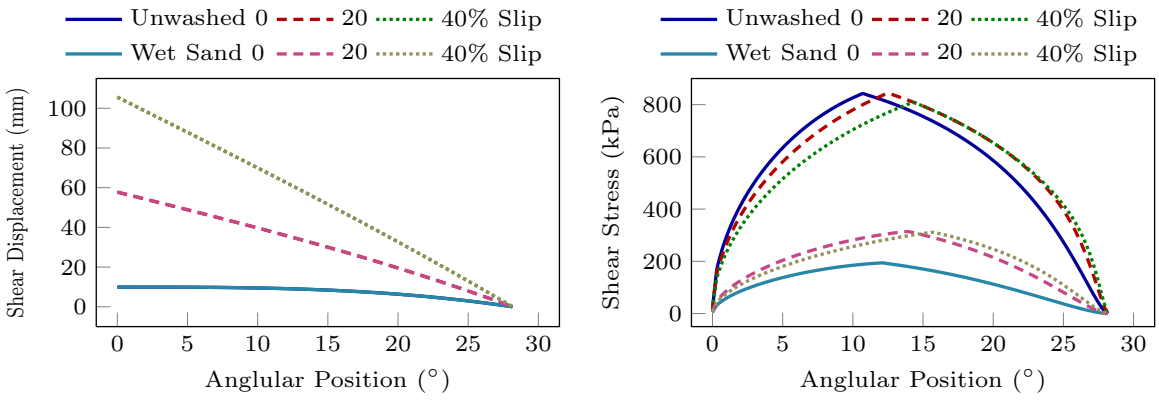

Figure 6.9: Theoretical (a) shear displacement and (b) shear stress distributions along the contact region for a rigid wheel driven at varying slip ratios under 60 mm sinkage on different soils

Figures 6.10(a) and 6.10(b) illustrate the driving force F_x and the resulting moment M_y developed for the selected soils at different slip ratios. According to Equation (6.6), the contact force F_x consists of two distinct terms: a positive *thrust* (F_τ) resulting from τ_x, and a negative *motion resistance* (F_σ) associated with σ_r. Figure 6.10(a) shows the variations in total F_x together with the thrust and resistant components as a function of the slip ratio. The thrust force approaches the peak at a very low slip and then declines with further increase in the slip. The variations in the resistant force are considerably small compared to the thrust force over the entire range of slip. This suggests that the resistant force F_σ is nearly independent of the slip. As a result, both the driving force and moment exhibit trends similar to the thrust force F_τ with varying slip. The observed trends in the total driving force, the thrust and resistant components, and the driving moment are comparable with those reported from experiments for a driven wheel on different sands [19, 149].

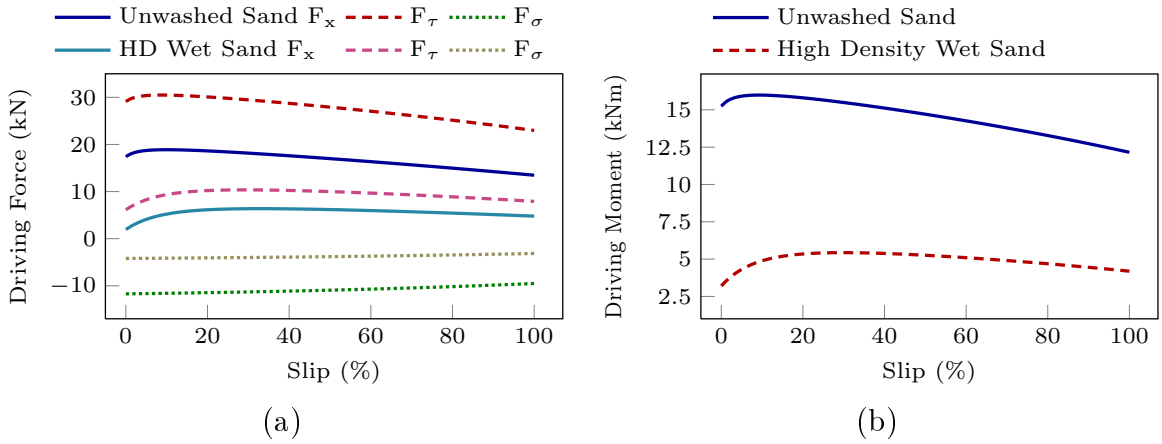

Figure 6.10: Theoretical (a) driving force together with its shearing and radial stress terms (F_τ and F_σ) and (b) driving moment as functions of slip for a rigid wheel driven at 60 mm sinkage on different soils

Figures 6.11(a) and 6.11(b) illustrate the time histories of the contact force F_x and the resulting moment M_y predicted from the FE and SPH models for the high density wet sand when subjected to a driven wheel at 2.74 rad/s angular speed and 60 mm penetration. The angular speed, applied in a ramp manner, resulted in the steady longitudinal speed of 1.11 m/s, and a slip ratio of 20%. The peak driving force from the FE and SPH soil models are

obtained as 6.75 and 5.77 kN, respectively. These are comparable with 6.1375 kN estimated from the theory based on the identified terramechanics models. Furthermore, the peak moments of 6.14 and 4.8 kNm obtained from the FE and SPH soil models, respectively, are also comparable with that estimated from the theory (5.344 kNm). Similar degree of agreement was also observed for the unwashed sand. The observed reasonable correlations between the simulation results and the theoretical estimations suggest that the identified terramechanics models can effectively predict traction forces and moments developed by a driven wheel on soft soils. As expected, the FE method overestimated and the SPH method underestimated the theory.

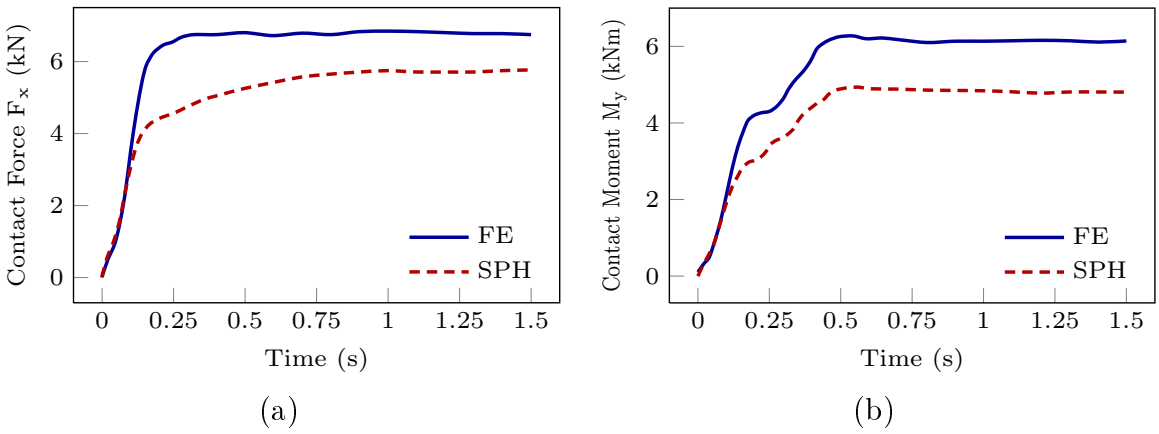

Figure 6.11: Time histories of (a) contact force F_x and (b) contact moment M_y developed by a driven wheel at 2.74 rad/s speed under 60 mm sinkage on the FE and SPH models of the high density wet sand

Towed wheel

Unlike the driven wheel, the front contact zone of shear stress due to a towed wheel is considerably large and cannot be neglected. The front contact zone is determined from the location of the transition point, θ_o, which is estimated from Equation (6.12) for a given skid. For the purpose of verification of the terramechanics-based model, the skid i is estimated from the computational model employing FE and SPH soil models. The simulations of the towed wheel at a forward speed of 5 km/h revealed angular speed of 2.33 rad/s, which resulted in skid ratio of 15% ($i = -0.15$). The location of the transition

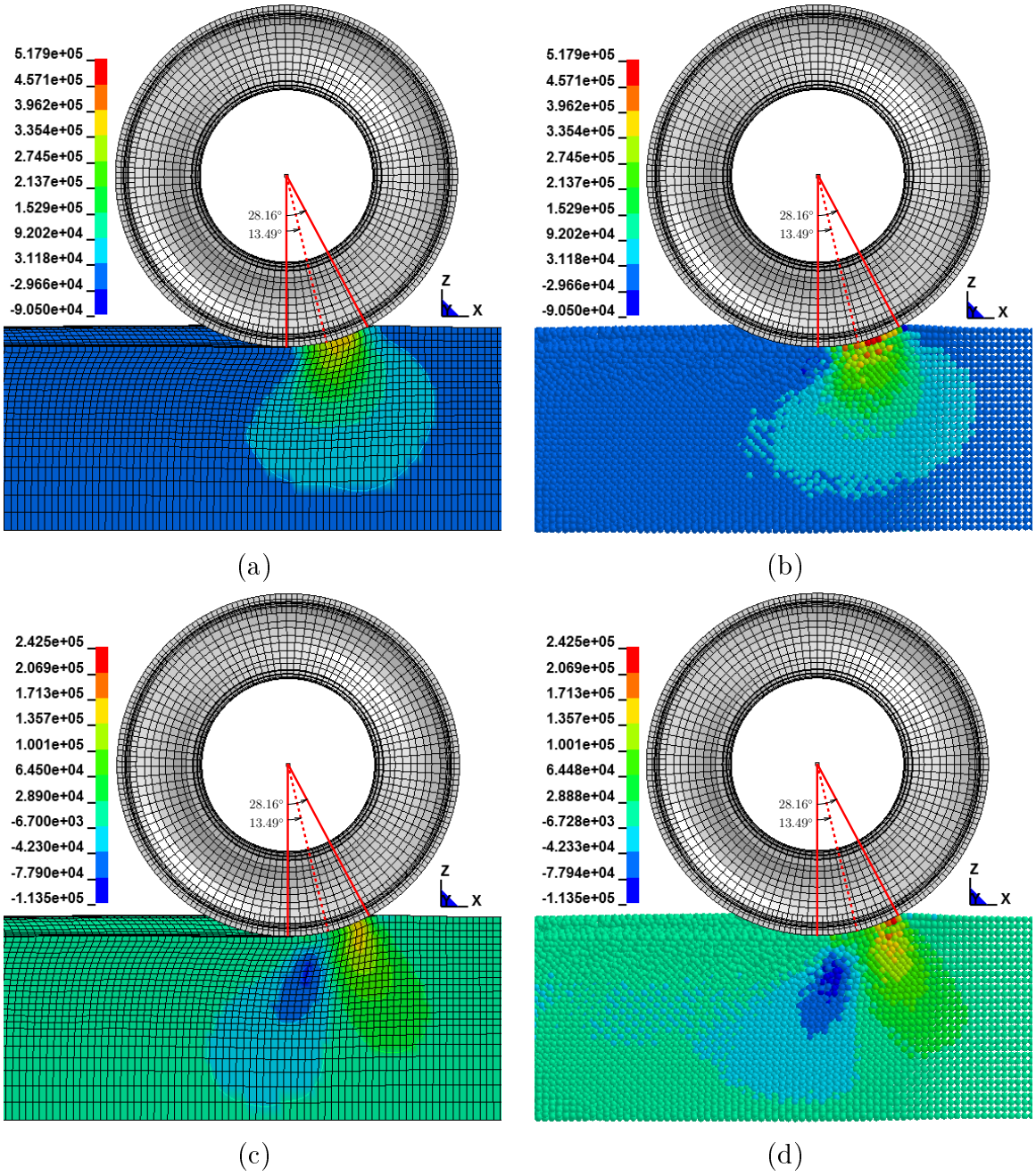

Figure 6.12: Comparisons of (a,b) pressure distributions and (c,d) shear stress distributions predicted using FE and SPH soil models representing high density wet sand under a towed rigid wheel

point, $\theta_{\circ}$, was subsequently determined as 13.49° for the high density wet sand. Figure 6.12 illustrates the deformed shapes as well as the radial and tangential stress distributions in

the FE and SPH soil models for the high density wet sand under the towed wheel. Figures 6.12(c) and 6.12(d) also show the estimated position of $\theta_\circ$ by dashed lines together with the shear stress contours predicted from the FE and SPH soil models. It is evident that this estimated location coincides well with the transition point in the shear stress, and with the maximum radial stress, as seen in Figures 6.12(a) and 6.12(b). The transition point location is also dependent on the skid ratio, as seen in Equation (6.12). The simulation results thus confirm the validity of the location of the maximum radial stress predicted from the theory based on the identified terramechanics model.

Figures 6.13(a) and 6.13(b) illustrate the local sinkage $\zeta(\theta)$ and the radial stress distribution $\sigma_r(\theta)$ considering different wheel skid ratios (10, 15 and 20%) based on the identified parameters of the terramechanics models for the two soils. The sinkage and radial stress distributions are obtained from Equations (6.5) and (6.3), while considering $\theta_\circ = \theta_m$. The results show strong dependence of sinkage and radial stress characteristics on the skid ratio. The peak radial stress and sinkage tend to shift forward with increasing skid. Furthermore, the peak sinkage and stress decrease with increasing skid. The maximum radial stress corresponding to 15% skid is estimated at 477 kPa for the high density wet sand (Figure 6.13(b)), which was comparable with those obtained from the computational models employing FE and SPH soil models at nearly 500 kPa.

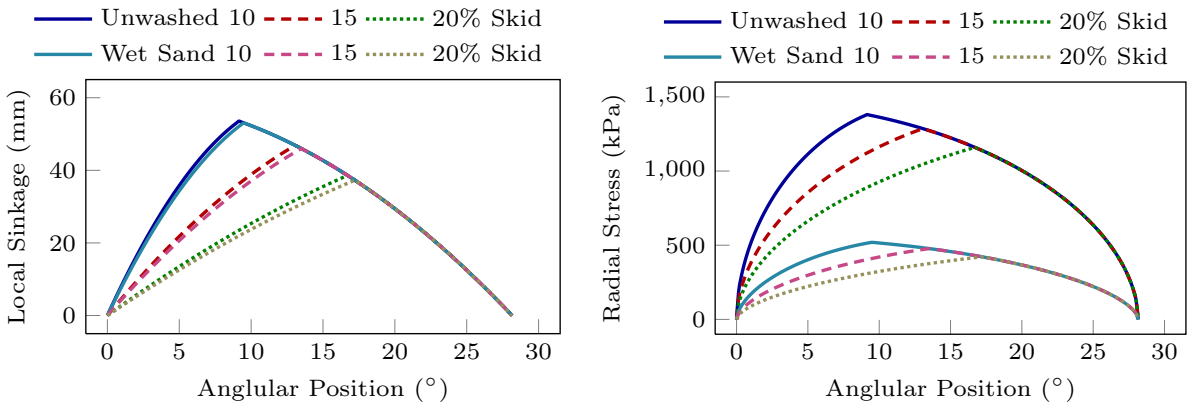

Figure 6.13: Theoretical (a) sinkage and (b) radial stress distributions along the contact region for a rigid wheel towed at varying skid ratios under 60 mm sinkage on different soils

Figures 6.14(a) and 6.14(b) illustrate distributions of the shear displacement $j_x(\theta)$ and the shear stress $\tau_x(\theta)$ over the contact region for the two soils at three different skid ratios (5, 10 and 15%). The shear stress distributions for the unwashed sand, however, are presented for relatively low skid ratios of 3, 4 and 5%, since this soil revealed extremely high shear stresses for skid ratio exceeding 5%. The shear displacement and stress distributions are obtained from Equations (6.13) and (6.9), respectively. The results show nearly identical shear displacement distributions for both soils over the range of skid ratios considered. The results also show maximum shear displacement at the extreme of the rear contact region ($\theta_2 = 0$) for both the soils, while it occurs in the rearward (negative) direction. The shear displacement approaches zero at the transition points $\theta_\circ$, which occurred near 5.1, 9.4 and 13.5° for 5, 10 and 15% skid, respectively. The displacement in the front contact region is also observed as zero at the extreme (θ_1) apart from the transition point ($\theta_\circ$), irrespective of the skid ratio. The distributions in the front region, however, show a slight peak in the displacement between $\theta_\circ$ and θ_1. The shear stress distributions in Figure 6.14(b) show two distinct zones of tangential stress around the transition point (point of zero shear stress) with rearward (negative) direction in the rear and forward (positive) direction in the front. The results clearly show the effect of skid on the transition point and thus the

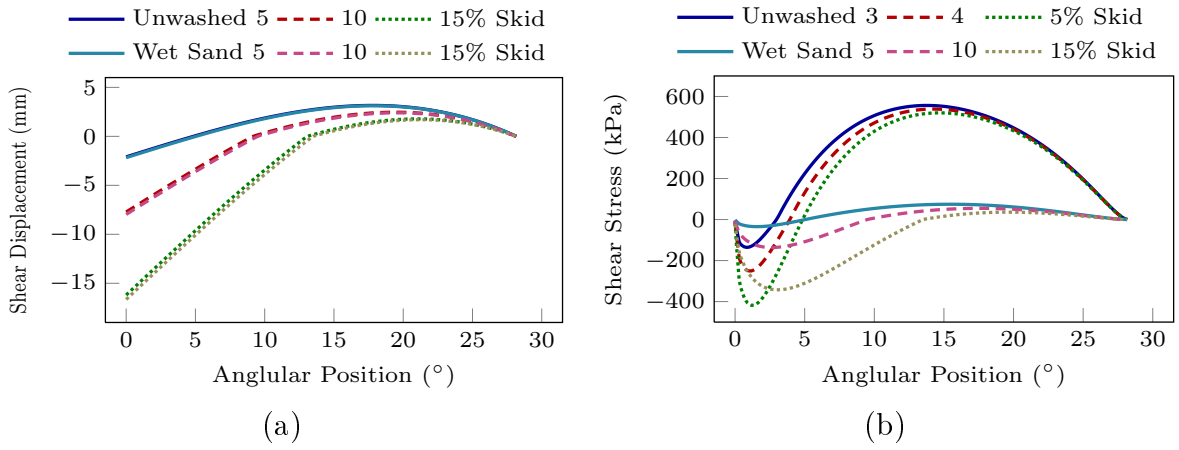

Figure 6.14: Theoretical (a) shear displacement and (b) shear stress distributions along the contact region for a rigid wheel towed at varying skid ratios under 60 mm sinkage on different soils

shear displacement and stress distributions. An increase in the skid causes the transition point to shift forward, while enhancing the size of the rear contact zone. This results in a rapid increase in the peak shear stress in the rear zone, and only a slight decrease in that in the front zone, as seen in Figure 6.14(b).

Figure 6.15(a) illustrates the towing (net contact) force F_x together with the thrust and resistant components (F_τ and F_σ) as a function of the skid ratio, obtained from Equation (6.6) for the two soils. The results are obtained in the 0 – 15% skid range for the high density wet sand, and in the 0 – 9% skid range for the unwashed sand. The results show that the thrust force F_τ is positive (forward) at lower skids and it decreases with the increase in skid, and approaches negative (rearward direction) under higher skid ratio. The resistant component F_σ, however, remains negative (rearward) in the entire skid range. The net contact force is negative at higher skid ratios for both the soils, which helps rotation of the wheel, while resisting against its longitudinal motion. The resulting contact moment, obtained from Equation (6.8), is positive (against the rotation direction) at low skids and approaches negative with increase in skid, as seen in Figure 6.15(b). The observed trends in the net contact force and its components, and the towing moment are comparable with the reported experimental results for a towed wheel on different sands [20, 149].

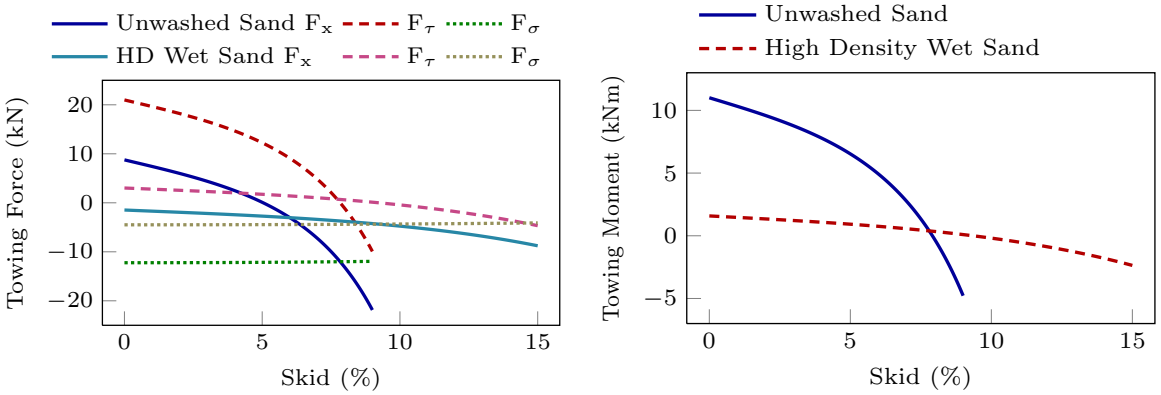

Figure 6.15: Theoretical (a) towing force together with its shearing and radial stress terms (F_τ and F_σ) and (b) towing moment as functions of skid for a rigid wheel towed at 60 mm sinkage on different soils

Figures 6.16(a) and 6.16(b) illustrate time histories of the contact force F_x and the resulting moment M_y predicted from the FE and SPH models for the high density wet sand coupled with a towed wheel at 5 km/h speed (1.389 m/s) and 60 mm penetration. The forward speed, applied in a ramp manner, resulted in a steady angular speed of 2.33 rad/s and a skid ratio of 15%. The computational models employing the FE and SPH soil models for the high density wet sand revealed peak towing forces of -9.56 and -8.24 kN, respectively, as seen in Figure 6.16(a). These are comparable with the towing force corresponding to 15% skid (-8.77 kN) estimated from the theory (Figure 6.15(a)) using the identified terramechanics model for the high density wet sand. The computational models also resulted in peak moments of -2.62 and -2.27 kNm for the FE and SPH soil models, respectively, which are also comparable with that estimated from the theory (-2.363 kNm). The observed reasonable correlations between the simulation and theoretical results suggest that the identified terramechanics model can effectively predict towing forces and moments developed by a towed wheel on a soft soil. The similar degree of correlation in the contact force and moment were also observed for the unwashed sand. Similar to the driven wheel, the FE soil model overestimated and the SPH model underestimated the theoretical forces and moments for the towed wheel.

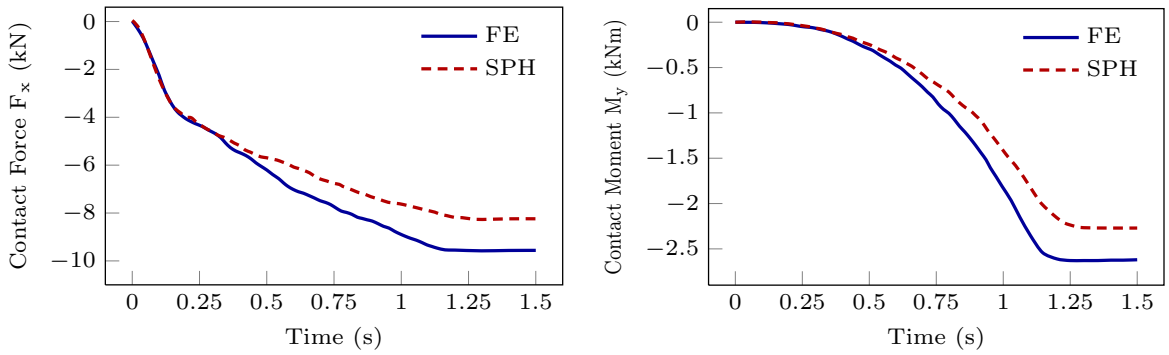

Figure 6.16: Time histories of (a) contact force F_x and (b) contact moment M_y developed by a towed wheel at 5 km/h speed under 60 mm sinkage on the FE and SPH models of the high density wet sand

6.4.3 Steered wheel

The effectiveness of the identified terramechanics models for predicting lateral force F_y and aligning moment M_z of a steered wheel is further evaluated through comparisons with those obtained from the computational model. The lateral force and the aligning moment developed by a steered wheel are obtained from the lateral shear displacement and shear stress distributions. Figures 6.17(a) and 6.17(b) illustrate lateral displacement $j_y(\theta)$ and the lateral shear stress $\tau_y(\theta)$ developed at the interface of the steered wheel and the soil corresponding to a 6° side-slip angle and three different slip ratios (0, 20 and 40%). These are obtained from Equations (6.17) and (6.16), respectively. Similar to the rolling wheel, the rut recovery is assumed negligible ($\eta = 0$), which resulted in similar contact angles ($\theta_1 = 28.16°$ and $\theta_2 = 0°$) from Equation (6.1), considering 60 mm sinkage. The peak lateral displacement occurs at the extreme of the rear contact region ($\theta_2 = 0$) and decreases with increase in the slip ratio, as seen in Figure 6.17(a) for both the soils. The lateral displacement decreases along the contact region in a linear manner and approaches zero at the front end of the contact region (θ_1). The lateral shear stress responses exhibit peak near θ_m, as it was observed for the peak radial stress (Figure 6.17(b)).

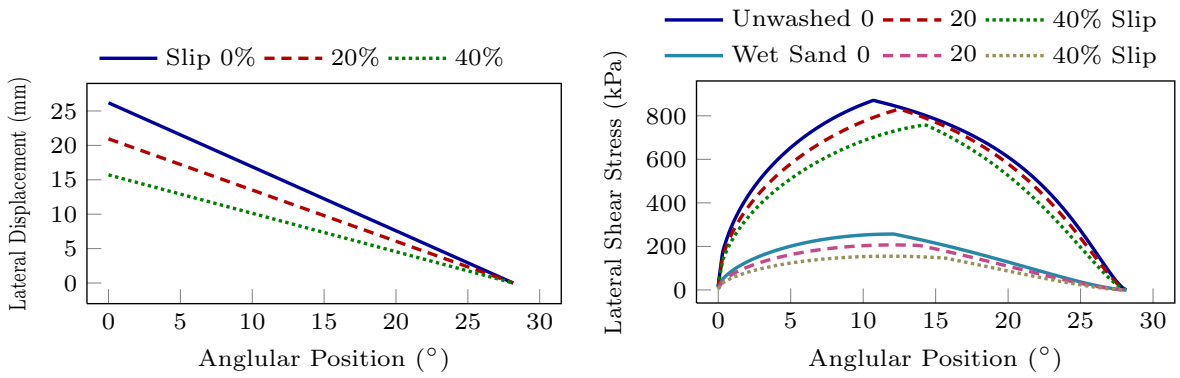

Figure 6.17: Theoretical (a) lateral displacement and (b) lateral shear stress distributions along the contact region for a rigid wheel steered at 6° side-slip angle and varying longitudinal slip ratios under 60 mm sinkage on different soils

Figures 6.18(a) and 6.18(b) illustrate variations in the lateral contact force F_y and

aligning moment M_z as a function of the side-slip angle α. The results are obtained using Equations (6.14) and (6.15) based on the identified terramechanics model parameters for the two soils. Both the F_y and M_z increase with the increase of the side-slip angle and approach saturation at higher side-slip angles. Both the F_y and M_z decrease with increase in the slip ratio.

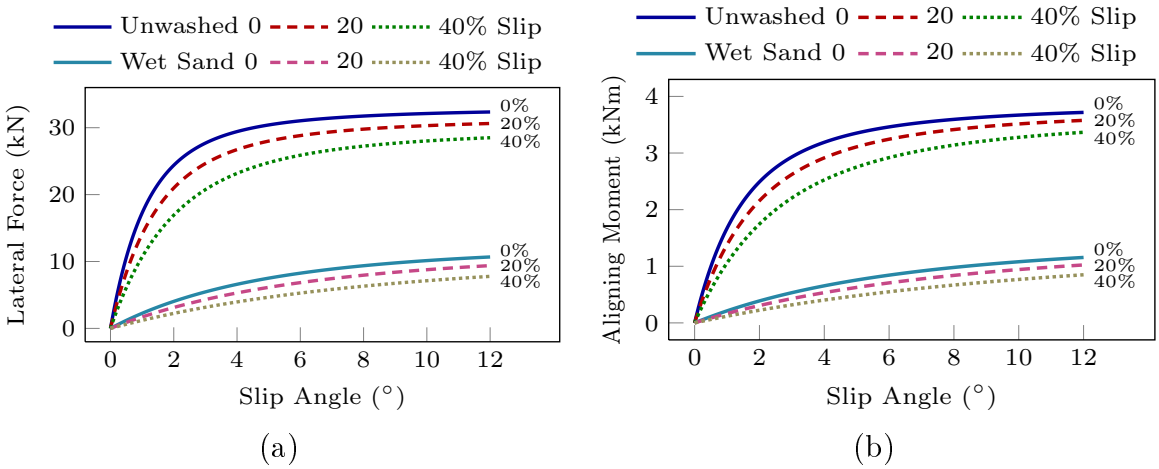

(a) (b)

Figure 6.18: Theoretical (a) lateral force and (b) aligning moment as functions of side-slip angle for a rigid wheel at varying longitudinal slip ratios under 60 mm sinkage on different soils

Figures 6.19(a) and 6.19(b) illustrate time histories of the lateral contact force F_y and the aligning moment M_z obtained from computational models employing the FE and SPH models for the high density wet sand, when subjected to 6° side-slip angle by a driven wheel with 2.74 rad/s angular speed and 20% slip ratio. The FE and SPH models for the high density wet sand revealed peak lateral forces of 7.8 and 5.9 kN, respectively, corresponding to 20% slip ratio and 6° side-slip angle (Figure 6.19(a)). These are comparable with 6.84 kN estimated from the identified terramechanics model (Figure 6.18(a)). Moreover, the peak moments of 0.85 and 0.6 kNm, obtained from the FE and SPH soil models, respectively (Figure 6.19(b)), are also comparable with that estimated from the identified terramechanics model (0.707 kNm), as illustrated in Figure 6.18(b). Similar degree of agreement was also observed for the unwashed sand. Relatively good agreements between

the computational model and theoretical results for the lateral contact force and the aligning moment suggest that the identified terramechanics formulations can effectively predict the lateral forces and moments developed by a steered wheel rolling on a soft soil. Similar to the rolling wheel, the theoretical estimations for the steered wheel lie in between those obtained from the FE and SPH models.

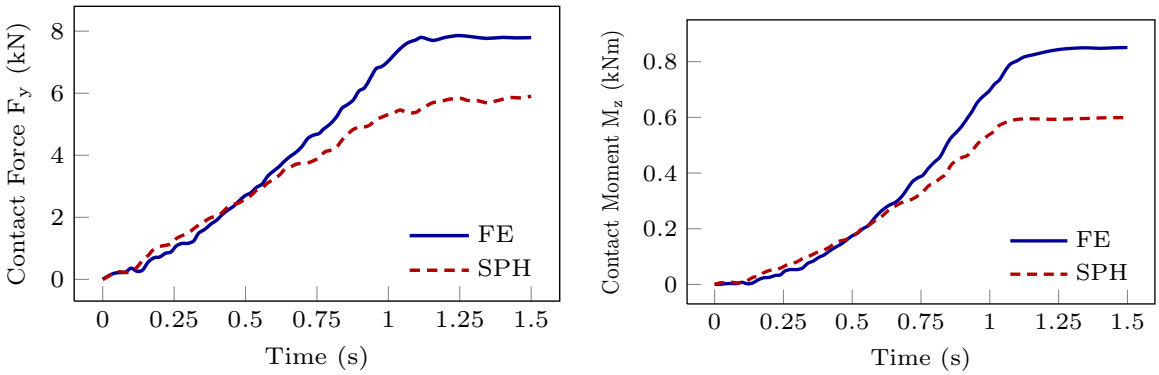

(a) (b)

Figure 6.19: Time histories of (a) contact force F_y and (b) contact moment M_z developed by a steered wheel at 5 km/h speed and 6° side-slip angle under 60 mm sinkage on the FE and SPH models of the high density wet sand

6.4.4 Processing times of simulations

The average processing times required for the FE and SPH soil models in different simulations together with the size of the soil domain and the number of elements in the FE model as well as the number of particles in the SPH model are summarized in Table 6.2. A 3.2 GHz Intel Xenon processor with 8 cores and 14 GB memory was used for the simulations. As mentioned in Part I, for the plate-sinkage simulations, the SPH method takes nearly 4.4 times longer than the FE method. In the test simulations involving a rigid wheel interactions with the soil, whether stationary, rolling or steered, the computing time for the SPH soil model, on the average, was near 5.7 times than that for the FE soil model. For a compliant tyre model, however, the computing times for the FE and SPH models were in excess of 29.5 and 226 hours, respectively. These are nearly 42 and 55 times of those required for the rigid wheel, being 0.7 and 4.1 hours. The ratio of the SPH to FE

processing time for the compliant tyre is thus 7.66. Chae et al. [12, 12] also conducted tyre-soil interaction simulations using a rigid wheel model, and reported that the CPU time required for a SPH soil model is about 4 to 7 times than that required for a similar FE soil model. The excessive computing times for the compliant tyre-soil simulations may be prohibitive, particularly for the rolling tyre tests, where lengthy routes of soil are required.

Table 6.2: Comparisons of processing times of the FE and SPH soil models together with soil domain size and number of elements/particles

Simulation type	*Simulation time (s)*	*CPU time (h)*		*Soil domain size (mm)*	*Soil elements/particles*	
		FE	*SPH*		*FE*	*SPH*
Wheel sinkage	6	0.7	4.1	$600 \times 600 \times 600$	20700	27000
Tyre sinkage	6	29.5	226	$600 \times 600 \times 600$	20700	27000
Driven wheel	3	2.15	12.22	$3980 \times 600 \times 600$	137310	179100
Towed wheel	3	2.07	11.7	$3980 \times 600 \times 600$	137310	179100
Steered wheel	4	7.79	43.78	$5380 \times 1200 \times 600$	371220	484200

6.5 Conclusions

A tyre/wheel-soil interaction simulation tool is developed by integrating a computationally efficient FE model of the tyre to the virtual soil test simulation models, reported in Part I of the study. The simulation tool is used to examine validity of the terramechanics-based models identified for different soils. It is shown that the identified terramechanics models can yield reasonably good predictions of normal and shear stress distributions and forces/moments developed at the interface of the stationary, rolling and steered tyre/wheel and the soil. The simulation results obtained from the stationary tyre penetrating into soils of different strengths demonstrated strong influences of the tyre and soil compliance on the tyre deflection and its sinkage, the radius and size of the contact arc, and the pressure distribution beneath the tyre/wheel. The pressure distributions and the normal force predicted from the terramechanics models revealed reasonably good agreements with those obtained from the simulations. The FE soil model revealed relatively higher contact

pressure compared to the SPH soil model although the deviation was smaller than that observed in the plate-sinkage tests. This suggested that the FE soil mesh can more effectively represent the soil deformation when penetrated by a tyre with arched geometry than by a flat plate with sharp edges. The FE soil model overestimates the radial stress and normal force compared to the SPH soil model, especially when a rigid wheel is considered. Relatively smaller differences between the predictions of the FE and SPH soil models, however, were observed for the low-pressure pneumatic tyre. The terramechanics models could also yield reasonably good predictions of the slip-dependent location of the maximum radial stress beneath a driven wheel, and the transition point in the shear stress under a towed wheel. The stress distributions obtained from the simulation models clearly illustrated two zones of shear stress beneath a rolling wheel, while the length of the front contact zone was negligible for the driven wheel but significant for the towed wheel. The radial and shear stresses, and the contact forces/moments obtained from the identified terramechanics models for rolling (driven/towed) and steered wheels were found to be comparable with those obtained from the FE and SPH soil models. The FE soil model, however, resulted in relatively higher magnitudes of forces/moments compared to the SPH soil model and those predicted from the terramechanics-based model. The processing times for the SPH soil model, however, were nearly 5.7 to 7.66 times longer than those of the FE soil model when coupled with the rigid wheel and pneumatic tyre models, respectively.

Chapter 7

Conclusions and Recommendations

7.1 Highlights and contributions

This dissertation research presented a virtual testing environment for rolling tyre interactions with rigid and soft terrains. Review of the literature was initially conducted to demonstrate the importance of estimating the forces and moments arising from the tyre-terrain interactions, and the limitations associated with the previously reported models and analysis methods. Comprehensive modeling and programming efforts have been carried out to design and implement a computational testing platform to describe the structural details of a pneumatic tyre as well as material constitutive behavior of soil in order to provide reliable predictions of dynamic responses of a pneumatic tyre when rolling on rigid as well as deformable terrains. A computationally efficient pre-processing algorithm has been developed to automate the tyre-soil model regenerations so as to facilitate repeated simulations for parametric studies. The developed platform in conjunction with the automatic model regeneration algorithm can be utilized as a virtual test tool for sensitivity analyses of design and operating tyre parameters as well as parametrization and evaluation of the terramechanics-based tyre-soil contact models. The following summarizes the highlights and contributions of the dissertation research:

1. Development and validation of a 3-D finite element model of a rolling radial-ply truck tyre to predict its dynamic responses at high speeds, and investigating the effects of various operating parameters on the tyre vertical and cornering characteristics;

2. Development of a pre-processing algorithm for automated model reformulations for efficient parametric sensitivity analyses;
3. Modal analysis of a rolling truck tyre as a pre-stressed structure under inflation and vertical loadings, and investigate influences of internal pressure, normal load and rolling speed on the tyre natural frequencies and mode shapes;
4. Development and verification of a computationally efficient rolling truck tyre model considering simplification of the multiple layers of rubber matrix and reinforcements into a single layer of shell elements with layered configuration using the Part-Composite approach in LS-DYNA;
5. Development of a computational soil model using Finite Element and Smoothed Particle Hydrodynamics methods in conjunction with a pressure-dependent strength material model calibrated on the basis of laboratory test data, and investigation of relative merits and limitations of the two methods;
6. Parametrization of terramechanics-based tyre-soil interaction formulations for estimating the normal and shearing characteristics of soil through pressure-sinkage and shear-box test simulations using the proposed SPH soil model;
7. Development of the rolling tyre-soil interaction model via integrating the proposed FE and SPH soil models to the simplified rolling truck tyre model;
8. Evaluation of the terramechanics-based tyre-soil interaction models through comparisons of the theoretical and simulation results in terms of the normal/shear stresses as well as the contact forces/moments for the stationary, driven, towed and steered tyre/wheel models;

7.2 Major conclusions

The major conclusions drawn from the study are summarized below:

1. The use of thick-shell element formulations for the poor-aspect-ratio solid elements of the rubber matrix in the carcass and belt plies could ensure stable model responses

at high speeds up to 100 km/h. The model, however, revealed unstable behavior at speeds above 100 km/h, which was evident from extremely large deformations of solid elements of the carcass.

2. The response characteristics of the proposed rolling truck tyre model showed reasonably good agreements with the reported measured tyre properties in terms of load-deflection, contact patch size, cornering force and free vertical vibration characteristics for a wide range of operating parameters. The self-aligning moment responses of the model, however, could be considered valid only in the range of side-slip angles less than 4°, although the simulation results at higher side-slip angles showed similar trends as the measured data.

3. The simulation results suggested that the vertical tyre stiffness increases with increase in inflation pressure and normal load, but rapidly decreases when the tyre starts to roll. The rolling dynamic stiffness of the tyre is nearly 5% lower than its static stiffness. The results also showed nonlinear and coupled effects of normal load and inflation pressure on cornering properties.

4. The modal properties of a pneumatic tyre subjected to inflation pressure, normal load and rolling speed can be evaluated by incorporating the resulting stresses in the eigenvalue analyses conducted in a sequential manner during an explicit dynamic simulation at instants when the tyre approaches steady responses under the given loading condition.

5. Some of the eigen-frequencies of the free tyre diverge into two distinct frequencies in the presence of tyre deflection and ground contact. One of the frequencies lies below the corresponding frequency of the free tyre under inflation alone, while the other occurs above that.

6. The rotational motion of the tyre results in a most dramatic reduction in the tyre stiffness and hence the natural frequencies compared to the stationary tyre, while increasing the rolling speed causes further reductions in the natural frequencies.

7. The Part-Composite approach could substantially reduce the computational demand

by simplifying the multi-layered tyre structure to a single layer of multi-layered element configuration. The simplified model provided results that were in good agreement with those of the comprehensive model, with substantial reduction in computing time by 79.14% for a load-deflection simulation, and 83.3% for a cornering test.

8. The shear-box test results suggest that the chosen soil material model could effectively represent the increase in the shear strength of soil with the increase of its confining pressure for four types of sandy soils with different moisture contents.

9. The SPH soil model could more realistically represent the penetration of the plate into the soil compared to the FE soil model. This was attributed to the sponge-like behavior of the FE model, which prevented the soil elements to envelop the plate as it penetrated. Moreover, the FE model resulted in relatively higher contact force than the SPH model, which originates from an undesirable tensile force produced by the stretched soil elements near the edges of the plate. The SPH model, however, poses relatively greater computational demands. For instance, the simulation time for plate-sinkage test with the SPH soil model was 4.4 times that with the FE model.

10. The SPH soil model also showed more effective simulation of the shear-box test, where the body of soil tends to disintegrate in response to large shear deformations.

11. The penetrations of the pneumatic tyre into soil is strongly dependent on the tyre compliance and the tyre deflection. It was further illustrated that the theoretical estimations for the normal contact force lie between those predicted from the FE and SPH soil models. The FE model tends to overestimate the tyre-terrain interface force compared to the SPH model. The difference between the two models, however, diminish for low inflation pressure.

12. The simulation results clearly illustrated two zones of the shear stress beneath the rolling wheel. The two zones were sufficiently large for the towed wheel to be considered in the theory. The leading zone for the driven wheel, however, was very small and could thus be neglected.

13. The radial and shear stresses as well as the contact forces and moments obtained from the FE and SPH simulations for the rolling wheel were in reasonably good

agreements with those predicted from the terramechanics soil model for both the driving and towing maneuvers. The simulation results showed good agreements with the reported measured data for somewhat different soils in a qualitative sense.

7.3 Recommendations for future studies

The computational testing platform presented in this study can be employed as a virtual laboratory test tool for simulating different maneuvers involving tyre-terrain interactions to investigate the deformations, stresses and contact force/moment responses. The proposed platform has been implemented in an automated and parametric manner, which highly facilitates repeated simulations by adjusting the loading and boundary conditions, material types and properties, mesh size, tyre cross-section and geometric details, soil domain size, element types and contact algorithms. This algorithm could be further extended to reduce the user's efforts when model reformulations are required for parametric and design sensitivity analyses. Furthermore, more efforts are desirable for developing more reliable and efficient tyre-soil interaction models. Some of the possible directions for future studies are:

1. It is suggested that the proposed truck tyre model together with the automated model regeneration algorithm is utilized for conducting sensitivity analyses on geometric, structural and material properties of the tyre constituents so as to seek optimal tyre design.

2. The proposed simulation platform is recommended to be exploited as a virtual tool for parameter identifications of the physics-based and phenomenological tyre models as an alternative to the costly hardware experiments.

3. It was demonstrated in the study that under unconfined conditions such as the pressure-sinkage test, the chosen material model, *Soil and Foam* in LS-DYNA, is unable to represent absolutely non-cohesive soils like dry sand. It is thus recommended to explore the applicability of other soil constitutive models such as *Pseudo Tensor* (type 16), *Geologic Cap* (type 25), *Concrete Damage* (type 72), *Hysteretic*

Soil (type 79), *FWHA* (type 147), *Mohr-Coulomb* (type 173) and *Drucker-Prager* (type 193) from the material library of LS-DYNA.

4. The default particle approximation theory together with the cubic B-spline smoothing function in LS-DYNA were used in the present study. It is recommended to explore alternate SPH formulations and kernel functions, and to conduct sensitivity studies on the SPH-related simulation parameters such as the smoothing length scale factors and the artificial viscous pressure term coefficients.

5. It was shown that the FE soil model is quicker in view of processing time, while the SPH soil model more realistically represents large deformations and disintegrations of soil materials. In order to improve computational efficiency, it is suggested to combine the two analysis methods using the SPH particles only for the regions subjected to large deformations and meshing the remaining domain with FE elements. It is further suggested to explore different contact methodologies for smoothly connecting the SPH particles to the FE elements so as to simulate a coherent soil domain with minimal effect of discontinuity.

6. Comparing the merits and limitations of the FE and SPH soil models revealed that the mesh-less nature of the SPH method can more accurately represent penetration of an object into soil. It is recommended to apply and compare other mesh-less analysis methods such as the *Discrete Element (DE)*, *Element Free Galerkin (EFG)*, and *Arbitrary Lagrangian Eulerian (ALE)* methods.

7. In the present study, the terramechanics-related soil parameters were identified and evaluated for a few types of soils, it is suggested to employ the proposed virtual testing platform for parameter identifications of the other types of soils for which the input parameters to the *Soil and Foam* material model are available.

8. Due to excessive computational demands, the pneumatic tyre compliance was only considered in the stationary tyre simulations on soft soil, while a rigid wheel model was used for the rolling tyre simulations. It is thus suggested to utilize the *High Performance Computing (HPC)* systems so as to be able to apply the pneumatic tyre model in the rolling tyre simulations on soft soil.

Bibliography

[1] K. M. Captain, A. B. Boghani, and D. N. Wormley. Analytical tire models for dynamic vehicle simulation. *Vehicle System Dynamics*, 8(1):1–32, 1979.

[2] E. Bakker, H. B. Pacejka, and L. Lidner. A new tire model with an application in vehicle dynamics studies. No. 890087, SAE Paper, 1989.

[3] P. W. A. Zegelaar and H. B. Pacejka. The in-plane dynamics of tyres on uneven roads. *Vehicle System Dynamics*, 25(S1):65–79, 1996.

[4] J. P. Maurice. *Short wavelength and dynamic tyre behavior under lateral and combined slip conditions*. Ph.D. dissertation, Delft University of Technology, 2000.

[5] A. J. C. Schmeitz and H. B. Pacejka. A semi-empirical, three-dimensional, tyre model for rolling over arbitrary road unevennesses. *Vehicle System Dynamics*, 41(S1):341–350, 2004.

[6] J. J. M. Van Oosten and E. Bakker. Determination of magic tyre model parameters. *Vehicle System Dynamics*, 21(S1):19–29, 1992.

[7] S. Bruni, F. Cheli, and F. Resta. On the identification in time domain of the parameters of a tyre model for the study of in-plane dynamics. *Vehicle System Dynamics*, 27(S1):136–150, 1997.

[8] D. Arosio, F. Braghin, F. Cheli, and E. Sabbioni. Identification of pacejka's scaling factors from full-scale experimental tests. *Vehicle System Dynamics*, 43(S1):457–474, 2005.

[9] X. Zhang. *Nonlinear Finite Element Modeling and Incremental Analysis of a Composite Truck Tire Structure*. Ph.D. dissertation, Concordia University, Montréal, Canada, 2001.

[10] W. Hall, J. T. Mottram, and R. P. Jones. Tire modeling methodology with the explicit finite element code LS-DYNA. *Tire Science and Technology*, 32(4):236–261, 2004.

[11] S. Chae. *Nonlinear Finite Element Modeling and Analysis of a Truck Tire*. Ph.D. dissertation, Pennsylvania State University, USA, 2006.

[12] S. Chae, J. Allen II, F. Öijer, M. El-Gindy, M. Trivedi, and I. Johansson. Dynamic response predictions of quarter-vehicle models using FEA and rigid ring truck tire models. In *ASME International Mechanical Engineering Congress and Exposition*, Illinois, 5–10 November 2006. American Society of Mechanical Engineers.

[13] X. Zhang, S. Rakheja, and R. Ganesan. Modal analysis of a truck tyre using FE tyre model. *International Journal of Heavy Vehicle Systems*, 11(2):133–154, 2004.

[14] X. Zhang, S. Rakheja, and R. Ganesan. Influence of structural and geometric parameters on the inter-ply shear stresses in a radial truck tire. *International Journal of Heavy Vehicle Systems*, 9(2):150–171, 2002.

[15] W. Hall, J. T. Mottram, and R. P. Jones. Finite element simulation of a rolling automobile tyre to understand its transient macroscopic behavior. *Proceedings of the Institution of Mechanical Engineers, Part D: Journal of Automobile Engineering*, 218(12):1393–1408, 2004.

[16] M. G. Bekker. *Theory of Land Locomotion*. The University of Michigan Press, Ann Arbor, 1956.

[17] M. G. Bekker. *Off-The-Road Locomotion: Research and Development in Terramechanics*. The University of Michigan Press, Ann Arbor, 1960.

[18] M. G. Bekker. *Introduction to Terrain-Vehicle Systems*. The University of Michigan Press, Ann Arbor, 1969.

[19] J. Y. Wong and A. R. Reece. Prediction of rigid wheel performance based on the analysis of soil-wheel stresses, part 1: Performance of driven rigid wheels. *Journal of Terramechanics*, 4(1):81–98, 1967.

[20] J. Y. Wong and A. R. Reece. Prediction of rigid wheel performance based on the analysis of soil-wheel stresses, part 2: Performance of towed rigid wheels. *Journal of Terramechanics*, 4(2):7–25, 1967.

[21] G. Ishigami, A. Miwa, K. Nagatani, and K. Yoshida. Terramechanics-based model for steering maneuver of planetary exploration rovers on loose soil. *Journal of Field Robotics*, 24(3):233–250, 2007.

[22] A. Azimi, M. Hirschkorn, B. Ghotbi, J. Kövecses, J. Angeles, P. Radziszewski, M. Teichmann, M. Courchesne, and Y. Gonthier. Terrain modeling in simulation-based performance evaluation of rovers. *Canadian Aeronautics and Space Journal*, 57(1):24–33, 2011.

[23] B. Ghotbi, F. Gonzalez, J. Kövecses, and J. Angeles. Vehicle-terrain interaction models for analysis and performance evaluation of wheeled rovers. In *IEEE/RSJ International Conference on Intelligent Robots and Systems (IROS)*, pages 3138–3143. IEEE, 2012.

[24] J. Slade, M. El-Gindy, R. Lescoe, F. Öijer, M. Trivedi, and I. Johansson. Off-road tire-soil modeling using finite element analysis technique. In *ASME International Design Engineering Technical Conference*, San Diego, California, August 2009. American Society of Mechanical Engineers.

[25] R. Lescoe, M. El-Gindy, K. Koudela, F. Öijer, M. Trivedi, and I. Johansson. Tire-soil modeling using finite element analysis and smooth particle hydrodynamics techniques. In *ASME International Design Engineering Technical Conference*, Montréal, Canada, 15–18 August 2010. American Society of Mechanical Engineers.

[26] R. S. Dhillon, R. Ali, M. El-Gindy, D. Philipps, F. Öijer, and I. Johansson. Development of truck tire-soil interaction model using FEA and SPH. No. 2013-01-0625, SAE Technical Paper, 2013.

[27] C. W. Fervers. Improved FEM simulation model for tire-soil interaction. *Journal of Terramechanics*, 41:87–100, 2004.

[28] J. P. Hambleton and A. Drescher. Modeling wheel-induced rutting in soils: Indentation. *Journal of Terramechanics*, 45(6):201–211, 2008.

[29] J. P. Hambleton and A. Drescher. Modeling wheel-induced rutting in soils: Rolling. *Journal of Terramechanics*, 46(2):35–47, 2009.

[30] K. Xia. Finite element modeling of tire/terrain interaction: Application to predicting soil compaction and tire mobility. *Journal of Terramechanics*, 48(2):113–123, 2011.

[31] H. Li and C. Schindler. Application of analytical and finite element method in tyre-soil modeling. *International Journal of Heavy Vehicle Systems*, 19(4):333–354, 2012.

[32] X. Zhang, S. Rakheja, and R. Ganesan. Nonlinear finite element modeling and incremental analysis of a truck tire. *International Journal of Heavy Vehicle Systems*, 9(3):253–279, 2002.

[33] B. Schlatter. *A Pedagogical Tool Using Smoothed Particle Hydrodynamics to Model Fluid Flow Past as System of Cylinders.* Ph.D. dissertation, Oregon State University, Corvallis, OR, 1999.

[34] R. A. Clegg, J. Sheridan, C. J. Hayhurst, and N. J. Francis. The application of SPH techniques in AUTODYN-2D to kinetic energy penetrator impacts on multi-layered soil and concrete targets. In *8th International Symposium on Interaction of the Effects of Munitions with Structures*, Virginia, USA, 22–25 April 1997. McLean.

[35] H. H. Bui, K. Sako, and R. Fukagawa. Numerical simulation of soil-water interaction using smoothed particle hydrodynamics (SPH) method. *Journal of Terramechanics*, 44(5):339–346, 2007.

[36] H. H. Bui, R. Fukagawa, K. Sako, and S. Ohno. Lagrangian meshfree particles method (SPH) for large deformation and failure flows of geomaterial using elastic-plastic soil constitutive model. *International Journal for Numerical and Analytical Methods in Geomechanics*, 32(12):1537–1570, 2008.

[37] R. Lescoe. *Improvement of Soil Modeling in a Tire-Soil Interaction Using Finite Element Analysis and Smooth Particle Hydrodynamics.* M.S. thesis, Pennsylvania State University, USA, 2010.

[38] M. Barsotti. Comparison of FEM and SPH for modeling a crushable foam aircraft arrestor bed. In *11th International LS-DYNA Users Conference*, Dearborn, MI, USA, June 2010.

[39] R. S. Dhillon. *Development of Truck Tire-Terrain Finite Element Analysis Models.* M.S. thesis, University of Ontario Institute of Technology, Canada, 2013.

[40] R. Dhillon, M. El-Gindy, R. Ali, D. Philipps, F. Öijer, and I. Johansson. Sensitivity analysis of smoothed particle hydrodynamics in pam-crash for modeling of soft soils. In *ASME 2013 International Design Engineering Technical Conferences and Computers and Information in Engineering Conference.* American Society of Mechanical Engineers, 2013.

[41] P. H. L. Groenenboom. Numerical simulation of 2D and 3D hypervelocity impact using the SPH option in PAM-SHOCK. *International Journal of Impact Engineering*, 20(1):309–323, 1997.

[42] M. Faraud, R. Destefanis, D. Palmieri, and M. Marchetti. SPH simulations of debris impacts using two different computer codes. *International Journal of Impact Engineering*, 23(1):249–260, 1999.

[43] C. Bojanowski and Kulak R. F. Comparison of lagrangian, SPH and MM-ALE approaches for modeling large deformations in soil. In *11th International LS-DYNA Users Conference*, Dearborn, MI, June 2010.

[44] Q. H. Shah and H. M. Abid. *LS-DYNA for beginners: an insight into LS-PrePost and LS-DYNA*. LAP LAMBERT Academic Publishing, 2012.

[45] R. F. Kulak and L. Schwer. Effect of soil material models on SPH simulations for soil-structure interaction. In *12th International LS-DYNA Users Conference*, Dearborn, MI, USA, June 2012.

[46] A. C. Reid, D. Philipps, F. Öijer, I. Johansson, and M. El-Gindy. Development of a modified off-road rigid ring tire model for heavy trucks. No. 2014-01-0878, SAE Technical Paper, 2013.

[47] M. Loo. A model analysis of tire behavior under vertical loading and straight-line free rolling. *Tire Science and Technology*, 13(2):67–90, 1985.

[48] J. Kisilowski and Z. Lozia. Modelling and simulating the braking process of automotive vehicle on uneven surface. *Vehicle System Dynamics*, 15(S1):250–263, 1986.

[49] J. M. Badalamenti and G. R. Doyle. Radial-interradial spring tire models. *Journal of Vibration, Acoustics Stress and Reliability in Design*, 110(1):70–75, 1988.

[50] K. Guo and Q. Liu. A model of tire enveloping properties and its application on modeling of automobile vibration systems. No. 980253, SAE Technical Paper, 1998.

[51] P. W. A. Zegelaar and H. B. Pacejka. Dynamic tyre responses to brake torque variations. *Vehicle System Dynamics*, 27(S1):65–79, 1997.

[52] S. J. Kim and A. R. Savkoor. The contact problem of in-plane rolling of tires on a flat road. *Vehicle System Dynamics*, 27(S1):189–206, 1997.

[53] M. Takayama and K. Yamagishi. Simulation model of tire vibration. *Tire Science and Technology*, 11(1):38–49, 1984.

[54] P. W. A. Zegelaar, S. Gong, and H. B. Pacejka. Tyre models for the study of in-plane dynamics. *Vehicle System Dynamics*, 23(S1):578–590, 1994.

[55] P. W. A. Zegelaar. *The dynamic response of tyres to brake torque variations and road unevennesses*. Ph.D. dissertation, Delft University of Technology, 1998.

[56] D. J. Allison and R. S. Sharp. On the low frequency in-plane forced vibrations of pneumatic tyre/wheel/suspension assemblies. *Vehicle System Dynamics*, 27(S1):151–162, 1997.

[57] S. Gong, A. R. Savkoor, and H. B. Pacejka. The influence of boundary conditions on the vibration transmission properties of tires. No. 931280, SAE Technical Paper, 1993.

[58] J. E. Bernard, L. Segel, and R. E. Wild. Tire shear force generation during combined steering and braking maneuvers. No. 770852, SAE Technical Paper, 1977.

[59] E. Fiala. Lateral forces on rolling pneumatic tires. *Zeitschrift VDI*, 96(29):973–979, 1954.

[60] H. Dugoff, P. S. Fancher, and L. Segel. An analysis of tire traction properties and their influence on vehicle dynamic performance. No. 700377, SAE Technical Paper, 1970.

[61] J. Deur, J. Asgari, and D. Hrovat. A 3D brush-type dynamic tire friction model. *Vehicle System Dynamics*, 42(3):133–173, 2004.

[62] J. P. Maurice, M. Berzeri, and H. B. Pacejka. Pragmatic tyre model for short wavelength side slip variations. *Vehicle System Dynamics*, 31(2):65–94, 1999.

[63] H. B. Pacejka and E. Bakker. The magic formula tire model. *Vehicle System Dynamics*, 21(1):1–18, 1992.

[64] H. B. Pacejka and I. J. M. Besselink. Magic formula tyre model with transient properties. *Vehicle system dynamics*, 27(S1):234–249, 1997.

[65] A. J. C. Schmeitz, I. J. M. Besselink, and S. T. H. Jansen. TNO MF-SWIFT. *Vehicle System Dynamics*, 45(S1):121–137, 2007.

[66] J. Svendenius and M. Gäfvert. A brush-model based semi-empirical tire-model for combined slips. No. 2004-01-1064, SAE Technical Paper, 2004.

[67] W. Hirschberg, G. L. Rill, and H. Weinfurter. User-appropriate tire-modeling for vehicle dynamics in standard and limit situations. *Vehicle System Dynamics*, 38(2):103–125, 2002.

[68] A. Schmeitz. *A semi-empirical three-dimensional model of the pneumatic tyre rolling over arbitrary uneven road surfaces.* Ph.D. dissertation, Delft University of Technology, 2004.

[69] P. Lugner, H. Pacejka, and M. Plöchl. Recent advances in tire models and testing procedures. *Vehicle System Dynamics*, 43(6):413–426, 2005.

[70] P. Lugner and M. Plöchl. Tyre model performance test: First experiences and results. *Vehicle System Dynamics*, 43(1):48–62, 2005.

[71] F. Mancosu, G. Matrascia, and F. Cheli. Techniques for determining the parameters of a two-dimensional tire model for the study of ride comfort. *Tire Science and Technology*, 25(3):187–213, 1997.

[72] H. P. Patel and R. H. Kennedy. Nonlinear finite element analysis for composite structures of axisymmetric geometry and loading. *Computers & Structures*, 15(1):79–84, 1982.

[73] K. Satyamurthy and L. R. Hirschfelt. An axisymmetric finite element and its use to examine the effects of construction variables on radial tires. *Tire Science and Technology*, 15(2):97–122, 1987.

[74] T. M. Kenny and R. A. Stechschulte. Applications of finite element analysis in tire design. *Tire Science and Technology*, 16(2):96–117, 1988.

[75] B. G. Kao and M. Muthukrishnan. Tire transient analysis with an explicit finite element program. *Tire Science and Technology*, 25(4):230–244, 1997.

[76] M. Koishi, K. Kabe, and M. Shiratori. Tire cornering simulation using an explicit finite element analysis code. *Tire Science and Technology*, 26(2):109–119, 1998.

[77] A. Kamoulakos and B. G. Kao. Transient dynamics of a tire rolling over small obstacles-a finite element approach with PAM-SHOCK. *Tire Science and Technology*, 26(2):84–108, 1998.

[78] X. Yan. Nonlinear three-dimensional finite element analysis of steady rolling radial tires. *Journal of reinforced plastics and composites*, 22(8):733–750, 2003.

[79] M. Shiraishi, N. Iwasaka, T. Saruwatari, and K. Hayashi. Developing a FE-Tire model library for durability and crash simulations. In *7th International LS-DYNA Users Conference*, 2001.

[80] M. Shiraishi, H. Yoshinaga, N. Iwasaka, and K. Hayashi. Making FEM tire model and applying it for durability simulations. In *6th International LS-DYNA Users Conference*, Detroit, 2000.

[81] T. Fukushima, H. Shimonishi, K. Hayashi, and M. Shiraishi. Simulation of a vehicle running on to a curb by using tire and vehicle models. In *4th European LS-DYNA Users Conference*, 2003.

[82] T. Fukushima and H. Shimonishi. Vehicle turn simulation using FE tire model. In *LS-DYNA Anwenderforum*, Bamberg, 2004.

[83] X. Zhang, S. Rakheja, and R. Ganesan. Stress analysis of the multi-layered system of a truck tire. *Tire Science and Technology*, 30(4):240–264, 2002.

[84] R. A. Ridha, K. Satyamurthy, and L. R. Hirschfelt. Finite element modeling of a homogeneous pneumatic tire subjected to footprint loadings. *Tire Science and Technology*, 13(2):91–110, 1985.

[85] V. Alkan, S. M. Karamihas, and G. Anlas. Finite element modeling of static tire enveloping characteristics. *International Journal of Automotive Technology*, 12(4):529–535, 2011.

[86] W. Wang, S. Yan, and S. Zhao. Experimental verification and finite element modeling of radial truck tire under static loading. *Journal of Reinforced Plastics and Composites*, 32(7):490–498, 2013.

[87] X. Zhang, S. Rakheja, and R. Ganesan. Estimation of tire-road contact pressure distribution based on nonlinear finite element analysis. *International Journal of Heavy Vehicle Systems*, 8(3/4):197–217, 2001.

[88] N. Korunović, M. Trajanović, and M. Stojković. Finite element model for steady-state rolling tire analysis. *Journal of the Serbian Society for Computational Mechanics*, 1(1):63–79, 2007.

[89] Y. S. Wang and J. Wu. Numberical analysis on the steady-state rolling of load-carrying tire. In *Second International Conference on Intelligent Computation Technology and Automation*, volume 4, pages 566–569. IEEE, 2009.

[90] N. Korunović, M. Trajanović, M. Stojković, D. Mišić, and J. Milovanović. Finite element analysis of a tire steady rolling on the drum and comparison with experiment. *Strojniski vestnik-Journal of Mechanical Engineering*, 57(12):888–897, 2011.

[91] K. Rao, R. Kumar, and P. Bohara. Transient finite element analysis of tire dynamic behavior. *Tire Science and Technology*, 31(2):104–127, 2003.

[92] S. Chae, M. El-Gindy, M. Trivedi, I. Johansson, and F. Öijer. Dynamic response predictions of a truck tire using detailed finite element and rigid ring models. In *ASME 2004 International Mechanical Engineering Congress and Exposition*, pages 861–871. American Society of Mechanical Engineers, 2004.

[93] H. H. Liu. Load and inflation effects on force and moment of passenger tires using explicit transient dynamics. *Tire Science and Technology*, 35(1):41–55, 2007.

[94] J. Allen II, M. El-Gindy, and K. Koudela. Development of a rigid ring quarter-vehicle model with an advanced road profile algorithm for durability and ride comfort predictions. In *ASME International Design Engineering Technical Conference*, New York, 3–6 August 2008. American Society of Mechanical Engineers.

[95] J. L. Slade. *Development of a New Off-Road Rigid Ring Model for Truck Tires Using Finite Element Analysis Techniques.* M.S. thesis, Pennsylvania State University, USA, 2009.

[96] R. Ali, R. Dhillon, M. El-Gindy, F. Öijer, I. Johanson, and M. Trivedi. Prediction of rolling resistance and steering characteristics using finite element analysis truck tyre model. *International Journal of Vehicle Systems Modelling and Testing*, 8(2):179–201, 2013.

[97] W. Hall. *Finite Element Modeling and Simulation for a 'Smart' Tyre.* Ph.D. dissertation, University of Warwick, Coventry, UK, 2003.

[98] J. D. Reid, D. A. Boesch, and R. W. Bielenberg. Detailed tire modeling for crash applications. *International Journal of Crashworthiness*, 12(5):521–529, 2007.

[99] F. Orengo, M. H. Ray, and C. A. Plaxico. Modeling tire blow-out in roadside hardware simulations using LS-DYNA. In *ASME 2003 International Mechanical Engineering Congress and Exposition*, Washington DC, USA, 2003.

[100] A. Wright. *Tire-Soil Interaction Modeling within a Virtual Proving Ground Environment.* Ph.D. dissertation, Cranfield University, UK, 2012.

[101] J. R. Cho, K. W. Kim, W. S. Yoo, and S. I. Hong. Mesh generation considering detailed tread blocks for reliable 3D tire analysis. *Advances in Engineering Software*, 35(2):105–113, 2004.

[102] Z. Li, Z. R. Li, and Y. M. Xia. An implicit to explicit FEA solving of tire F&M with detailed tread blocks. *Tire Science and Technology*, 40(2):83–107, 2012.

[103] A. Goldstein. Finite element analysis of a quasi-static rolling tire model for determination of truck tire forces and moments. *Tire Science and Technology*, 24(4):278–293, 1996.

[104] LS-DYNA keyword user's manual, volume 2: Material models. Livermore Software Technology Corporation, California, March 2015.

[105] J. O. Hallquist. LS-DYNA theory manual. Livermore Software Technology Corporation, California, March 2015.

[106] K. D. Papoulia. Mixed and selective reduced integration procedures in large strain hyper-elastic analysis of nearly incompressible solids. *Computational Mechanics*, 23(1):63–74, 1999.

[107] LS-DYNA keyword user's manual, volume 1. Livermore Software Technology Corporation, California, June 2013.

[108] C. Oertel and Y. Wei. Tyre rolling kinematics and prediction of tyre forces and moments: part I – theory and method. *Vehicle System Dynamics*, 50(11):1673–1687, 2012.

[109] S. Shokouhfar, S. Rakheja, and M. El-Gindy. Development of a rolling truck tyre model using an automatic model regeneration algorithm. *International Journal of Vehicle Systems Modelling and Testing*, 11(1):68–95, 2016.

[110] R. C. Chiroux, W. A. Foster, C. E. Johnson, S. A. Shoop, and R. L. Raper. Three-dimensional finite element analysis of soil interaction with a rigid wheel. *Applied mathematics and computation*, 162(2):707–722, 2005.

[111] B. J. Chan and C. Sandu. Development of a 3-d quasi-steady-state tyre model for on-road and off-road vehicle dynamics simulations: Part II – off-road rigid wheel model. *International Journal of Vehicle Systems Modelling and Testing*, 9(2):107–136, 2014.

[112] G. R. Potts. Application of holography to the study of tire vibration. *Tire Science and Technology*, 1(3):255–266, 1973.

[113] G. R. Potts and T. T. Csora. Tire vibration studies: The state of the art. *Tire Science and Technology*, 3(3):196–210, 1975.

[114] L. H. Yam, D. H. Guan, and A. Q. Zhang. Three-dimensional mode shapes of a tire using experimental modal analysis. *Experimental Mechanics*, 40(4):369–375, 2000.

[115] P. Kindt, P. Sas, and W. Desmet. Measurement and analysis of rolling tire vibrations. *Optics and Lasers in Engineering*, 47(3):443–453, 2009.

[116] G. R. Potts, C. A. Bell, L. T. Charek, and T. K. Roy. Tire vibrations. *Tire Science and Technology*, 5(4):202–225, 1977.

[117] Charles J. Hunckler, T. Y. Yang, and W. Soedel. A geometrically nonlinear shell finite element for tire vibration analysis. *Computers & Structures*, 17(2):217–225, 1983.

[118] L. E. Kung, W. Soedel, T. Y. Yang, and L. T. Charek. Natural frequencies and mode shapes of an automotive tire with interpretation and classification using 3-d computer graphics. *Journal of Sound and Vibration*, 102(3):329–346, 1985.

[119] S. Saigal, T. Y. Yang, H. W. Kim, and W. Soedel. Free vibrations of a tire as a toroidal membrane. *Journal of Sound and Vibration*, 107(1):71–82, 1986.

[120] S. C. Huang. The vibration of rolling tyres in ground contact. *International Journal of Vehicle Design*, 13(1):78–95, 1992.

[121] S. C. Huang and C. K. Su. In-plane dynamics of tires on the road based on an experimentally verified rolling ring model. *Vehicle System Dynamics*, 21(1):247–267, 1992.

[122] P. W. A. Zegelaar. Modal analysis of tire in-plane vibration. No. 971101, SAE Technical Paper, 1997.

[123] A. M. Burke and O. A. Olatunbosun. New techniques in tyre modal analysis using MSC/NASTRAN. *International journal of vehicle design*, 18(2):203–212, 1997.

[124] Y. Zhang, T. Palmer, and A. Farahani. A finite element tire model and vibration analysis: A new approach. *Tire Science and Technology*, 26(3):149–172, 1998.

[125] M. Shiraishi and K. Hayashi. Developing FE-Tire model for road noise simulation. In *5th European LS-DYNA Users Conference, Methods and Techniques*, 2005.

[126] W. Soedel and M. G. Prasad. Calculation of natural frequencies and modes of tires in road contact by utilizing eigenvalues of the axisymmetric non-contacting tire. *Journal of Sound and Vibration*, 70(4):573–584, 1980.

[127] Y. B. Chang, T. Y. Yang, and W. Soedel. Dynamic analysis of a radial tire by finite elements and modal expansion. *Journal of Sound and Vibration*, 96(1):1–11, 1984.

[128] L. E. Kung, W. Soedel, and T. Y. Yang. Free vibration of a pneumatic tire-wheel unit using a ring on an elastic foundation and a finite element model. *Journal of Sound and Vibration*, 107(2):181–194, 1986.

[129] W. Soedel. On the dynamic response of rolling tires according to thin shell approximations. *Journal of Sound and Vibration*, 41(2):233–246, 1975.

[130] L. E. Kung, W. Soedel, and T. Y. Yang. On the dynamic response at the wheel axle of a pneumatic tire. *Journal of Sound and Vibration*, 107(2):195–213, 1986.

[131] M. Brinkmeier, U. Nackenhorst, S. Petersen, and O. Von Estorff. A finite element approach for the simulation of tire rolling noise. *Journal of Sound and Vibration*, 309(1):20–39, 2008.

[132] U. Nackenhorst. Finite element analysis of tires in rolling contact. *GAMM-Mitteilungen*, 37(1):27–65, 2014.

[133] M. Takayama and K. Yamagishi. Simulation model of tire vibration. *Tire Science and Technology*, 11(1):38–49, 1983.

[134] E. Negrus, G. Anghelache, and A. Stanescu. Finite element analysis and experimental analysis of natural frequencies and mode shapes for a non-rotating tyre. *Vehicle System Dynamics*, 27(S1):221–224, 1997.

[135] V. Kerchman. Tire-suspension-chassis dynamics in rolling over obstacles for ride and harshness analysis. *Tire Science and Technology*, 36(3):158–191, 2008.

[136] B. Kao, M. Riesner, and P. Surulinarayanasami. Modal analysis of a tire and wheel and its application for vehicle ride evaluation. No. 860826, SAE Technical Paper, 1986.

[137] G. Anghelache and R. Moisescu. Analysis of rubber elastic behaviour and its influence on modal properties. *MATERIALE PLASTICE*, 45(2):143–148, 2008.

[138] O. A. Olatunbosun and A. M. Burke. Finite element modeling of rotating tires in the time domain. *Tire Science and Technology*, 30(1):19–33, 2002.

[139] T. R. Richards, L. T. Charek, and R. W. Scavuzzo. The effects of spindle and patch boundary conditions on tire vibration modes. No. 860243, SAE Technical Paper, 1986.

[140] E. M. Negrus, G. Anghelache, and S. Sorohan. Tire radial vibrations at high speed of rolling. No. 980260, SAE Paper, 1998.

[141] J. Y. Wong. *Terramechanics and Off-Road Vehicle Engineering.* Butterworth-Heinemann, Oxford, UK, 2nd edition, 2010.

[142] J. Y. Wong. *Theory of Ground Vehicles.* John Wiley & Sons, New York, 4th edition, 2001.

[143] A. Okello. A review of soil strength measurement techniques for prediction of terrain vehicle performance. *Journal of agricultural engineering research*, 50:129–155, 1991.

[144] R. D. Wismer and H. J. Luth. Off-road traction prediction for wheeled vehicles. *Journal of Terramechanics*, 10(2):49–61, 1973.

[145] A. R. Reece and J. O. Peca. An assessment of the value of the cone penetrometer in mobility prediction. In *7th International Conference of ISTVS*, volume 3, 1981.

[146] M. A. Thomas, D. E. Chitty, M. L. Gildea, and C. M. T'Kindt. Constitutive soil properties for unwashed sand and Kennedy Space Center. Tech. Rep. NASA/CR-2008-215334, National Aeronautics and Space Administration, Langley Research Center, Hampton, Virginia, July 2008.

[147] Soil Testing Lab, Direct Shear Test, Indian Institute of Technology Gandhinagar. http://www.iitgn.ac.in/research/stl/directshear.php.

[148] O. Onafeko. Instrumentation for measuring radial and tangential stresses beneath rigid wheels. *Journal of Terramechanics*, 1(3):61–68, 1964.

[149] O. Onafeko and A. R. Reece. Soil stresses and deformations beneath rigid wheels. *Journal of Terramechanics*, 4(1):59–80, 1967.

[150] H. Li and C. Schindler. Investigation of tire-soil interaction with analytical and finite element method. *Mechanics Based Design of Structures and Machines*, 41(3):293–315, 2013.

[151] H. Li. *Analysis of Off-Road Tire-Soil Interaction through Analytical and Finite Element Methods.* Ph.D. dissertation, Technische Universität Kaiserslautern, 2013.

[152] I. Schmid and J. Ludewig. Improved calculation of sinkage of a wheel on soft ground. In *5th European Conference ISTVS*, Budapest, September 1991.

[153] C. Harnisch, B. Lach, R. Jakobs, M. Troulis, and O. Nehls. A new tyre–soil interaction model for vehicle simulation on deformable ground. *Vehicle System Dynamics*, 43(S1):384–394, 2005.

[154] B. J. Chan and C. Sandu. Development of a 3-d quasi-steady state tyre model for on-road and off-road vehicle dynamics simulations: Part III – off-road flexible tyre model. *International Journal of Vehicle Systems Modelling and Testing*, 9(2):151–176, 2014.

[155] Z. J. Janosi. Analysis and presentation of soil-vehicle mechanics data. *Journal of Terramechanics*, 2(3):69–79, 1965.

[156] M. S. Osman. The measurement of soil shear strength. *Journal of Terramechanics*, 1(3):54–60, 1964.

[157] L. Myers, R. Roque, B. Ruth, and C. Drakos. Measurement of contact stresses for different truck tire types to evaluate their influence on near-surface cracking and rutting. *Journal of the Transportation Research Board*, 1655:175–184, 1999.

[158] T. M. Yu. *The tractive performance of a friction-based prototype track*. Ph.D. dissertation, University of Pretoria, Pretoria, South Africa, 2005.

[159] X. Zhang, B. Sun, Q. Sun, and N. Chen. Vehicle and terrain interaction based on ADAMS-MATLAB co-simulation. *Journal of Southeast University (English Edition)*, 25(3):335–339, 2009.

[160] S. Oida, E. Seta, H. Heguri, and K. Kato. Soil/tire interaction analysis using FEM and FVM. *Tire Science and Technology*, 33(1):38–62, 2005.

[161] M. Grujicic, H. Marvi, G. Arakere, and I. Haque. A finite element analysis of pneumatic-tire/sand interactions during off-road vehicle travel. *Multidiscipline Modeling in Materials and Structures*, 6(2):284–308, 2010.

[162] H. Li and C. Schindler. Three-dimensional finite element and analytical modelling of tyre-soil interaction. *Proceedings of the Institution of Mechanical Engineers, Part K: Journal of Multi-body Dynamics*, pages 42–60, 2012.

[163] A. Mohsenimanesh, S. M. Ward, P. O. Owende, and A. Javadi. Modeling of pneumatic tractor tyre interaction with multi-layered soil. *Biosystems Engineering*, 104(2):191–198, 2009.

[164] J. Allen II, M. El-Gindy, B. Shoffner, M. Trivedi, F. Öijer, and I. Johansson. Predictions of tire-terrain interactions using finite element analysis models. In *ASME International Design Engineering Technical Conference*, Las Vegas, Nevada, 4–7 September 2007. American Society of Mechanical Engineers.

[165] Ragheb H. *Torque Control Strategy for Off-Road Vehicle Mobility*. Ph.D. dissertation, University of Ontario Institute of Technology, Oshawa, Canada, 2014.

[166] J. D. Reid, B. A. Coon, B. A. Lewis, S. H. Sutherland, and Y. D. Murray. Evaluation of ls-dyna soil material model 147. Tech. Rep. FHWA-HRT-04-094, U.S. Department of Transportation, Federal Highway Administration, McLean, VA, November 2004.

[167] L. Schwer. Introduction to geomaterials. Class Notes: Concrete and Geomaterial Modeling with LS-DYNA, Schwer Engineering and Consulting Services, March 2009.

[168] R. D. Krieg. A simple constitutive description for cellular concrete. Tech. Rep. SC-DR-72-0883, Sandia National Laboratories, Albuquerque, 1972.

[169] E. L. Fasanella, K. E. Jackson, and S. Kellas. Soft soil impact testing and simulation of aerospace structures. In *10th International LS-DYNA Users Conference*, Dearborn, MI, USA, June 2008.

[170] L. Resende and J. B. Martin. Formulation of drucker-prager cap model. *Journal of Engineering Mechanics*, 111(7):855–881, 1985.

[171] O. G. Cueto, C. E. I. Coronel, C. A. R. Morfa, G. U. Sosa, L. H. H. Gómez, G. U. Calderón, and M. H. Suárez. Three dimensional finite element model of soil compaction caused by agricultural tire traffic. *Computers and electronics in agriculture*, 99:146–152, 2013.

[172] M. Namjoo and H. Golbakhshi. Numerical simulation of tire/soil interaction using a verified 3D finite element model. *Journal of Central South University*, 21(2):817–821, 2014.

[173] O. G. Cueto, C. E. I. Coronel, E. Bravo, C. A. R. Morfa, and M. H. Suárez. Modelling in FEM the soil pressures distribution caused by a tyre on a rhodic ferralsol soil. *Journal of Terramechanics*, 63:61–67, 2016.

[174] A. M. Recuero, U. Contreras, M. Patel, and A. A. Shabana. ANCF continuum-based soil plasticity for wheeled vehicle off-road mobility. *Journal of Computational and Nonlinear Dynamics*, 11(4):044504, 2016.

[175] L. Schwer. Laboratory tests for characterizing geomaterials. Class Notes: Concrete and Geomaterial Modeling with LS-DYNA, Schwer Engineering and Consulting Services, December 2001.

[176] R. F. Kulak and C. Bojanowski. Modeling of cone penetration test using SPH and MM-ALE approaches. In *8th European LS-DYNA Users Conference*, Strasbourg, France, May 2011.

[177] V. K. Ramalingam and H. M. Lankarani. Analysis of impact on soft soil and its application to aircraft crashworthiness. *International journal of crashworthiness*, 7(1):57–66, 2002.

[178] D. Marzougui, P. Mohan, and C. Kan. Evaluation of rail height effects on the safety performance of w-beam barriers. In *6th European LS-DYNA Conference*, Gothenburg, Sweden, 29–30 May 2007.

[179] H. Li and C. Schindler. Analysis of soil compaction and tire mobility with finite element method. *Proceedings of the Institution of Mechanical Engineers, Part K: Journal of Multi-body Dynamics*, 227(3):275–291, 2013.

[180] C. Goodin and J. D. Priddy. Comparison of SPH simulations and cone index tests for cohesive soils. *Journal of Terramechanics*, 66:49–57, August 2016.

[181] H. Nakashima, H. Fujii, A. Oida, M. Momozu, H. Kanamori, S. Aoki, T. Yokoyama, H. Shimizu, J. Miyasaka, and K. Ohdoi. Discrete element method analysis of single wheel performance for a small lunar rover on sloped terrain. *Journal of Terramechanics*, 47(5):307–321, 2010.

[182] C. Zhao and M. Zang. Analysis of rigid tire traction performance on a sandy soil by 3D finite element–discrete element method. *Journal of Terramechanics*, 55:29–37, 2014.

[183] M. Michael, F. Vogel, and B. Peters. Dem–fem coupling simulations of the interactions between a tire tread and granular terrain. *Computer Methods in Applied Mechanics and Engineering*, 289:227–248, 2015.

[184] D. Melanz, P. Jayakumar, and D. Negrut. Experimental validation of a differential variational inequality-based approach for handling friction and contact in vehicle/granular-terrain interaction. *Journal of Terramechanics*, 65:1–13, 2016.

[185] L. B. Lucy. A numerical approach to the testing of the fission hypothesis. *Astronomical Journal*, 82(1):1013–1024, 1977.

[186] R. A. Gingold and J. J. Monaghan. Smoothed particle hydrodynamics: theory and application to non-spherical stars. *Monthly notices of the royal astronomical society*, 181(3):375–389, 1977.

[187] H. Takeda, S. M. Miyama, and M. Sekiya. Numerical simulation of viscous flow by smoothed particle hydrodynamics. *Progress of Theoretical Physics*, 92(5):939–960, 1994.

[188] J. J. Monaghan. Simulating free surface flows with SPH. *Journal of computational physics*, 110(2):399–406, 1994.

[189] L. D. Libersky and A. G. Petschek. Smooth particle hydrodynamics with strength of materials. In *Advances in the free-Lagrange method including contributions on adaptive gridding and the smooth particle hydrodynamics method*, pages 248–257, Berlin, Heidelberg, 1991. Springer.

[190] S. Shokouhfar, S. Rakheja, and M. El-Gindy. Modal analysis of a rolling truck tyre subjected to inflation pressure and vertical deflection. *International Journal of Vehicle Systems Modelling and Testing*, 11(2):116–141, 2016.

[191] S. Shokouhfar, S. Rakheja, and M. El-Gindy. A simplified model for rolling tyre interactions with rigid surfaces using Part-Composite approach in LS-DYNA. *International Journal of Vehicle Systems Modelling and Testing*, 11(2):142–164, 2016.

[192] S. Shokouhfar, S. Rakheja, and M. El-Gindy. A virtual test platform for analyses of rolling tyre-soil interactions: Part I – Parametrization of terramechanics models. *Journal of Terramechanics*, 2016. (submitted).

[193] S. Shokouhfar, S. Rakheja, and M. El-Gindy. A virtual test platform for analyses of rolling tyre-soil interactions: Part II – Evaluations of terramechanics models. *Journal of Terramechanics*, 2016. (submitted).

[194] L. Lidner. Experience with the magic formula tyre model. *Vehicle System Dynamics*, 21(S1):30–46, 1992.

[195] W. Hall, R. P. Jones, and J. T. Mottram. Modeling of an automobile tyre using LS-DYNA3D. In *3rd European LS-DYNA Conference*, 2002.

[196] T. Takeyama, J. Matsui, and M. Hijiri. *Mechanics of Pneumatic Tires*, chapter Tire Cord and Cord to Rubber Bonding. U.S. Department of Transportation, National Highway Traffic Safety Administration (NHTSA), Washington DC, 1981.

[197] J. D. Walter. *Mechanics of Pneumatic Tires*, chapter Cord Reinforced Rubber. U.S. Department of Transportation, National Highway Traffic Safety Administration (NHTSA), Washington DC, 1981.

[198] S. K. Clark. *Mechanics of Pneumatic Tires*. U.S. Department of Transportation, National Highway Traffic Safety Administration (NHTSA), Washington DC, 1981.

[199] T. Belytschko, J. Lin, and C. S. Tsay. Explicit algorithms for the nonlinear dynamics of shells. *Computer Methods in Applied Mechanics and Engineering*, 42(2):225–251, 1984.

[200] W. T. Thomson and M. D. Dahleh. *Theory of vibration with applications*. Prentice Hall, New Jersey, USA, 5th edition, 1998.

[201] T. L. Ford and F. S. Charles. Heavy duty truck tire engineering. No. 880001, SAE Technical Paper, 1988.

[202] R. W. Scavuzzo, T. R. Richards, and L. T. Charek. Tire vibration modes and effects on vehicle ride quality. *Tire Science and Technology*, 21(1):23–39, 1993.

[203] R. K. Taylor, L. L. Bashford, and M. D. Schrock. Methods for measuring vertical tire stiffness. *Transactions of the American Society of Agricultural Engineers (ASAE)*, 43(6):1415–1420, 2000.

[204] P. S. Fancher. Descriptive parameters used in analyzing the braking and handling of heavy trucks - measurements of the longitudinal and lateral traction properties of truck tires, data volume iii. Tech. Rep. UM-HSRI-81-19-3-4, University of Michigan, Highway Safety Research Institute, 1981.

[205] H. Van Eldik Thieme, A. J. Dijks, and S. Bobo. *Mechanics of Pneumatic Tires*, chapter Measurement of tire properties. U.S. Department of Transportation, National Highway Traffic Safety Administration (NHTSA), Washington DC, 1981.

[206] Y. Wei, C. Oertel, and X. Shen. Tyre rolling kinematics and prediction of tyre forces and moments: part II – simulation and experiment. *Vehicle System Dynamics*, 50(11):1689–1706, 2012.

[207] G. Baffet, A. Charara, and D. Lechner. Estimation of vehicle side-slip, tire force and wheel cornering stiffness. *Control Engineering Practice*, 17(11):1255–1264, 2009.

[208] J. E. Longhouser. Investigation of the cornering dynamics of a military tire. Tech. Rep. SIT-DL-72-1609, Davidson Lab, Stevens Institute of Technology, Hoboken, New Jersey, 1972.

[209] T. Belytschko, W. K. Liu, and B. Moran. *Nonlinear Finite Elements for Continua and Structures*. John Wiley & Sons Ltd, England, 2000.

[210] Klaus-Jürgen Bathe. *Finite Element Procedures*. Prentice Hall, New Jersey, USA, 2006.

[211] P. Kohnke. Theory reference for the mechanical APDL and mechanical applications. ANSYS, Inc., Release 12, 2009.

[212] B. G. Kao. Tire vibration modes and tire stiffness. *Tire Science and Technology*, 30(3):136–155, 2002.

[213] G. Gim and P. Nikravesh. An analytical model of pneumatic tyres for vehicle dynamic simulations, part 2: Comprehensive slips. *International journal of vehicle design*, 12(1):19–39, 1991.

[214] Ch. Oertel and A. Fandre. Ride comfort simulations and steps towards life time calculations: RMOD-K and ADAMS. In *International ADAMS User Conference*, Berlin, Germany, 1999.

[215] G. Gim and Y. Choi. Role of tire modeling on the design process of a tire and vehicle system. In *ADMAS User Conference*, Busan, Korea, November 2001. Hankook Tires.

[216] J. Svendenius and M. Gäfvert. A semi-empirical tyre model for combined slips including the effects of cambering. *Vehicle System Dynamics*, 43(S1):317–328, 2005.

[217] K. Guo, D. Lu, S. K. Chen, W. C. Lin, and X. Lu. Uni Tire model: a non-steady tire model for vehicle dynamic simulation. *Vehicle System Dynamics*, 43(S1):341–358, 2005.

[218] M. Gipser. FTire: the tire simulation model for all applications related to vehicle dynamics. *Vehicle System Dynamics*, 45(S1):139–151, 2007.

[219] S. Kim, P. Nikravesh, and G. Gim. A two-dimensional tire model on uneven roads for vehicle dynamic simulation. *Vehicle System Dynamics*, 46(10):913–930, 2008.

[220] E. L. Fasanella, K. H. Lyle, and K. E. Jackson. Developing soil models for dynamic impact simulations. Tech. Rep. NASA/LF99-7733, National Aeronautics and Space Administration, Langley Research Center, Hampton, Virginia, May 2009.

[221] Z. Janosi and B. Hanamoto. Analytical determination of drawbar pull as a function of slip on tracked vehicles in deformable soils. In *1st International Conference on Terrain-Vehicles Systems*, Turin, 1961.

[222] L. L. Karafiath. Plasticity theory and the stress distribution beneath wheels. *Journal of Terramechanics*, 8(2):49–60, 1971.

[223] C. W. Plackett. A review of force prediction methods for off-road wheels. *Journal of Agricultural Engineering Research*, 31(1):1–29, 1985.

[224] J. Maciejewski and A. Jarzebowski. Experimental analysis of soil deformation below a rolling rigid cylinder. *Journal of Terramechanics*, 41(4):223–241, 2004.

[225] G. Gim and P. Nikravesh. An analytical model of pneumatic tires for vehicle dynamic simulations, part 1: Pure slips. *International Journal of Vehicle Design*, 11:589–618, 1990.

[226] B. J. Chan and C. Sandu. Development of a 3-d quasi-static tyre model for on-road and off-road vehicle dynamics simulations: Part I – on-road flexible tyre model. *International Journal of Vehicle Systems Modelling and Testing*, 9(1):77–105, 2014.

[227] G. Krick. Radial and shear stress distribution beneath rigid wheels and pneumatic tyres on yielding soils with regard to tyre deformation. *Journal of Terramechanics*, 6(3):73–98, 1969.

[228] C. H. Liu, J. Y. Wong, and H. A. Mang. Large strain finite element analysis of sand: model, algorithm and application to numerical simulation of tire–sand interaction. *Computers & Structures*, 74(3):253–265, 2000.